University of Alberta

Orthogonal Frequency Division Multiplexing Data Transmission System Designs for Intercarrier Interference Mitigation

by

Peng Tan ©

A thesis submitted to the Faculty of Graduate Studies and Research in partial fulfillment of the requirements for the degree of **Doctor of Philosophy**.

Department of Electrical and Computer Engineering

Edmonton, Alberta

Fall 2006

Your file Votre référence
ISBN: 978-0-494-23116-6
Our file Notre référence
ISBN: 978-0-494-23116-6

Abstract

Orthogonal frequency division multiplexing (OFDM) is being widely used in several wireless communications physical layer specifications due to its ability to effectively convert a frequency-selective fading channel into several flat fading channels. However, it is highly sensitive to frequency offset which introduces inter-carrier interference (ICI) and, hence, performance degradation. This thesis contributes to the exact bit error rate (BER) performance analysis of OFDM systems in the presence of carrier frequency offset in additive white Gaussian noise (AWGN) environments and in wireless transmission environments, as well as contributes to the design and assessment of several ICI cancellation schemes.

An exact analytical BER expression is derived for a $\pi/4$-DQPSK OFDM system with multi-channel reception in the presence of carrier frequency offset over frequency-selective fast Rayleigh fading channels. By using the precise BER expression, an optimum number of subcarriers can be found, and the allowable carrier frequency offset, Doppler shift, and mean delay spread for given operating conditions can be determined.

Several ICI cancellation schemes are investigated. The "better than" raised-cosine pulse (BTRC) and the Franks pulse are proposed to use in the OFDM transmitter pulse-shaping and the receiver windowing to reduce ICI power and improve BER performance. A zero-padded discrete cosine transform (DCT)-based OFDM scheme is proposed, and its per-

formance is examined in multipath fading environments. Analysis and simulation results show that the DCT-OFDM system outperforms the conventional discrete Fourier transform (DFT)-based OFDM system in the presence of frequency offset, and in frequency-selective fading environments. In other contributions to ICI cancellation schemes, the partial-response pulse-shaped OFDM system and the widely linear minimum mean-square error (MMSE) equalizer for real-valued modulation formats are proposed in this thesis to mitigate ICI and improve BER performance.

Channel estimation error also introduces performance degradation in OFDM systems. Therefore, in another contribution of this thesis, a characteristic function-based method is used to derive closed-form BER expressions for OFDM systems in the presence of channel estimation error over frequency-selective Rayleigh fading channels and frequency-selective Ricean fading channels. By using these BER expressions, the performances of two interpolation methods, a sinc interpolator with Hamming windowing and a Wiener interpolator are compared.

Acknowledgements

First, I would like to express my sincere gratitude to my Ph.D. program supervisor, Professor Norman C. Beaulieu, for his continuous encouragement, invaluable guidance and support throughout my doctoral research. Without him, this thesis would never have been possible. I have also benefited greatly from his serious-minded attitude toward work and study, clarity in thinking, and professional integrity.

I would like to thank Dr. Leonard J. Cimini Jr., a pioneer in the application of OFDM to high-speed wireless systems, for his willingness to serve as my external examiner. I would also like to thank Dr. Byron Schmuland, Dr. Bruce F. Cockburn, Dr. Behrouz Nowrouzian, and Dr. Masoud Ardakani for serving on my committee.

It has been my pleasure to work at the *i*CORE wireless communications lab where I have been offered great opportunities to conduct my research, and to learn from other wonderful people in this team.

My special gratitude goes to my wife, Jia, for her continuous encouragement and numerous technical discussions with me.

I feel particularly indebted to my parents for their understanding, unconditional support, encouragement, and endless love throughout years.

Last, I would like to thank the Alberta Ingenuity Fund, the Alberta Informatics Circle of Research Excellence (*i*CORE), as well as China Scholarship Council for their financial support.

To Jia and my parents

Contents

1 Introduction **1**

1.1 A Brief History of OFDM 1

1.2 Basic Principles of OFDM 2

1.3 Mobile Radio Channels 6

1.4 Thesis Outline and Contributions 9

2 Precise BER Analysis of $\pi/4$-DQPSK OFDM with Carrier Frequency Offset Over Frequency Selective Fast Fading Channels **14**

2.1 Introduction 14

2.2 System Model 17

2.3 Precise BER Analysis 20

2.3.1 BER for Single Branch Reception 24

2.3.2 BER for Multi-Branch Reception 26

2.4 Examples and Discussion 28

2.5 Summary 39

3 Exact BER Analysis of OFDM Systems over Rayleigh and Ricean Fading Channels in the Presence of Channel Estimation Error **40**

3.1 Introduction 40

3.2 System Model 42

3.3 Rayleigh Fading Channels 47

3.4 Ricean Fading Channels 52

3.5 Examples and Discussion 54

3.6 Summary 60

4 The Effect of Transmitter Nyquist Shaping on ICI Reduction in OFDM Systems with Carrier Frequency Offset 63

4.1 Introduction 63

4.2 System Model 68

4.3 ICI and SIR Analysis 71

4.4 Bit Error Rate Performance 85

4.4.1 BPSK-OFDM 89

4.4.2 QPSK-OFDM 90

4.4.3 16QAM-OFDM 91

4.5 Numerical Results and Discussions 92

4.5.1 Numerical Results 92

4.5.2 Bandwidth Efficiency 102

4.6 Summary 105

5 Correlative Coding and Partial-Response Pulse-Shaping in OFDM Systems 106

5.1 Introduction 106

5.2 Partial-Response Pulse-Shaped OFDM 108

5.3 BER Analysis over AWGN Channels 114

5.4 Summary 118

6 Receiver Windowing in OFDM Systems 121

6.1 Introduction 121

6.2 System Model 123

6.3 Intercarrier Interference 127

6.4 Bit Error Rate Analysis 129

6.5 Summary 139

7 A DCT-Based OFDM Data Transmission Scheme 142

7.1 Introduction 142

7.2 System Model 145

7.3 Intercarrier Interference Analysis 149
7.4 Exact BER Analysis on AWGN Channels 155
7.4.1 QPSK modulation 155
7.4.2 16-ary QAM 158
7.4.3 Numerical Results 161
7.5 Performance Over Frequency-Selective Fast Fading Channels 165
7.5.1 MMSE Detection 168
7.5.2 MMSE Decision-Feedback Detection with Ordering 168
7.5.3 Computational Complexity 170
7.5.4 Computer Simulations 171
7.6 Summary 175

8 Widely Linear MMSE Equalization for One-Dimensional Modulation OFDM Systems 179
8.1 Introduction 179
8.2 System Model 180
8.3 Widely Linear MMSE receiver for 1-D modulation formats 182
8.4 Simulation Results 186
8.5 Summary 192

9 Conclusions and Future Work 193
9.1 Conclusions 193
9.2 Suggestions for Future Work 197

References 199

Appendix A 214

Appendix B 217

List of Figures

1.1 A parallel data transmission system. 3
1.2 A typical wireless OFDM architecture 5

2.1 The contour for the integral in eq. (2.37) 25
2.2 The effect of different normalized Doppler shift values on the system BER performance for $\Delta f T_u = \overline{\tau}/T_u = 0.002$, $N = 8$. 29
2.3 The effect of different normalized mean delay spread values on the system BER performance for $f_D T_u = \Delta f T_u = 0.002$, $N = 64$. 33
2.4 The system BER as a function of the number of subcarriers. 35
2.5 The effect of Doppler shift and carrier frequency offset on the system BER performance for $\bar{\tau}/T_u = 0.002$, $N = 64$, and $D = 2, 3$ and 4. 36
2.6 The BER versus the normalized carrier frequency offset, versus the normalized Doppler shift, and versus the normalized mean delay spread with $N = 64$ and SNR=20 dB. 38

3.1 The BER performance of a 16-QAM-OFDM system over a Rayleigh fading channel with a sinc interpolator, Wiener interpolator, and perfect channel information, for I reception branches. 55
3.2 The BER performance of a 16-QAM-OFDM system over a Ricean fading channel with a sinc interpolator, Wiener interpolator, and perfect channel information, for I reception branches and Ricean factor $K = 2$ dB. 56
3.3 The BER performance of a 16-QAM-OFDM system over a Ricean fading channel with Wiener interpolator, single channel reception, $\xi = \eta = 0.02$, and Ricean factors $K = 3$ dB, 5 dB, 7 dB and 9 dB. 58

3.4 The BER performance of a 16-QAM-OFDM system over a Rayleigh fading channel with a sinc interpolator and Wiener interpolator, $\eta = 0.02$, and normalized maximum Doppler shift $\xi = 0.01$ and 0.1. 59
3.5 The effect of pilot spacing on the BER performance of a 16-QAM-OFDM system over a Ricean fading channel with Wiener interpolator, diversity branches $I = 4$, Ricean factor $K = 2$ dB, normalized maximum Doppler shift $\xi = 0.02$, and normalized mean delay spread $\eta = 0.02$. 61

4.1 The time domain waveform of the raised-cosine pulse ($\alpha = 0.25$). 72
4.2 The time domain waveform of the "better than" raised-cosine pulse ($\alpha = 0.25$). 73
4.3 The time domain waveform of the SOCW pulse ($\alpha = 0.25$). 74
4.4 The time domain waveform of the polynomial pulse ($\alpha = 0.25$). 75
4.5 The time domain waveform of the Franks pulse ($\alpha = 0.25$). 76
4.6 The time domain waveform of the double-jump pulse ($\alpha = 0.25$). 77
4.7 The frequency spectra of different pulse-shaping functions ($\alpha = 0.25$). . . . 81
4.8 The frequency spectra of different pulse-shaping functions ($\alpha = 1.0$). . . . 82
4.9 The ICI power in a 64-subcarrier OFDM system with the employment of different pulse-shaping functions ($\alpha = 0.25$). 85
4.10 The signal-to-interference ratio in a 64-subcarrier OFDM system with the employment of different pulse-shaping functions ($\alpha = 0.25$). 86
4.11 The ICI power in a 64-subcarrier OFDM system with the employment of different pulse-shaping functions ($\alpha = 1.0$). 87
4.12 The signal-to-interference ratio in a 64-subcarrier OFDM system with the employment of different pulse-shaping functions ($\alpha = 1.0$). 88
4.13 The average BER performance of a BPSK-OFDM system with the employment of different pulse-shaping functions ($\alpha = 0.25$) in the presence of normalized frequency offset $\Delta f T_u = 0.2$. 93
4.14 The average BER performance of a BPSK-OFDM system with the employment of different pulse-shaping functions ($\alpha = 0.25$) in the presence of normalized frequency offset $\Delta f T_u = 0.1$. 94

4.15 The average BER performance of a BPSK-OFDM system with the employment of different pulse-shaping functions ($\alpha = 1.0$) in the presence of normalized frequency offset $\Delta f T_u = 0.1$ and 0.2. 95
4.16 The average BER performance of a QPSK-OFDM system with the employment of different pulse-shaping functions ($\alpha = 0.25$) in the presence of normalized frequency offset $\Delta f T_u = 0.08$ and 0.1. 98
4.17 The average BER versus roll-off factor α for a 64-subcarrier BPSK-OFDM system with the employment of different pulse-shaping functions for $\Delta f T_u = 0.1$ and $E_b/N_0 = 10$ dB. 99
4.18 The average BER versus roll-off factor α for a 64-subcarrier QPSK-OFDM system with the employment of different pulse-shaping functions for $\Delta f T_u = 0.12$ and $E_b/N_0 = 20$ dB. 100
4.19 The average BER performance of a 16QAM-OFDM system with the employment of different pulse-shaping functions ($\alpha = 0.25$) in the presence of normalized frequency offset $\Delta f T_u = 0.03$ and 0.05. 101
4.20 Comparison of several pulse-shaped OFDM systems at a BER of 10^{-5}, $\alpha = 0.25$, $\Delta f T_u = 0.04$. 103
4.21 Comparison of several pulse-shaped OFDM systems at a BER of 10^{-5}, $\alpha = 0.25$, $\Delta f T_u = 0.1$. 104

5.1 The Fourier transforms of the partial-response pulse and the rectangular pulse. 113
5.2 The receiver decision regions for the pulse-shaped OFDM system and the rectangular pulse-shaped OFDM system. 114
5.3 Comparisons of the system BERs with partial-response pulse-shaping (or correlative coding) and the system with rectangular pulse-shaping (without correlative coding) transmitted over an AWGN channel in the presence of normalized frequency offsets 0.02, 0.05 and 0.1. 119
5.4 Comparisons of the system BERs with partial-response pulse-shaping (or correlative coding) and the system with rectangular pulse-shaping (without correlative coding) transmitted over an AWGN channel in the presence of normalized frequency offsets 0.15, 0.2, 0.25 and 0.3. 120

6.1 The SIR in a 64-subcarrier OFDM receiver windowing with the employment of different window functions ($\alpha = 0.3$, and 1.0). 130
6.2 The frequency spectra of different window functions ($\alpha = 0.3$). 131
6.3 The bit error rate in 64-subcarrier QPSK-OFDM receiver windowing with the employment of different window functions ($\alpha = 0.3$). 134
6.4 The bit error rate in 64-subcarrier QPSK-OFDM receiver windowing with the employment of different window functions ($\alpha = 1.0$). 135
6.5 The bit error rate in 64-subcarrier QPSK-OFDM receiver windowing with the employment of the BTRC window functions, $\varepsilon = 0.1$, and $\alpha = 0.1, 0.2$, 0.4, 0.6, 0.8 and 1.0. 136
6.6 The bit error rate as a function of roll-off factor α for 64-subcarrier QPSK-OFDM windowing reception with the employment of different window functions, $E_b/N_0 = 50$ dB, $\varepsilon = 0.1$. 140
6.7 The bit error rate in 64-subcarrier QPSK-OFDM receiver windowing with the employment of the Franks window functions, $\alpha = 0.5$, $\varepsilon = 0.02$, and $\eta = 0.01, 0.05, 0.1$ and 0.4. 141

7.1 The power spectral density of (a) a 64-subcarrier DFT-OFDM baseband signal and (b) a 64-subcarrier DCT-OFDM baseband signal. 147
7.2 The DCT-based orthogonal frequency-division multiplexing system. 149
7.3 The ICI weighting coefficients $|S^I_{n,k}|$ in a 64-subcarrier BPSK DCT-OFDM system and $|\Re\{F_{n-k}\}|$ in a 64-subcarrier BPSK DFT-OFDM system (a) $\Delta f T_u = 0.2$, (b) $\Delta f T_u = 0.05$, and $k = 32$. 153
7.4 The SIR of the DCT-OFDM system and the DFT-OFDM system as a function of the normalized carrier frequency offset. 156
7.5 The BER performances of 64-subcarrier DCT-OFDM with BPSK modulation and 64-subcarrier DFT-OFDM with BPSK modulation in the presence of normalized frequency offset $\Delta f T_u = 0.02, 0.1$ and 0.2. 161
7.6 The BER performances of 64-subcarrier DCT-OFDM with QPSK modulation and 64-subcarrier DFT-OFDM with QPSK modulation in the presence of normalized frequency offset $\Delta f T_u = 0.05, 0.08, 0.1$ and 0.12. 162

7.7 The BER performances of 64-subcarrier DCT-OFDM with 16-QAM signaling and 64-subcarrier DFT-OFDM with 16-QAM signaling in the presence of normalized frequency offset $\Delta f T_u = 0.02, 0.03, 0.04$ and 0.05. 163

7.8 The BER performance of the MMSE receiver for 64-subcarrier ZP-DCT-OFDM, ZP-DFT-OFDM, and CP-DFT-OFDM, with BPSK modulation and perfect channel state information. 173

7.9 The BER performance of the MMSE receiver for a 64-subcarrier QPSK ZP-DCT-OFDM and a 64-subcarrier QPSK ZP-DFT-OFDM with convolutional coding and interleaving. 174

7.10 The BER performance of the MMSE DFD with ordering scheme for a 64-subcarrier QPSK ZP-DCT-OFDM and a 64-subcarrier QPSK ZP-DFT-OFDM. 176

7.11 The BER performances of the MMSE receiver for 64-subcarrier QPSK ZP-DCT-OFDM and 64-subcarrier QPSK ZP-DFT-OFDM with channel estimation. 177

8.1 The average error power of a 64-subcarrier ZP-DFT-OFDM (BPSK) system with the linear MMSE equalizer in (8.8) and with the widely linear MMSE equalizer for 1-D modulation formats in (8.28). 188

8.2 The BERs of a 64-subcarrier ZP-DFT-OFDM (BPSK) system and a 64-subcarrier CP-DFT-OFDM (BPSK) system with the employment of a linear MMSE equalizer and a widely linear MMSE equalizer, $f_d T_u = 0.05$. 189

8.3 The BERs of a 64-subcarrier ZP-DFT-OFDM (4PAM) system and a 64-subcarrier CP-DFT-OFDM (4PAM) system with the employment of a linear MMSE equalizer and a widely linear MMSE equalizer, $f_d T_u = 0.05$. 190

8.4 The BERs of a 64-subcarrier ZP-DCT-OFDM (BPSK) with the employment of a linear MMSE equalizer and a widely linear MMSE equalizer, $f_d T_u = 0.001, 0.02, 0.05, 0.1$ and 0.2. 191

List of Acronyms

List of Acronyms	Definition
ADSL	asymmetric digital subscriber line
AWGN	additive white Gaussian noise
BER	bit error rate
BEP	bit error probability
BPSK	binary phase shift keying
BTRC	"better than" raised-cosine
CDF	cumulative distribution function
CHF	characteristic function
CIR	channel impulse response
CFT	chirp Fourier transform
CP	cyclic prefix
CSI	channel state information
DAB	digital audio broadcasting
DCT	discrete cosine transform
DFD	decision feedback detection
DFT	discrete Fourier transform
DQPSK	differentially encoded quadrature phase shift keying
DVB-T	digital video broadcasting over terrestrial
ETSI	European Telecommunications Standard Institute
FFT	fast Fourier transform
GMSK	Gaussian minimum shift keying
ICI	inter-carrier interference

IDCT	inverse discrete cosine transform
IDFT	inverse discrete Fourier transform
IFFT	inverse fast Fourier transform
i.i.d.	independent and identically distributed
ISI	intersymbol interference
LAN	local area network
LOS	line-of-sight
MAN	metropolitan area network
MCM	multicarrier modulation
ML	maximum-likelihood
MMSE	minimum mean-square error
MRC	maximum ratio combining
OFDM	orthogonal frequency division multiplexing
OQPSK	offset quadrature phase-shift keying
PAM	pulse amplitude modulation
PDF	probability density function
PSK	phase shift keying
QAM	quadrature amplitude modulation
QPSK	quadrature phase shift keying
SAW	surface acoustic wave
SIR	signal-to-interference ratio
SNR	signal-to-noise ratio
SOCW	second-order continuous window
SSB	single-sideband
WLAN	wireless local area network
WSSUS	wide-sense stationary uncorrelated scattering
ZP	zero padding

List of Symbols

Symbol	Definition
α	pulse roll-off factor
$\mathbf{A}^{\mathbb{H}}$	Hermitian transpose of matrix **A**
$\mathbf{A}^{\mathbb{T}}$	transpose of matrix **A**
B_c	coherence bandwidth
$\mathbf{C}$	covariance matrix for the MMSE estimation error
$\mathbf{C}_{cp}$	cyclic prefix matrix
$\mathbf{C}_{zp}$	zero-padding matrix
$\mathbf{R}_{cp}$	cyclic prefix removal matrix
C_n^k	the number of combinations of n indistinguishable things taken k at a time
$\mathbf{d}$	data symbol vector in one OFDM symbol
$\mathbf{D}$	DCT matrix
$D_{i,n}$	complex symbol modulated onto the nth subcarrier in the ith OFDM symbol
$\hat{D}_{i,n}$	decision statistics for $D_{i,n}$
$D(r,c)$	the rth row and cth column element of matrix **D**
$\delta[n]$	unit sample sequence
Δt	OFDM symbol index
Δf	frequency offset or OFDM subcarrier index
$\Delta\phi_n$	differential phase
ε	normalized carrier frequency offset
E_b	energy per bit

E_s	energy per symbol
$\mathbf{E}(X)$	expectation of X
η	normalized mean delay spread
f_c	carrier frequency
f_d	maximum Doppler shift
f_m	frequency of the mth subcarrier
$f(p,q,\Delta t,\Delta f)$	interpolation function
F	frequency-domain spacing
$\mathbf{F}$	IDFT matrix
F_n	ICI weighting coefficient for DFT-OFDM, subcarrier index n
$S_{n,k}$	ICI weighting coefficient for DCT-OFDM, desired subcarrier index k, and subcarrier index n
$S^I_{n,k}$	real part of $S_{n,k}$
$S^Q_{n,k}$	imaginary part of $S_{n,k}$
$F_X(x)$	CDF of X
F_Δ	minimum subcarrier frequency spacing
$\mathbf{G}$	equalization matrix with widely linear MMSE
$\mathbf{G}_x$	the matrix whose elements are the real parts of the corresponding elements of the matrix $\mathbf{G}$
$\mathbf{G}_y$	the matrix whose elements are the imaginary parts of the corresponding elements of the matrix $\mathbf{G}$
$\mathbf{G}_1$	equalization matrix with linear MMSE
$h(\tau,t)$	channel impulse response
$h_l(t)$	complex amplitude of the lth fading path
$\mathbf{H}_0$	channel convolutional matrix
$H(t,f)$	channel response at the time instant t and frequency f
$\mathbf{H}^\dagger$	pseudo-inverse of matrix $\mathbf{H}$
$\Im\{X\}$	imaginary part of X
$\mathbf{I}_N$	$N\times N$ identity matrix
$I_n(\cdot)$	modified Bessel function of the first kind of order n
j	imaginary unit, $j=\sqrt{-1}$

$J_0(\cdot)$	Bessel function of the first kind of order 0
K	Ricean K parameters
$\mathbf{M}$	covariance matrix
$\oplus$	modulo-2 addition
μ	ratio of CP time to "useful" time
N	the number of subcarriers
$\lfloor a \rfloor$	a nearest integer less than or equal to a
ϕ_n	phase of the symbol modulated on the nth subcarrier
$\Phi(\omega)$	characteristic function
$\Psi(\omega)$	characteristic function
P_b	average bit error probability
$P_{b,BPSK}$	average bit error probability for BPSK modulation
$P_{b,QPSK}$	average bit error probability for QPSK modulation
$P_{b,16QAM}$	average bit error probability for 16-ary QAM
P_m	precoded sequence
p_m	samples of the Nyquist pulse
$p_{rc}(t)$	raised-cosine pulse
$P_{rc}(f)$	Fourier transform of $p_{rc}(t)$
$p_{btrc}(t)$	"better than" raised-cosine pulse
$P_{btrc}(f)$	Fourier transform of $p_{btrc}(t)$
$p_{socw}(t)$	Second-order continuous window pulse
$P_{socw}(f)$	Fourier transform of $p_{socw}(t)$
$p_{poly}(t)$	polynomial pulse
$P_{poly}(f)$	Fourier transform of $p_{poly}(t)$
$p_f(t)$	Franks pulse
$P_f(f)$	Fourier transform of $p_f(t)$
$p_{dj}(t)$	double-jump pulse
$P_{dj}(f)$	Fourier transform of $p_{dj}(t)$
$p_r(t)$	rectangular pulse
$P_r(f)$	Fourier transform of $p_r(t)$
$\tilde{p}_{pr}(t)$	time domain response of the duobinary partial-response pulse

$\tilde{P}_{pr}(f)$	Fourier transform of $\tilde{p}_{pr}(t)$
$p_{pr}(t)$	time domain response of the duobinary partial-response pulse under a new frequency origin to transform $\tilde{p}_{pr}(t)$ to a real pulse
$P_{pr}(f)$	Fourier transform of $p_{pr}(t)$
$p_{pr}^{d}(t)$	time delay version of $p_{pr}(t)$
$p_{pr}^{s}(t)$	scaled version of $p_{pr}^{d}(t)$ with normalized pulse energy
$\mathrm{Prob}(A\|B)$	probability of event A conditioned on event B
$Q(a,b)$	Marcum Q function with arguments a and b
$\Re\{X\}$	real part of X
X^*	conjugate of X
$r_{d,p}$	received signal for the pth subcarrier from the dth diversity branch
$s(t)$	continuous-time baseband OFDM signal
$\mathbb{S}$	symbol set
σ^2	noise variance
σ_f^2	fading variance
σ_{ICI}^2	ICI power
σ_s^2	desired subcarrier signal power
$tr(\mathbf{A})$	trace of matrix **A**
$\bar{\tau}$	mean delay spread
τ_l	propagation delay of the lth fading path
t_c	coherence time
T	time-domain spacing
T_m	maximum excess delay
T_g	duration of cyclic prefix
T_s	duration of one OFDM symbol ($T_s = T_u + T_g$)
T_u	duration of one OFDM symbol without guard interval
$u(t)$	unit step function
$w(t)$	zero-mean complex Gaussian noise process
w_m	zero-mean complex Gaussian noise sample
ξ	normalized maximum Doppler shift

Chapter 1

Introduction

1.1 A Brief History of OFDM

The history of orthogonal frequency division multiplexing (OFDM) can be dated back to the end of the 1950s [1] when Collins Radio Co. developed a 20-channel parallel data transmission system operating over the telephone voice band. Later, the employment of band-limited orthogonal signals for multi-channel data transmission was studied in [2–4]. In this system, data signals are frequency-multiplexed simultaneously on a number of mutually orthogonal carriers such that overlapping, but band-limited, frequency spectra are produced without causing inter-carrier interference (ICI) and intersymbol interference (ISI).

From the practical point of view, a major disadvantage of the systems above is that the numbers of banks of carrier oscillators and coherent demodulators required become unreasonably expensive and complex for a large number of carriers. An approach to use the inverse discrete Fourier transform (IDFT)/discrete Fourier transform (DFT), and further their fast algorithm inverse fast Fourier transform (IFFT)/fast Fourier transform (FFT), to implement the modulation and demodulation processes in OFDM systems was proposed in [5]. Although their system does not obtain perfect orthogonality between subcarriers over a dispersive channel, it is a major contribution to OFDM technology. Instead of using an empty guard time between OFDM symbols, reference [6] introduced a cyclic prefix (CP) in OFDM systems. This ensures that delayed replicas of the OFDM symbols always have an integer number of cycles within the DFT interval, as long as the delay is smaller than the guard time. As a result, the orthogonality between the subcarriers will not be destroyed even in a dispersive channel.

OFDM is a very attractive technology for broadband wireless communications because it converts a frequency-selective fading channel into several nearly flat-fading channels, which can simplify the channel equalization needs. The application of OFDM has been considered in several broadband data transmission systems, such as digital wireless communications [7], asymmetric digital subscriber line (ADSL) [8, 9], and broadcasting systems [10]. Particularly, OFDM-based physical layer technologies are being widely used in several wireless local area networks (LAN) and metropolitan area networks (MAN) standards, such as IEEE 802.11a [11] and IEEE 802.16 [12, 13]. This technology is also being used in many systems proposed by the European Telecommunications Standard Institute (ETSI), such as, digital audio broadcasting (DAB) [14], digital video broadcasting over terrestrial (DVB-T) [15] and HIPERLAN/2 [16]. Furthermore, there is growing interest in using OFDM for the next generation of land mobile communication systems.

1.2 Basic Principles of OFDM

The basic principle of OFDM can be explained by first considering the parallel data transmission system shown in Fig. 1.1.

A serial source bit stream at RN bits/s is transformed into N parallel source bit streams each with data rate R bits/s. Then, the N encoders map these data bits onto complex-valued points in a signal space diagram as $d_m^I + jd_m^Q$, $m = 0, 1, \cdots, N-1$ where $j = \sqrt{-1}$. At the

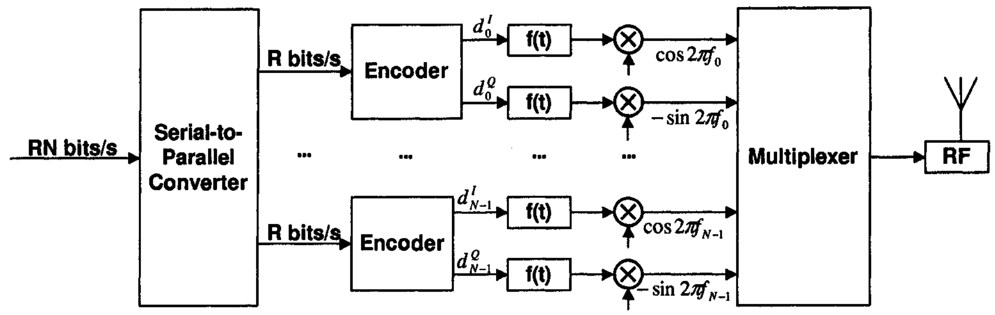

Fig. 1.1. A parallel data transmission system.

transmitter, N carriers are modulated by N data symbols according to

$$d_m^I f(t)\cos 2\pi f_m t - d_m^Q f(t)\sin 2\pi f_m t \tag{1.1}$$

where

$$f_m = \frac{m}{T_u} \tag{1.2}$$

is the frequency of the mth subcarrier, T_u is the duration of one data symbol, and $f(t)$ is the signal pulse defined by

$$f(t) = \begin{cases} 1, & 0 \le t < T_u \\ 0, & \text{otherwise.} \end{cases} \tag{1.3}$$

The sum of N modulated signals is transmitted at one time, so one OFDM symbol $x(t)$ is given as

$$x(t) = \Re\left[\sum_{m=0}^{N-1}(d_m^I + jd_m^Q)f(t)e^{j2\pi f_m t}\right] \tag{1.4}$$

where $\Re\{\gamma\}$ denotes the real part of γ. It is easy to show that

$$\frac{1}{T_u}\int_0^{T_u} e^{j2\pi f_m t}\cdot e^{-j2\pi f_n t}\,dt = \delta_{mn}(m-n) \tag{1.5}$$

where $\delta_{mn}(m-n)$ denotes the Kronecker delta function that is defined as

$$\delta_{mn}(m-n) = \begin{cases} 1, & \text{if } m = n \\ 0, & \text{otherwise.} \end{cases} \tag{1.6}$$

Therefore, the sub-carrier signals are mutually orthogonal and the data symbols can be recovered by using a correlation technique, although at this time the spectrum of the parallel system is the sum of N overlapping sinc functions [17].

One of the disadvantages of the system above is that we must employ N modulators, N demodulators and N oscillators to complete modulation and demodulation, and this is very inconvenient and costly from the implementation point of view. Next, we will show that one can use an IDFT to implement the system.

Sampling the signal $x(t)$ at time instants $t_n = \{\frac{nT_u}{N}\}_{n=0}^{N-1}$ gives N samples described by

$$\begin{aligned} Y_n &= \Re\left[\sum_{m=0}^{N-1}(d_m^I + jd_m^Q)f(t_n)e^{j2\pi\frac{m}{T_u}\frac{nT_u}{N}}\right] \\ &= \Re\left[\sum_{m=0}^{N-1}(d_m^I + jd_m^Q)e^{\frac{j2\pi nm}{N}}\right] \\ &= \Re\left\{\mathrm{IDFT}[d_m^I + jd_m^Q]_{m=0}^{N-1}\right\} \quad n = 0, 1, \cdots, N-1. \end{aligned} \tag{1.7}$$

Clearly, the N samples consist of the real part of an N-point IDFT of source data symbols $\{d_m^I + jd_m^Q\}_{m=0}^{N-1}$. From the sampling theorem [17, 18], the continuous-time signals can be restored from the discrete samples by passing them through an ideal reconstruction filter.

In wireless communications systems, it is a common configuration to modulate baseband signals to the required radio frequency band by employing both in-phase and quadrature modulators to implement complex data symbol transmission. Hence, one can transmit both the real and the imaginary components of the IDFT in the system. Moreover, in many treatments [17, 19–21], to make the discrete Fourier transforms unitary, the multiplicative factor $1/N$ in IDFT is usually redistributed between the DFT and IDFT. That is, the N-point DFT of sequence $\{x_n\}_{n=0}^{N-1}$ is defined as

$$X_k = \frac{1}{\sqrt{N}}\sum_{n=0}^{N-1} x_n e^{-\frac{j2\pi nk}{N}} \tag{1.8}$$

and the N-point IDFT of $\{X_k\}_{k=0}^{N-1}$ is defined as

$$x_n = \frac{1}{\sqrt{N}}\sum_{k=0}^{N-1} X_k e^{\frac{j2\pi nk}{N}}. \tag{1.9}$$

Hence, one baseband OFDM symbol is usually expressed as

$$x_b(t) = \frac{1}{\sqrt{N}} \sum_{m=0}^{N-1} (d_m^I + j d_m^Q) f(t) e^{j2\pi f_m t} \tag{1.10}$$

and one bandpass OFDM symbol is

$$x_p(t) = \Re\{x_b(t) e^{j2\pi f_c t}\} \tag{1.11}$$

where f_c is the carrier frequency. The receiver operations are essentially the reverse of those in the transmitter (using the DFT instead of the IDFT). At this time, the parallel data transmission system that performs the modulation and demodulation by an IDFT and a DFT, and further their fast algorithms IFFT and FFT, becomes a typical OFDM system as it appears in most references in the literature [5, 7]. Many modulation schemes can be used along with OFDM, depending on the desired number of bits per symbol. For example, the IEEE 802.11a [11] physical layer can provide data rates ranging from 6 Mbits/s to 54 Mbits/s by a link adaptation scheme with different modulation formats from binary phase shift keying (BPSK) to 64-ary quadrature amplitude modulation (64-QAM). Meanwhile, to allow for a low-cost receiver without channel estimation, $\pi/4$-shifted differentially encoded quadrature phase shift keying ($\pi/4$-DQPSK) is adopted in the DAB standard [14].

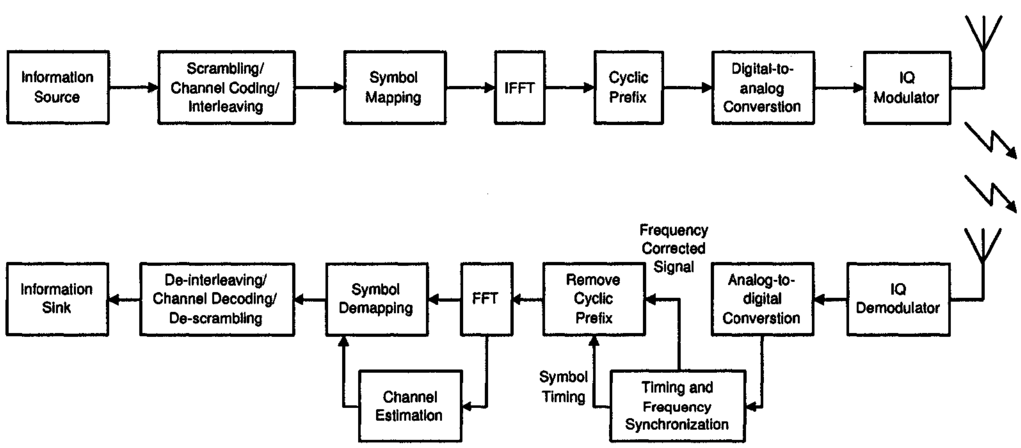

Fig. 1.2. A typical wireless OFDM architecture.

Fig. 1.2 gives a clear block diagram of a typical wireless OFDM system architecture. Before transmission, a CP is inserted at the beginning of the OFDM symbol to avoid interference between consecutive symbols. The CP is a copy of the last part of the OFDM symbol, and it makes the transmitted signal periodic. Hence, the linear convolution performed by the channel looks like a cyclic convolution to the data if the CP is longer than channel impulse response (CIR) and the CIR does not change during one OFDM symbol interval. The receiver removes the CP part and performs the FFT with the remainder of the received samples.

Proper coding design is usually employed in wireless OFDM systems to achieve a reasonable error probability. Coding in OFDM can be implemented in the time and frequency domains such that both dimensions are utilized to achieve better immunity against frequency and time selective fading. For example, the combination of a Reed-Solomon outer code and a rate-compatible convolutional inner code along with proper time/frequency interleaving constitutes a powerful concatenated coding strategy [12]. Other advanced coding techniques, such as turbo codes and low-density parity-check (LDPC) codes, also seem promising for some multicarrier applications [19, 22, 23].

1.3 Mobile Radio Channels

In this thesis, we will evaluate the performance of OFDM systems in wireless transmission environments. Therefore, in this section, we briefly review the characteristics of mobile radio channels.

Digital communications over mobile radio channels usually suffer from serious performance degradation without proper fading mitigation schemes. The deleterious effects inherent in mobile radio channels can be modeled as two types of fading effects, large-scale fading and small-scale fading. In addition to fading, the transmitted signal is attenuated by path loss.

The average path loss (in dB) $\overline{PL}(r)$ for a transmitter and receiver distance r can be predicted by [24]

$$\overline{PL}(r) = \overline{PL}(r_0) + 10n\log_{10}\left(\frac{r}{r_0}\right) \tag{1.12}$$

where n is the path loss exponent whose typical value in urban areas is from 2.7 to 3.5, r_0 is the close-in reference distance, and $\overline{PL}(r_0)$ is the average received power (in dB) at a distance of r_0. The value $\overline{PL}(r_0)$ can be obtained from the Friis free space equation [24].

The effects of log-normal shadowing, due to the receiver being shadowed by prominent terrain contours (hills, forests, high-rise buildings, etc.), are usually considered to be combined with path loss. Therefore, the loss $P_{dB}(r)$ at a specific distance r is log-normally distributed. That is

$$P_{dB}(r) = \overline{PL}(r) + N_\sigma \tag{1.13}$$

where N_σ, measured in dB, is a zero-mean Gaussian random variable with variance σ^2 which also has units of dB.

On the other hand, small-scale fading is caused by multipath propagation and time-variant behaviors of the channel. The received signal on mobile radio channels is made up of several copies of the transmitted signal with different amplitudes and propagation delays (and hence random phases). The destructive superposition of the transmitted signal with random phases leads to rapid fading in the received signal. What's more, as the receiver moves, the channel between the transmitter and the receiver varies with time.

Under the assumption of wide-sense stationary uncorrelated scattering (WSSUS), a group of parameters including maximum excess delay, T_m, coherence bandwidth, B_c, Doppler spread, f_d, and coherence time, t_c, is used to categorize the small-scale fading channel into different types. If we assume that the signal symbol length is T_s, the channel is said to be a frequency-selective fading channel if $T_m > T_s$, frequency non-selective, or flat fading if $T_m < T_s$. Coherence bandwidth represents a bandwidth interval over which frequency components have a strong correlation, for example, above 0.9. An approximate estimation of coherence bandwidth is given by $\frac{1}{T_m}$. Using B_c as a criterion, we can decide that frequency-selective (frequency non-selective) fading occurs whenever $B_c < W$ ($B_c > W$), where $W(\approx \frac{1}{T_s})$ is the signal bandwidth. Doppler spread and coherence time indicate the changing state of a fading channel. There exists a similar approximate relationship between coherence time and Doppler spread, that is, $t_c \approx \frac{1}{f_d}$, as the approximate relationship between coherence bandwidth and maximum excess delay. Therefore, the channel is termed as fast fading (slow fading) whenever $t_c < T_s$ or $f_d > W$ ($t_c > T_s$ or $f_d < W$).

Considered as a random process, the fading channel is also described in terms of several probability distributions to model its statistical characteristics [17]. When the received signal consists of multiple rays without line-of-sight (LOS) components, the envelope, R, of the channel response, is Rayleigh-distributed as

$$f_R(r) = \frac{2r}{\Omega} e^{-r^2/\Omega}, \quad r \geq 0 \tag{1.14}$$

where $\Omega = E(R^2)$, at any time instant and the phase is uniformly distributed over the interval $(0, 2\pi)$. However, Ricean fading occurs in the presence of a LOS (unfaded) component. The Rice distribution [17] is used to model the statistical fluctuations of the received signals over Ricean fading channels. Another two-parameter distribution, the Nakagami-m distribution, provides greater flexibility to model fading channels. Its probability density function (PDF) is given by

$$f_R(r) = \frac{2}{\Gamma(m)} (\frac{m}{\Omega})^m r^{2m-1} e^{-\frac{mr^2}{\Omega}}, \tag{1.15}$$

where $\Omega = E(R^2)$, and the fading figure m is defined as

$$m = \frac{\Omega^2}{E[(R^2-\Omega)^2]}, \quad m \geq \frac{1}{2} \tag{1.16}$$

and

$$\Gamma(m) = \int_0^{+\infty} t^{m-1} e^{-t}\, dt, \quad m > 0 \tag{1.17}$$

is the usual Gamma function [25]. The Nakagami-m distribution can be reduced to the Rayleigh distribution by setting $m = 1$. This allows us to model different fading conditions by adjusting m.

Different mitigation methods can be used to combat different types of channel distortion [26]. Frequency-selective fading introduces serious ISI, for which an equalizer is usually inserted to make the combination of channel and equalizer give a flat response with linear phase. Other methods, such as spread spectrum, OFDM, and pilot signals are also regarded as effective schemes to combat frequency-selective fading. Fast fading can be avoided by increasing the signalling rate so that it is greater than the channel fading rate. Flat and slow fading mainly leads to a loss in signal-to-noise ratio (SNR). In this case, some form of diversity (time diversity, frequency diversity, spatial diversity, etc.) can provide the receiver with additional, and uncorrelated replicas of the signal. Then, by employing a proper combining algorithm, the receiver can achieve an improved SNR.

1.4 Thesis Outline and Contributions

OFDM system will suffer from performance degradation in wireless transmission environments. The performance degradation may be caused by Doppler shift, carrier frequency offset and imperfect CIR estimation. In this thesis, we give an exact mathematical analysis to evaluate the performance degradation quantitatively for OFDM systems caused by carrier frequency offset, Doppler shift, and channel estimation error. On the other hand, we investigate several ICI reduction schemes, including transmitter pulse-shaped OFDM, receiver pulse-shaping, partial-response pulse-shaped OFDM system, discrete cosine transform (DCT)-based OFDM system, and widely linear MMSE OFDM equalizer. This thesis is organized as follows.

In Chapter 2, an exact closed-form bit error rate (BER) expression is derived for an OFDM system, each subcarrier modulated by $\pi/4$-DQPSK, in the presence of carrier frequency offset over frequency-selective fast Rayleigh fading channels. Both single channel reception and multi-channel reception with maximal ratio combining (MRC) diversity are considered. For a small number of subcarriers, the BER expression can be calculated directly. A Monte Carlo method is designed to evaluate the BER for a large number of subcarriers. The analytical expression can be used to investigate the effect of several channel parameters, including mean delay spread and maximum Doppler shift, on the system BER performance. In particular, the effect of carrier frequency offset on the system performance can be studied for a more realistic wireless channel environment model. By using the exact closed-form BER expression, an optimum number of subcarriers can be found, and the maximum allowable carrier frequency offset, Doppler shift, and mean delay spread for given operating conditions can be determined.

In Chapter 3, we examine the BER performance degradation of OFDM systems due to imperfect channel knowledge. A characteristic function-based method is used to derive closed-form BER expressions for OFDM systems in the presence of channel estimation error over frequency-selective Rayleigh fading channels and frequency-selective Ricean fading channels. Both single channel reception and diversity reception with MRC are examined. The BER expressions are shown to be sums of several conditional probability functions which can be calculated by using proper complex Gaussian random variable theory and a characteristic function method. The closed-form BER expressions can be used to accurately investigate the BER performance degradation caused by channel estimation error under different wireless channel environment models. The performance of two interpolation methods, a sinc interpolator with Hamming windowing and a Wiener interpolator, are compared.

It is interesting to investigate the schemes that can reduce ICI and improve BER performance of OFDM systems in the presence of frequency offset. In Chapter 4, the effect of several transmitter Nyquist pulse-shapings, including the Franks pulse, the raised-cosine pulse, the "better than" raised-cosine (BTRC) pulse, the second-order continuous window (SOCW), the double-jump pulse, and the polynomial pulse on ICI reduction and BER improvement in OFDM systems with carrier frequency offset is studied. The effect of different Nyquist pulses on ICI power reduction is first examined. An exact method for calculating the BER of the pulse-shaped OFDM system is then derived. This method represents a unified way to calculate the BER of the pulse-shaped OFDM system with different one-dimensional and two-dimensional subcarrier modulation formats. The effects of Nyquist pulse-shaping on the BER of the system with frequency offset are examined. The dependence of the BER on the roll-off factor of the pulse employed for a specific system in the presence of frequency offset is investigated. Bandwidth efficiency is studied. Analysis and numerical results show that compared with rectangular pulse-shaped OFDM system, although the other six pulse-shaped OFDM system can achieve smaller ICI and BER in most cases, they require increased symbol duration proportional by the roll-off factor α. The prolonged symbol duration will lead to a reduced data rate which may not be desired in some cases. In the following four chapters, other ICI reduction schemes without sacrifice in data rates are investigated.

In Chapter 5, we first exploit an equivalence between correlative coding and partial-response signaling. A BER performance measure is then employed to assess the performance of OFDM systems using correlative coding. Although recent published work suggests that correlative coding can improve OFDM performance by several dB, they does not consider fully a BER performance measure for the OFDM systems. It is shown in this chapter that although partial-response pulse-shaping or correlative coding can reduce ICI due to carrier frequency offset, they do not necessarily improve the system BER performance because of the introduction of multilevel signaling with associated reduced receiver decision distance. It is observed that BER performance improvement for symbol-by-symbol detection can be achieved only in some cases of large frequency offset. In the case of smaller, practical, values of frequency offset the BER is increased by correlative coding or partial-response pulse-shaping.

In Chapter 6, pulse-shaping is used at the receiver side. The effects of several widely referenced Nyquist pulses on the performance of the system are examined based on both the BER measure and the signal-to-interference ratio (SIR) measure. It is found that the SIR comparison is not necessarily consistent with the BER comparison. The BTRC windowing gives the smallest BER among the windowing functions considered for small to medium values of pulse roll-off factor. However, the Franks windowing or SOCW windowing shows better BER performance when the roll-off factor approaches one.

In Chapter 7, we investigate a DCT-based OFDM system. Through ICI and SIR analysis, we first show the reason why the DCT-OFDM outperforms the conventional DFT-OFDM. A precise method for calculating the BER of the DCT-OFDM system on AWGN channels in the presence of frequency offset is then derived. These accurate results are used to examine and compare the BER performance of a DCT-OFDM system and the conventional DFT-based OFDM system in an AWGN environment. We also propose a zero-padding DCT-OFDM scheme. The performance of the DCT-OFDM with the zero-padding guard interval scheme is then compared with a zero-padded DFT-OFDM with the employment of minimum mean-square error (MMSE) detection and MMSE decision feedback detection with ordering scheme over frequency-selective fast Rayleigh fading channels. Analysis and simulation results show that the DCT-OFDM system outperforms the DFT-OFDM system in the presence of frequency offset, and in frequency-selective fast fading environments.

In Chapter 8, a widely linear MMSE equalizer is used in OFDM systems with one-dimensional modulation formats to mitigate the ICI caused by fast fading environments. It is found that by using the widely linear MMSE equalizer, smaller average error power and BER can be achieved, compared with conventional linear MMSE equalizer.

Chapter 9 concludes this thesis by summarizing the major contributions and suggesting future work.

Chapter 2

Precise BER Analysis of $\pi/4$-DQPSK OFDM with Carrier Frequency Offset Over Frequency Selective Fast Fading Channels

2.1 Introduction

OFDM is sensitive to carrier frequency offset which introduces ICI and, hence, performance degradation. This kind of performance degradation was studied in [27, 28], and the references therein. These works were limited to the development of expressions for the SNR degradation due to carrier frequency offset over additive white Gaussian noise (AWGN) channels and multipath fading channels. Meanwhile, in practical digital wireless communications systems, the error rate is a more meaningful performance measure than the SNR degradation. In this regard, reference [29] proposed a precise symbol error rate analysis of an OFDM system with several modulation formats in the presence of frequency offset based on a Fourier series method [30, 31]. The effect of Wiener phase noise in OFDM systems is studied in [32]. However, these works considered only ideal AWGN channels. Recently, using a Gaussian approximation method, reference [33] compared the performance of several diversity schemes for an OFDM system with BPSK modulation in the presence of frequency offset, phase noise and channel estimation errors over frequency selective, quasi-static fading channels. An improved Gaussian approximation method was used in [34] to provide a very good BER performance prediction for OFDM systems with QPSK and QAM signaling impaired by carrier frequency offset in multipath fading channels. The channel was assumed to be constant over one OFDM symbol in these analyses. However, the channel may change in one OFDM symbol in fast fading environments. The channel time variation, measured by the maximum Doppler shift, will also introduce ICI and degrade the system performance. A frequency-selective fast fading channel environment is thus considered in our BER analysis. Additionally, differential modulation schemes can be used in OFDM system to allow a low-cost receiver design without channel estimation. In particular, an OFDM system with $\pi/4$-DQPSK modulation has been adopted in the DAB standard [14]. It is, therefore, important to consider the performance of OFDM systems with differential modulation schemes. In this regard, the BER performances of several differential modulation schemes, including MDPSK and $\pi/4$-DQPSK, were examined in [35–38] by using Gaussian approximation methods.

The difficulty in evaluating the BER performance of an OFDM system in the presence of ICI lies in the fact that the exact distribution of the ICI is not known. The ICI is not Gaussian distributed, although it was approximated as a complex Gaussian random variable in [33–38]. In fact, we will show in this chapter that the ICI has a probability density function (PDF) of a mixture of complex Gaussian random variables. We then use a different method from [33–38] to derive an exact closed-form BER expression for a $\pi/4$-DQPSK OFDM system operating with diversity reception and maximal ratio combiner (MRC) in the presence of frequency offset over frequency-selective fast Rayleigh fading channels. Our exact BER expressions are obtained by noting that the received signal conditioned on data symbols is Gaussian distributed. Proper complex Gaussian random process theory and a characteristic function method [39–41] are then applied in the development of the BER expressions. The closed-form BER expressions obtained can be calculated directly for a small number of subcarriers. In the case of a large number of subcarriers, the closed-form BER expression can be evaluated by using a Monte-Carlo method described in [42]. We use these BER expressions to examine the system performance degradations, introduced by carrier frequency offset, Doppler shift, and mean excess delay. The effect of diversity on combating these performance degradations is also assessed. The results indicate that, for the $\pi/4$-DQPSK OFDM system, small carrier frequency offsets and small Doppler shifts do not have much influence on the BER performance. However, keeping other conditions the same, Doppler shift leads to more system BER performance degradation than the same amount of carrier frequency offset because the effect of carrier frequency offset can be partly canceled by the differential demodulation scheme. Increased mean delay spread gives a greater frequency selectivity, which will significantly affect the performance of differential detection of $\pi/4$-DQPSK in the frequency domain. Diversity is effective in reducing the performance degradations caused by these factors. Several important OFDM system parameters can be determined with the employment of the obtained closed-form BER expression.

The remainder of this chapter is organized as follows. In Section 2.2, the system model is given. Then, the receiver decision statistic is developed. The BER expressions are derived in Section 2.3 using a characteristic function method. Some discussion of the results together with theoretical and simulated BER curves are presented in Section 2.4. Lastly, Section 2.5 summarizes the chapter results.

2.2 System Model

A continuous-time baseband OFDM signal, $s(t)$, including CP can be expressed as

$$s(t) = \frac{1}{\sqrt{N}} \sum_{i=-\infty}^{+\infty} \sum_{n=0}^{N-1} D_{i,n} e^{\frac{j2\pi n(t-T_g-iT_s)}{T_u}} u(t-iT_s) \tag{2.1}$$

where $D_{i,n}$ is the complex symbol modulated onto the nth subcarrier in the ith OFDM symbol, T_u is the useful signal duration, T_g is the length of the cyclic prefix, $T_s = T_u + T_g$ is the duration of an OFDM symbol, and $u(t)$ is defined as

$$u(t) = \begin{cases} 1, & 0 \leq t < T_s \\ 0, & \text{otherwise.} \end{cases} \tag{2.2}$$

The complex symbol $D_{i,n}$ is differentially modulated using $\pi/4$-DQPSK as

$$D_{i,n} = D_{i,n-1} e^{j\Delta\phi_n} = \sqrt{2E_b} e^{j(\phi_{n-1}+\Delta\phi_n)} \tag{2.3}$$

where E_b is the average energy per bit, ϕ_{n-1} is the phase of the symbol modulated on the $(n-1)$th subcarrier, and $\Delta\phi_n \in \{\pm\pi/4, \pm 3\pi/4\}$ is the differential phase carrying the information bits. The differential encoding is performed in the frequency domain by the subcarrier. The data in one OFDM symbol can be written as a vector

$$\begin{aligned} \mathbf{d} &= \begin{bmatrix} D_{i,0} & D_{i,1} & \cdots & D_{i,N-1} \end{bmatrix} \\ &= \begin{bmatrix} \sqrt{2E_b} & \sqrt{2E_b} e^{j\Delta\phi_1} & \sqrt{2E_b} e^{j(\Delta\phi_1+\Delta\phi_2)} & \cdots & \sqrt{2E_b} e^{j(\Delta\phi_1+\cdots+\Delta\phi_{N-1})} \end{bmatrix} \end{aligned} \tag{2.4}$$

where $D_{i,0}$ in each OFDM symbol is always assumed to be $\sqrt{2E_b}$ as a reference for differential detection at the receiver side. Although the channel may vary in one OFDM symbol, the differential detection of the DQPSK signal is effective provided there are no significant channel phase shift variations between two neighboring subcarriers.

The channel impulse response (CIR) of the time-variant L-path fading channel considered is [17]

$$h(t,\tau) = \sum_{l=0}^{L-1} h_l(t) \delta(\tau - \tau_l) \tag{2.5}$$

where $h_l(t)$ and τ_l is the complex amplitude and propagation delay of the lth path, respectively. We further assume that

$$\tau_0 \leq \tau_1 \leq \cdots \leq \tau_{L-1} \tag{2.6}$$

and that the complex stochastic processes $h_l(t)$ are Gaussian distributed. The time-variant transfer function of the channel is thus

$$H(t,f) = \sum_{l=0}^{L-1} h_l(t) e^{-j2\pi f \tau_l} \tag{2.7}$$

which represents the channel response at the time instant t and frequency f. By design, the cyclic prefix T_g is usually much larger than the maximum channel delay $\tau_{max} = \tau_{L-1}$. In addition, the duration of one OFDM symbol is long enough that the ISI occurs only between two adjacent, *i.e.* the $(k-1)$th and kth, OFDM symbols. As a result, the received signal in the presence of carrier frequency offset Δf is then

$$\begin{aligned} y(t) &= e^{j2\pi\Delta f t} \sum_{l=0}^{L-1} h_l(t) s(t-\tau_l) + w(t) \\ &= \frac{1}{\sqrt{N}} e^{j2\pi\Delta f t} \sum_{l=0}^{L-1} h_l(t) \sum_{i=k-1}^{k} \sum_{n=0}^{N-1} D_{i,n} e^{\frac{j2\pi n(t-T_g-iT_s-\tau_l)}{T_u}} u(t-iT_s-\tau_l) + w(t) \end{aligned} \tag{2.8}$$

where $w(t)$ is a zero-mean, complex Gaussian noise process with variance σ^2 per dimension.

One assumes that the receiver is synchronized to the 0th path with delay $\tau_0 = 0$, and sampled at the instants

$$t_m = kT_s + T_g + \frac{mT_u}{N}, \quad m = 0, 1, \cdots, N-1 \tag{2.9}$$

since the samples within the cyclic prefix T_g are discarded before further processing. Thus, the received N samples in one OFDM symbol are

$$y_m = \frac{1}{\sqrt{N}} e^{j2\pi\Delta f(kT_s+T_g)} \sum_{n=0}^{N-1} D_{k,n} H(t_m, f_n) e^{\frac{j2\pi(n+\varepsilon)m}{N}} + w_m \tag{2.10}$$

where $\varepsilon = \Delta f T_u$ is the normalized carrier frequency offset, w_m are zero-mean complex Gaussian random variables with variance σ^2 per dimension, H_{t_m,f_n} is the channel response at the sampling time instant t_m and the subcarrier frequency $f_n = n/T_u$, and

$$H(t_m, f_n) = \sum_{l=0}^{L-1} h_l(t_m) e^{\frac{-j2\pi n \tau_l}{T_u}}. \tag{2.11}$$

The channel responses

$$H(t_m, f_n) = X_{m,n} + jY_{m,n} \tag{2.12}$$

where $j = \sqrt{-1}$, at different times and frequencies are zero-mean complex Gaussian random variables. The correlations and variances of the real parts and imaginary parts of these complex Gaussian random variables are [43–45]

$$\mathbf{E}[X_{m,n}X_{m,n}] = \mathbf{E}[Y_{m,n}Y_{m,n}] = \sigma_f^2 \tag{2.13a}$$

$$\mathbf{E}[X_{m,n}Y_{m,n}] = \mathbf{E}[Y_{m,n}X_{m,n}] = 0 \tag{2.13b}$$

$$\mathbf{E}[X_{m,n}X_{s,t}] = \mathbf{E}[Y_{m,n}Y_{s,t}] = \frac{\sigma_f^2 J_0(2\pi\xi|m-s|/N)}{1+[2\pi(n-t)\eta]^2} \tag{2.13c}$$

$$\mathbf{E}[X_{m,n}Y_{s,t}] = -\mathbf{E}[X_{s,t}Y_{m,n}] = \frac{-2\sigma_f^2\pi(t-n)\eta J_0(2\pi|m-s|\xi/N)}{1+[2\pi(n-t)\eta]^2} \tag{2.13d}$$

where $\mathbf{E}[X]$ is the expectation of the random variable X, $J_0(\cdot)$ is the Bessel function of the first kind of order 0, $\xi = f_D T_u$ is the normalized maximum Doppler shift, and $\eta = \bar{\tau}/T_u$ is the normalized mean delay spread measure given in [43].

Performing a DFT on $\{y_m\}_{m=0}^{N-1}$ gives the data sequence $\{r_p\}_{p=0}^{N-1}$ as

$$r_p = \frac{1}{N} e^{j2\pi\Delta f(kT_s+T_g)} \left(C_{p,p}D_{k,p} + \sum_{\substack{n \neq p \\ n=0}}^{N-1} C_{n,p}D_{k,n} \right) + n_p, \quad p = 0, \cdots, N-1 \tag{2.14a}$$

where $C_{n,p}$ is defined as

$$C_{n,p} = \sum_{m=0}^{N-1} H(t_m, f_n) e^{\frac{j2\pi(n-p+\varepsilon)m}{N}} \tag{2.14b}$$

and n_p is a zero-mean, complex Gaussian random variable with variance σ^2 per dimension. With the employment of differential detection and MRC at the receiver, the decision statistics can be written as

$$\hat{D}_{k,p} = \sum_{d=1}^{D} r_{d,p} r_{d,p-1}^{*} \tag{2.15}$$

where $r_{d,p}$ is the received signal from the dth diversity branch, and $r_{d,p-1}^{*}$ represents the conjugate of $r_{d,p-1}$. For $\pi/4$-DQPSK demodulation, the two bits can be decided independently by the real part, $\hat{D}_{k,p}^{I}$, and the imaginary part, $\hat{D}_{k,p}^{Q}$, of $\hat{D}_{k,p}$, respectively [46].

2.3 Precise BER Analysis

In this section, we will first derive the characteristic function of the decision statistics. From eq. (2.15), the decision statistics for the I-bit and the Q-bit of symbol $D_{k,p}$ are

$$\hat{D}_{k,p}^{I} = \sum_{d=1}^{D} \Re\{r_{d,p} r_{d,p-1}^{*}\} \tag{2.16}$$

and

$$\hat{D}_{k,p}^{Q} = \sum_{d=1}^{D} \Im\{r_{d,p} r_{d,p-1}^{*}\} \tag{2.17}$$

respectively, where $\Re\{X\}$ denotes the real part of X and $\Im\{X\}$ denotes the imaginary part of X. Under the assumption of independent and identically distributed (i.i.d.) diversity branches, the decision statistics $\hat{D}_{k,p}^{I}$ and $\hat{D}_{k,p}^{Q}$ are each a sum of statistically independent random variables [17], and the characteristic function (CHF) of each can be written as the product of the characteristic functions of the terms in each sum. Hence, the work at hand is to derive the CHF of $\Re\{r_{d,p} r_{d,p-1}^{*}\}$ and $\Im\{r_{d,p} r_{d,p-1}^{*}\}$.

By defining the $1 \times N$ vector $\mathbf{c}_p$

$$\mathbf{c}_p = \begin{bmatrix} C_{0,p}^{*} & C_{1,p}^{*} & \cdots & C_{N-1,p}^{*} \end{bmatrix} \tag{2.18}$$

one can write $r_{d,p}$ as

$$r_{d,p} = \frac{1}{N} e^{j2\pi\Delta f(kT_s+T_g)} \mathbf{d}\mathbf{c}_p^{\mathrm{H}} + n_p \tag{2.19}$$

where $\mathbf{c}_p^{\mathrm{H}}$ denotes the Hermitian (conjugate transpose) of the vector $\mathbf{c}_p$. The received signal $r_{d,p}$ is not Gaussian distributed. However, it is noted that $r_{d,p}$ is a conditional complex Gaussian random variable, conditioned on a given data sequence $\mathbf{d}_l$ or a given phase sequence $\Delta\phi_1, \Delta\phi_2, \cdots, \Delta\phi_{N-1}$. The reason for this is that the channel responses $H(t_m, f_n)$ at different time instants and different subcarrier frequencies are joint complex Gaussian random variables [43]. For a given data sequence or a differential phase sequence, $r_{d,p}$ is a sum of several joint complex Gaussian random variables. It is, therefore, a complex Gaussian random variable [47] with mean zero and variance

$$\sigma_l^2 = \frac{1}{N^2} \mathbf{d}_l \Lambda_{p,p} \mathbf{d}_l^{\mathrm{H}} + 2\sigma^2 \tag{2.20}$$

where Λ_{p_1,p_2} is the $N \times N$ correlation matrix defined as

$$\Lambda_{p_1,p_2} = \mathbf{E}[\mathbf{c}_{p_1}^{\mathrm{H}} \mathbf{c}_{p_2}]. \tag{2.21}$$

Recalling the channel correlation functions in (2.13), one can give the element at the n_1th row and the n_2th column, $0 \le n_1, n_2 \le N-1$, of the matrix Λ_{p_1,p_2} as

$$\begin{aligned}
\lambda_{n_1,n_2} &= \mathbf{E}[C_{n_1,p_1} C_{n_2,p_2}^*] \\
&= \sum_{m_1=0}^{N-1} \sum_{m_2=0}^{N-1} \mathbf{E}[H(t_{m_1,f_{n_1}}) H(t_{m_2,f_{n_2}})^*] e^{j2\pi(n_1-p_1+\varepsilon)m_1/N} e^{-j2\pi(n_2-p_2+\varepsilon)m_2/N} \\
&= \frac{2\sigma_f^2}{1 - j2\pi(n_2-n_1)\eta} \sum_{m_1=0}^{N-1} \sum_{m_2=0}^{N-1} J_0[2\pi(m_1-m_2)\xi/N] e^{j2\pi\varepsilon(m_1-m_2)/N} \\
&\quad \times e^{j2\pi(n_1-p_1)m_1/N} e^{-j2\pi(n_2-p_2)m_2/N}.
\end{aligned} \tag{2.22}$$

The unconditional PDF of the received signal $r_{d,p}$, $f(x)$, can be written as the sum of several conditional PDFs, that is,

$$f(x) = \sum_{l=1}^{K} f(x|\mathbf{d}_l)\mathrm{Prob}(\mathbf{d}_l) = \sum_{l=1}^{K} \frac{1}{\pi\sigma_l^2} e^{\frac{-x^* x}{\sigma_l^2}} \mathrm{Prob}(\mathbf{d}_l) \tag{2.23}$$

where x is a complex variable, and K represents the number of all possible data sequences $\mathbf{d}$ or phase sequences $\Delta\phi_1, \Delta\phi_2, \cdots, \Delta\phi_{N-1}$, and $\mathrm{Prob}(\mathbf{d}_l)$ represents the probability of a specific data sequence $\mathbf{d}_l$. Since different data sequences will give a different variance value σ_l^2, the PDF in (2.23) is not necessarily a Gaussian PDF except when $C_{0,p}, C_{1,p}, \cdots, C_{N-1,p}$ are independent, which is not the case in the OFDM system. The PDF in (2.23) was called a mixture of complex Gaussian distributions in [48]. Similarly, $r_{d,p-1}$ is also a conditional complex Gaussian random variable. Moreover, $r_{d,p}$ and $r_{d,p-1}$ are conditional proper complex Gaussian random variables [39,41] since

$$\mathbf{E}[r_{d,p} r_{d,p-1} \mid \Delta\phi_1, \Delta\phi_2, \cdots, \Delta\phi_{N-1}] = 0. \tag{2.24}$$

Note that $\Re\{r_{d,p} r_{d,p-1}^*\}$ and $\Im\{r_{d,p} r_{d,p-1}^*\}$ can be written as Hermitian quadratic forms

$$\Re\{r_{d,p} r_{d,p-1}^*\} = R^{\mathrm{H}} Q_r R \tag{2.25a}$$

and

$$\Im\{r_{d,p} r_{d,p-1}^*\} = R^{\mathrm{H}} Q_i R \tag{2.25b}$$

respectively, where the complex Gaussian random vector R is defined as

$$R = \begin{bmatrix} r_{d,p} \\ r_{d,p-1} \end{bmatrix} \tag{2.26}$$

and the Hermitian matrices Q_r and Q_i are

$$Q_r = \begin{bmatrix} 0 & \frac{1}{2} \\ \frac{1}{2} & 0 \end{bmatrix} \quad \text{and} \quad Q_i = \begin{bmatrix} 0 & -\frac{1}{2j} \\ \frac{1}{2j} & 0 \end{bmatrix}$$

respectively. Then, the CHF of $\Re\{r_{d,p} r_{d,p-1}^*\}$ conditioned on

$$\mathbf{g} = \begin{bmatrix} \Delta\phi_1 & \cdots & \Delta\phi_{p-1} & \Delta\phi_{p+1} & \cdots & \Delta\phi_{N-1} \end{bmatrix} \tag{2.27}$$

and $\Delta\phi_p$ can be written as [39]

$$\Phi^I(\omega \mid \mathbf{g}, \Delta\phi_p) = |I_2 - j\omega M Q_r|^{-1} \tag{2.28}$$

where I_2 is the 2×2 identity matrix, $|X|$ is the determinant of the matrix X, and $\mathbf{M}$ is the covariance matrix defined as

$$\mathbf{M} = \mathbf{E}[RR^{\mathbb{H}} \mid \mathbf{g}, \Delta\phi_p] = \begin{bmatrix} \theta & \alpha + j\beta \\ \alpha - j\beta & \rho \end{bmatrix} \tag{2.29}$$

where θ, ρ, α, and β are parameters conditioned on differential phase sequence $\mathbf{g}$ and $\Delta\phi_p$. They are given as

$$\theta = \mathbf{E}[r_{d,p} r_{d,p}^* \mid \mathbf{g}, \Delta\phi_p] = \frac{1}{N^2} \mathbf{d} \Lambda_{p,p} \mathbf{d}^{\mathbb{H}} + 2\sigma^2 \tag{2.30a}$$

$$\rho = \mathbf{E}[r_{d,p-1} r_{d,p-1}^* \mid \mathbf{g}, \Delta\phi_p] = \frac{1}{N^2} \mathbf{d} \Lambda_{p-1,p-1} \mathbf{d}^{\mathbb{H}} + 2\sigma^2 \tag{2.30b}$$

$$\alpha + j\beta = \mathbf{E}[r_{d,p} r_{d,p-1}^* \mid \mathbf{g}, \Delta\phi_p] = \frac{1}{N^2} \mathbf{d} \Lambda_{p,p-1} \mathbf{d}^{\mathbb{H}} \tag{2.30c}$$

where $\mathbf{d}$ is the data symbol sequence obtained from differential phase sequence $\mathbf{g}$ and $\Delta\phi_p$ following (2.4). Similarly, the CHF of $\Im\{r_{d,p} r_{d,p-1}^*\}$ conditioned on $\mathbf{g}$ and $\Delta\phi_p$ can be derived as

$$\Phi^Q(\omega \mid \mathbf{g}, \Delta\phi_p) = \frac{1}{1 - j\omega\beta - \frac{1}{4}\omega^2(\alpha^2 + \beta^2 - \rho\theta)} \tag{2.31}$$

Under the assumption of i.i.d. diversity branches, the CHF of $\hat{D}_{k,p}^I$ and $\hat{D}_{k,p}^Q$ can be written as

$$\Psi^I(\omega \mid \mathbf{g}, \Delta\phi_p) = \left[\Phi^I(\omega \mid \mathbf{g}, \Delta\phi_p)\right]^D \tag{2.32}$$

and

$$\Psi^Q(\omega \mid \mathbf{g}, \Delta\phi_p) = \left[\Phi^Q(\omega \mid \mathbf{g}, \Delta\phi_p)\right]^D \tag{2.33}$$

respectively. The BER of the single branch reception and multi-branch reception will be derived using a characteristic function method in Sections 2.3.1 and 2.3.2.

2.3.1 BER for Single Branch Reception

The decision rules for the I-bit and the Q-bit can be summarized as follows:

$$\begin{array}{lll}
\text{if} & \hat{D}^{I}_{k,p} \geq 0, & \text{then bit } I = 1 \\
\text{if} & \hat{D}^{I}_{k,p} < 0, & \text{then bit } I = 0 \\
\text{if} & \hat{D}^{Q}_{k,p} \geq 0, & \text{then bit } Q = 1 \\
\text{if} & \hat{D}^{Q}_{k,p} < 0, & \text{then bit } Q = 0.
\end{array}$$

Therefore the I-bit error probability of the pth subcarrier conditioned on a specific phase sequence

$$\mathbf{g}_l = \begin{bmatrix} \Delta\phi_{1,l} & \cdots & \Delta\phi_{p-1,l} & \Delta\phi_{p+1,l} & \cdots & \Delta\phi_{N-1,l} \end{bmatrix} \tag{2.34}$$

in the case of single branch reception, $P^{1}_{p,I}(\mathbf{g}_l)$, is

$$\begin{aligned}
P^{1}_{p,I}(\mathbf{g}_l) &= \frac{1}{4}P^{1}_{p,I}\left(\mathbf{g}_l, \Delta\phi_p = \frac{\pi}{4}\right) + \frac{1}{4}P^{1}_{p,I}\left(\mathbf{g}_l, \Delta\phi_p = \frac{3\pi}{4}\right) + \frac{1}{4}P^{1}_{p,I}\left(\mathbf{g}_l, \Delta\phi_p = -\frac{\pi}{4}\right) \\
&\quad + \frac{1}{4}P^{1}_{p,I}\left(\mathbf{g}_l, \Delta\phi_p = -\frac{3\pi}{4}\right) \\
&= \frac{1}{4}\text{Prob}\left\{\hat{D}^{I}_{k,p} < 0 \,\middle|\, \mathbf{g}_l, \Delta\phi_p = \frac{\pi}{4}\right\} + \frac{1}{4}\text{Prob}\left\{\hat{D}^{I}_{k,p} \geq 0 \,\middle|\, \mathbf{g}_l, \Delta\phi_p = \frac{3\pi}{4}\right\} \\
&\quad + \frac{1}{4}\text{Prob}\left\{\hat{D}^{I}_{k,p} < 0 \,\middle|\, \mathbf{g}_l, \Delta\phi_p = \frac{-\pi}{4}\right\} + \frac{1}{4}\text{Prob}\left\{\hat{D}^{I}_{k,p} \geq 0 \,\middle|\, \mathbf{g}_l, \Delta\phi_p = \frac{-3\pi}{4}\right\}.
\end{aligned} \tag{2.35}$$

The four conditional probabilities in eq. (2.35) can be evaluated by using the characteristic function method [31] and the inversion theorem [49–52], that is,

$$\begin{aligned}
F_X(x) &= \text{Prob}\{X \leq x\} \\
&= \frac{1}{2} - \int_0^{+\infty} \frac{\Im\{\Phi(\omega)\}\cos\omega x - \Re\{\Phi(\omega)\}\sin\omega x}{\pi\omega}\, d\omega
\end{aligned} \tag{2.36}$$

where X is a random variable with an absolutely continuous cumulative distribution function (CDF) $F_X(x)$, and $\Phi(\omega)$ is the characteristic function of this random variable.

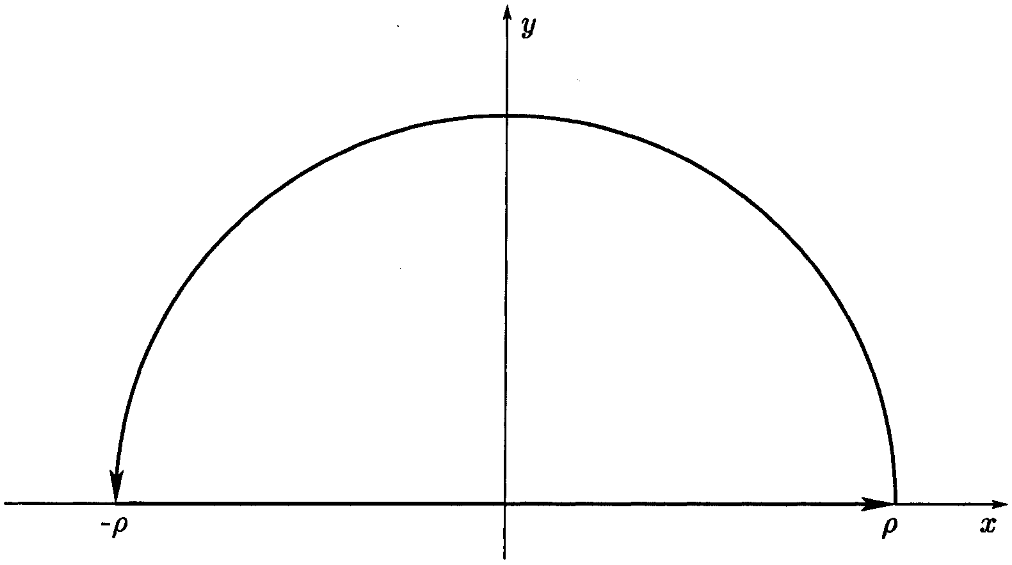

Fig. 2.1. The contour for the integral in eq. (2.37)

For single branch reception, one has $D = 1$, and

$$\begin{aligned} P_{p,l}^{1}\left(\mathbf{g}_l, \Delta\phi_p = \frac{\pi}{4}\right) &= \text{Prob}\left\{\hat{D}_{k,p}^{l} < 0 \;\middle|\; \mathbf{g}_l, \Delta\phi_p = \frac{\pi}{4}\right\} \\ &= \frac{1}{2} - \int_0^{+\infty} \frac{\Im\{\Phi^l(\omega \mid \mathbf{g}_l, \Delta\phi_p)\}}{\pi\omega} d\omega \\ &= \frac{1}{2} - \frac{16\alpha_{1,l}}{\pi v_{1,l}^2} \int_0^{+\infty} \frac{v_{1,l}^2 \, d\omega}{\omega^4 v_{1,l}^2 + 16\omega^2(\alpha_{1,l}^2 + 0.5 v_{1,l}) + 16} \\ &= \frac{1}{2} - \frac{\alpha_{1,l}}{2\sqrt{\theta_{1,l}\rho_{1,l} - \beta_{1,l}^2}} \end{aligned} \tag{2.37}$$

where $v_{1,l} = \theta_{1,l}\rho_{1,l} - \alpha_{1,l}^2 - \beta_{1,l}^2$, and $\rho_{1,l}$, $\theta_{1,l}$, $\alpha_{1,l}$ and $\beta_{1,l}$ are evaluated according to eqs. (2.30a)-(2.30c) by letting $\mathbf{g} = \mathbf{g}_l$ and $\Delta\phi_p = \pi/4$. The integration in eq. (2.37) is calculated by summing the values of the complex residues inside the contour plotted in Fig. 2.1 [53].

Similarly, one can calculate the other three conditional probabilities. Subsequently, the l-bit error probability conditioned on $\mathbf{g}_l$ is

$$P_{p,l}^{1}(\mathbf{g}_l) = \frac{1}{2} - \sum_{u=1}^{4} \frac{\sqrt{2}\cos(\Delta\phi_{p,u})\alpha_{u,l}}{8\sqrt{\theta_{u,l}\rho_{u,l} - \beta_{u,l}^2}} \tag{2.38}$$

where $\Delta\phi_{p,1} = \pi/4$, $\Delta\phi_{p,2} = 3\pi/4$, $\Delta\phi_{p,3} = -3\pi/4$, and $\Delta\phi_{p,4} = -\pi/4$. Following the same approach, the Q-bit error probability can be obtained as

$$P^1_{p,Q}(\mathbf{g}_l) = \frac{1}{2} - \sum_{u=1}^{4} \frac{\sqrt{2}\sin(\Delta\phi_{p,u})\beta_{u,l}}{8\sqrt{\theta_{u,l}\rho_{u,l} - \alpha^2_{u,l}}}. \tag{2.39}$$

The symbol $D_{i,0}$ on subcarrier 0 is used as a phase reference symbol. Hence, averaging over the remaining $N-1$ subcarriers, one can obtain the conditional system BER as

$$P^1_b(\mathbf{g}_l) = \frac{1}{2(N-1)} \sum_{p=1}^{N-1} \left[P^1_{p,I}(\mathbf{g}_l) + P^1_{p,Q}(\mathbf{g}_l) \right]. \tag{2.40}$$

For the $\pi/4$-DQPSK modulation, there are 4^{N-2} possibilities for the phase sequence $\mathbf{g}$. Averaging over all possible phase sequences, one can get the average BER as

$$P^1_b = \frac{1}{4^{N-2}} \sum_{l=1}^{4^{N-2}} P^1_b(\mathbf{g}_l). \tag{2.41}$$

For a small number of subcarriers, the BER can be evaluated directly by calculating eq. (2.41). However, for a large number of subcarriers, the number of terms in the summation is prohibitively large, and direct calculation will become intractable. In this case, we may resort to the Monte Carlo method [42] which can give an excellent estimate of (2.41) by choosing randomly M phase sequences and averaging as

$$P_e = \frac{1}{M} \sum_{l=1}^{M} P^1_b(\mathbf{g}_l). \tag{2.42}$$

Through extensive experimentation, a value of $M = 100$ was found large enough to give a result in excellent agreement with exact calculation for small numbers of subcarriers, for example $N = 8$. Therefore, we use the Monte Carlo method to determine the theoretical BER results for $N = 64$ in the sequel.

2.3.2 BER for Multi-Branch Reception

We will first consider the I-bit error probability. Under the assumption that received signals come from D i.i.d. diversity branches and a maximal ratio combiner is employed at the receiver, from eq. (2.32), the CHF of $\hat{D}^I_{k,p}$ can be written as

$$\Psi^I(\omega|\mathbf{g},\Delta\phi_p) = \frac{1}{\left(\frac{1}{4}\omega^2\nu - j\omega\alpha + 1\right)^D} = \frac{1}{(1-jA\omega)^D(1+jB\omega)^D} \tag{2.43}$$

where $\nu = \theta\rho - \alpha^2 - \beta^2$, $A = (\alpha + \sqrt{\alpha^2+\nu})/2$ and $B = (-\alpha + \sqrt{\alpha^2+\nu})/2$. It is noted in [46] that $\Psi^I(\omega|\mathbf{g},\Delta\phi_p)$ is the CHF of $\frac{A}{2}X_1 - \frac{B}{2}X_2$ where X_1 and X_2 are two independent Chi-square random variables with $2D$ degrees of freedom and $\mathbf{E}[X_1] = \mathbf{E}[X_2] = 2D$. Therefore, the error probability conditioned on $\mathbf{g}_l$ and $\Delta\phi_p = \pi/4$ is

$$\begin{aligned}
&P^D_{p,I}\left(\mathbf{g}_l,\Delta\phi_p = \frac{\pi}{4}\right)\\
&= \text{Prob}\left\{\hat{D}^I_{k,p} < 0 \mid \mathbf{g}_l,\ \Delta\phi_p = \frac{\pi}{4}\right\}\\
&= \text{Prob}\left\{\frac{A}{2}X_1 - \frac{B}{2}X_2 < 0 \mid \mathbf{g}_l,\ \Delta\phi_p = \frac{\pi}{4}\right\}\\
&= \int_0^{+\infty} \frac{x_1^{D-1}e^{-x_1/2}}{2^D(D-1)!}\int_{Ax_1/B}^{+\infty}\frac{x_2^{D-1}e^{-x_2/2}}{2^D(D-1)!}\,dx_2\,dx_1\\
&= \left(\frac{B}{A+B}\right)^D \sum_{d=0}^{D-1}\frac{(D+d-1)!}{(D-1)!d!}\left(\frac{A}{A+B}\right)^d\\
&= \left[P^1_{p,I}\left(\mathbf{g}_l,\Delta\phi_p = \frac{\pi}{4}\right)\right]^D \sum_{d=0}^{D-1}\frac{(D+d-1)!}{(D-1)!d!}\left[1 - P^1_{p,I}\left(\mathbf{g}_l,\Delta\phi_p = \frac{\pi}{4}\right)\right]^d
\end{aligned} \tag{2.44}$$

where $P^1_{p,I}\left(\mathbf{g}_l,\Delta\phi_p = \frac{\pi}{4}\right)$ is the conditional error probability evaluated in eq. (2.37) in the case of single branch. Similarly, one can obtain

$$\begin{aligned}
&P^D_{p,I}\left(\mathbf{g}_l,\Delta\phi_p = \frac{3\pi}{4}\right)\\
&= \text{Prob}\left\{\hat{D}^I_{k,p} \geq 0 \mid \mathbf{g}_l,\ \Delta\phi_p = \frac{3\pi}{4}\right\}\\
&= \int_0^{+\infty} \frac{x_2^{D-1}e^{-x_2/2}}{2^D(D-1)!}\int_{Bx_2/A}^{+\infty}\frac{x_1^{D-1}e^{-x_1/2}}{2^D(D-1)!}\,dx_1\,dx_2\\
&= \left(\frac{A}{A+B}\right)^D \sum_{d=0}^{D-1}\frac{(D+d-1)!}{(D-1)!d!}\left(\frac{B}{A+B}\right)^d\\
&= \left[P^1_{p,I}\left(\mathbf{g}_l,\Delta\phi_p = \frac{3\pi}{4}\right)\right]^D \sum_{d=0}^{D-1}\frac{(D+d-1)!}{(D-1)!d!}\left[1 - P^1_{p,I}\left(\mathbf{g}_l,\Delta\phi_p = \frac{3\pi}{4}\right)\right]^d.
\end{aligned} \tag{2.45}$$

The I-bit error probability conditioned on $\mathbf{g}_l$ can then be written as

$$P_{p,I}^{D}(\mathbf{g}_l) = \frac{1}{4}\sum_{u=1}^{4} P_{p,I}^{D}(\mathbf{g}_l, \Delta\phi_p = \Delta\phi_{p,u}). \tag{2.46}$$

Following the same approach, one can obtain $P_{p,Q}^{D}(\mathbf{g}_l)$, the Q-bit error probability conditioned on $\mathbf{g}_l$. Averaging over all N subcarriers, and all possible phase sequences, as in eqs. (2.40) and (2.41), one can finally obtain the average BER in the case of D diversity branches as

$$P_b^D = \frac{1}{4^{N-2}(N-1)} \sum_{l=1}^{4^{N-2}} \sum_{p=1}^{N-1} \frac{1}{2}\left[P_{p,I}^{D}(\mathbf{g}_l) + P_{p,Q}^{D}(\mathbf{g}_l)\right]. \tag{2.47}$$

For large N, (2.47) can be evaluated by the Monte Carlo method.

2.4 Examples and Discussion

We will examine the BER performance of the $\pi/4$-DQPSK OFDM system under different wireless channel environments in this section. Tables 2.1-2.3 gives typical values and their normalized values for a set of parameters, including Doppler shift, carrier frequency offset, and mean delay spread.

The theoretical BER curves obtained by using the Monte Carlo method [42] in eq. (2.42), the direct calculation method in eqs. (2.41) and (2.47), and a direct simulation method are shown in Fig. 2.2, where the number of subcarriers is $N = 8$. As a reference for differentially encoding other subcarriers, the amplitude and phase of the $\pi/4$-DQPSK data symbol at the 0th subcarrier of each OFDM symbol is fixed to be $\sqrt{2E_b}$ and 0, respectively; that is $D_{i,0} = \sqrt{2E_b}$. We further assume that the average bit energy $E_b = 1$ and fading power $\sigma_f^2 = 1$ for theoretical calculations and simulations in the sequel. In the case of direct calculation, all 4^6 possible values of the data sequence are generated to calculate the BER according to eq. (2.41). In the case of the Monte Carlo method, the theoretical results are obtained by evaluating eq. (2.42) with $M = 100$ randomly chosen differential phase

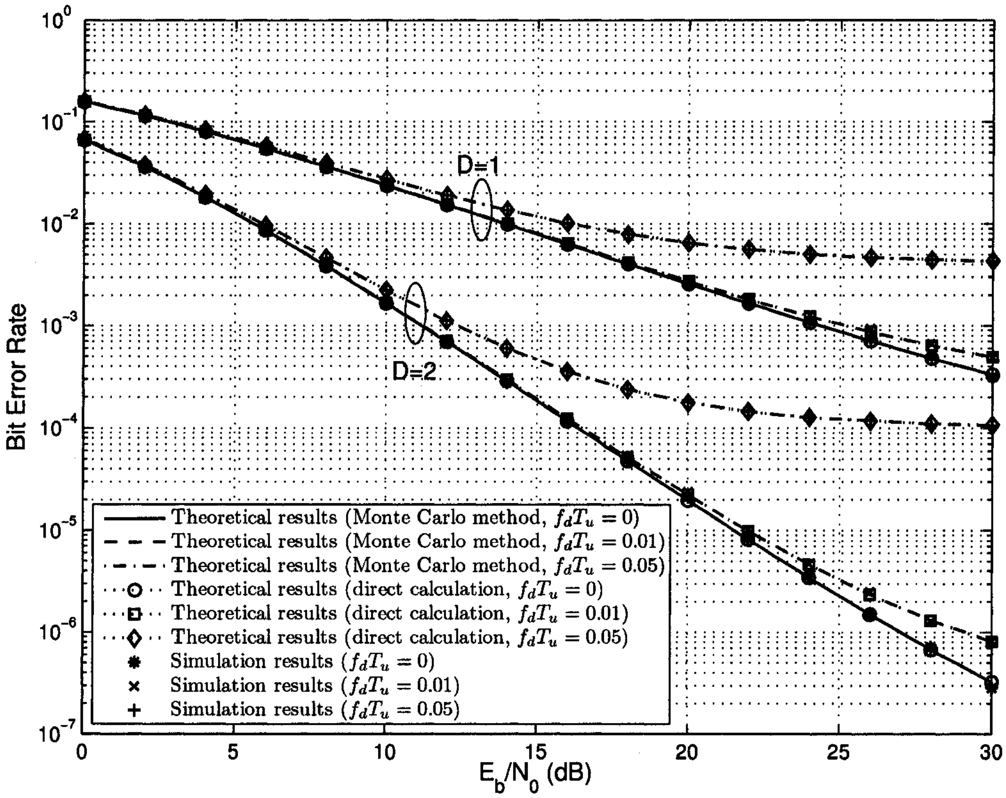

Fig. 2.2. The effect of different normalized Doppler shift values on the system BER performance for $\Delta f T_u = \overline{\tau}/T_u = 0.002$, $N = 8$.

TABLE 2.1

Typical values and normalized values for Doppler shift

Velocity m/s	Doppler shift Hz	Normalized Doppler shift $f_c = 5.35$ GHz, $T_u = 3.2\ \mu$s
0.1	1.78	5.70×10^{-6}
1	17.83	5.71×10^{-5}
50	891.67	2.85×10^{-3}
100	1783.33	5.71×10^{-3}
500, aircraft velocity [54]	8916.67	2.85×10^{-2}

TABLE 2.2

Typical values and normalized values for mean delay spread

Mean delay spread ns	Normalized mean delay spread $T_u = 3.2\ \mu$s
20	6.25×10^{-3}
50	1.5625×10^{-2}
100	3.125×10^{-2}
1,000	0.3125

TABLE 2.3

Typical values and normalized values for carrier frequency offset

Carrier frequency offset	Normalized carrier frequency offset
Hz	$T_u = 3.2\ \mu$s
100	3.2×10^{-4}
500	1.6×10^{-3}
1,000	3.2×10^{-3}
10,000	3.2×10^{-2}

sequences. We also give BER performance results for the system obtained from direct simulation. To reduce the variance of the simulation estimates, 10^6 OFDM symbols, each with 8 subcarriers and $\pi/4$-DQPSK modulation, are generated. The decision statistics are then formulated as eqs. (2.16) and (2.17) for the I-bit and Q-bit, respectively. One can see that the theoretical results obtained by using the Monte Carlo method and direct calculation method coincide exactly. For a large number of subcarriers, for example $N = 64$, it is not practical to give the theoretical results using the direct calculation method. So in the sequel, when considering 64-subcarrier OFDM system, we present only the results obtained using the Monte Carlo method. The simulated BER values are also in excellent agreement with the theoretical results. Several normalized Doppler shift values, $\xi = f_d T_u = 0, 0.01$ and 0.05 are considered in this figure. The extremely large normalized Doppler shift values 0.01 and 0.05 are shown in this figure for the purpose of comparison. For small normalized Doppler shift values, say 5×10^{-6}, the BER curve will almost coincide with the $f_d T_u = 0$ curve. The normalized frequency offset and the normalized mean delay spread are both 0.002. For single branch reception, when the normalized Doppler shift changes from 0 to

0.01, an increment of 0.87 dB in SNR can be observed to keep the same BER of 10^{-3}. The system performance is improved significantly by using dual branch diversity. For example, in the presence of a normalized Doppler shift of 0.01, given a SNR value of 20 dB, the system can achieve a BER of 2.70×10^{-3} using single channel reception, and a BER of 2.23×10^{-5} using dual branch diversity reception, respectively.

Fig. 2.3 examines the effect of different mean delay spread values on the system BER with single branch reception and dual branch reception for a 64-subcarrier $\pi/4$-DQPSK OFDM system. Typical mean delay spread values are on the order of microseconds in outdoor environments and nanoseconds in indoor wireless communications [24]. Hence, we choose the normalized mean delay spread as $0, 0.005, 0.01$ and 0.02, that is $\bar{\tau}$ from 0 to 64 ns in this figure. The normalized frequency offset and the normalized Doppler shift are set to 0.002. Both the theoretical results by using Monte Carlo method and the simulated BER results are shown in this figure. One can see that the theoretical results obtained by using Monte Carlo method can exactly predict the simulated BER values. It is noted that the system is sensitive to mean delay spread change. For example, with the mean delay spread increment from 0 ns to 16 ns, system performance is deteriorated by as much as 3 dB in SNR at a bit error rate 10^{-3} without diversity. The reason is that the differential encoding is performed subcarrier-by-subcarrier in the frequency domain. Moreover, the duration of one OFDM symbol is not long enough to combat the channel frequency selectivity effectively. Therefore, even small variations of mean delay spread will change the frequency domain characteristics notably at different subcarriers, which will affect the performance of differential decoding at the receiver. Keeping the OFDM system bandwidth constant, one can decrease the subcarrier frequency spacing by using more subcarriers, which will at the same time increase the duration of the OFDM symbol. This is beneficial to the performance of the frequency domain differential decoding because the channel variations at different subcarrier frequencies may be negligible for small frequency spacing.

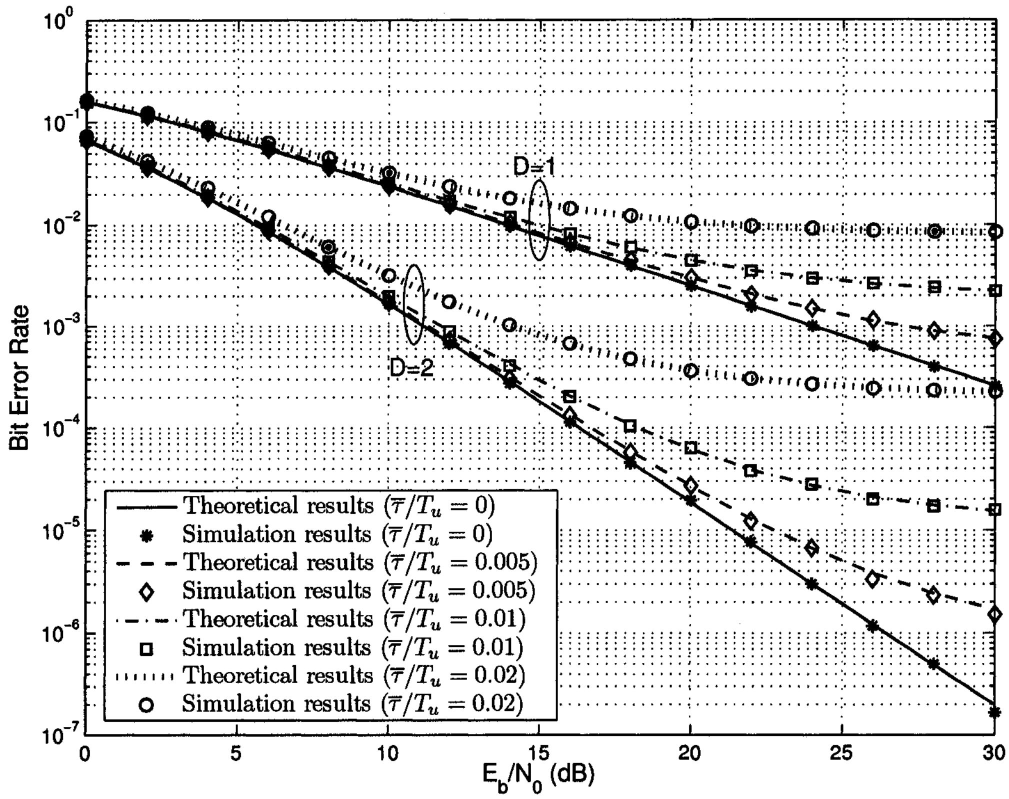

Fig. 2.3. The effect of different normalized mean delay spread values on the system BER performance for $f_D T_u = \Delta f T_u = 0.002$, $N = 64$.

One can see in eq. (2.14) that the system performance is affected by the time selectivity (measured by the Doppler shift), frequency selectivity (measured by the mean delay spread), and the carrier frequency offset. Time selectivity and carrier frequency offset will destroy the orthogonality among the subcarriers, and introduce ICI which becomes evident with the increase of N. The influence of frequency selectivity on the system performance, on the other hand, will decrease with the increase of the number of subcarriers, as seen from the preceding analysis. When N is small, the dominant interference is caused by the frequency selectivity so that the ICI introduced by the channel time selectivity and carrier frequency offset can be ignored. Therefore, the system performance will become better when N increases. However, when N is large enough that the dominant interference is from ICI, the system performance will become worse as N increases. Hence, there exists an optimum value of N for a set of given system parameters. This can be observed in Fig. 2.4 where the BER versus the number of subcarriers is plotted using the system parameters listed in Table 2.4 for both the case of single channel reception ($D = 1$) and the case of dual-branch diversity ($D = 2$) with maximal ratio combining. The BER curves for both the $D = 1$ and $D = 2$ cases at first decrease as N increases for a small number of subcarriers. However, for larger N, there is a slight increase as N increases. It is found that the optimum N for the configuration in Table 2.4 is about 224 and 248 for $D = 1$ and $D = 2$, respectively. In a practical system, 256 may be used for the convenience of FFT and IFFT implementation.

Fig. 2.5, where the normalized mean delay spread $\bar{\tau}/T_u$ is fixed at 0.002, shows the effect of Doppler shift and carrier frequency offset on system BER performance with multi-branch reception. In order to compare the effect of normalized carrier frequency offset with the same amount of normalized Doppler shift on the system BER performance, we set one parameter to be some value and the other to be zero, and vice versa. One can see that Doppler shift always leads to worse BER performance than the same amount of carrier frequency offset because part of interference due to the fixed carrier frequency offset

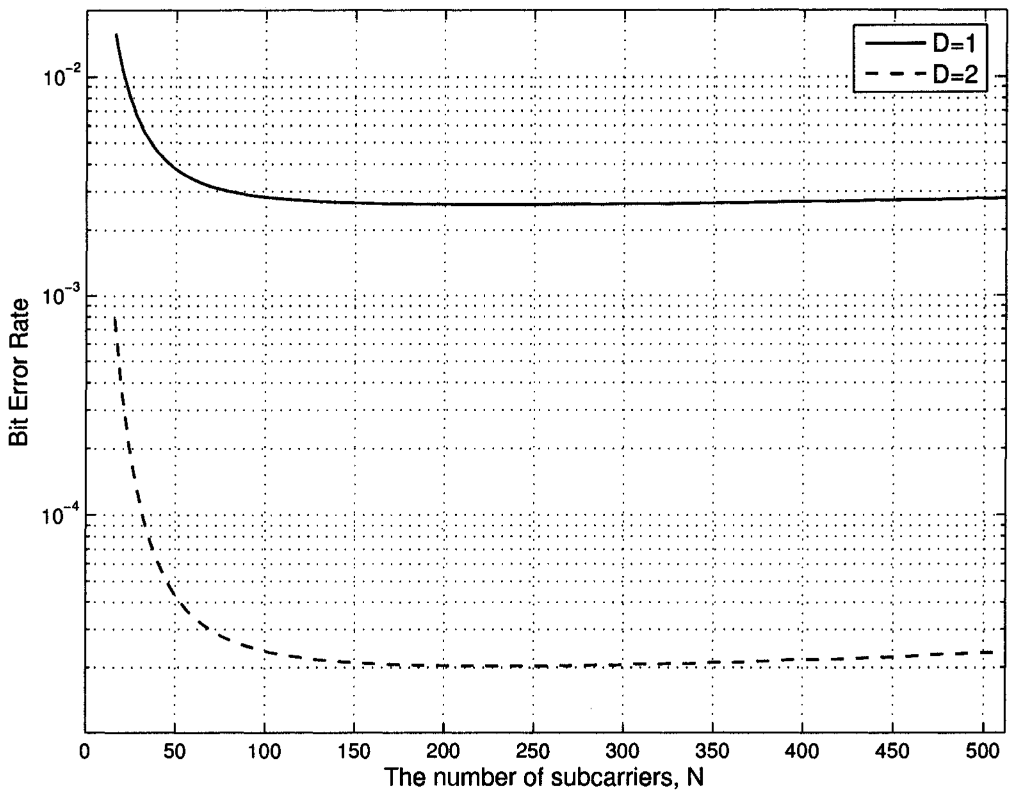

Fig. 2.4. The system BER as a function of the number of subcarriers.

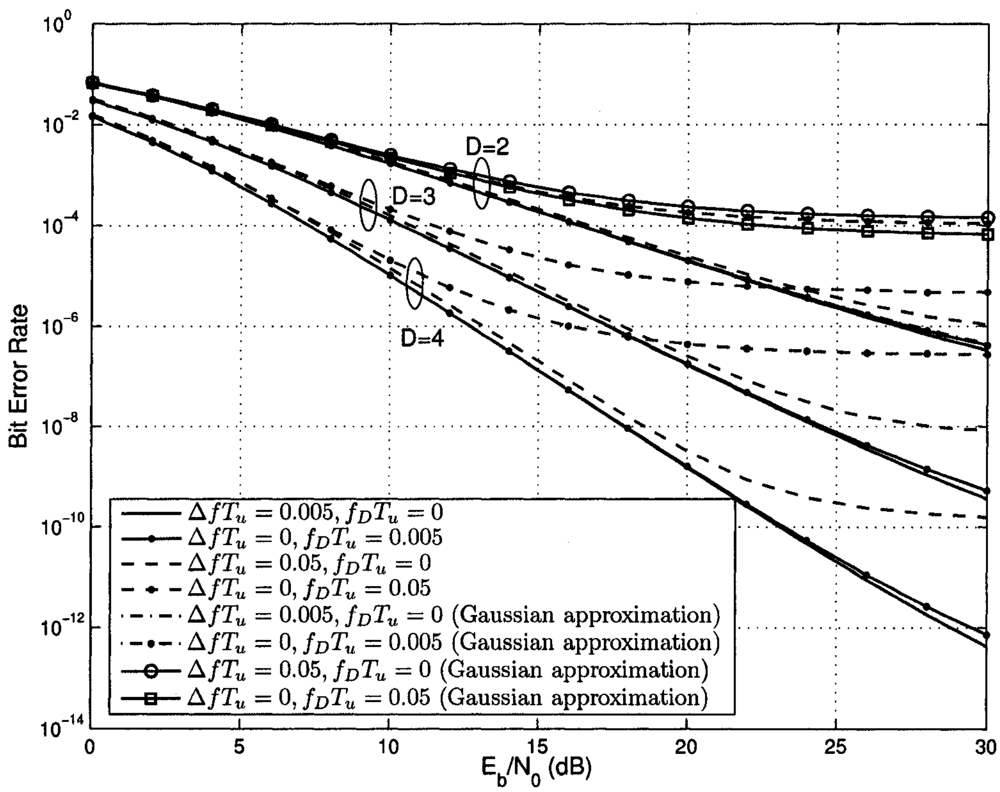

Fig. 2.5. The effect of Doppler shift and carrier frequency offset on the system BER performance for $\bar{\tau}/T_u = 0.002$, $N = 64$, and $D = 2, 3$ and 4.

TABLE 2.4

Parameter Values for Fig. 2.4

Parameter	Value
Signal-to-noise ratio	20 dB
Maximum Doppler shift f_D	500 Hz
Carrier frequency offset Δf	500 Hz
Mean delay spread $\bar{\tau}$	20 ns
Bandwidth	20 MHz
Useful signal duration T_u	3.2 μs
Carrier frequency f_c	5.35 GHz

has been partly canceled by differential detection at the receiver. The BER curves for the case of dual-branch diversity obtained using a Gaussian approximation method [35] are shown in the same figure. One can see that for small normalized Doppler shift values and normalized frequency offsets, the Gaussian approximation results are almost the same as the accurate results. However, for large Doppler shifts and frequency offsets, there are wide discrepancies between the approximate results and the accurate results.

The BER versus the normalized carrier frequency offset $\Delta f T_u$, versus the normalized Doppler shift $f_D T_u$, and versus the normalized mean delay spread $\bar{\tau}/T_u$ for a value of 20 dB SNR are plotted in Fig. 2.6. The system is more sensitive to Doppler shift and mean delay spread than to frequency offset. For example, with two-branch diversity reception and at a BER of 10^{-4}, the maximum allowable normalized mean delay spread and the Doppler shift are 0.013, 0.040, respectively. However, under the same conditions, the maximum allowable normalized frequency offset is larger than 0.1.

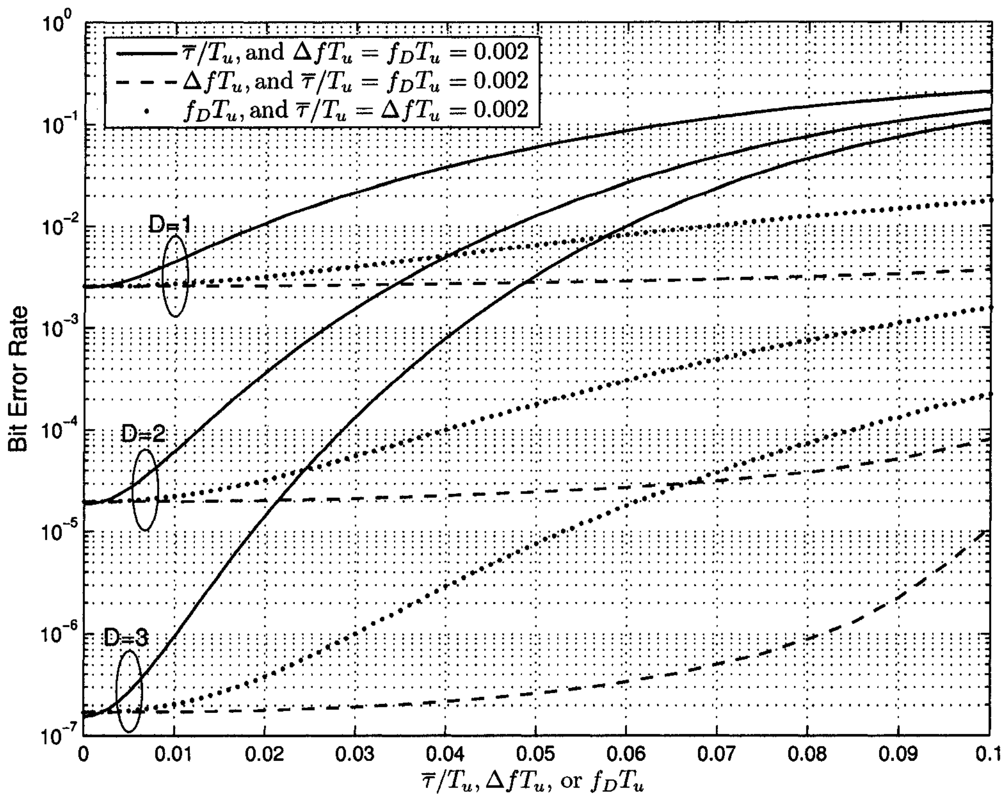

Fig. 2.6. The BER versus the normalized carrier frequency offset, versus the normalized Doppler shift, and versus the normalized mean delay spread with $N = 64$ and SNR=20 dB.

2.5 Summary

In this chapter, we developed an exact method for calculating the BER of a $\pi/4$-DQPSK OFDM system in the presence of frequency offset over frequency-selective fast Rayleigh fading channels. An analytical BER expression was obtained. The closed-form BER expression can be calculated directly for a small number of subcarriers. In the case of a large number of subcarriers, the BER expression can be evaluated by using a devised Monte Carlo method. The theoretical analysis results are in excellent agreement with simulation results. The exact BER expression was used to analyze the system performance under several wireless channel configurations. Doppler shift and delay spread will cause significant performance degradation. Particularly, Doppler shift usually results in more performance degradation than the same amount of carrier frequency offset. Important parameters, such as optimum number of subcarriers, tolerable mean delay spread, carrier frequency offset and Doppler shift, can be determined by using the exact closed-form BER expression. It was shown that multi-branch diversity can greatly reduce the system performance degradation caused by carrier frequency offset, time selectivity and frequency selectivity of channels.

Chapter 3

Exact BER Analysis of OFDM Systems over Rayleigh and Ricean Fading Channels in the Presence of Channel Estimation Error

3.1 Introduction

Channel state information (CSI) estimation is an indispensable part for coherent detection in OFDM systems. Different CSI estimation methods, including decision-directed channel estimation and pilot-symbol-aided channel estimation have been extensively studied in the literature [55–59]. However, it is not possible to acquire exact CSI at the receiver due to the influence of noise, and hence channel estimation error is inevitable. The performance degradation due to channel estimation error in a single carrier system for pilot-symbol-aided channel estimation has been studied in references [60–63]. Unlike single carrier systems, two-dimensional (2-D) time-frequency interpolation algorithms are usually used in pilot-symbol-aided channel estimation for OFDM systems to improve the channel estimation performance.

Several works on BER evaluation for OFDM systems in the presence of channel estimation error when using pilot-symbol-aided channel estimation schemes have been reported. Reference [33] gave a semi-analytical BER expression for binary phase shift keying (BPSK) modulation conditioned on channel fading for OFDM systems with channel estimation errors. The average BER can then be obtained by using Monte Carlo simulation to average out the channel fading. The effect of channel estimation error in OFDM-based wireless local area network (WLAN) was examined in [64]. Several approximate BER expressions for QPSK and M-QAM were given. Reference [65] presented a systematic approach for analyzing the BER of OFDM systems with channel estimation errors over Rayleigh fading channels. The BER performance of multichannel receivers and the BER performance over Ricean fading channels were not considered there.

In this work, we will develop exact closed-form BER expressions for an OFDM system operating in the presence of channel estimation errors over frequency-selective Rayleigh fading channels and frequency-selective Ricean fading channels. Our analysis includes the case of multichannel reception, which can improve the system performance significantly. Proper complex Gaussian random process theory [41] is applied in the development of a characteristic function analysis method. The BER expressions are then obtained using the characteristic function method. This method is different from the method used in [33, 64, 65]. Moreover, this method can be further extended to multichannel reception and Ricean fading environments, which were not studied in [33, 64, 65]. We consider 16-QAM modulation, which is essential for high data rate applications, and two interpolation schemes, including Wiener filtering, and sinc function interpolation. However, the analysis method presented in this chapter can be used for other modulation formats and for any linear interpolation schemes. The BER expressions can be written as sums of several conditional probability functions which can be accurately evaluated by using proper complex Gaussian random process theory and a characteristic function method. The closed-form BER expressions obtained are then used to evaluate the system performance with different system configurations. We compare the performance of a sinc interpolation method and a Wiener interpolation method. It is found that the sinc interpolator gives worse BER performance than the Wiener interpolator in the considered scenarios although it has a simpler implementation. The effects of channel estimation error on OFDM systems with different numbers of diversity branches, and different Ricean factors are examined as well. We also study the effect of different pilot placement spacings on the system BER performance by using the accurate closed-form BER expressions.

The reminder of this chapter is organized as follows. In Section 3.2, the system model is given. Then the BER expressions for Rayleigh fading channels and Ricean fading channels are derived by using a characteristic function method in Section 3.3 and Section 3.4, respectively. Some discussion of the results together with Monte Carlo simulation results are presented in Section 3.5. Lastly we summarize our results in Section 3.6.

3.2 System Model

As shown in Chapter 2, a continuous-time N-subcarrier baseband OFDM signal, $s(t)$, including CP can be expressed as

$$s(t) = \frac{1}{\sqrt{N}} \sum_{i=-\infty}^{+\infty} \sum_{n=0}^{N-1} D_{i,n} e^{\frac{j2\pi n(t-T_g-iT_s)}{T_u}} u(t-iT_s). \tag{3.1}$$

We assume that the receiver is synchronized to the 0th path with delay $\tau_0 = 0$, and sampled at the instants

$$t_m = kT_s + T_g + \frac{mT_u}{N}, \quad m = 0, 1, \cdots, N-1 \tag{3.2}$$

since the samples within the cyclic prefix T_g are discarded before further processing. Thus, the received N samples on the dth diversity branch in one OFDM symbol are

$$y_m^d = \frac{1}{\sqrt{N}} \sum_{l=0}^{L-1} h_l[m,k] \sum_{i=k-1}^{k} \sum_{n=0}^{N-1} D_{i,n} e^{\frac{j2\pi n\left[(k-i)T_s+mT_u/N-\tau_l\right]}{T_u}} u\left[(k-i)T_s+T_g-\tau_l+mT_u/N\right]+w_m \tag{3.3}$$

where $h_l[m,k] = h_l(kT_s + T_g + \frac{mT_u}{N})$, and w_m are zero-mean complex Gaussian random variables with variance $\sigma^2/2$ per dimension. Since $T_g \geq \tau_l$, $u[(k-i)T_s + T_g - \tau_l + mT_u/N] \neq 0$ only when $i = k$. Different from Chapter 2, in this chapter we assume that the channel is a slowly fading channel so that $h_l[m,k]$ does not vary according to sample location m in the kth OFDM symbol, that is

$$h_l[m,k] = h_l[0,k] = h_l[k]. \tag{3.4}$$

Thus one has

$$\begin{aligned} y_m^d &= \frac{1}{\sqrt{N}} \sum_{l=0}^{L-1} h_l[k] \sum_{n=0}^{N-1} D_{k,n} e^{\frac{j2\pi nm}{N}} e^{\frac{-j2\pi n\tau_l}{T_u}} + w_m \\ &= \frac{1}{\sqrt{N}} \sum_{n=0}^{N-1} D_{k,n} H_d[t_m, f_n] e^{\frac{j2\pi nm}{N}} + w_m \end{aligned} \tag{3.5}$$

where

$$H_d[t_m, f_n] = \sum_{l=0}^{L-1} h_l[k] e^{\frac{-j2\pi n\tau_l}{T_u}} \tag{3.6}$$

is the channel response at the sampling time instant t_m and the subcarrier frequency $f_n = n/T_u$. Performing a DFT on $\{y_m^d\}_{m=0}^{N-1}$, with the assumption that the channel will not change within one OFDM symbol duration one can obtain the received signal on the S_fth subcarrier of the S_tth OFDM symbol as

$$r_d[S_t, S_f] = H_d[S_t, S_f] D[S_t, S_f] + w_d[S_t, S_f] \tag{3.7}$$

where $D[S_t, S_f]$ is the complex symbol modulated on the S_fth subcarrier in the S_tth OFDM symbol, and $w_d[S_t, S_f]$ is the AWGN with mean zero and variance σ^2.

The channel response $H_d[S_t, S_f]$ at time S_t and frequency S_f is a proper complex Gaussian random variable. In the case of Rayleigh fading channels

$$\mathbf{E}\Big\{H_d[S_t, S_f]\Big\} = 0 \tag{3.8}$$

where $\mathbf{E}[X]$ denotes the expectation of the random variable X. Under the assumption of exponential distribution of the multipath time delays, the correlation between $H_d[S_{t_1}, S_{f_1}]$ and $H_d[S_{t_2}, S_{f_2}]$ is given in [43,45,66] as

$$\mathbf{E}\Big\{H_d[S_{t_1}, S_{f_1}]H_d^*[S_{t_2}, S_{f_2}]\Big\} = \frac{2\sigma_f^2 J_0\left[2\pi(S_{t_1} - S_{t_2})\xi\right]}{1 - j2\pi(S_{f_2} - S_{f_1})\eta} \tag{3.9}$$

where $*$ denotes complex conjugation, $J_0(\cdot)$ is the Bessel function of the first kind of order 0, $\xi = f_D T_u$ is the normalized maximum Doppler shift, and $\eta = \bar{\tau}/T_u$ is the normalized mean delay spread measure given in [43]. In the case of Ricean fading channels, we assume that

$$H_d[S_t, S_f] = m_{LOS} + H_d^{sca}[S_t, S_f] \tag{3.10}$$

where m_{LOS} and $H_d^{sca}[S_t, S_f]$ are the line-of-sight (LOS) component and multipath scatter component, respectively. One can then derive

$$\begin{aligned}\mathbf{E}\Big\{H_d[S_{t_1}, S_{f_1}]H_d^*[S_{t_2}, S_{f_2}]\Big\} &= |m_{LOS}|^2 + \frac{2\sigma_f^2 J_0[2\pi(S_{t_1} - S_{t_2})\xi]}{1 - j2\pi(S_{f_2} - S_{f_1})\eta} \\ &= \frac{P_t}{K+1}\left\{K + \frac{J_0[2\pi(S_{t_1} - S_{t_2})\xi]}{1 - j2\pi(S_{f_2} - S_{f_1})\eta}\right\}\end{aligned} \tag{3.11}$$

where $P_t = |m_{LOS}|^2 + 2\sigma_f^2$ and the Ricean K parameter is defined as $K = |m_{LOS}|^2/2\sigma_f^2$. When the Ricean K parameter $K = 0$, the Ricean fading channel becomes a Rayleigh fading channel, and (3.11) reduces to (3.9).

In a practical system, the channel response $H_d[S_t, S_f]$ can be obtained from pilot-symbol-aided channel estimation [56,58,60]. We assume that the pilot symbols are placed on a two-dimensional rectangular time-frequency grid evenly with spacing T in the time-domain and spacing F in the frequency-domain. However, extension of the BER analysis method in this chapter to any pilot placements is straightforward. The pilot symbols $P[Tu,Fv]$ with energy $|P[Tu,Fv]|^2 = E_p$, known at the receiver, are placed on the Fvth subcarrier of the Tuth OFDM symbol where u and v are integers, $-\infty < u < \infty$ and $0 \leq Fv \leq N-1$. The spacing T and F are chosen to satisfy a 2-D sampling theorem so that $f_D T_s T \leq 0.5$ and $\tau_{max} F/T_u \leq 0.5$. The received signal at the pilot positions can then be written as

$$r_d[Tu,Fv] = H_d[Tu,Fv]P[Tu,Fv] + w_d[Tu,Fv]. \tag{3.12}$$

Thus, the channel estimation at pilot positions can be obtained as [56]

$$\begin{aligned}\tilde{H}_d[Tu,Fv] &= r_d[Tu,Fv]P^*[Tu,Fv]/E_p \\ &= H_d[Tu,Fv] + \overline{w}_d[Tu,Fv]\end{aligned} \tag{3.13}$$

where $\overline{w}_d[Tu,Fv] = P^*[Tu,Fv]w_d[Tu,Fv]/E_p$ is the AWGN with mean zero and variance σ^2/E_p. The channel estimation $\hat{H}_d[S_t,S_f]$ for data positions of the S_fth subcarrier and the S_tth OFDM symbol, where

$$S_t = Tu + \Delta t, \quad 1 \leq \Delta t \leq T-1 \tag{3.14}$$

$$S_f = Fv + \Delta f, \quad 1 \leq \Delta f \leq F-1 \tag{3.15}$$

can then be obtained by interpolation using the channel estimation at the pilot positions as

$$\begin{aligned}\hat{H}_d[S_t,S_f] &= \sum_{p=p_1}^{p_2}\sum_{q=q_1}^{q_2} f(p,q,\Delta t,\Delta f)\tilde{H}_d[T(u+p),F(v+q)] \\ &= \sum_{p=p_1}^{p_2}\sum_{q=q_1}^{q_2} f(p,q,\Delta t,\Delta f)\Big\{H_d[T(u+p),F(v+q)] + \overline{w}_d[T(u+p),F(v+q)]\Big\}\end{aligned} \tag{3.16}$$

where $f(p,q,\Delta t,\Delta f)$ is a one-dimensional (1-D), double 1-D or two-dimensional (2-D) interpolation function.

When using the Wiener filtering method from [58], one can obtain the 2-D interpolation function with the employment of orthogonal projection theorem [67]

$$\mathbf{E}\left\{\left(\hat{H}_d[S_t,S_f] - H_d[S_t,S_f]\right)\tilde{H}_d^*[T(u+l),F(v+m)]\right\} = 0$$

which can be further simplified to

$$\sum_{p=p_1}^{p_2} \sum_{q=q_1}^{q_2} f(p,q,\Delta t,\Delta f) \mathbf{E}\left\{\tilde{H}_d[T(u+p),F(v+q)]\tilde{H}_d^*[T(u+l),F(v+m)]\right\}$$
$$= \mathbf{E}\left\{H_d[S_t,S_f]\tilde{H}_d^*[T(u+l),F(v+m)]\right\} \tag{3.17}$$

where $l = p_1,\cdots,p_2$ and $m = q_1,\cdots,q_2$. Using the knowledge of the channel correlation functions in eq. (3.11), one can then derive

$$\mathbf{E}\left\{\tilde{H}_d[T(u+p),F(v+q)]\tilde{H}_d^*[T(u+l),F(v+m)]\right\}$$
$$= \begin{cases} P_t + \sigma^2/E_p, & p = l \text{ and } q = m \\ \frac{P_t}{K+1}\left\{K + \frac{J_0[2\pi T(l-p)\xi]}{1-j2\pi F(m-q)\eta}\right\}, & p \neq l \text{ or } q \neq m \end{cases} \tag{3.18}$$

and

$$\mathbf{E}\left\{H_d[S_t,S_f]\tilde{H}_d^*[T(u+l),F(v+m)]\right\}$$
$$= \frac{P_t}{K+1}\left\{K + \frac{J_0[2\pi(Tl-\Delta t)\xi]}{1-j2\pi(Fm-\Delta f)\eta}\right\}. \tag{3.19}$$

Note that eq. (3.17) can be written in matrix form as

$$\mathbf{Rc} = \mathbf{p} \tag{3.20}$$

where the $PQ \times PQ$ matrix $\mathbf{R}$ has the element $\mathbf{E}\left\{\tilde{H}_d[T(u+p),F(v+q)]\tilde{H}_d^*[T(u+l),F(v+m)]\right\}$ at the $[(l-p_1)Q+m-q_1+1]$th row and the $[(p-p_1)Q+q-q_1+1]$th column, the $[(p-p_1)Q+q-q_1+1]$th row element of the $PQ \times 1$ vector $\mathbf{c}$ is $f(p,q,\Delta t,\Delta f)$, the $[(l-p_1)(q_2-q_1+1)+m-q_1+1]$th row element of the $PQ \times 1$ vector $\mathbf{p}$ is $\mathbf{E}\left\{H_d[S_t,S_f]\tilde{H}_d^*[T(u+l),F(v+m)]\right\}$, and $P = p_2-p_1+1$, $Q = q_2-q_1+1$, $p = p_1,\cdots,p_2$, $q = q_1,\cdots,q_2$. Therefore, the interpolation coefficient matrix is $\mathbf{c} = \mathbf{R}^{-1}\mathbf{p}$.

In the case of sinc interpolation, the interpolation function can be written as [68]

$$f(p,q,\Delta t,\Delta f) = \operatorname{sinc}\left(\frac{\Delta t}{T} - p\right)\operatorname{sinc}\left(\frac{\Delta f}{F} - q\right) \tag{3.21}$$

where the sinc function is defined as

$$\operatorname{sinc}(t) = \begin{cases} 1, & t = 0 \\ \sin(\pi t)/\pi t, & t \neq 0. \end{cases} \tag{3.22}$$

A Hamming window is usually applied to this interpolator to reduce the influence of the abrupt truncation of the rectangular window.

We consider a receiver with I diversity channels that are mutually independent. The maximal-ratio combining scheme is used, where the channel information is obtained from the pilot-symbol-aided channel estimation method described above. The decision statistic $\hat{D}[S_t, S_f]$ of the data symbol on the S_fth subcarrier and the S_tth OFDM symbol is, thus,

$$\hat{D}[S_t, S_f] = \frac{\sum_{d=1}^{I} r_d[S_t, S_f]\hat{H}_d^*[S_t, S_f]}{\sum_{d=1}^{I} |\hat{H}_d[S_t, S_f]|^2}. \tag{3.23}$$

The BERs of the OFDM system with channel estimation error in Rayleigh fading channels and in Ricean fading channels are then evaluated in Section 3.3 and in Section 3.4, respectively.

3.3 Rayleigh Fading Channels

In the BER analysis, we choose 16-QAM as the subcarrier modulation format. However, the analysis method presented in this chapter can be used for other modulation formats. The Gray-coded 16-QAM constellation specified in the IEEE802.11a and IEEE 802.16a standards is used in this chapter. In 16-QAM signaling, $D[S_t, S_f] = D^I[S_t, S_f] + jD^Q[S_t, S_f]$ is a complex symbol, and $D^I[S_t, S_f]$ and $D^Q[S_t, S_f]$ are chosen independently from the set $\{-3d, -d, d, 3d\}$. The four bits $b1$ $b2$ $b3$ $b4$ in one 16-QAM symbol are divided into two groups [69], in-phase bits $(b1, b2)$ and quadrature bits $(b3, b4)$, so the decision on the in-phase bits is determined only by the real-part of the decision statistic $\hat{D}[S_t, S_f]$ in eq. (3.23). The imaginary part of $\hat{D}[S_t, S_f]$ determines the decision of the quadrature bits $b3$ and $b4$.

The decision rules for the in-phase bits can be summarized as follows:

$$\text{if } \hat{D}^I[S_t, S_f] \geq 0, \text{ then } b1 = 0$$

$$\text{if } \hat{D}^I[S_t, S_f] < 0, \text{ then } b1 = 1$$

$$\text{if } \hat{D}^I[S_t, S_f] \geq 2d \text{ or } \hat{D}^I[S_t, S_f] < -2d, \text{ then } b2 = 1$$

$$\text{if } -2d \leq \hat{D}^I[S_t, S_f] < 2d, \text{ then } b2 = 0.$$

There are similar decision rules for the quadrature bits $b3$ and $b4$. Thus, the BERs of the $b1$ bit and $b2$ bit can be calculated as

$$\begin{aligned} P_{b1} = & \frac{1}{2}\text{Prob}\{ \hat{D}^I[S_t, S_f] \geq 0 \mid D^I[S_t, S_f] < 0 \} \\ & + \frac{1}{2}\text{Prob}\{ \hat{D}^I[S_t, S_f] < 0 \mid D^I[S_t, S_f] \geq 0 \} \end{aligned} \tag{3.24}$$

and

$$\begin{aligned} P_{b2} = & \frac{1}{4}\text{Prob}\{ \hat{D}^I[S_t, S_f] \geq 2d \text{ or } \hat{D}^I[S_t, S_f] < -2d \mid D^I[S_t, S_f] = d \} \\ & + \frac{1}{4}\text{Prob}\{ \hat{D}^I[S_t, S_f] \geq 2d \text{ or } \hat{D}^I[S_t, S_f] < -2d \mid D^I[S_t, S_f] = -d \} \\ & + \frac{1}{4}\text{Prob}\{ -2d \leq \hat{D}^I[S_t, S_f] < 2d \mid D^I[S_t, S_f] = 3d \} \\ & + \frac{1}{4}\text{Prob}\{ -2d \leq \hat{D}^I[S_t, S_f] < 2d \mid D^I[S_t, S_f] = -3d \} \end{aligned} \tag{3.25}$$

respectively. Noting the symmetries of the BER expressions in eqs. (3.24) and (3.25), one can immediately obtain that

$$P_{b1} = \frac{1}{8} \sum_{D[S_t, S_f] \in \mathbb{S}_1 \cup \mathbb{S}_2} \text{Prob}\{\hat{D}^I[S_t, S_f] < 0 \mid D[S_t, S_f]\} \tag{3.26}$$

$$\begin{aligned} P_{b2} = & \frac{1}{8} \sum_{D[S_t, S_f] \in \mathbb{S}_3} \text{Prob}\{\hat{D}^I[S_t, S_f] < -2d \mid D[S_t, S_f]\} \\ & + \frac{1}{8} \sum_{D[S_t, S_f] \in \mathbb{S}_1} \text{Prob}\{\hat{D}^I[S_t, S_f] < -2d \mid D[S_t, S_f]\} \\ & + \frac{1}{8} \sum_{D[S_t, S_f] \in \mathbb{S}_2} \text{Prob}\{\hat{D}^I[S_t, S_f] < 2d \mid D[S_t, S_f]\} \end{aligned}$$

$$-\frac{1}{8}\sum_{D[S_t,S_f]\in\mathbb{S}_2}\text{Prob}\left\{\hat{D}^I[S_t,S_f]<-2d\mid D[S_t,S_f]\right\} \tag{3.27}$$

where $\mathbb{S}_1,\cdots,\mathbb{S}_3$ are the following symbol sets

$$\mathbb{S}_1=\{\ d+jd,\ d-jd,\ d+j3d,\ d-j3d\ \}$$

$$\mathbb{S}_2=\{\ 3d+jd,\ 3d-jd,\ 3d+j3d,\ 3d-j3d\ \}$$

$$\mathbb{S}_3=\{\ -d+jd,-d-jd,-d+j3d,-d-j3d\ \}.$$

Observe from eqs. (3.26) and (3.27) that, if we define the following conditional probability function

$$F^I_{prob}(a,D[S_t,S_f])=\text{Prob}\left\{\hat{D}^I[S_t,S_f]<a\mid D[S_t,S_f]\right\} \tag{3.28}$$

where a is a real number and superscript I denotes I diversity channels, then the $b1$ bit and $b2$ bit error probabilities can be further written as

$$P_{b1}=\frac{1}{8}\sum_{D[S_t,S_f]\in\mathbb{S}_1\cup\mathbb{S}_2}F^I_{prob}(0,D[S_t,S_f]) \tag{3.29}$$

and

$$\begin{aligned}P_{b2}=&\frac{1}{8}\sum_{D[S_t,S_f]\in\mathbb{S}_3}F^I_{prob}(-2d,D[S_t,S_f])+\frac{1}{8}\sum_{D[S_t,S_f]\in\mathbb{S}_1}F^I_{prob}(-2d,D[S_t,S_f])\\&+\frac{1}{8}\sum_{D[S_t,S_f]\in\mathbb{S}_2}F^I_{prob}(2d,D[S_t,S_f])-\frac{1}{8}\sum_{D[S_t,S_f]\in\mathbb{S}2}F^I_{prob}(-2d,D[S_t,S_f]).\end{aligned} \tag{3.30}$$

Thus, the problem at hand is to derive the probability function $F^I_{prob}(a,D[S_t,S_f])$. In the following developments, the conditional probability function in the single channel reception case, $F^1_{prob}(a,D[S_t,S_f])$, is first derived. We then show that the conditional probability function in the case of any I number of diversity branches, $F^I_{prob}(a,D[S_t,S_f])$, is a function of $F^1_{prob}(a,D[S_t,S_f])$ under the assumption of independent diversity branches. The error probability function $F^1_{prob}(a,D[S_t,S_f])$ for single channel reception can be written as

$$F^1_{prob}(a,D[S_t,S_f])=\text{Prob}\left\{\Re\left\{\hat{D}[S_t,S_f]\right\}<a\mid D[S_t,S_f]\right\}$$

$$= \text{Prob}\left\{\Re\left\{\frac{r_d[S_t,S_f]\hat{H}_d^*[S_t,S_f]}{|\hat{H}_d[S_t,S_f]|^2}\right\} < a \mid D[S_t,S_f]\right\}$$
$$= \text{Prob}\left\{\Re\left\{\hat{H}_d^*[S_t,S_f]\left(r_d[S_t,S_f] - a\hat{H}_d[S_t,S_f]\right)\right\} < 0 \mid D[S_t,S_f]\right\} \tag{3.31}$$

Now defining the proper complex Gaussian random variables [41] A_d and B_d as

$$A_d = \hat{H}_d[S_t,S_f] \tag{3.32}$$

and

$$B_d = r_d[S_t,S_f] - a\hat{H}_d[S_t,S_f] \tag{3.33}$$

respectively, and then putting them into (3.31) yields

$$F_{prob}^1(a, D[S_t,S_f]) = \text{Prob}\left\{\frac{1}{2}(A_d^*B_d + A_dB_d^*) < 0 \mid D[S_t,S_f]\right\}. \tag{3.34}$$

The probability in (3.34) can be calculated using a characteristic function method. Noting that $\frac{1}{2}(A_d^*B_d + A_dB_d^*)$ is a Hermitian quadratic form [39] in complex Gaussian random variables, one can write its characteristic function conditioned on data symbol $D[S_t,S_f]$ as

$$\Phi(\omega|D[S_t,S_f]) = \mathbf{E}\left\{e^{j\omega\frac{1}{2}(A_d^*B_d+A_dB_d^*)} \mid D[S_t,S_f]\right\}$$
$$= \frac{1}{1+\frac{1}{4}\omega^2\nu - j\omega\alpha} \tag{3.35}$$

where $\alpha = \Re\{\sigma_{AB}\}$ and $\nu = \sigma_A\sigma_B - |\sigma_{AB}|^2$. Since the correlation matrix is almost always positive definite [70], one has $\nu > 0$. The variances $\mathbf{E}(A_dA_d^*) = \sigma_A$, $\mathbf{E}(B_dB_d^*) = \sigma_B$, and the complex covariance between A_d and B_d, $\mathbf{E}(A_d^*B_d) = \sigma_{AB}$ are given in eqs. (3.36)-(3.38)

$$\sigma_A = \mathbf{E}(A_dA_d^*)$$
$$= \sum_{p=p_1}^{p_2}\sum_{q=q_1}^{q_2}\sum_{l=p_1}^{p_2}\sum_{m=q_1}^{q_2} f(p,q,\Delta t,\Delta f)f^*(l,m,\Delta t,\Delta f)$$
$$\times \mathbf{E}\left\{H_d[T(u+p),F(v+q)]H_d^*[T(u+l),F(v+m)]\right\}$$
$$+ \sum_{p=p_1}^{p_2}\sum_{q=q_1}^{q_2}\sum_{l=p_1}^{p_2}\sum_{m=q_1}^{q_2} f(p,q,\Delta t,\Delta f)f^*(l,m,\Delta t,\Delta f)$$

$$
\begin{aligned}
&\times \mathbf{E}\left\{\overline{w}_d[T(u+p),F(v+q)]\overline{w}_d^*[T(u+l),F(v+m)]\right\} \\
&= \sum_{p=p_1}^{p_2}\sum_{q=q_1}^{q_2}\sum_{l=p_1}^{p_2}\sum_{m=q_1}^{q_2} f(p,q,\Delta t,\Delta f)f^*(l,m,\Delta t,\Delta f)\frac{2\sigma_f^2 J_0[2\pi T(l-p)\xi]}{1-j2\pi F(m-q)\eta} \\
&+ \sum_{p=l=p_1}^{p_2}\sum_{q=m=q_1}^{q_2} |f(p,q,\Delta t,\Delta f)|^2\sigma^2/E_p
\end{aligned} \tag{3.36}
$$

$$
\begin{aligned}
\sigma_B &= \mathbf{E}(B_d B_d^*) \\
&= 2\sigma_f^2|D[S_t,S_f]|^2 + \mathbf{E}\left(w_d[S_t,S_f]w_d^*[S_t,S_f]\right) + a^2\sigma_A \\
&\quad - 2a\Re\left\{D^*[S_t,S_f]\sum_{p=p_1}^{p_2}\sum_{q=q_1}^{q_2} f(p,q,\Delta t,\Delta f)\mathbf{E}\left(H_d[T(u+p),F(v+q)]H_d^*[S_t,S_f]\right)\right\} \\
&= 2\sigma_f^2|D[S_t,S_f]|^2 + \sigma^2 + a^2\sigma_A \\
&\quad - 2a\Re\left\{D^*[S_t,S_f]\sum_{p=p_1}^{p_2}\sum_{q=q_1}^{q_2} f(p,q,\Delta t,\Delta f)\frac{2\sigma_f^2 J_0[2\pi(Tp-\Delta t)\xi]}{1-j2\pi(\Delta f-Fq)\eta}\right\}
\end{aligned} \tag{3.37}
$$

$$
\begin{aligned}
\sigma_{AB} &= \mathbf{E}(A_d B_d^*) \\
&= \sum_{p=p_1}^{p_2}\sum_{q=q_1}^{q_2} f(p,q,\Delta t,\Delta f)D^*[S_t,S_f]\mathbf{E}\left\{H_d[T(u+p),F(v+q)]H_d^*[S_t,S_f]\right\} - a\sigma_A \\
&= \sum_{p=p_1}^{p_2}\sum_{q=q_1}^{q_2} f(p,q,\Delta t,\Delta f)D^*[S_t,S_f]\frac{2\sigma_f^2 J_0[2\pi(Tp-\Delta t)\xi]}{1-j2\pi(\Delta f-Fq)\eta} - a\sigma_A.
\end{aligned} \tag{3.38}
$$

Applying the inversion theorem in [49–52], one can then obtain a closed-form expression for the probability in (3.34) as

$$
\begin{aligned}
F_{prob}^1(a,D[S_t,S_f]) &= \text{Prob}\left\{\frac{1}{2}(A_d^*B_d + A_dB_d^*) < 0 \mid D[S_t,S_f]\right\} \\
&= \frac{1}{2} - \int_0^{+\infty}\frac{\Im\left\{\Phi(\omega|D[S_t,S_f])\right\}}{\pi\omega}d\omega \\
&= \frac{1}{2} - \frac{\alpha}{2\sqrt{\alpha^2+\nu}}
\end{aligned} \tag{3.39}
$$

where $\Im\left\{\Phi(\omega|D[S_t,S_f])\right\}$ denotes the imaginary part of $\Phi(\omega|D[S_t,S_f])$.

In the case of I independent diversity channels, the probability function $F_{prob}^I(a,D[S_t,S_f])$ becomes

$$
F_{prob}^I(a,D[S_t,S_f]) = \text{Prob}\left\{\frac{1}{2}\sum_{d=1}^{I}(A_d^*B_d + A_dB_d^*) < 0 \mid D[S_t,S_f]\right\}. \tag{3.40}
$$

The characteristic function $\Phi(\omega)$ of the sum $\frac{1}{2}\sum_{d=1}^{I}(A_d^*B_d+A_dB_d^*)$ can be written as

$$\Phi(\omega)=\frac{1}{(1-jC_1\omega)^I(1-jC_2\omega)^I} \tag{3.41}$$

where $C_1=(\alpha+\sqrt{\alpha^2+v})/2$ and $C_2=(-\alpha+\sqrt{\alpha^2+v})/2$. Recalling that $v>0$, one has $C_1>0$ and $C_2>0$. It is noted in [46] that $\Phi(\omega)$ is the characteristic function of $\frac{C_1}{2}X_1-\frac{C_2}{2}X_2$ where X_1 and X_2 are two independent chi-square random variables with $2I$ degrees of freedom and $\mathbf{E}[X_1]=\mathbf{E}[X_2]=2I$. Using (3.41) with (3.40) yields

$$\begin{aligned}F_{prob}^I(a,D[S_t,S_f]) &= \text{Prob}\left\{\frac{C_1}{2}X_1<\frac{C_2}{2}X_2\mid D[S_t,S_f]\right\}\\ &=\int_0^\infty\frac{1}{2^{2I}[(I-1)!]^2}x_1^{I-1}e^{-x_1/2}\int_{C_1x_1/C_2}^\infty x_2^{I-1}e^{-x_2/2}\,dx_2\,dx_1\\ &=F_{prob}^1(a,D[S_t,S_f])^I\sum_{i=0}^{I-1}\frac{(I+i-1)!}{(I-1)!i!}[1-F_{prob}^1(a,D[S_t,S_f])]^i.\end{aligned} \tag{3.42}$$

The quadrature bits $b3$ and $b4$ have the same BERs as the in-phase bits $b1$ and $b2$, respectively. Therefore, combining eqs. (3.29) and (3.30), the average BER of the 16-QAM modulated OFDM system with channel estimation error is

$$P_b=\frac{1}{2}(P_{b1}+P_{b2}). \tag{3.43}$$

3.4 Ricean Fading Channels

In the case of Ricean fading channels, $F_{prob}^I(a,D[S_t,S_f])$ in eq. (3.40) can be calculated using the results in [71], that is

$$F_{prob}^1(a,D[S_t,S_f])=Q(\bar{a},\bar{b})-\frac{v_2}{v_1+v_2}I_0(\bar{a}\bar{b})e^{-\frac{\bar{a}^2+\bar{b}^2}{2}} \tag{3.44}$$

for $I=1$, and

$$\begin{aligned}F_{prob}^I(a,D[S_t,S_f]) &= Q(\bar{a},\bar{b})-I_0(\bar{a}\bar{b})e^{-\frac{\bar{a}^2+\bar{b}^2}{2}}+\frac{I_0(\bar{a}\bar{b})e^{-\frac{\bar{a}^2+\bar{b}^2}{2}}}{(1+v_2/v_1)^{2I-1}}\sum_{k=0}^{I-1}C_{2I-1}^k(v2/v1)^k\\ &+\frac{e^{-\frac{\bar{a}^2+\bar{b}^2}{2}}}{(1+v_2/v_1)^{2I-1}}\sum_{n=1}^{I-1}I_n(\bar{a}\bar{b})\left\{\sum_{k=0}^{I-1-n}C_{2I-1}^k\left[(\bar{b}/\bar{a})^n(v_2/v_1)^k-(\bar{a}/\bar{b})^n(v_2/v_1)^{2I-1-k}\right]\right\}\end{aligned} \tag{3.45}$$

for $I > 1$ where $Q(\bar{a},\bar{b})$ is the Marcum Q function with arguments $\bar{a}$ and $\bar{b}$, $I_n(\cdot)$ is the modified Bessel function of the first kind of order n, C_{2I-1}^{k} denotes the number of combinations of $2I-1$ things taken k at a time, and

$$
\begin{aligned}
w &= \frac{2\Re\{m_{xy}\}}{m_{xx}m_{yy}-|m_{xy}|^2} \\
v_1 &= \sqrt{w^2+\frac{4}{m_{xx}m_{yy}-|m_{xy}|^2}}-w \\
v_2 &= \sqrt{w^2+\frac{4}{m_{xx}m_{yy}-|m_{xy}|^2}}+w \\
a_1 &= \frac{I}{4}\left[|m_x|^2 m_{yy}+|m_y|^2 m_{xx}-2\Re\{m_x^* m_y m_{xy}\}\right] \\
a_2 &= I\cdot\Re\{m_x^* m_y\} \\
m_x &= \mathbf{E}\left[A_d\right] = \sum_{p=p_1}^{p_2}\sum_{q=q_1}^{q_2} f(p,q,\Delta t,\Delta f)m_{LOS} \\
m_y &= \mathbf{E}\left[B_d\right] = m_{LOS}\left(D[S_t,S_f]-a\sum_{p=p_1}^{p_2}\sum_{q=q_1}^{q_2} f(p,q,\Delta t,\Delta f)\right) \\
m_{xx} &= \mathbf{E}\left[(A_d-m_x)(A_d-m_x)^*\right] = \sigma_A \\
m_{yy} &= \mathbf{E}\left[(B_d-m_y)(B_d-m_y)^*\right] = \sigma_B \\
m_{xy} &= \mathbf{E}\left[(A_d-m_x)(B_d-m_y)^*\right] = \sigma_{AB} \\
\bar{a} &= \sqrt{2v_1^2 v_2(a_1 v_2-a_2)/(v_1+v_2)^2} \\
\bar{b} &= \sqrt{2v_1 v_2^2(a_1 v_1+a_2)/(v_1+v_2)^2}.
\end{aligned}
$$

Note that when the Ricean parameter $K=0$, the Ricean fading channel becomes a Rayleigh fading channel. In this case, it is easy to verify that eq. (3.44) becomes $F_{prob}^{1}(a,D[S_t,S_f])$ in eq. (3.39) for Rayleigh fading environments. However, in the case of multichannel reception, eq. (3.45) can not be applied for Rayleigh fading cases because $\bar{a}=\bar{b}=0$ when $K=0$. For multichannel reception over Rayleigh fading channels, one can use the simple expression in eq. (3.42) derived in Section 3.3.

Following the same approach, the BER for the OFDM systems with perfect channel information can be obtain immediately by letting $A_d = H_d[S_t, S_f]$ and $B_d = r_d[S_t, S_f] - aH_d[S_t, S_f]$.

3.5 Examples and Discussion

The theoretical results in Section 3.3 and Section 3.4 are compared to Monte Carlo simulation results in Figs. 3.1 and 3.2. To reduce the variance of the simulation estimates, 10^7 16-QAM data symbols were generated to obtain each BER value. We assume the average 16-QAM symbol energy and the energy of the pilot symbols E_p are both $10d^2$ and $d = 1$ in the simulations. The fading power σ_f is normalized to 1. The normalized maximum Doppler shift ξ and the normalized mean delay spared η are both 0.02. We further assume that the time-domain pilot spacing T and the frequency-domain pilot spacing F are both 4, $\Delta t = \Delta f = 1$, $p_1 = q_1 = -4$, and $p_2 = q_2 = 4$. Hamming windowing is applied to the case of sinc interpolation. The theoretical results and simulation results are in excellent agreement in both figures.

Figs. 3.1 and 3.2 examine the effect of channel estimation errors on the BER performance of OFDM systems with diversity reception over frequency-selective Rayleigh fading channels and over frequency-selective Ricean fading channels, respectively. Solid lines, dashed lines and dash-dot lines represent results obtained from the exact analysis in Section 3.3 and 3.4, and symbols (circles, asterisks, *etc.*) denote the average BER's obtained from Monte Carlo simulations. One observes from Fig. 3.1 that, compared with the case of perfect channel information, the channel estimation error will introduce significant performance degradation. In particular, 4.2 dB and 1.3 dB loss in signal-to-noise ratio (SNR) can be observed at a bit error rate of 10^{-3} for dual branch reception when using sinc interpolation and Wiener interpolation, respectively. In the system configurations considered, the sinc interpolation gives much worse BER performance than the Wiener interpolation

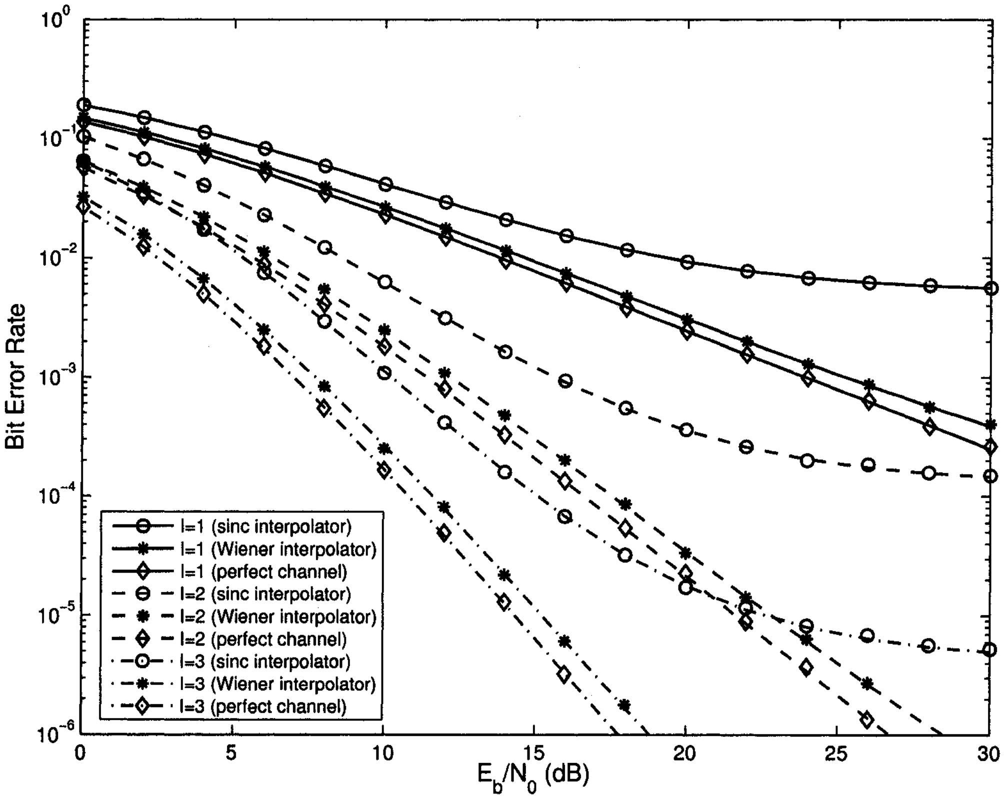

Fig. 3.1. The BER performance of a 16-QAM-OFDM system over a Rayleigh fading channel with a sinc interpolator, Wiener interpolator, and perfect channel information, for *I* reception branches.

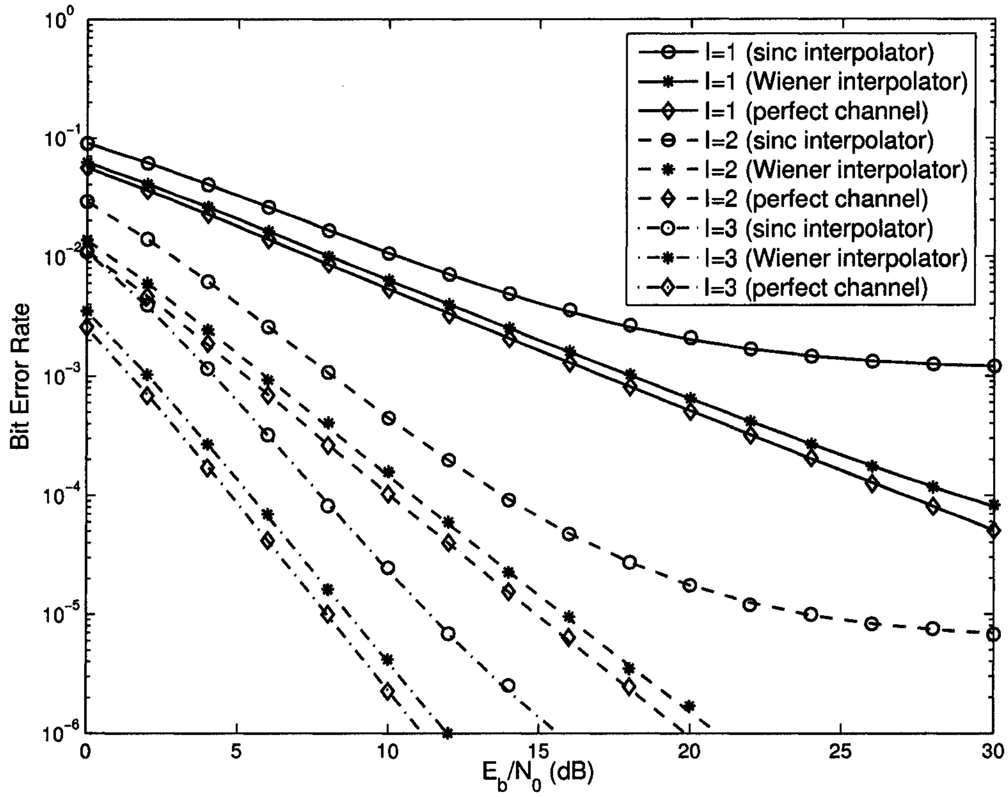

Fig. 3.2. The BER performance of a 16-QAM-OFDM system over a Ricean fading channel with a sinc interpolator, Wiener interpolator, and perfect channel information, for I reception branches and Ricean factor $K = 2$ dB.

method. An error rate floor occurs in the high SNR region when using the sinc interpolation method. Although Wiener interpolation method can give better performance than the sinc interpolation method, it is more complex than the sinc interpolation method because channel parameters, such as Doppler shift, mean delay spread, and noise variance, must be acquired to construct the Wiener interpolation coefficients. Practical system design must consider the trade-off between complexity and performance. In the case of Ricean fading channels, the superiority of Wiener interpolation can be observed in Fig. 3.2. Nonetheless, diversity reception is still an effective way to improve system performance even with imperfect channel information. At a bit error rate of 10^{-2}, using Wiener interpolation, compared with single branch reception, a 7.3 dB gain can be observed with dual-branch reception.

In Fig. 3.3, we investigate the system performance of single channel reception using a Wiener interpolation method over Ricean fading channels with different Ricean factors $K = 3$ dB, 5 dB, 7 dB and 9 dB. As expected, an increased Ricean factor will give better BER performance because of the larger LOS component. In particular, at a BER of 10^{-3}, one can obtain 4.6 dB, 9.7 dB and 14.3 dB gain in SNR when the K factor increases from 3 dB to 5 dB, to 7 dB and to 9 dB, respectively.

Fig. 3.4 considers the effect of Doppler shift on the system performance with different interpolation methods. As the Doppler shift increases, the channel varies more rapidly and thus system performance becomes worse. The worst performance is bounded by a extremly large and impractical normalized Doppler shift value 0.1 in this figure. One can also see that in the low SNR region, the system performance changes only slightly for different maximum Doppler shift values when using the sinc interpolator which is not related to channel state parameters. However, in the high SNR region ($E_b/N_0 > 10$ dB in this figure), the performance changes significantly. The reason for that is for small SNR values, the AWGN is the dominant factor affecting the accuracy of channel estimation. However, in the high SNR region, mismatch of the sinc interpolator with the channel variations becomes

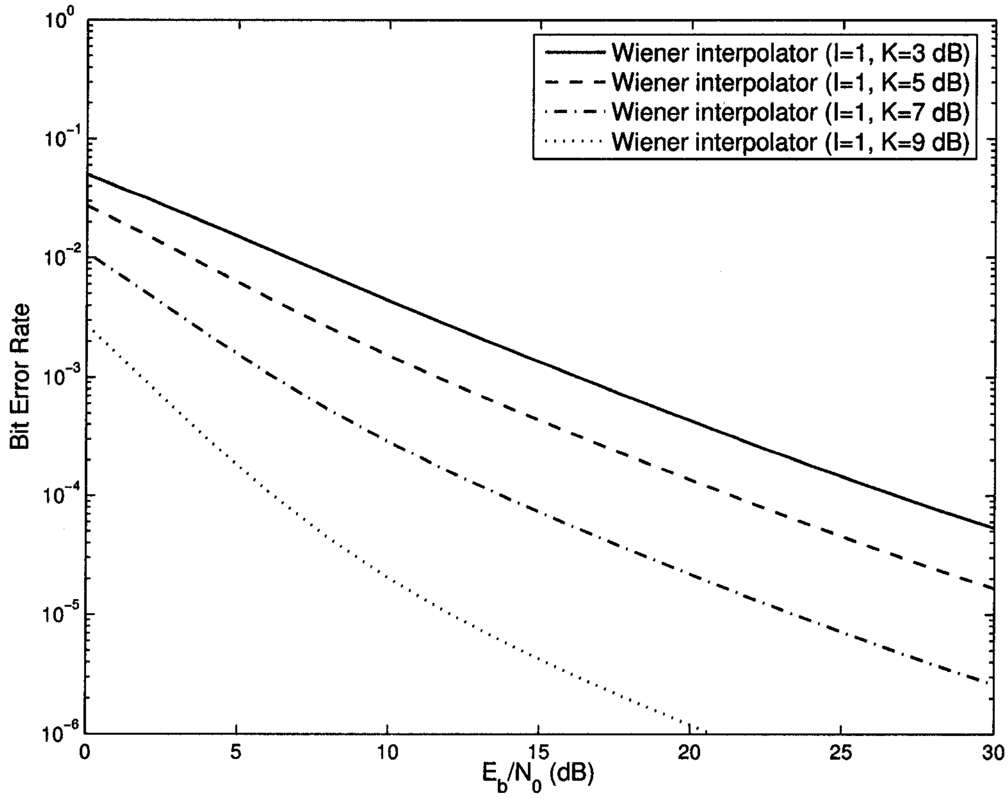

Fig. 3.3. The BER performance of a 16-QAM-OFDM system over a Ricean fading channel with Wiener interpolator, single channel reception, $\xi = \eta = 0.02$, and Ricean factors $K = 3$ dB, 5 dB, 7 dB and 9 dB.

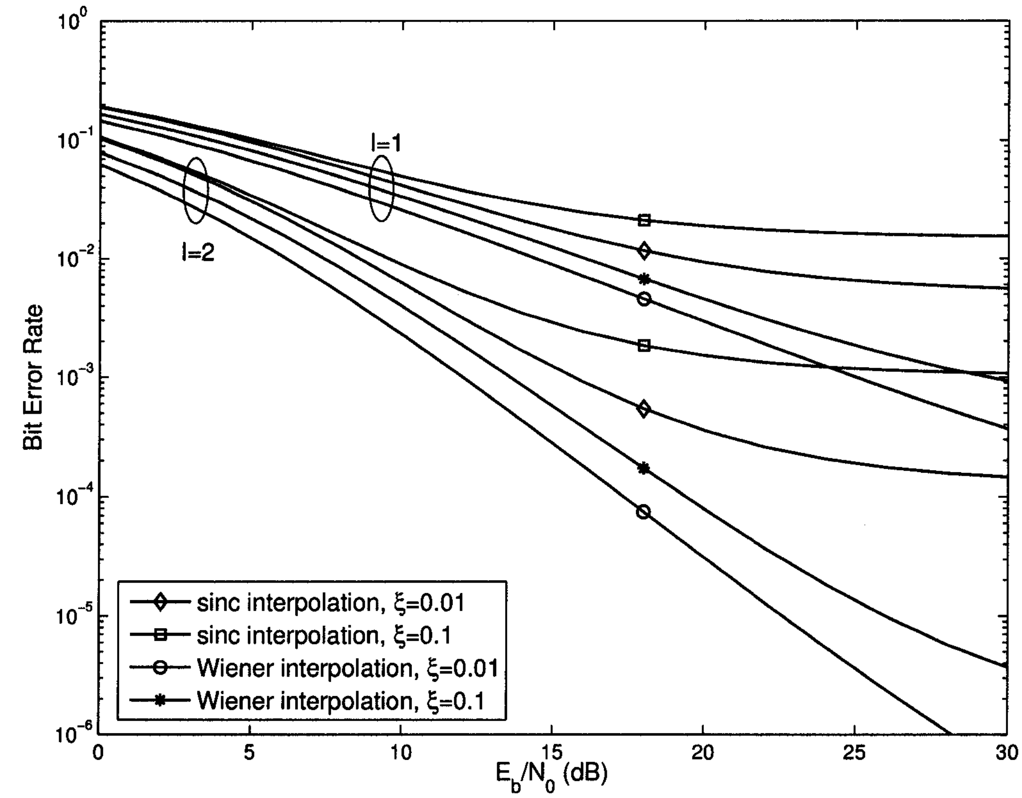

Fig. 3.4. The BER performance of a 16-QAM-OFDM system over a Rayleigh fading channel with a sinc interpolator and Wiener interpolator, $\eta = 0.02$, and normalized maximum Doppler shift $\xi = 0.01$ and 0.1.

the dominant cause limiting the system performance. The Wiener interpolation, on the other hand, employs the channel parameter information to construct optimized interpolation coefficients, and thus achieves a better BER performance. One can see that for a fixed BER value, in the high SNR region, the variation of the BER curve in the case of sinc interpolation is greater than in the case of Wiener interpolation. For example, at a BER of 2×10^{-3} and with two diversity branches, in the case of Wiener interpolation, there is about 1.6 dB performance degradation when the normalized maximum Doppler shift increases from 0.01 to 0.1. The same measure, in the case of sinc interpolation, is about 4 dB.

It is also interesting to study the effect of pilot spacing T in the time-domain and pilot spacing F in the frequency-domain on the system BER performance. In Fig. 3.5, we compare the system BER performance with different pilot spacings and different data symbol positions. The first data symbol after the pilot symbol and the middle data symbol between two neighboring pilot symbols are considered. One can see that increased pilot spacing can lead to significant performance degradation. In particular, at a bit error rate of 10^{-5}, increasing pilot spacing from $T = F = 4$ to $T = F = 8$ will introduce around 2 dB loss in SNR. Small BER values, as small as 10^{-15}, are shown in this figure to indicate that in the case of $T = F = 4$, the first data symbol position and the second data symbol position have almost the same BER performance. However, slight performance improvement of the first data symbol position over the second data symbol position can be seen only in the impractical high SNR and small BER region.

3.6 Summary

In this chapter, we developed an exact method for calculating the BER of an OFDM system in the presence of channel estimation error over frequency-selective Rayleigh fading channels and frequency-selective Ricean fading channels. Closed-form BER expressions were

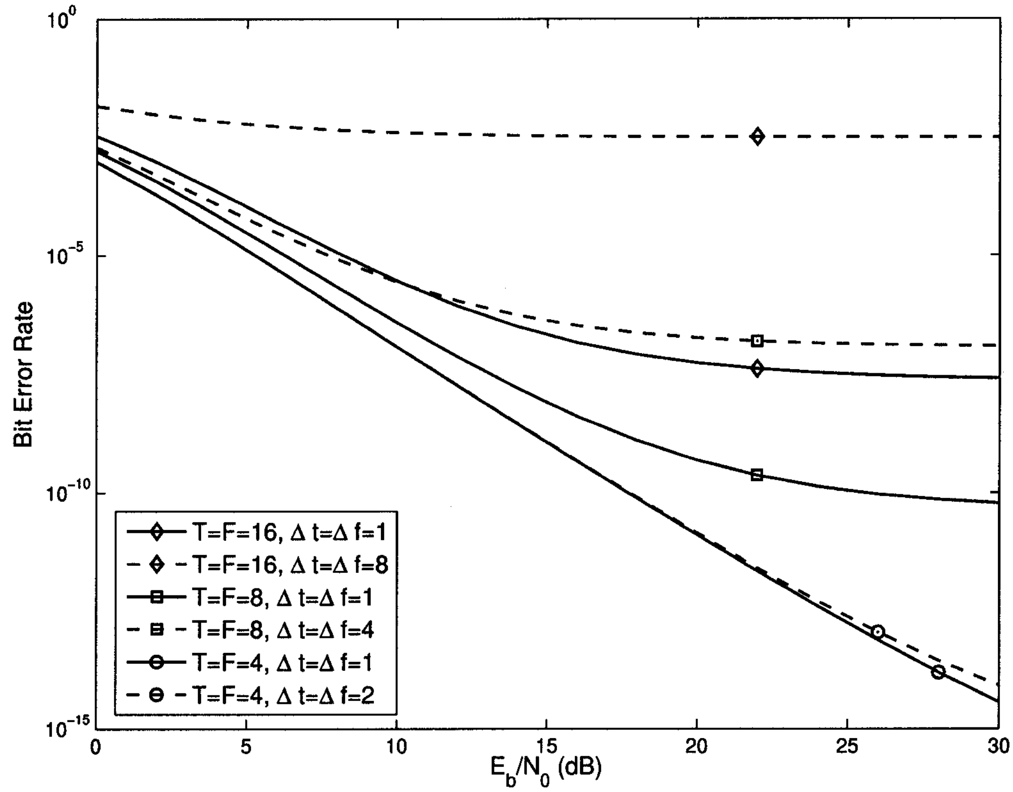

Fig. 3.5. The effect of pilot spacing on the BER performance of a 16-QAM-OFDM system over a Ricean fading channel with Wiener interpolator, diversity branches $I = 4$, Ricean factor $K = 2$ dB, normalized maximum Doppler shift $\xi = 0.02$, and normalized mean delay spread $\eta = 0.02$.

obtained. The theoretical analysis results are in excellent agreement with Monte Carlo simulation results. The exact BER expressions were used to examine the system performance under several wireless channel configurations, and with sinc interpolation and Wiener interpolation. It was seen that diversity reception is still an effective method to improve system BER performance even with imperfect channel estimation. It was shown that, the sinc interpolation gives worse BER performance than the Wiener interpolation method.

Chapter 4

The Effect of Transmitter Nyquist Shaping on ICI Reduction in OFDM Systems with Carrier Frequency Offset

4.1 Introduction

It was shown in Chapter 2 that OFDM is sensitive to carrier frequency offset which introduces ICI in OFDM receivers. Frequency offset can be compensated by frequency offset estimation. However, estimation error is inevitable and hence residue frequency offset usually exists in OFDM systems. Therefore, it is of interest to investigate schemes that are robust to frequency offset. ICI reduction techniques using coding were studied in [72–75]. Transmitter pulse-shaping can also realize ICI power reduction. As classified in [76], three types of pulse shaping have been examined in the literature for ICI reduction.

The first type, pulses of infinite time duration, were studied in [2, 3, 77–80]. Reference

[2,3,77] considered band-limited Nyquist pulses in multichannel data transmission systems. The pulse is chosen as $g(t) = \mathbb{F}^{-1}\{\sqrt{G(f)}\}$ where $G(f)$ is a band-limited Nyquist filter with roll-off factor α and $\mathbb{F}^{-1}\{\cdot\}$ denotes the inverse Fourier transform. Other infinite-duration pulses were designed in [78–80] under the framework of the Weyl-Heisenberg system of functions. The second type comprises pulses of finite duration that is longer than one OFDM symbol interval. These pulses were developed for an OFDM system with offset QAM in an AWGN environment based on an optimization criterion that maximizes the in-band energy under the constraint of zero ISI and ICI [76]. The pulse shapes in these two categories are usually obtained by numerical computation [76,78–80]. In particular, the pulse shape design methods in [76,78] involve the solution of highly nonlinear optimization problems. The third category also consists of pulses of finite duration. But different from the second category, the pulses have a specified length of one OFDM symbol interval. These pulses are usually chosen to be Nyquist pulses in the time domain, that is $G(t)$. In this regard, [81] used a raised-cosine pulse in their time-limited orthogonal multicarrier modulation schemes.

Note that conventional OFDM systems employ the rectangular pulse so that digital modulation and demodulation can be realized with the IDFT and DFT, respectively [5]. In pulse-shaped OFDM systems, the conventional IDFT/DFT implementation structure can not be applied directly because the data symbols have been weighted by different pulse samples. In this case, additional filtering operations must be performed for each OFDM symbol both at the receiver and transmitter. However, the pulse-shaped OFDM can still be implemented digitally. Several discrete implementation structures with modified IDFT/DFT methods for pulse-shaped OFDM have been discussed in the literature. A filter bank - based scheme is discussed in the Appendix C of reference [79]. This scheme allows efficient digital implementation by using DFT filter banks. More filterbank discrete-time implementations for pulse-shaped OFDM are discussed in [82] and [83]. Reference [84] proposed using a fractional Fourier transform [85] to realize pulse-shaped OFDM systems in a discrete-time implementation. On the other hand, the surface acoustic wave (SAW) chirp Fourier transform (CFT) provides an analog implementation for the pulse-shaped OFDM systems [81]. One extraordinary benefit of this scheme is that the implementation of pulse-shaping OFDM in SAW CFT is independent of the number of subcarriers employed.

In this chapter, we consider the third category of pulse shapes, that is time-limited Nyquist pulses having closed-form expressions and a length of one OFDM symbol interval, in ICI reduction for OFDM systems in the presence of carrier frequency offset. Although these pulses overlap in the frequency domain, the orthogonality property of the Nyquist pulses ensures the separation of the data symbols on different subcarriers. Several Nyquist pulse shapes have been introduced in the literature. Optimal pulse design problems based on a MMSE criterion were investigated in [86] and [87]. Reference [86] developed an optimal Nyquist pulse, called the Franks pulse in this thesis, for a single-sideband carrier system in the presence of ISI caused by timing mismatch. The Franks pulse is a frequency offset-independent pulse, and can also be employed in the OFDM scenario to reduce ICI. On the other hand, by minimizing the ICI power caused by carrier frequency offset in OFDM systems, [87] derived a frequency offset-dependent pulse. Since the frequency offset is unknown, a pulse shape which is independent of frequency offset is required for practical implementation. Reference [87] derives a pulse shape that was dubbed the "constant Nyquist shape". This pulse, called the double-jump pulse in this thesis, was previously derived as an optimal solution to minimizing the mean square error when considering phase error only [86]. Reference [88] constructed a BTRC pulse, which exhibits better BER performance than the raised-cosine pulse in both ISI environments and cochannel interference environments [89]. More recently, reference [90] proposed a second-order continuous window (SOCW) shape, and applied it in OFDM receiver windowing to reduce ICI. Reference [91] proposed a family of ISI free polynomial pulses which can be used in the OFDM transmitter shaping to reduce ICI. These two pulses can give better performance than the conventional raised-cosine pulse in the aspect of ICI reduction in OFDM systems with carrier frequency offset, by using a set of properly chosen parameters.

A complete comparison of the performance of these pulses in OFDM systems is not available in the literature. In this chapter, we assume there exists a carrier frequency offset of Δf between the transmitter and receiver oscillators in an N-subcarrier OFDM system with subcarrier frequency spacing $1/T_u$ operating in an AWGN channel. We then compare the effect of using these six widely referenced Nyquist pulse-shaping functions, i.e., the raised-cosine pulse, the Franks pulse, the double-jump pulse, the BTRC pulse, the SOCW pulse, and the polynomial pulse on the ICI power reduction and SIR enhancement.

Just as for other digital communication systems, the ICI and SIR analyses offer a simple, and quick "pretty good" answer. However, in some cases, a more accurate yet more complicated answer is desired, in terms of the BER which is a more meaningful measure for a digital communications system. Error rate evaluations of OFDM systems in the presence of frequency offset have mainly been done using Gaussian approximation methods due to the difficulty of obtaining an exact distribution for the ICI [21, 27, 92, 93]. References [29, 94] showed that Gaussian approximation is only acceptable for small frequency offsets and small SNR values in AWGN channels. Further, [29] proposed a precise symbol error rate analysis of an OFDM system with BPSK, QPSK and 16-QAM over AWGN channels in the presence of frequency offset based on a Fourier series method [30, 31]. Since the in-phase and quadrature components of the QPSK and 16-QAM modulation formats considered are not independent, they wrote the correct detection probability as the product of two error functions, and then used the joint characteristic function and a Fourier series to calculate the symbol error probability. Hence, this analysis is inherently a two-dimensional analysis. Moreover, this work did not consider the effects of pulse-shaping on the BER performance of the OFDM system.

Therefore, in this chapter, we also develop a theoretical framework for analyzing the effects of transmitter Nyquist pulse-shaping on the BER of an uncoded OFDM system in the presence of frequency offset. The characteristic function method is used to derive analytical BER expressions for pulse-shaped OFDM systems with different modulation schemes, such as BPSK, QPSK and 16-QAM in the presence of frequency offset over AWGN channels. We then examine and compare the BER performance of OFDM systems using different Nyquist pulse-shapings. Different from the method in [29], we assume square constellations with Gray encoding for QPSK and 16-QAM. This configuration is common in practical communications systems using QPSK or QAM [11, 12, 69]. The benefit of this assumption lies in that we can use a one-dimensional analysis, and less computation effort is required for the BER calculation than is needed using the approach in [29]. Another contribution in this work is to investigate the dependence of the BER on the roll-off factor of the pulse employed for a specific system in the presence of frequency offset. Our method for calculating the BER of a pulse-shaped OFDM system with frequency offset can be used to determine the optimal roll-off factor by constructing average BER versus roll-off factor curves. Our theoretical BER analysis is in excellent agreement with results obtained from computer simulation, and it provides an exact prediction tool for the BER performance of OFDM systems in AWGN environments when using different ICI-reducing pulse shapes.

The remainder of this Chapter is organized as follows. In Section 4.2, the system model is given. The ICI and SIR analyses are then presented in 4.3. The BER expressions for transmission over AWGN channels are derived in Section 4.4. Some numerical results, simulation results, and the bandwidth efficiency of the pulse-shaped OFDM system are presented in Section 4.5. In Section 4.6, we summarize our chapter results.

4.2 System Model

The complex envelope of one radio frequency (RF) N-subcarrier OFDM symbol with pulse-shaping is expressed as [27]

$$x(t) = e^{j2\pi f_c t} \sum_{k=0}^{N-1} D_k p(t) e^{j2\pi f_k t} \tag{4.1}$$

where f_c is the carrier frequency, f_k is the subcarrier frequency of the kth subcarrier, $p(t)$ is the time-limited pulse-shaping function and D_k is the data symbol transmitted on the kth subcarrier. We assume that D_k has mean zero and normalized average symbol energy. We further assume that the data symbols are uncorrelated. That is,

$$\mathbf{E}\left[D_k D_m^*\right] = \begin{cases} 1, & k = m \\ 0, & k \neq m \end{cases} \tag{4.2}$$

where D_m^* denotes the complex conjugate of D_m. One also has that

$$f_k - f_m = \frac{k-m}{T_u} \tag{4.3}$$

to ensure subcarrier orthogonality [17]; that is,

$$\int_{-\infty}^{+\infty} p(t) e^{j2\pi(f_k - f_m)t}\, dt = \begin{cases} 1, & k = m \\ 0, & k \neq m \end{cases} \tag{4.4}$$

where $\frac{1}{T_u}$ is the minimum subcarrier frequency spacing required. Eq. (4.4) also indicates the important condition that the Fourier transform of the pulse $p(t)$ should have spectral nulls at the frequencies $\pm\frac{1}{T_u}, \pm\frac{2}{T_u}, \cdots$ to ensure subcarrier orthogonality.

We consider here six time-limited Nyquist pulses in the time domain. Let $p_{rc}(t)$, $p_{btrc}(t)$, $p_{socw}(t)$, $p_{poly}(t)$, $p_f(t)$, and $p_{dj}(t)$ denote the raised-cosine pulse, the BTRC pulse, the SOCW pulse [90], the polynomial pulse [91], the Franks pulse [86], and the double-jump pulse [86, 87] defined as follows:

$$p_{rc}(t) = \begin{cases} \frac{1}{T_u}, & |t| < \frac{T_u(1-\alpha)}{2} \\ \frac{1}{2T_u}\left\{1+\cos\left[\frac{\pi}{\alpha T_u}\left(|t| - \frac{T_u(1-\alpha)}{2}\right)\right]\right\}, & \frac{T_u(1-\alpha)}{2} \le |t| < \frac{T_u(1+\alpha)}{2} \\ 0, & \text{otherwise} \end{cases} \quad (4.5)$$

$$p_{btrc}(t) = \begin{cases} \frac{1}{T_u}, & |t| < \frac{T_u(1-\alpha)}{2} \\ \frac{1}{T_u} e^{\frac{-2\ln 2}{\alpha T_u}\left[|t| - \frac{T_u(1-\alpha)}{2}\right]}, & \frac{T_u(1-\alpha)}{2} \le |t| < \frac{T_u}{2} \\ \frac{1}{T_u}\left\{1 - e^{\frac{-2\ln 2}{\alpha T_u}\left[\frac{T_u(1+\alpha)}{2} - |t|\right]}\right\}, & \frac{T_u}{2} \le |t| < \frac{T_u(1+\alpha)}{2} \\ 0, & \text{otherwise} \end{cases} \quad (4.6)$$

$$p_{socw}(t) = \begin{cases} \frac{1}{T_u}, & |t| < \frac{T_u(1-\alpha)}{2} \\ \frac{1}{T_u}\left[1 - f(-\frac{2|t|}{\alpha T_u} + \frac{1}{\alpha})\right], & \frac{T_u(1-\alpha)}{2} \le |t| < \frac{T_u}{2} \\ \frac{1}{T_u} f(\frac{2|t|}{\alpha T_u} - \frac{1}{\alpha}), & \frac{T_u}{2} \le |t| < \frac{T_u(1+\alpha)}{2} \\ 0, & \text{otherwise} \end{cases} \quad (4.7)$$

where $f(t) = 0.5 + a_1 t - (0.5 + a_1)t^2$,

$$p_{poly}(t) = \begin{cases} \frac{1}{T_u}, & |t| < \frac{T_u(1-\alpha)}{2} \\ \frac{1}{T_u} g\left[\frac{|t| - T_u(1-\alpha)/2}{\alpha T_u}\right], & \frac{T_u(1-\alpha)}{2} \le |t| < \frac{T_u}{2} \\ \frac{1}{T_u}\left\{1 - g\left[\frac{T_u(1+\alpha)/2 - |t|}{\alpha T_u}\right]\right\}, & \frac{T_u}{2} \le |t| < \frac{T_u(1+\alpha)}{2} \\ 0, & \text{otherwise} \end{cases} \quad (4.8)$$

where $g(t) = \sum_{i=0}^{n} b_i t^i$,

$$p_f(t) = \begin{cases} \frac{1}{T_u}, & |t| < \frac{T_u(1-\alpha)}{2} \\ \frac{1}{T_u}\left(1 - \frac{|t|}{T_u}\right), & \frac{T_u(1-\alpha)}{2} \le |t| < \frac{T_u(1+\alpha)}{2} \\ 0, & \text{otherwise} \end{cases} \quad (4.9)$$

and

$$p_{dj}(t) = \begin{cases} \frac{1}{T_u}, & 0 \leq |t| < \frac{T_u(1-\alpha)}{2} \\ \frac{1}{2T_u}, & \frac{T_u(1-\alpha)}{2} \leq |t| < \frac{T_u(1+\alpha)}{2} \\ 0, & \text{otherwise} \end{cases} \tag{4.10}$$

with Fourier transforms

$$P_{rc}(f) = \text{sinc}(fT_u)\frac{\cos(\pi\alpha t T_u)}{1-4\alpha^2 t^2 T_u^2} \tag{4.11}$$

$$P_{btrc}(f) = \text{sinc}(fT_u)\frac{2\pi\alpha f T_u \sin(\pi\alpha f T_u)/\ln 2 + 2\cos(\pi\alpha f T_u) - 1}{(\pi\alpha f T_u/\ln 2)^2 + 1} \tag{4.12}$$

$$P_{socw}(f) = \text{sinc}(fT_u)\Big[2(1+a_1)\text{sinc}(\alpha f T_u) - (1+2a_1)\text{sinc}^2(\alpha f T_u/2)\Big] \tag{4.13}$$

$$\begin{aligned} P_{poly}(f) = \text{sinc}(fT_u)\Big\{&(1+\frac{b_2}{2}+\frac{b_3}{4}+\frac{b_4}{8})\text{sinc}(\alpha f T_u) - \frac{b_2}{2}\text{sinc}^2(\alpha f T_u/2) \\ &+\frac{3b_3}{2}\frac{[\text{sinc}(\alpha f T_u) - 1]}{(\pi\alpha f T_u)^2} + \frac{3b_4}{8}\frac{\text{sinc}^2(\pi\alpha f/2) - 1}{(\pi\alpha f T_u/2)^2}\Big\} \end{aligned} \tag{4.14}$$

for a fourth degree polynomial,

$$P_f(f) = \text{sinc}(fT_u)\Big[(1-\alpha)\cos(\pi\alpha f T_u) + \alpha\,\text{sinc}(\alpha f T_u)\Big] \tag{4.15}$$

and

$$P_{dj}(f) = \text{sinc}(fT_u)\cos(\pi\alpha f T_u) \tag{4.16}$$

respectively, where

$$\text{sinc}(x) = \begin{cases} 1, & x = 0 \\ \frac{\sin(\pi x)}{\pi x} & x \neq 0 \end{cases} \tag{4.17}$$

and α, $0 \le \alpha \le 1$, is the roll-off factor. When $\alpha = 0$, all of these six pulses coalesce into the rectangular pulse

$$p_r(t) = \begin{cases} \frac{1}{T_u}, & |t| < T_u/2 \\ 0, & \text{otherwise} \end{cases} \tag{4.18}$$

One can verify that if $g(t) = 1 - f(-2t+1)$, the polynomial pulse and the SOCW pulse have the same form. The SOCW pulse is a special case of the polynomial pulse when $g(t)$ is chosen as a second-order polynomial. It is also interesting to note that $p_{socw}(t) = p_f(t)$ for the special case of $\alpha = 1.0$ and $a_1 = -0.5$, although this pulse is not a SOCW because it is not second-order continuous. This equality does not hold for other values of α.

The time domain waveforms of these pulses in the case of $\alpha = 0.25$ are shown in Figs. 4.1 - 4.6.

In a practical system implementation, a time delay $\frac{T_u}{2}(1+\alpha)$ is required since the duration of the pulse starts before the pulse sampling instant. Let $p^d(t)$ represent the time delayed version of $p(t)$, where

$$p^d(t) = p\left[t - \frac{T_u}{2}(1+\alpha)\right], \quad 0 \le t \le T_u(1+\alpha) \tag{4.19}$$

The Fourier transform of $p^d(t)$ is

$$P^d(f) = P(f)e^{-j\pi f T_u(1+\alpha)}. \tag{4.20}$$

4.3 ICI and SIR Analysis

To study the effect of different pulse-shapings on the ICI reduction of an OFDM system in the presence of frequency offset, we first consider an imperfect receiver with frequency offset, $\Delta f (\Delta f \ge 0)$, operating on an ideal AWGN channel in the following analysis. The frequency offset may come from the receiver crystal oscillator inaccuracy, residual frequency

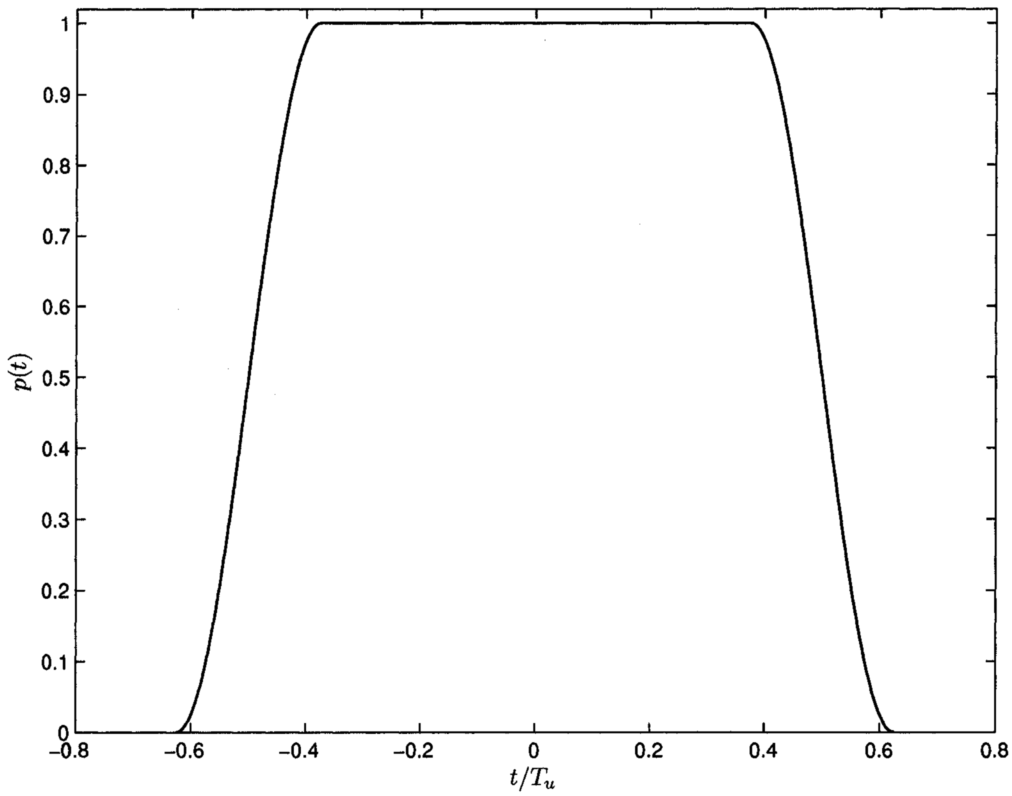

Fig. 4.1. The time domain waveform of the raised-cosine pulse ($\alpha = 0.25$).

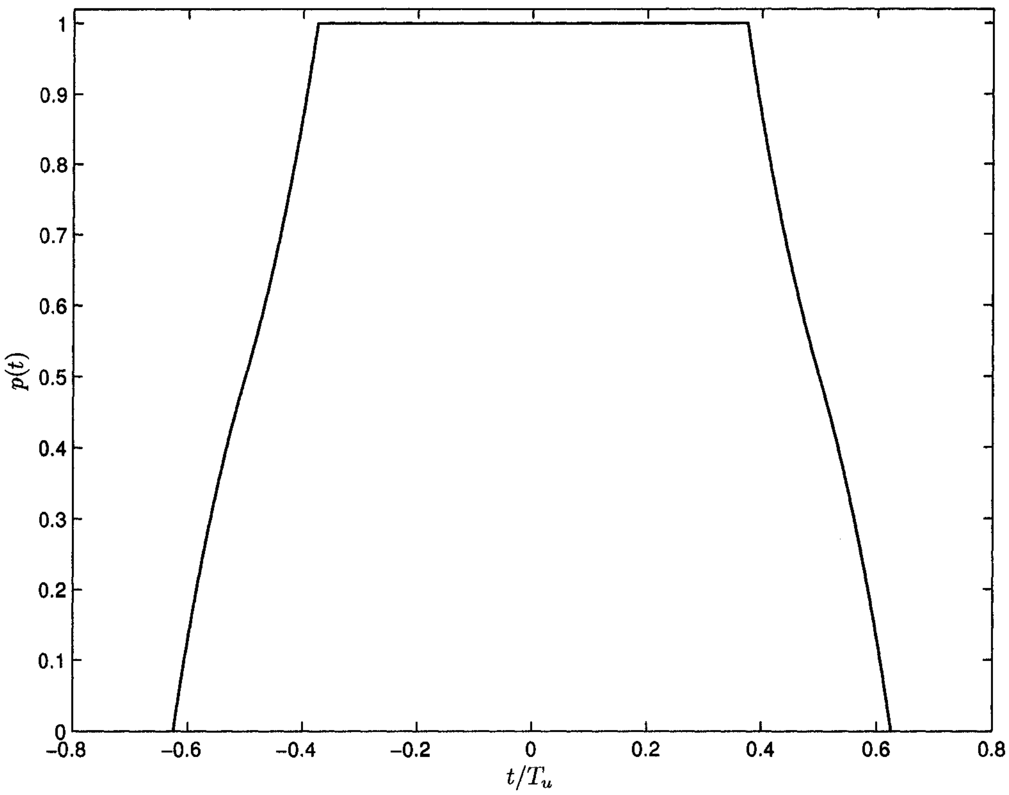

Fig. 4.2. The time domain waveform of the "better than" raised-cosine pulse ($\alpha = 0.25$).

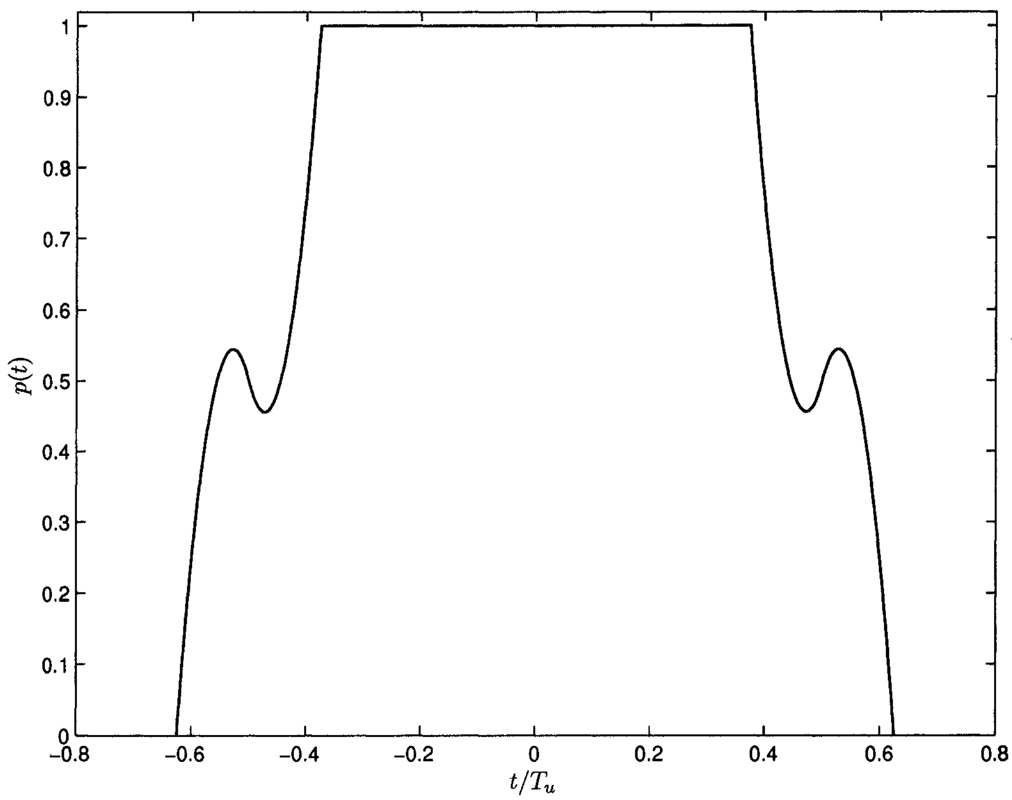

Fig. 4.3. The time domain waveform of the SOCW pulse ($\alpha = 0.25$).

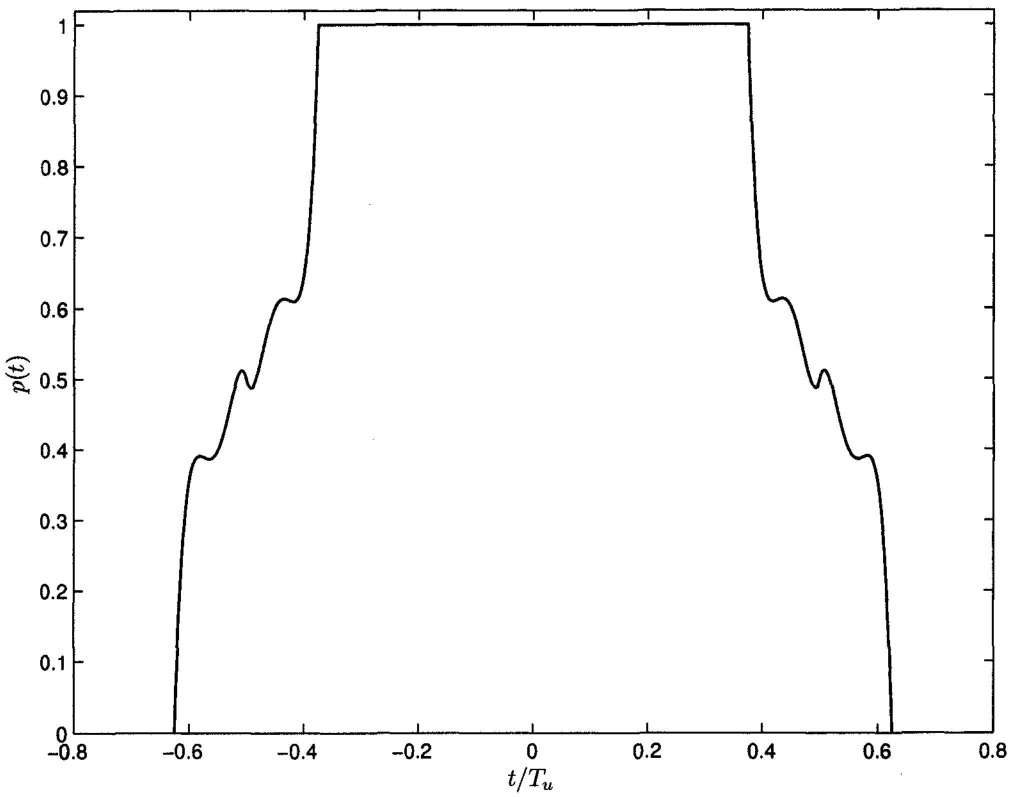

Fig. 4.4. The time domain waveform of the polynomial pulse ($\alpha = 0.25$).

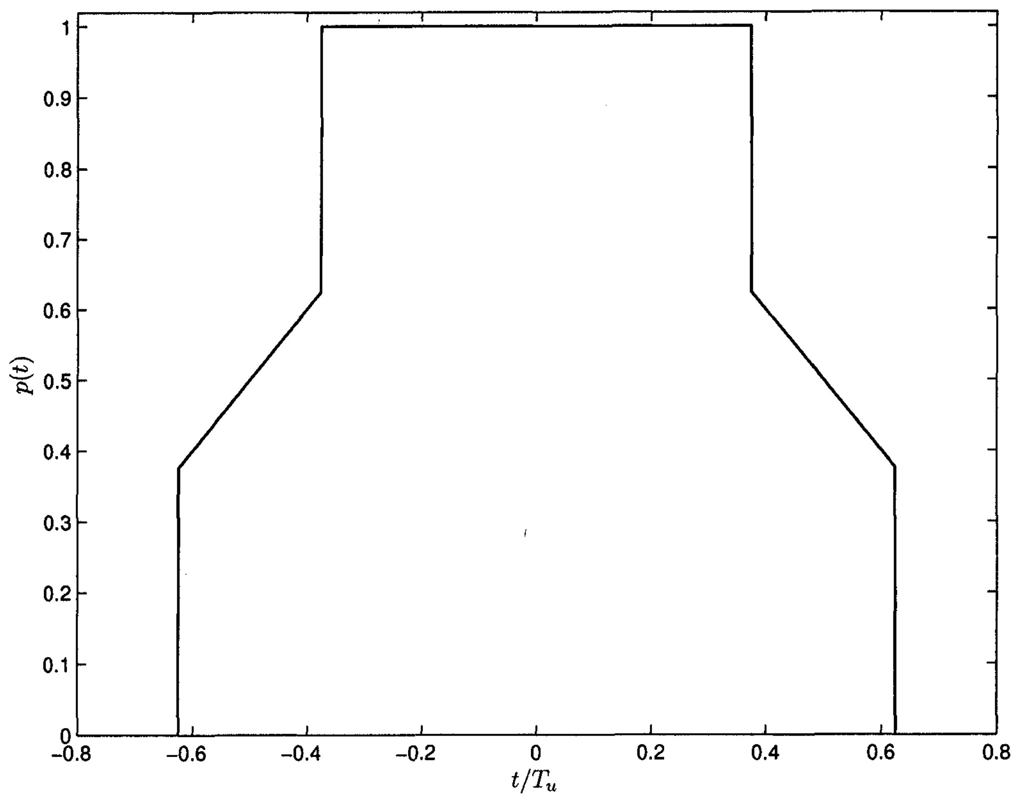

Fig. 4.5. The time domain waveform of the Franks pulse ($\alpha = 0.25$).

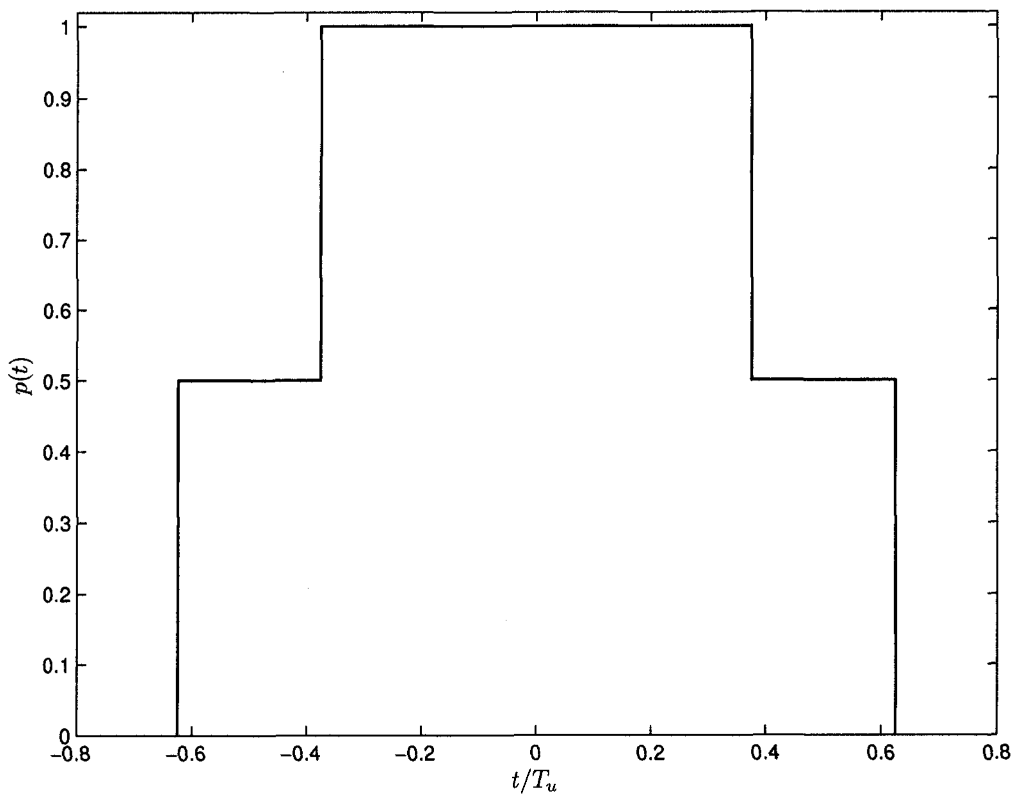

Fig. 4.6. The time domain waveform of the double-jump pulse ($\alpha = 0.25$).

offset after frequency offset estimation, or Doppler shift introduced by the time variation in one OFDM symbol.

ISI is not encountered in the AWGN channel model, so it is not necessary to employ a guard interval here. The received signal after multiplication by $e^{-j2\pi(f_c-\Delta f)t}$ becomes,

$$r(t) = e^{j2\pi\Delta ft}\sum_{k=0}^{N-1} D_k\sqrt{p^d(t)}e^{j2\pi f_k t} + n(t) \tag{4.21}$$

where the real part $n_I(t)$ and imaginary part $n_Q(t)$ of the complex noise process $n(t)$ are independent and Gaussian-distributed with zero-mean and variance $\sigma^2 = \frac{N_0}{2}$. Optimal, minimum probability of error, detection is realized using a correlation demodulator. The mth subchannel correlation demodulator gives the decision variable, $\hat{D}_m$, for transmitted symbol, D_m, where

$$\begin{aligned}\hat{D}_m &= \int_{-\infty}^{+\infty} r(t)\sqrt{p^d(t)}e^{-j2\pi f_m t}\,dt \\ &= D_m\int_{-\infty}^{+\infty} p^d(t)e^{j2\pi\Delta ft}\,dt + \sum_{\substack{k\neq m\\k=0}}^{N-1} D_k\int_{-\infty}^{+\infty} p^d(t)e^{j2\pi(f_k-f_m+\Delta f)t}\,dt + N_m. \end{aligned} \tag{4.22}$$

The first term in the sum in (4.22) contains the desired signal component, and the second term in the sum is the ICI. The noise component $\{N_m\}_{m=0}^{N-1}$ is a zero-mean, independent complex Gaussian random variable whose real part N_m^I and imaginary part N_m^Q have common variance σ^2 since

$$\begin{aligned}\mathbf{E}\left(N_k^I N_m^I\right) &= \mathbf{E}\left(N_k^Q N_m^Q\right) \\ &= \int_0^{T_u(1+\alpha)}\int_0^{T_u(1+\alpha)} \mathbf{E}[n_I(t)n_I^*(\tau)]\sqrt{p^d(t)}\sqrt{p^d(\tau)}e^{-j2\pi f_m t}e^{j2\pi f_k\tau}\,dt\,d\tau \\ &= \sigma^2\int_0^{T_u(1+\alpha)} p^d(t)e^{-j2\pi(f_m-f_k)t}\,dt \\ &= \begin{cases}\sigma^2, & k=m\\ 0, & k\neq m.\end{cases}\end{aligned} \tag{4.23}$$

Combining (4.3) with (4.22) gives,

$$\hat{D}_m = D_m c_0 + \sum_{\substack{k\neq m\\k=0}}^{N-1} D_k c_{k-m} + N_m \tag{4.24a}$$

where

$$c_{k-m} = P\left(\frac{k-m}{T_u} + \Delta f\right) e^{j\pi(k-m+\Delta f T_u)(1+\alpha)} \tag{4.24b}$$

with real part c^I_{k-m} and imaginary part c^Q_{k-m}. The first term in the sum in (4.24a) contains the desired signal component, and the second term in the sum is the ICI. The average power of the desired signal is

$$\sigma_s^2 = \mathbf{E}\left[|D_m|^2\right] |P(\Delta f)|^2 = |P(\Delta f)|^2 \tag{4.25}$$

since we assume that $\mathbf{E}\left[|D_m|^2\right] = 1$ in (4.2). In the presence of frequency offset, the desired signal amplitude is attenuated by a factor $|P(\Delta f)|$ which is the amplitude of the main lobe of the spectrum of the pulse-shaping function at the frequency offset Δf. The average ICI power, averaged across different sequences is

$$\begin{aligned}
\sigma_{ICI}^2 &= \sum_{\substack{k\neq m\\k=0}}^{N-1} \sum_{\substack{n\neq m\\n=0}}^{N-1} \mathbf{E}\left[D_k D_n^*\right] c_{k-m} c_{n-m}^* \\
&= \sum_{\substack{k\neq m\\k=0}}^{N-1} \sum_{\substack{n\neq m\\n=0}}^{N-1} \mathbf{E}\left[D_k D_n^*\right] P\left(\frac{k-m}{T_u} + \Delta f\right) P^*\left(\frac{n-m}{T_u} + \Delta f\right) \\
&= \sum_{\substack{k\neq m\\k=0}}^{N-1} \left| P\left(\frac{k-m}{T_u} + \Delta f\right)\right|^2 .
\end{aligned} \tag{4.26}$$

One sees that the average ICI power for the mth symbol depends on the number of sub-carriers and on the spectral magnitudes of the pulse-shaping function at the frequencies $\left(\frac{k-m}{T_u} + \Delta f\right)$, $k \neq m$, $k = 0, 1, \cdots, N-1$. By design, the spectra of the pulses have nulls at the frequency points $\frac{m-k}{T_u}(m \neq k)$, and hence no ICI occurs when $\Delta f = 0$. However, in the presence of frequency offset, it is observed that if the spectrum of one pulse-shaping function has smaller side-lobes than another, then the application of this pulse-shaping function in OFDM systems will lead to less ICI power. For example, by examining the frequency spectra of the different pulses in Fig. 4.7 and Fig. 4.8 for $\alpha = 0.25$ and $\alpha = 1.0$, respectively, for the raised-cosine pulse, one has

$$\left|P_{rc}\left(\frac{k-m}{T_u}+\Delta f\right)\right| \geq \left|P_{btrc}\left(\frac{k-m}{T_u}+\Delta f\right)\right| \tag{4.27}$$

and

$$\left|P_{rc}\left(\frac{k-m}{T_u}+\Delta f\right)\right| \geq \left|P_{f}\left(\frac{k-m}{T_u}+\Delta f\right)\right|. \tag{4.28}$$

Therefore, it is expected that both the BTRC pulse-shaped OFDM system and the Franks pulse-shaped OFDM system will have a reduced ICI power relative to a raised-cosine pulse-shaped OFDM system.

One can also consider the comparative performances of the different pulses in terms of the average signal power to average ICI power ratio [27], defined as

$$SIR = \frac{|P(\Delta f)|^2}{\sum_{\substack{k \neq m \\ k=0}}^{N-1} \left|P\left(\frac{k-m}{T_u}+\Delta f\right)\right|^2}. \tag{4.29}$$

Figs. 4.9 - 4.12 show the variation of the ICI power and SIR as a function of the normalized carrier frequency offset, $\Delta f T_u$. The number of subcarriers is 64, and the desired subchannel index is 32 in these comparisons. The parameter $a_1 = -0.5$ and 0.4 in the case of $\alpha = 1.0$ and 0.25, respectively for the SOCW pulse. A family of polynomial pulses with asymptotic decay rate of t^{-2} is used for the comparisons with other pulses because of their small side lobe amplitudes. The parameter set b_i is chosen as $\{b_0 = 1, b_1 = -1.6875, b_2 = 5, b_3 = -13, b_4 = 11.5\}$ in the case of $\alpha = 1.0$, and $\{b_0 = 1, b_1 = -6.625, b_2 = 40, b_3 = -100, b_4 = 85\}$ in the case of $\alpha = 0.25$ [91].

One can see in Figs. 4.9 and 4.10 that the Franks pulse is superior to the other pulses in terms of both ICI power reduction and SIR enhancement. In particularly, one can observe in Fig. 4.10 that, to obtain a SIR of 20 dB, the maximum allowable normalized carrier frequency offset values are 0.067, 0.075, 0.079, 0.081, 0.083, 0.084 for the raised-cosine pulse, the BTRC pulse, the SOCW pulse, the polynomial pulse, the double-jump pulse, and

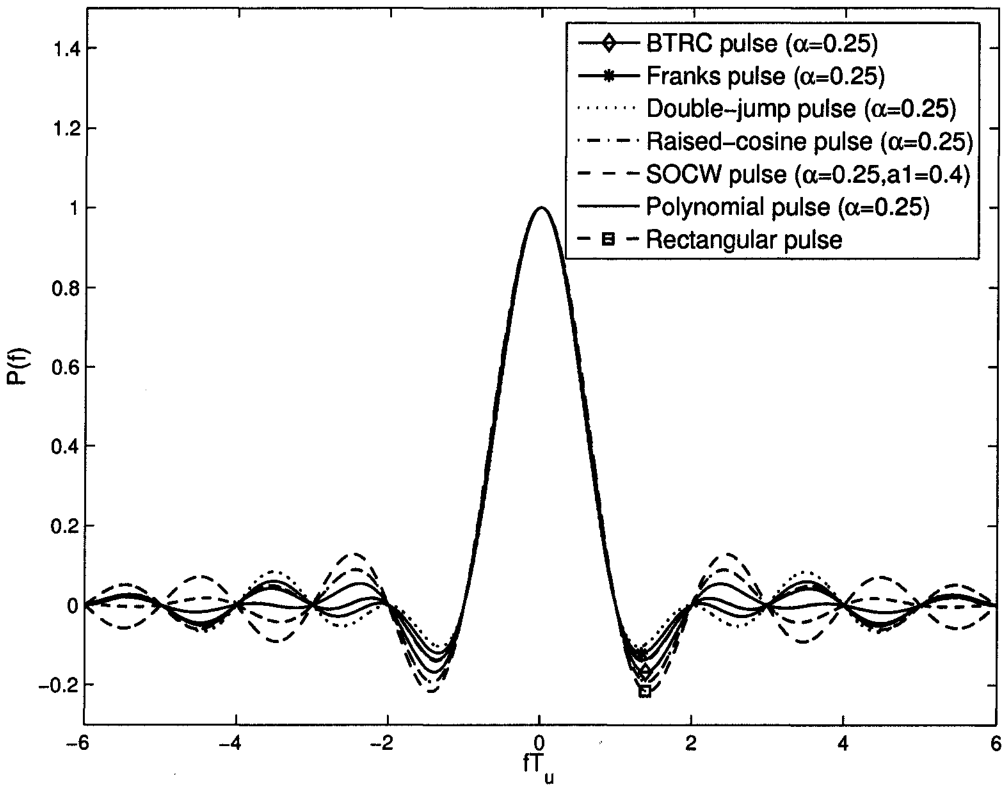

Fig. 4.7. The frequency spectra of different pulse-shaping functions ($\alpha = 0.25$).

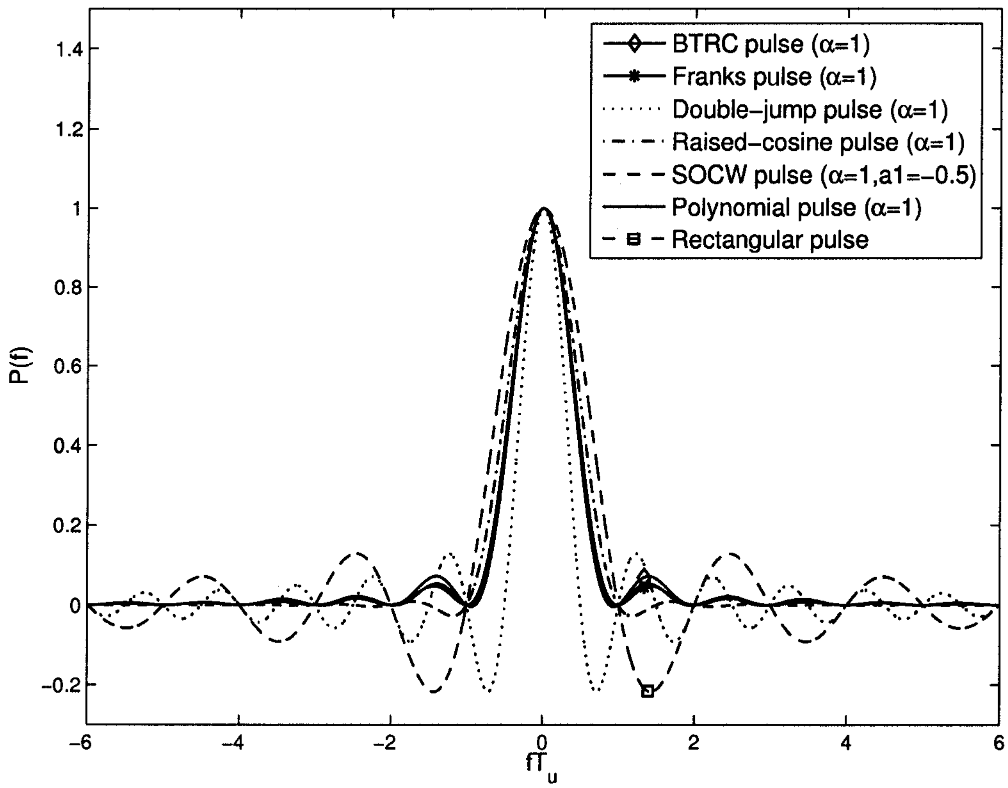

Fig. 4.8. The frequency spectra of different pulse-shaping functions ($\alpha = 1.0$).

the Franks pulse, respectively. With the employment of these pulses, the OFDM symbol interval is $T_u(1+\alpha)$. The rectangular pulse-shaped system is also shown in these figures as a reference. It should be noted that the OFDM symbol interval is T_u for the rectangular pulse-shaped system. Therefore, although the rectangular pulse-shaped system gives a larger ICI power and a smaller SIR than the other pulses, it has a shorter symbol interval. Since both the duration T_u rectangular pulse-shaped system and the other duration $T_u(1+\alpha)$ pulse-shaped systems have a subcarrier frequency spacing $1/T_u$, the systems compared have the same bandwidth N/T_u. On the other hand, if one keeps the symbol durations of all of the systems the same, for example $T_u(1+\alpha)$, the bandwidth requirements for the rectangular pulse-shaped system and the other systems will be $N/T_u(1+\alpha)$ Hz and N/T_u Hz, respectively. A detailed discussion of the bandwidth efficiency is given in Section 4.5.2.

In Figs. 4.11 and 4.12 where the roll-off factor $\alpha = 1.0$, it is noted that the SOCW pulse is the same as the Franks pulse. For small normalized frequency offset values, the Franks pulse achieves the smallest ICI power and the greatest SIR. However, in the case of medium normalized frequency offset values, from 0.12 to 0.39, the BTRC pulse-shaped OFDM system or the polynomial pulse-shaped system slightly outperforms the Franks pulse-shaped system. Numerically, in the presence of normalized frequency offset 0.05, by using the Franks pulse-shape, one obtains 5.2 dB, 8.7 dB, 16.4 dB, and 27.7 dB less ICI power than the polynomial, the BTRC, the raised-cosine, and the double-jump shapings, respectively. On the other hand, in the presence of normalized carrier frequency offset of 0.2, it is better to use the polynomial pulse. In this case one can obtain a gain of 0.5 dB, 1.2 dB, 7.3 dB, and 14.5 dB over the BTRC pulse, the Franks pulse, the raised-cosine pulse, and the double-jump pulse respectively. However, both the SOCW pulse and the polynomial pulse need a set of properly chosen parameters for different roll-off factor values to give good performance. Both the Franks pulse and the BTRC pulse have fixed forms for any roll-off factor values. For frequency offset values larger than 0.39 in Fig. 4.11, one sees that the double-jump pulse-shaped system has the smallest ICI power. This can be explained by examining Fig. 4.8 where one has

$$
\begin{aligned}
&\left|P_{others}\left(-\frac{1}{T_u}+\Delta f\right)\right|^2-\left|P_{dj}\left(-\frac{1}{T_u}+\Delta f\right)\right|^2 \\
&>\left|P_{dj}\left(\frac{k-m}{T_u}+\Delta f\right)\right|^2-\left|P_{others}\left(\frac{k-m}{T_u}+\Delta f\right)\right|^2, \; k-m\neq -1, \text{ and } \Delta f T_u > 0.39
\end{aligned}
\tag{4.30}
$$

where $P_{others}(f)$ denotes the frequency spectra of pulses other than the double-jump pulse. In spite of this fact, one can see that the double-jump pulse gives the worst SIR among the six pulses compared in the case of $\alpha = 1.0$, even when $\Delta f T_u > 0.39$ in Fig. 4.12. This is because the existence of frequency offset attenuates the power of the transmitted signal by $|P(\Delta f)|^2$. Observing the frequency functions of the six considered pulses in Fig. 4.8 one sees that

$$
\left|P_{dj}(\Delta f)\right|^2 < \left|P_{others}(\Delta f)\right|^2. \tag{4.31}
$$

Therefore, achieving the smallest ICI power with the employment of the double-jump pulse for $\Delta f T_u > 0.39$ does not necessarily give the largest SIR in this case. On the other hand, it is interesting to note that the system with the employment of the double-jump pulse has exactly the same SIR as the system with the employment of the rectangular pulse in the entire frequency offset range although they have different ICI since the double-jump pulse-shaped system has the SIR

$$
\begin{aligned}
SIR_{dj} &= \frac{\left|\mathrm{sinc}(\Delta f T_u)\cos(\pi \Delta f T_u)\right|^2}{\sum\limits_{\substack{k\neq m\\ k=0}}^{N-1}\left|\mathrm{sinc}(k-m+\Delta f T_u)\cos\left[\pi(k-m+\Delta f T_u)\right]\right|^2} \\
&= \frac{\left|\mathrm{sinc}(\Delta f T_u)\right|^2}{\sum\limits_{\substack{k\neq m\\ k=0}}^{N-1}\left|\mathrm{sinc}(k-m+\Delta f T_u)\right|^2}
\end{aligned}
\tag{4.32}
$$

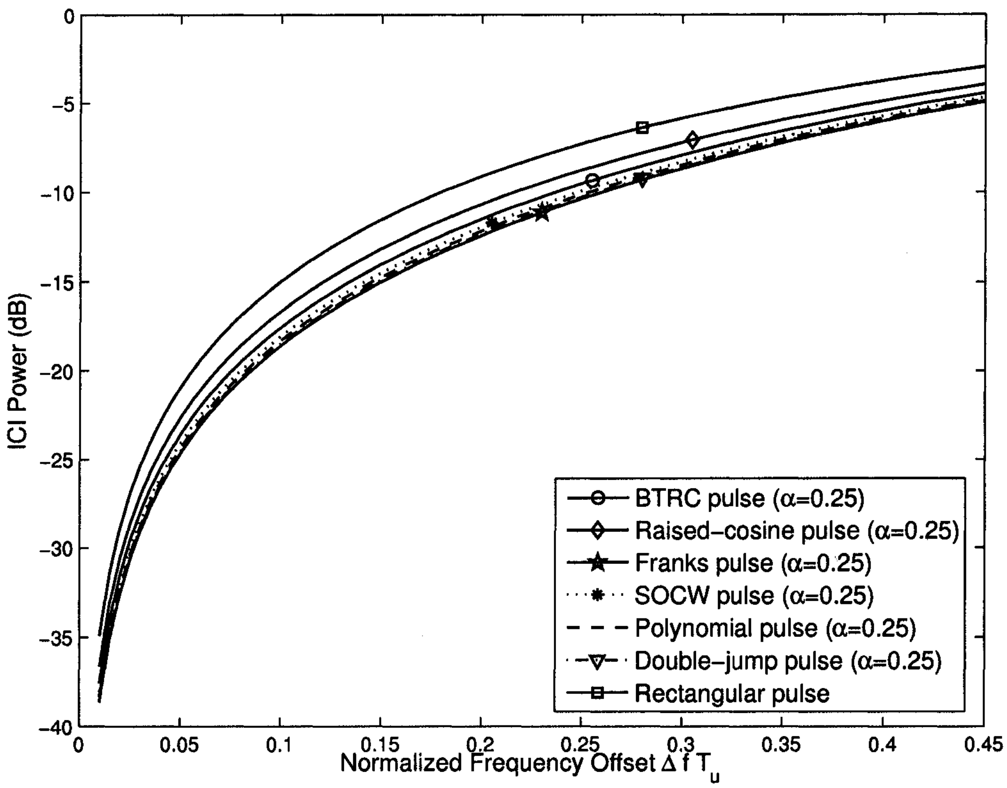

Fig. 4.9. The ICI power in a 64-subcarrier OFDM system with the employment of different pulse-shaping functions ($\alpha = 0.25$).

since $\cos[\pi(k-m+\Delta f T_u)] = \cos(\pi \Delta f T_u)$, and the rectangular pulse-shaped system has the SIR

$$SIR_r = \frac{\left|\text{sinc}(\Delta f T_u)\right|^2}{\sum\limits_{\substack{k \neq m \\ k=0}}^{N-1} \left|\text{sinc}(k-m+\Delta f T_u)\right|^2}. \tag{4.33}$$

4.4 Bit Error Rate Performance

In this section we perform a precise BER analysis for an OFDM system with different pulse-shaping functions by using a characteristic function method [30, 31, 95]. Our goal is to develop a theoretical framework for analyzing the effects of different pulse-shapings

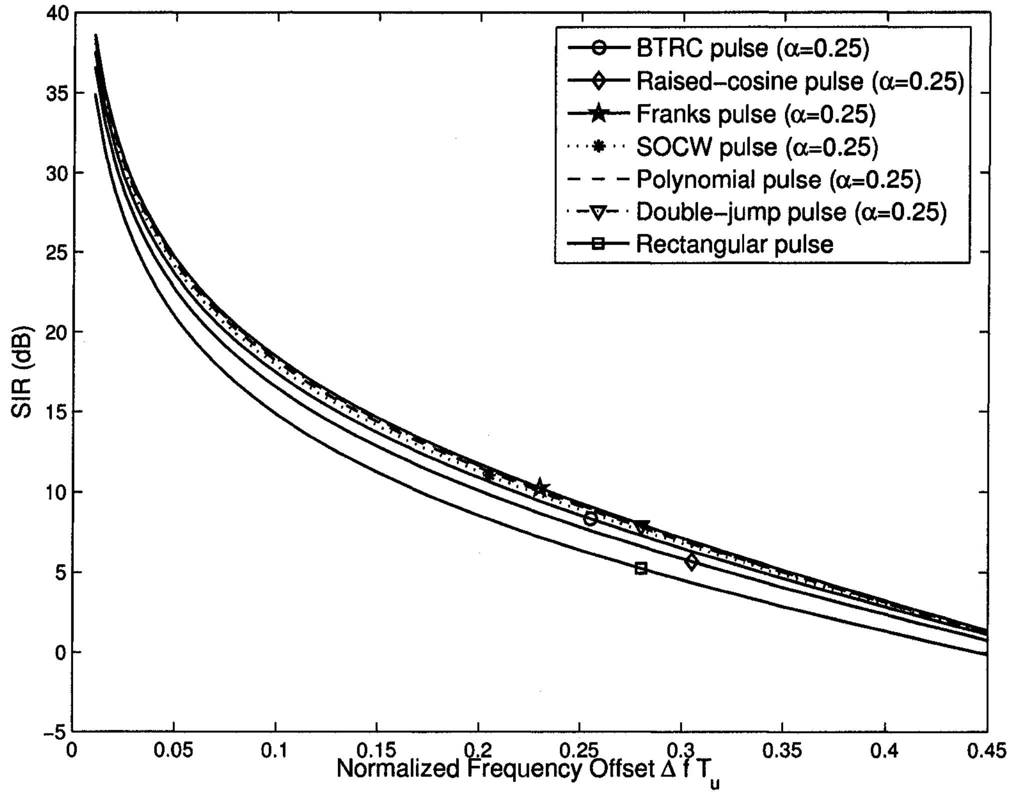

Fig. 4.10. The signal-to-interference ratio in a 64-subcarrier OFDM system with the employment of different pulse-shaping functions ($\alpha = 0.25$).

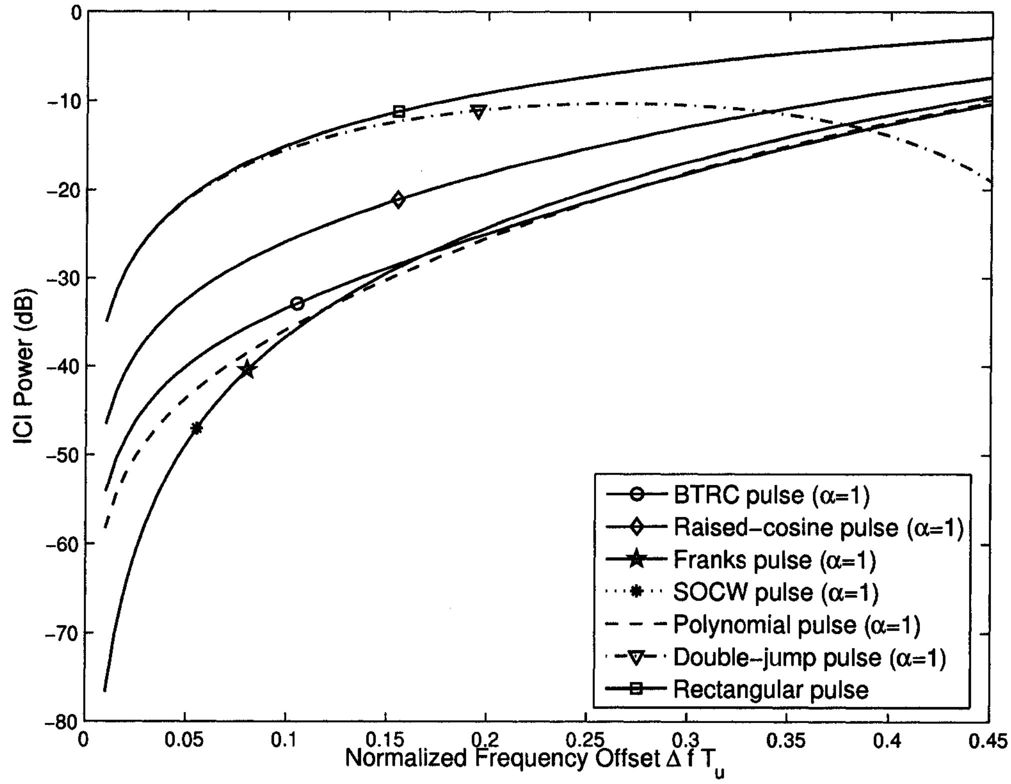

Fig. 4.11. The ICI power in a 64-subcarrier OFDM system with the employment of different pulse-shaping functions ($\alpha = 1.0$).

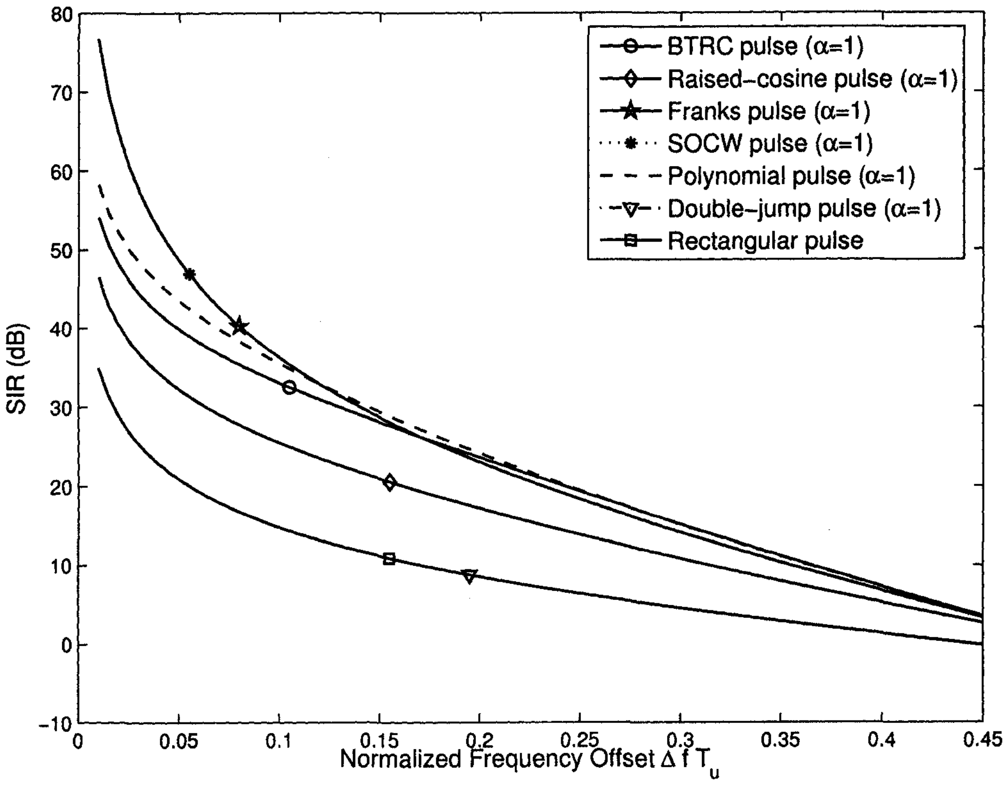

Fig. 4.12. The signal-to-interference ratio in a 64-subcarrier OFDM system with the employment of different pulse-shaping functions ($\alpha = 1.0$).

on the BER of an OFDM system in the presence of frequency offset, and then to compare six widely referenced pulse-shapings. Different from [29], we employ a one-dimensional analysis rather than a two-dimensional analysis, which is more complex and which costs more computer time. Our simpler analysis is applicable to all two-dimensional modulation formats that have the property that the in-phase and quadrature data streams can be demodulated independently.

4.4.1 BPSK-OFDM

In BPSK signaling, $D_m \in \{-\sqrt{E_b}, \sqrt{E_b}\}$ and the receiver decision statistic is

$$\Re\{\hat{D}_m\} = D_m c_0^I + \sum_{\substack{k\neq m\\k=0}}^{N-1} D_k c_{k-m}^I + N_m^I \tag{4.34}$$

The characteristic function of the mth subchannel decision statistic, conditioned on D_m and Δf, can be written as

$$\begin{aligned}\Phi_m(\omega|D_m,\Delta f) &= e^{j\omega D_m c_0^I} E(e^{j\omega N_m^I}) \prod_{\substack{k\neq m\\k=0}}^{N-1} E(e^{j\omega D_k c_{k-m}^I}) \\ &= e^{j\omega D_m c_0^I - \frac{1}{2}\omega^2\sigma^2} \prod_{\substack{k\neq m\\k=0}}^{N-1} \cos(\sqrt{E_b}\,\omega c_{k-m}^I).\end{aligned} \tag{4.35}$$

Combining (??) and (4.35) gives the BER of the mth sample in an OFDM symbol,

$$\begin{aligned}P_b(m) &= \frac{1}{2}\text{Prob}\{\Re\{\hat{D}_m\} \leq 0 \mid D_m = \sqrt{E_b}\} + \frac{1}{2}\text{Prob}\{\Re\{\hat{D}_m\} > 0 \mid D_m = -\sqrt{E_b}\} \\ &= \text{Prob}\{\Re\{\hat{D}_m\} \leq 0 \mid D_m = \sqrt{E_b}\} \\ &= \frac{1}{2} - \int_0^{+\infty} \frac{\Im\{\Phi_m(\omega|D_m,\Delta f)\}}{\pi\omega}\, d\omega \\ &= \frac{1}{2} - \int_0^{+\infty} \frac{\sin(\sqrt{E_b}\,\omega c_0^I)}{\pi\omega} e^{-\frac{1}{2}\omega^2\sigma^2} \prod_{\substack{k\neq m\\k=0}}^{N-1} \cos(\sqrt{E_b}\,\omega c_{k-m}^I)\, d\omega.\end{aligned} \tag{4.36}$$

Note that the BER is a function of the sample location, m. This is because the ICI is a function of the sample location. The average bit error rate is $P_b = \sum_{m=0}^{N-1} P_b(m)/N$.

4.4.2 QPSK-OFDM

In QPSK signaling, $D_m = D_m^I + jD_m^Q$ is a complex symbol in which D_m^I and D_m^Q are chosen independently from the set $\{-\sqrt{E_b}, \sqrt{E_b}\}$. The decision statistic is given by

$$\hat{D}_m = D_m c_0 + \sum_{\substack{k \neq m \\ k=0}}^{N-1} D_k c_{k-m} + N_m. \tag{4.37}$$

Eq. (4.37) indicates that there is crosstalk, or interference, between the two quadrature components. However, for the Gray-coded QPSK constellation, which is employed in the IEEE 802.11a standard [11] and IEEE 802.16a standard [12], the receiver can decide the bits from the in-phase component $\Re\{\hat{D}_m\} = \hat{D}_m^I$ and quadrature component $\Im\{\hat{D}_m\} = \hat{D}_m^Q$ independently according to the following rules:

$$\begin{aligned}
&\text{if} \quad \hat{D}_m^I \geq 0, \quad \text{then} \quad i1 = 0 \\
&\text{if} \quad \hat{D}_m^I < 0, \quad \text{then} \quad i1 = 1 \\
&\text{if} \quad \hat{D}_m^Q \geq 0, \quad \text{then} \quad q1 = 0 \\
&\text{if} \quad \hat{D}_m^Q < 0, \quad \text{then} \quad q1 = 1
\end{aligned}$$

where $i1$ and $q1$ are two bits constituting a QPSK symbol. Since the $i1$ bit and $q1$ bit have the same bit error rate, the BER for the mth sample location is

$$\begin{aligned}
P_b(m) &= \frac{1}{2}\text{Prob}\{\hat{D}_m^I < 0 | D_m^I = \sqrt{E_b}\} + \frac{1}{2}\text{Prob}\{\hat{D}_m^I \geq 0 | D_m^I = -\sqrt{E_b}\} \\
&= \frac{1}{2}\text{Prob}\{\hat{D}_m^I < 0 | D_m^I = \sqrt{E_b}, D_m^Q = -\sqrt{E_b}\} + \frac{1}{2}\text{Prob}\{\hat{D}_m^I < 0 | D_m^I = \sqrt{E_b}, D_m^Q = \sqrt{E_b}\} \\
&= \frac{1}{2} - \int_0^{+\infty} \sin(\omega\sqrt{E_b}c_0^I)\cos(\omega\sqrt{E_b}c_0^Q)\gamma(\omega)\,d\omega
\end{aligned} \tag{4.38a}$$

where

$$\gamma(\omega) = \frac{e^{-\frac{1}{2}\omega^2\sigma^2}}{\pi\omega} \prod_{\substack{k \neq m \\ k=0}}^{N-1} \cos(\omega\sqrt{E_b}c_{k-m}^I)\cos(\omega\sqrt{E_b}c_{k-m}^Q). \tag{4.38b}$$

4.4.3 16QAM-OFDM

In 16-QAM signaling, $D_m = D_m^I + jD_m^Q, m = 0, \cdots, N-1$ is a complex symbol in which D_m^I and D_m^Q are chosen independently from the set $\{-3d, -d, d, 3d\}$. To derive the BER, we divide the four bits $i1$ $i2$ $q1$ $q2$ in one 16-QAM symbol into two groups [69]: in-phase bits $(i1, i2)$ and quadrature bits $(q1, q2)$. The decision on the in-phase bits is determined only by the real part of the received signal $\hat{D}_m$ in (4.37). The imaginary part of $\hat{D}_m$ determines the decision of the quadrature bits $q1$ and $q2$. The decision rules for in-phase bits can be summarized as follows :

$$
\begin{aligned}
\text{if} \quad \hat{D}_m^I \geq 0, &\quad \text{then} \quad i1 = 0 \\
\text{if} \quad \hat{D}_m^I < 0, &\quad \text{then} \quad i1 = 1 \\
\text{if} \quad \hat{D}_m^I \geq 2d \quad \text{or} \quad \hat{D}_m^I < -2d, &\quad \text{then} \quad i2 = 1 \\
\text{if} \quad -2d \leq \hat{D}_m^I < 2d, &\quad \text{then} \quad i2 = 0.
\end{aligned}
$$

There are similar decision rules for the quadrature bits $q1$ and $q2$. The BERs of the $i1$ bit and the $i2$ bit of the mth sample can be calculated as

$$
\begin{aligned}
P_{i1}(m) &= \frac{1}{2}\text{Prob}\{\ \hat{D}_m^I \geq 0 \mid D_m^I < 0\ \} + \frac{1}{2}\text{Prob}\{\ \hat{D}_m^I < 0 \mid D_m^I \geq 0\ \} \\
&= \frac{1}{2}\text{Prob}\{\ \hat{D}_m^I < 0 \mid D_m^I = d\ \} + \frac{1}{2}\text{Prob}\{\ \hat{D}_m^I < 0 \mid D_m^I = 3d\ \}
\end{aligned} \tag{4.39}
$$

and

$$
\begin{aligned}
P_{i2}(m) = &\frac{1}{2}\text{Prob}\{\ \hat{D}_m^I \geq 2d \text{ or } \hat{D}_m^I < -2d \mid D_m^I = d\ \} \\
&+ \frac{1}{2}\text{Prob}\{\ -2d \leq \hat{D}_m^I < 2d \mid D_m^I = 3d\ \}
\end{aligned} \tag{4.40}
$$

respectively. The characteristic function of $\hat{D}_m^I$, conditioned on D_m and Δf is

$$
\begin{aligned}
\Phi_m^I(\omega|D_m, \Delta f) = &e^{j\omega(D_m^I c_0^I - D_m^Q c_0^Q) - \frac{1}{2}\omega^2\sigma^2} \\
&\times \prod_{\substack{k \neq m \\ k=0}}^{N-1} \cos(2\omega d c_{k-m}^I) \cos(\omega d c_{k-m}^I) \cos(2\omega d c_{k-m}^Q) \cos(\omega d c_{k-m}^Q).
\end{aligned} \tag{4.41}
$$

Combining (??) with (4.41), and applying the results to (4.39) and (4.40) gives the BER for the $i1$ bit as

$$P_{i1}(m) = \frac{1}{2} - \int_0^{+\infty} \cos(2\omega dc_0^Q)\cos(\omega dc_0^Q)\sin(2\omega dc_0^I)\cos(\omega dc_0^I)\beta(\omega)\,d\omega \tag{4.42a}$$

and for the $i2$ bit as

$$P_{i2}(m) = \frac{1}{2} - \int_0^{+\infty} 2\sin(2\omega d)\sin(2\omega dc_0^I)\sin(\omega dc_0^I)\cos(2\omega dc_0^Q)\cos(\omega dc_0^Q)\beta(\omega)\,d\omega \tag{4.42b}$$

where

$$\beta(\omega) = \frac{e^{-\frac{1}{2}\omega^2\sigma^2}}{\pi\omega} \prod_{\substack{k\neq m\\k=0}}^{N-1} \cos(2\omega dc_{k-m}^I)\cos(\omega dc_{k-m}^I)\cos(2\omega dc_{k-m}^Q)\cos(\omega dc_{k-m}^Q). \tag{4.42c}$$

According to symmetry, the $i1$ bit has the same BER as the $q1$ bit, and the $i2$ bit has the same BER as the $q2$ bit. Therefore, the average BER can be given as

$$P_b = \frac{1}{2N}\sum_{m=0}^{N-1}\left[P_{i1}(m) + P_{i2}(m)\right]. \tag{4.43}$$

4.5 Numerical Results and Discussions

4.5.1 Numerical Results

In Section 4.4, we derived precise BER expressions for pulse-shaped OFDM systems over AWGN channels. In this section, we will use these results to examine the performance of systems with different pulse-shaping functions. In the examples, we choose frequency offset parameters that are consistent with useful error rates.

Fig. 4.13 shows the average BER versus the SNR per bit for a 64-subcarrier BPSK-OFDM system assuming the employment of different pulse shaping functions in the presence of normalized frequency offsets $\Delta f T_u = 0.2$. Computer simulation results are also shown to substantiate the theoretical results. To ensure the reliability of the computer simulation, 10^6 OFDM frames are generated to obtain each BER value in this figure. Lines

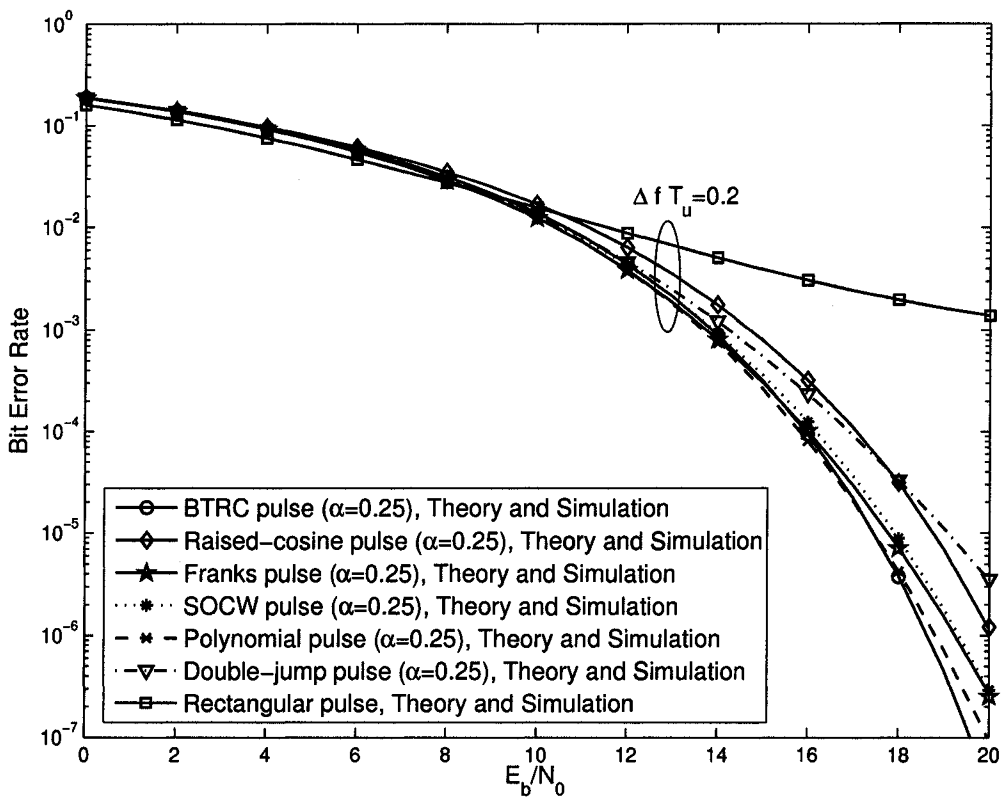

Fig. 4.13. The average BER performance of a BPSK-OFDM system with the employment of different pulse-shaping functions ($\alpha = 0.25$) in the presence of normalized frequency offset $\Delta f T_u = 0.2$.

(solid lines, dashed lines, and so on) represent results obtained from the exact analysis of Section 4.4 and symbols (circles, diamonds, squares, and so on) denote the average BERs obtained from simulations. The theoretical results and the simulation results are in excellent agreement. Therefore, in the remaining examples we will only show numerical results obtained using the precise analytical expression.

The BER performance of a rectangular pulse-shaped system where the OFDM symbol duration is T_u is also shown in Fig. 4.13 as a reference. Compared with the rectangular pulse-shaped system, the systems shaped by pulses with duration $T_u(1+\alpha)$ substantially improve BER performance at the expense of increased OFDM symbol time duration pro-

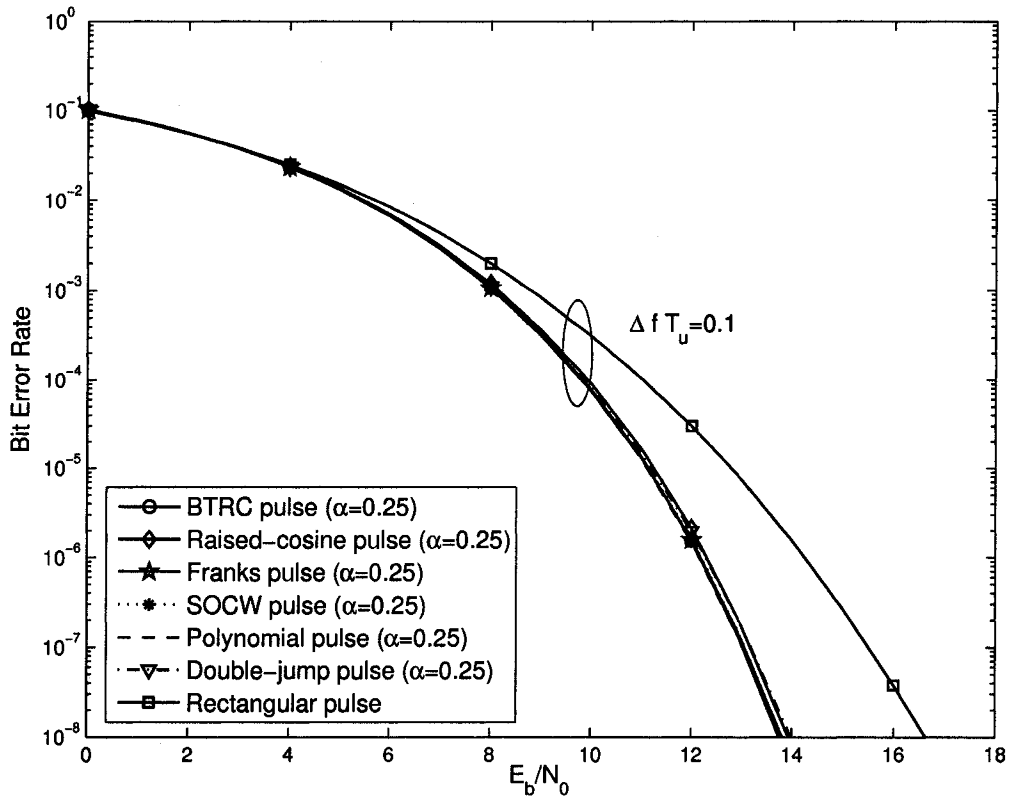

Fig. 4.14. The average BER performance of a BPSK-OFDM system with the employment of different pulse-shaping functions ($\alpha = 0.25$) in the presence of normalized frequency offset $\Delta f T_u = 0.1$.

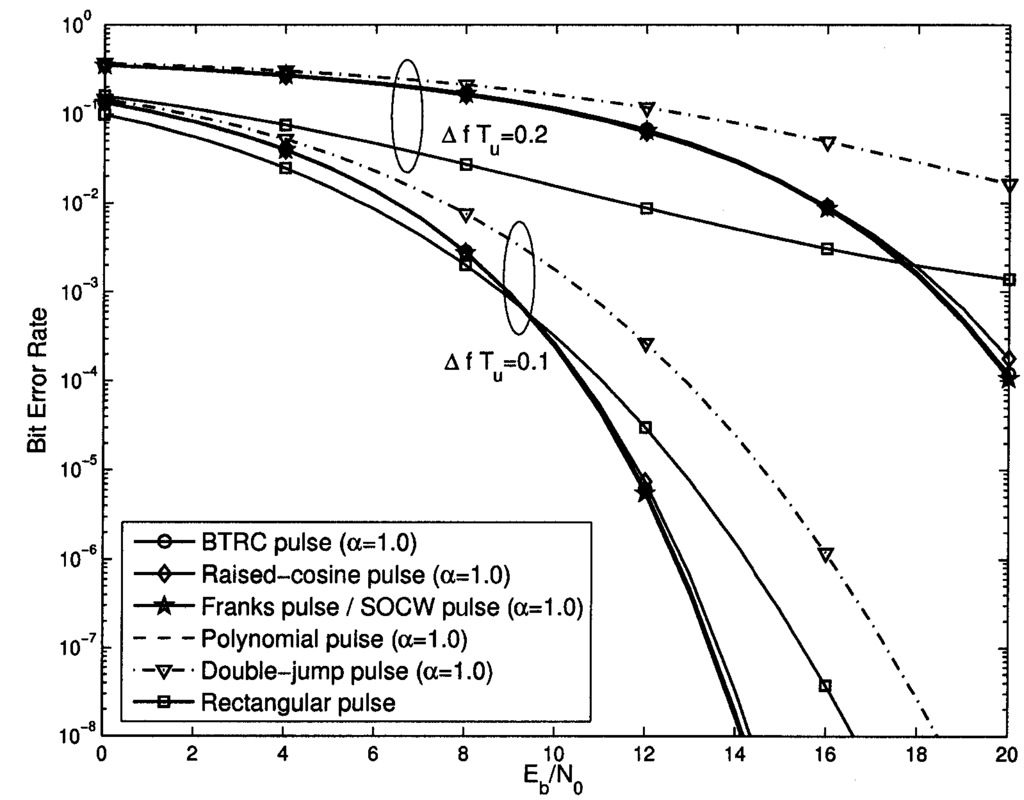

Fig. 4.15. The average BER performance of a BPSK-OFDM system with the employment of different pulse-shaping functions ($\alpha = 1.0$) in the presence of normalized frequency offset $\Delta f T_u = 0.1$ and 0.2.

portionally by α. Specifically, in the case of $\Delta f T_u = 0.2$, an error floor occurs for the rectangular pulse-shaped system, whereas, no error floor occurs for other pulses in this case. The reason for this is that the magnitude of the ICI term (the second term) in (4.22) can exceed the magnitude of the desired signal component (the first term) in (4.22) for the rectangular pulse but not in the cases of other pulses. If the OFDM symbol time duration can be allowed to be $T_u(1+\alpha)$, at a BER of 10^{-3}, one can observe that the polynomial pulse-shaped system requires the smallest SNR, about 13.68 dB. However, for large SNR values, the BTRC pulse-shaped system achieves the smallest BER among all of the pulses considered. For a smaller normalized frequency offset value, $\Delta f T_u = 0.1$ in Fig. 4.14, the BER performances of duration $T_u(1+\alpha)$ pulse-shaped systems are quite similar because the ICI power in the case of small frequency offsets is negligible.

One observes in Fig. 4.15, that in the case of $\alpha = 1.0$, the duration $T_u(1+\alpha)$ pulse-shaped systems perform even worse than the duration T_u rectangular pulse-shaped system at small values of SNR but better at large values of SNR. This result is, in fact, expected. To clarify this behavior, first note that the BER is dominated by the influence of the additive noise at small SNR and dominated by the ICI at large SNR. Now, another factor influencing the BER is the attenuation of the desired signal component caused by the frequency offset. From eq. (4.25), it can been seen that the existence of frequency offset attenuates the power of the transmitted signal by $|P(\Delta f)|^2$. Observing the frequency functions of the considered pulses in Fig. 4.8 one sees that

$$|P_{others}(\Delta f)|^2 \leq |P_r(\Delta f)|^2 \tag{4.44}$$

where $\Delta f T_u = 0.1$ and 0.2, and $P_{others}(f)$ denotes the frequency spectra of pulses other than the rectangular pulse. Therefore, the rectangular pulse will perform best when the SNR is small and the BER is dominated by the additive noise. At large values of SNR, the BER is dominated by the ICI and the rectangular pulse performs poorer than the other pulses.

Another interesting observation is that although the double-jump pulse-shaped OFDM system and the rectangular pulse-shaped system have the same SIR, their BER performances are not necessarily the same. Actually, the rectangular pulse-shaped OFDM system outperforms the double-jump pulse-shaped OFDM system over the entire range of SNR values shown.

The BER performance comparisons of the QPSK-OFDM systems that employ different pulse-shapings in the presence of normalized frequency offset $\Delta f T_u = 0.08$ and 0.1 are shown in Fig. 4.16. In particular, by using the Franks pulse, one can achieve 0.76 dB and 2.1 dB performance gain in signal-to-noise ratio (SNR) at a BER of 10^{-4} compared to using the raised-cosine pulse in the case of $\Delta f T_u = 0.08$ and $\Delta f T_u = 0.1$, respectively. One can also observe that in the high SNR region, and with $\Delta f T_u = 0.1$, the BTRC pulse slightly outperforms the other pulses.

We have seen that the BER performance of a specific pulse-shaped OFDM system in the presence of a frequency offset depends not only on the SNR per bit E_b/N_0 but also on the pulse roll-off factor α. In some cases, for a fixed E_b/N_0 and normalized frequency offset $\Delta f T_u$, there exists an optimal value of α that minimizes the BER. In these cases, we can find the optimal value of α by using the results derived here to plot the average BER versus the roll-off factor α. For example, Fig. 4.17 shows that the optimal α for the BTRC pulse is about 0.43 in the case of pulse-shaped BPSK-OFDM when $\Delta f T_u = 0.1$ and $E_b/N_0 = 10$ dB. Interestingly, the raised-cosine pulse also has an optimum value of α and it is about the same as the optimum value of α for the BTRC pulse for these values of $\Delta f T_u$ and SNR. On the other hand, an optimum value of α may not exist in some cases. Fig. 4.18 indicates that the optimal roll-off factor α is 0.25 for BTRC pulse in the case of a 64-subcarrier QPSK-OFDM system with $\Delta f T_u = 0.12$ and $E_b/N_0 = 20$ dB. Yet, the raised-cosine pulse performs increasingly poorer as α increases and does not achieve a local minimum.

We also examine the performance of a pulse-shaped 16QAM-OFDM system in Fig.

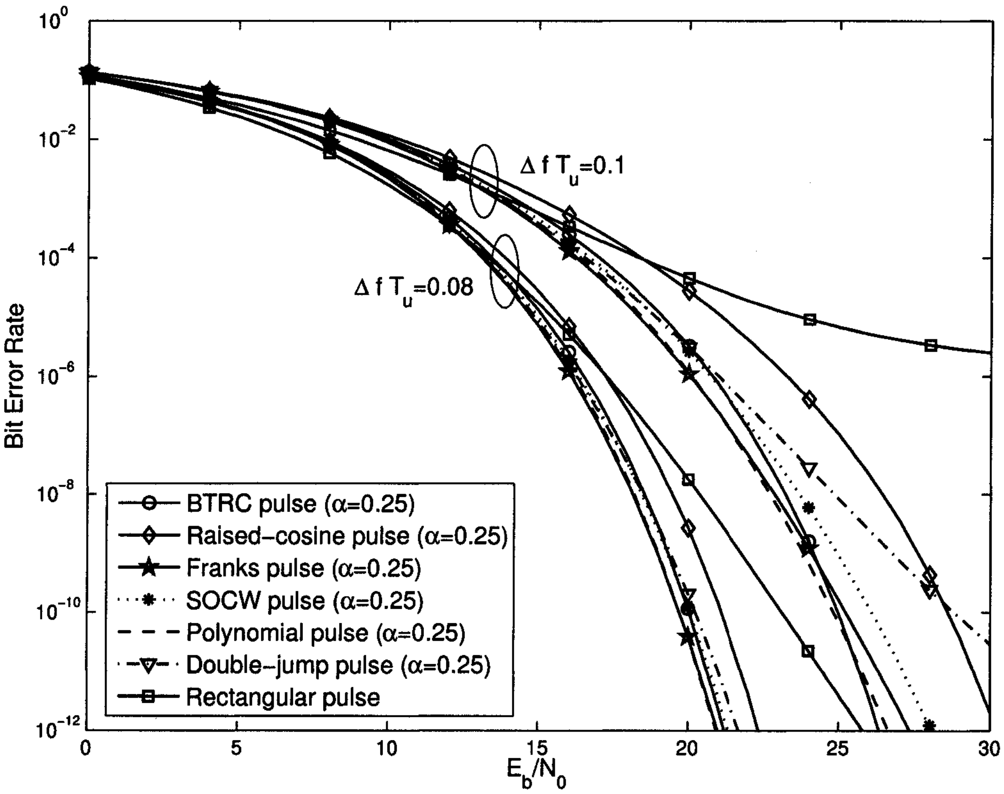

Fig. 4.16. The average BER performance of a QPSK-OFDM system with the employment of different pulse-shaping functions ($\alpha = 0.25$) in the presence of normalized frequency offset $\Delta f T_u = 0.08$ and 0.1.

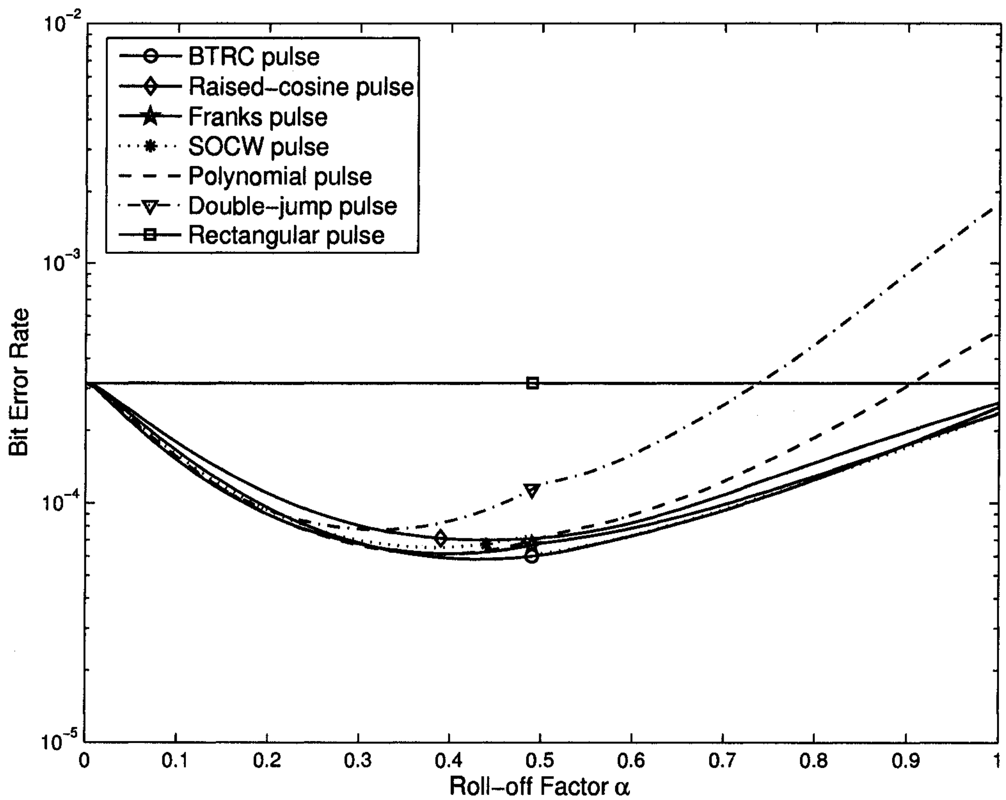

Fig. 4.17. The average BER versus roll-off factor α for a 64-subcarrier BPSK-OFDM system with the employment of different pulse-shaping functions for $\Delta f T_u = 0.1$ and $E_b/N_0 = 10$ dB.

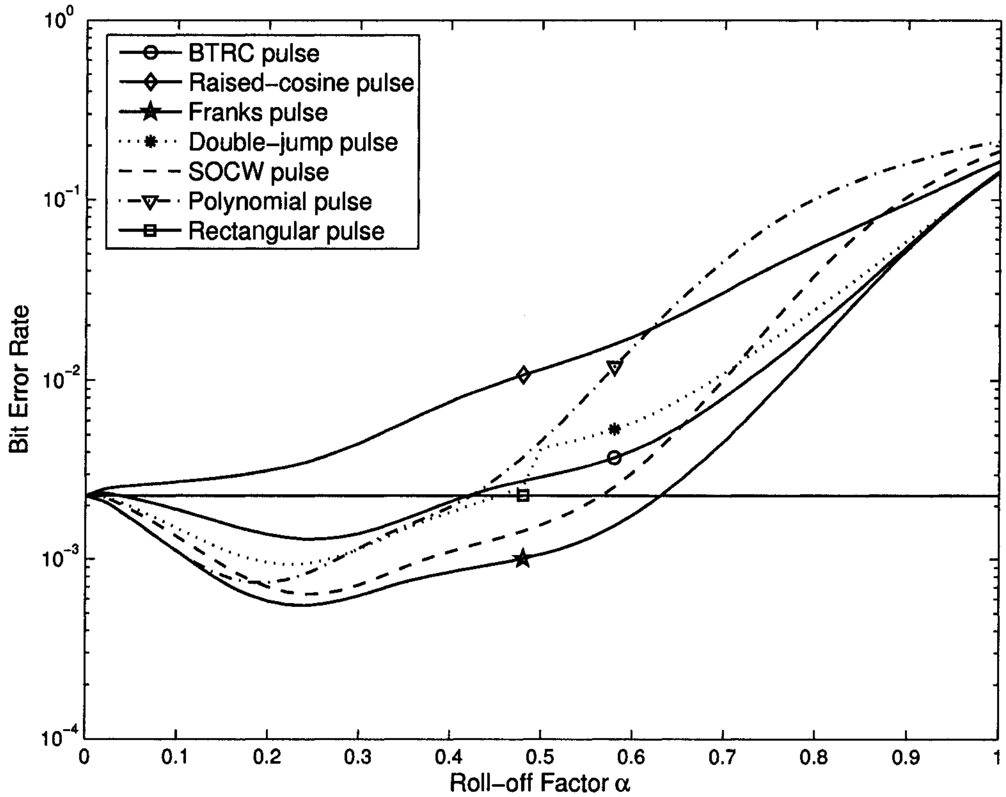

Fig. 4.18. The average BER versus roll-off factor α for a 64-subcarrier QPSK-OFDM system with the employment of different pulse-shaping functions for $\Delta f T_u = 0.12$ and $E_b/N_0 = 20$ dB.

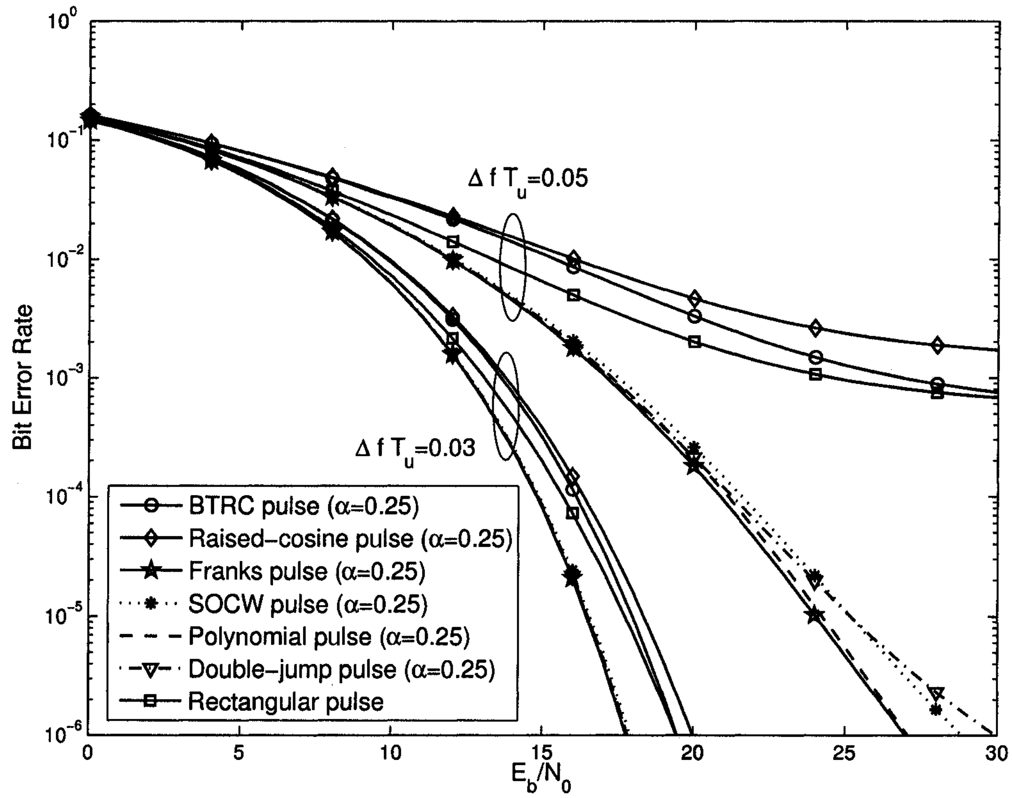

Fig. 4.19. The average BER performance of a 16QAM-OFDM system with the employment of different pulse-shaping functions ($\alpha = 0.25$) in the presence of normalized frequency offset $\Delta f T_u = 0.03$ and 0.05.

4.19. The parameters chosen here are $\alpha = 0.25$, the number of subcarriers $N = 64$, and the normalized frequency offset $\Delta f T_u = 0.03$ and 0.05. The average signal energy per bit is $E_b = 2.5d^2$. One can see that systems with Franks pulse shaping, double-jump pulse-shaping, SOCW pulse-shaping, and polynomial pulse-shaping can achieve much better performance than systems with BTRC pulse-shaping, or raised-cosine pulse-shaping and rectangular pulse-shaping.

4.5.2 Bandwidth Efficiency

In Section 4.5.1, we have presented the BER performance of the pulse-shaped OFDM system with frequency offset in an AWGN environment. The OFDM symbol duration is T_u and $T_u(1+\alpha)$ when one uses the rectangular pulse and the other Nyquist pulses in this chapter, respectively. Therefore, they have different data transmission rates. The subcarrier frequency spacing in all of these cases is $1/T_u$ Hz, so the total bandwidth required is the same for these systems.

TABLE 4.1

Bandwidth Efficiency (bits/s/Hz) of an N-subcarrier pulse-shaped OFDM system

	BPSK	QPSK	16QAM
The rectangular pulse with duration T_u	1	2	4
Other Nyquist pulses with duration $T_u(1+\alpha)$	$1/(1+\alpha)$	$2/(1+\alpha)$	$4/(1+\alpha)$

One can compare the bandwidth efficiency (normalized data rate), defined as the data transmission rate to bandwidth ratio [17], of these pulse-shaped OFDM systems. Table 4.1 gives the bandwidth efficiency of an N-subcarrier pulse-shaped OFDM system with different modulation formats. Figs. 4.20 and 4.21 show the bandwidth efficiency of the pulse-shaped OFDM systems as a function of the SNR per bit with a given BER of 10^{-5}.

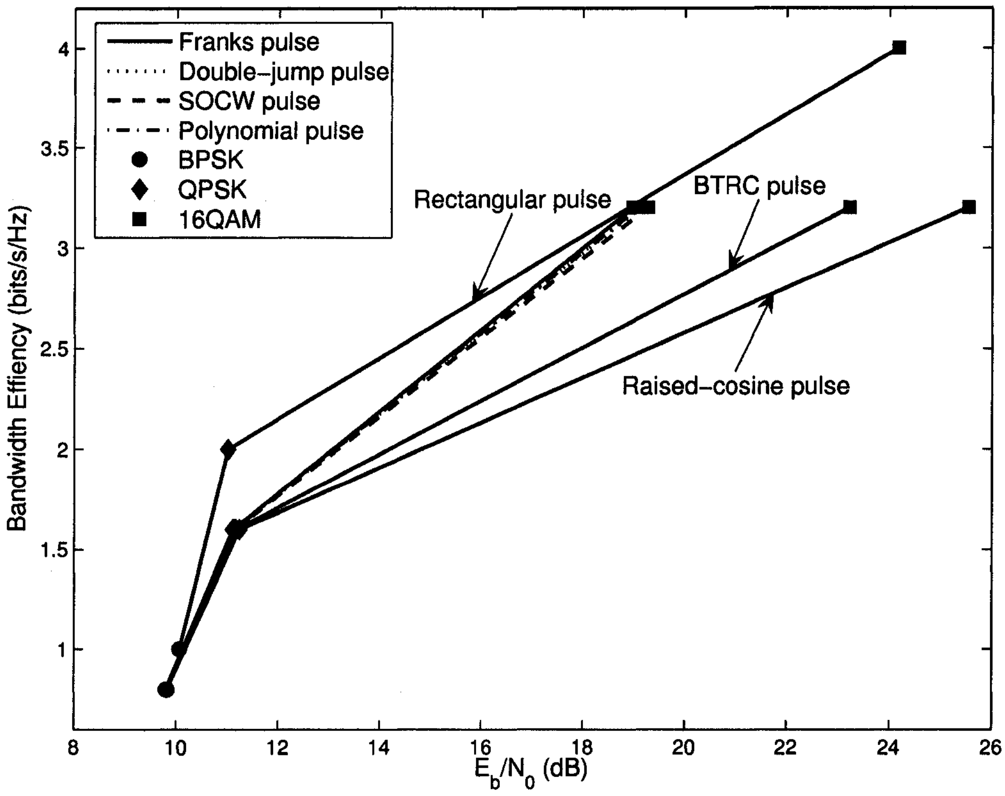

Fig. 4.20. Comparison of several pulse-shaped OFDM systems at a BER of 10^{-5}, $\alpha = 0.25$, $\Delta f T_u = 0.04$.

One can see from Fig. 4.20, in the case of 16-QAM, the rectangular pulse-shaped system, with the bandwidth efficiency of 4 bits/s/Hz, requires SNR per bit, around 24.17 dB to achieve the given BER of 10^{-5}. To achieve the same BER, the Franks pulse-shaped system requires only 18.98 dB in SNR. However, the cost of the smaller SNR requirement is a decrease in bandwidth efficiency to 3.2 bits/s/Hz. Also observed, the raised-cosine pulse-shaped system has the worst performance, both in terms of SNR requirement and bandwidth efficiency. Similar observations can be made in Fig. 4.21 where 16-QAM case is not shown because an unusable error floor occurs in this case.

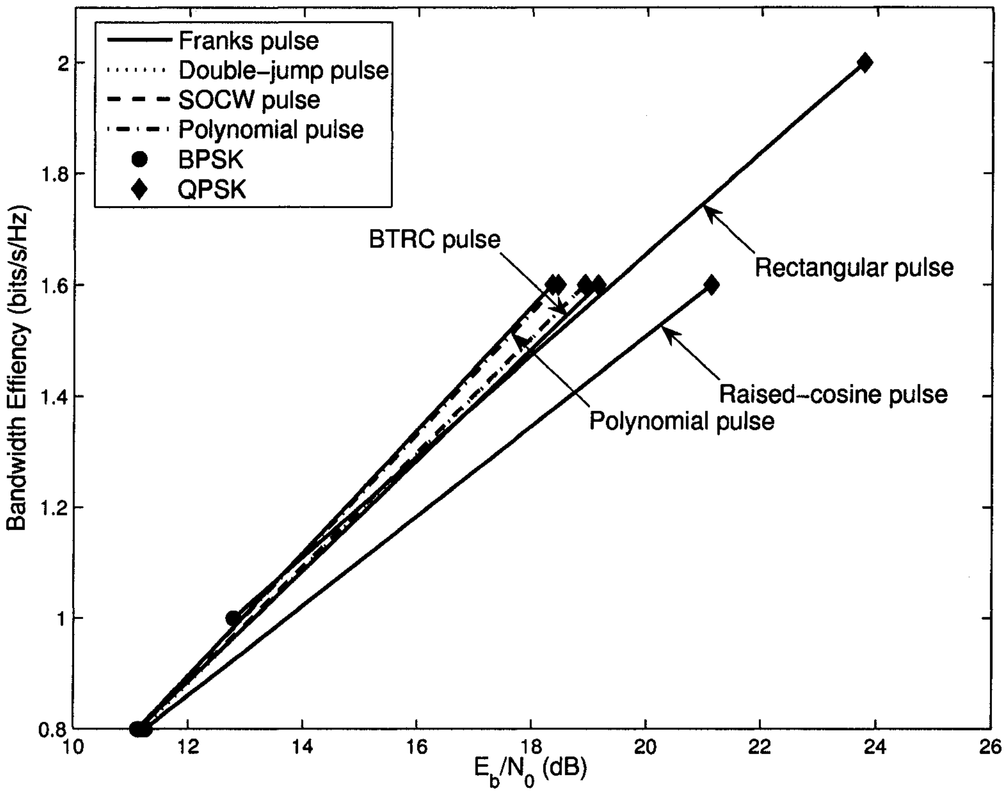

Fig. 4.21. Comparison of several pulse-shaped OFDM systems at a BER of 10^{-5}, $\alpha = 0.25$, $\Delta f T_u = 0.1$.

4.6 Summary

In this chapter, the effect of several Nyquist pulses on ICI reduction and SIR enhancement of OFDM systems in the presence of frequency offset was first examined. The relationship between two recently proposed Nyquist pulses, the SOCW pulse and the polynomial pulse, were disclosed. The Franks pulse, which was previously proved to be optimal in the sense of MMSE for small timing offset and small roll-off factor values in single-carrier ISI environments, was employed in OFDM systems to reduce ICI.

Analytical BER expressions for an uncoded pulse-shaped OFDM system in AWGN environments in the presence of carrier frequency offset were then derived. The BER performance of pulse-shaped OFDM systems with frequency offset was compared for six widely referenced Nyquist pulses. It was shown the Franks pulse exhibits best performance among the Nyquist pulses considered in most cases.

The bandwidth efficiencies of the pulse-shaped systems were examined. Compared with rectangular pulse-shaped OFDM system, although the other six pulse-shaped OFDM system can achieve smaller ICI and BER in most cases, they require increased symbol duration proportional by the roll-off factor α. The prolonged symbol duration will lead to a reduced data rate which may not be desired in some cases. In the following two chapters, two ICI reduction schemes without sacrifice in data rates, including the partial-response pulse-shaped (correlative coding) system and the receiver windowing are investigated.

Chapter 5

Correlative Coding and Partial-Response Pulse-Shaping in OFDM Systems

5.1 Introduction

We have shown in Chapter 4 that transmitter pulse-shaping can effectively reduce ICI introduced by frequency offset in OFDM systems. However, when using a Nyquist pulse with roll-off factor α, the OFDM symbol time duration will increase proportionally by α. Thus, the data transmission rate will decrease. Partial-response signals can also be used in OFDM transmitter pulse-shaping to reduce ICI. The principle of partial-response signaling is to introduce some known ICI. At the receiver, the intentionally introduced ICI can be removed since it is known. Significantly, the data transmission rate will not be decreased by using partial-response pulse-shaping. This scenario is similar to the partial-response pulse design problem for single carrier systems in ISI environments.

Correlative coding across subcarriers in OFDM systems was proposed, in reference

[96], as an ICI reduction scheme. It was shown that, compared to a system without correlative coding, the SIR of the system with correlative coding can be improved by 3.5 dB in SIR. In further investigation, reference [75] studied the optimum frequency-domain correlative coding for ICI reduction in OFDM systems. The optimum two-tap correlative coding can reduce the ICI due to Doppler shift and the ICI due to carrier offset by about 4.0 dB and 4.5 dB in ICI power, respectively. However, as pointed out in [96], correlative coding introduces multilevel signaling which increases the system BER. The use of either a SIR measure or an ICI power measure to assess performance in an OFDM system with ICI does not map directly to a quantifiable improvement in BER performance. Sometimes, these measures can be misleading as shown in Chapter 4, since greater SIR does not necessarily mean smaller BER. Therefore, it is not clear that benefits predicted by a SIR measure or a ICI power measure will be real. Reference [96] did not examine quantitatively the BER performance of the correlative coding OFDM systems. Reference [75] gave simulation results for the word error rate of a Reed-Solomon coded OFDM system with correlative coding employed over a hilly-terrain channel exclusively for the case of large normalized Doppler shift of 0.1. Although the results indicate that the error rate floor due to Doppler shift is reduced from 10^{-2} to 10^{-3} with the employment of correlative coding, whether the benefit can be achieved in the case of other frequency offset values was not reported in that work.

In this chapter, we derive expressions for the BER of pulse-shaped OFDM systems with symbol-by-symbol detection, and show, using these BER results as the performance measure, that in fact, only for large frequency offsets can partial-response pulse-shaping in the time domain, which is equivalent to correlative coding in the frequency domain, reduce ICI and improve system BER performance. For small frequency offset values, the performance gain achieved from ICI reduction can not compensate for the performance loss due to multilevel signaling, and thus there is no benefit in BER performance from using partial-response pulse-shaping, or correlative coding across subcarriers.

The reminder of this chapter is organized as follows. In Section 5.2, the system model is given. Then we derive BER expressions for symbol-by-symbol detection for the partial-response pulse-shaping OFDM system operated over AWGN channels in the presence of frequency offset in Section 5.3. Performance comparisons between the system with partial-response pulse-shaping and the system with rectangular pulse-shaping are presented. Lastly, we summarize our findings of this chapter in Section 5.4.

5.2 Partial-Response Pulse-Shaped OFDM

In this section, we develop a partial-response pulse-shaped OFDM signaling model that provides an alternative, though equivalent, view of an OFDM system with correlative coding. We choose the duobinary partial-response pulse [17] for pulse-shaping in the frequency-domain. Then, in this application, the time domain response is

$$\tilde{p}_{pr}(t) = \begin{cases} \frac{2}{T_u} e^{j\pi t/T_u} \cos(\pi t/T_u), & |t| < \frac{T_u}{2} \\ 0, & \text{otherwise} \end{cases} \tag{5.1}$$

where T_u is the OFDM symbol length. The Fourier transform of $\tilde{p}_{pr}(t)$ is

$$\tilde{P}_{pr}(f) = \mathrm{sinc}(fT_u) + \mathrm{sinc}(fT_u - 1). \tag{5.2}$$

The complex pulse in (5.1) can be transformed to a real pulse to facilitate implementation by choosing $\frac{1}{2T_u}$ as the new frequency origin. Under this new frequency origin, the time-domain expression $p_{pr}(t)$ and the frequency-domain expression $P_{pr}(f)$ become

$$p_{pr}(t) = \begin{cases} \frac{2}{T_u} \cos(\pi t/T_u), & |t| < \frac{T_u}{2} \\ 0, & \text{otherwise} \end{cases} \tag{5.3}$$

and

$$P_{pr}(f) = \mathrm{sinc}(fT_u + \frac{1}{2}) + \mathrm{sinc}(fT_u - \frac{1}{2}) \tag{5.4}$$

respectively. In a practical system implementation, a time delay $\frac{T_u}{2}$ is required since the duration of the pulse starts before the pulse sampling instant. The time delayed version of $p_{pr}(t)$ is $p_{pr}^d(t)$, and

$$p_{pr}^d(t) = p_{pr}(t - \frac{T_u}{2}) = \begin{cases} \frac{2}{T_u}\sin(\pi t/T_u), & 0 \le t < T_u \\ 0, & \text{otherwise.} \end{cases} \tag{5.5}$$

The Fourier transform of $p_{pr}^d(t)$ is $P_{pr}^d(f) = P_{pr}(f)e^{-j\pi f T_u}$.

One pulse-shaped OFDM symbol with length T_u can thus be written as

$$s(t) = \sum_{n=0}^{N-1} a_n e^{j2\pi nt/T_u}\sqrt{p_{pr}^d(t)} \tag{5.6}$$

where we assume a_n is a BPSK data symbol, and a_n takes values $\sqrt{E_b}$ or $-\sqrt{E_b}$ with equal probability. In the case of transmission over an AWGN channel, a matched-filter receiver for the mth subcarrier gives

$$\begin{aligned} \hat{a}_m &= \int_0^{T_u} s(t)e^{-j2\pi mt/T_u}\sqrt{p_{pr}^d(t)}e^{j\pi t/T_u}\,dt + w_m \\ &= \int_0^{T_u}\sum_{n=0}^{N-1} a_n e^{-j2\pi(m-n-0.5)t/T_u} p_{pr}^d(t)\,dt + w_m \\ &= a_m P_{pr}^d(-\frac{1}{2T_u}) + a_{m-1}P_{pr}^d(\frac{1}{2T_u}) + w_m \\ &= j(a_m - a_{m-1}) + w_m \end{aligned} \tag{5.7}$$

for $m = 1, 2, \cdots, N-1$ and

$$\hat{a}_0 = ja_0 + w_0 \tag{5.8}$$

where the term $e^{j\pi t/T_u}$ in (5.7) is used to compensate the frequency origin change in (5.4), $P_{pr}^d(-\frac{1}{2T_u}) = j$, and $P_{pr}^d(\frac{1}{2T_u}) = -j$. The complex additive Gaussian noise samples, $w_m = w_m^I + jw_m^Q$, are the symbol-spaced matched filter output samples resulting from the input white Gaussian noise process.

The receiver can use the imaginary part of $\hat{a}_m$ in (5.7)

$$\Im\{\hat{a}_m\} = a_m - a_{m-1} + w_m^Q \tag{5.9}$$

for $m = 1,2,\cdots,N-1$ and $\Im\{\hat{a}_0\} = a_0 + w_0^Q$ as its estimate of the transmitted symbol. In eq. (5.9), the first term represents the desired symbol, the second term, represents ICI corresponding to the previous symbol. The intentionally introduced ICI can be removed at the receiver by adding a_{m-1} from the received signal. However, in this way, the decision of mth subcarrier will depend on the $(m-1)$th subcarrier, and thus, error propagation is introduced.

The error propagation can be avoided by using a precoding technique [17]. In the case of duobinary pulse, the precoded sequence P_m is defined as

$$P_m = D_m \oplus P_{m-1} \tag{5.10}$$

where $\oplus$ denotes modulo-2 addition, D_m is a source binary data sequence, and D_m taking values 0 or 1 independently with probability 0.5. The transmitted BPSK data symbol with precoding is then $a_m = \sqrt{E_b}(2P_m - 1)$. When the precoding is used, the matched-filter output signal values are $2\sqrt{E_b}$, $-2\sqrt{E_b}$ and 0, and the decoder decides that a "1" bit was transmitted if $|\hat{D}_m| > \sqrt{E_b}$, and otherwise it decides that a "0" bit was transmitted.

Comparison of the procedure described above with the procedure shown in [96, Fig. 1] indicates that the time-domain precoded partial-response pulse-shaping OFDM model is equivalent to the frequency domain correlative coding model using the correlation polynomial $F(D) = 1 - D$ in [75, 96].

The OFDM system without correlative coding is equivalent to a system with rectangular pulse-shaping $p_r(t)$

$$p_r(t) = \begin{cases} \frac{1}{T_u}, & 0 \le t < T_u \\ 0, & \text{otherwise.} \end{cases} \tag{5.11}$$

It is noted that the energy of one partial response pulse-shaped OFDM symbol is

$$E_s = \int_0^{T_u} \mathbf{E}[|s(t)|^2]\,dt = NE_b \int_0^{T_u} |p_{pr}^d(t)|\,dt = \frac{4}{\pi} NE_b \tag{5.12}$$

since $\int_{-T/2}^{T/2} |p_{pr}^d(t)|\,dt = \frac{4}{\pi}$ and

$$\mathbf{E}[a_n a_m^*] = \begin{cases} E_b, & n = m \\ 0, & \text{otherwise.} \end{cases} \tag{5.13}$$

However, the energy of one rectangular pulse-shaped OFDM symbol is NE_b. One can use a scaling factor of $\pi/4$ in (5.5) to ensure normalized pulse energy, that is $\int_0^{T_u} |p_{pr}^s(t)|\,dt = 1$ where

$$p_{pr}^s(t) = \begin{cases} \frac{\pi}{2T_u}\sin(\pi t/T_u), & 0 \le t < T_u \\ 0, & \text{otherwise.} \end{cases} \tag{5.14}$$

With these definitions, the energy of one OFDM symbol with pulse-shaping $p_{pr}^s(t)$ is the same as the energy of one conventional OFDM symbol with rectangular pulse-shaping. Therefore, we will use $p_{pr}^s(t)$ in the following development.

In the presence of frequency offset, the received OFDM symbol can be written as

$$r(t) = e^{j2\pi\Delta f t} \sum_{n=0}^{N-1} a_n e^{j2\pi nt/T_u} \sqrt{p_{pr}^s(t)} + w(t) \tag{5.15}$$

where $w(t)$ is a white Gaussian random process. The correlator (matched-filter) for the mth subcarrier gives

$$\begin{aligned} \hat{a}_m &= \int_0^{T_u} e^{j2\pi\Delta f t} \sum_{n=0}^{N-1} a_n e^{j2\pi(n-m+0.5)t/T_u} p_{pr}^s(t)\,dt + w_m \\ &= \sum_{n=0}^{N-1} a_n \int_0^{T_u} p_{pr}^s(t) e^{-j2\pi(m-n-\varepsilon-0.5)t/T_u}\,dt + w_m \\ &= \sum_{n=0}^{N-1} a_n P_{pr}^s\left(\frac{m-n-\varepsilon-0.5}{T_u}\right) + w_m \end{aligned} \tag{5.16}$$

where $\varepsilon = \Delta f T_u$, and $P_{pr}^s(f) = \frac{\pi}{4} P_{pr}(f) e^{-j\pi f T_u}$. The imaginary part of $\hat{a}_m$, namely

$$\hat{D}_m = \Im\{\hat{a}_m\} = \frac{\pi}{4} a_m P_{pr}\left(\frac{-\varepsilon-0.5}{T_u}\right)\cos(\pi\varepsilon) + \frac{\pi}{4} a_{m-1} P_{pr}\left(\frac{0.5-\varepsilon}{T_u}\right)\cos[\pi(1-\varepsilon)]$$

$$+\sum_{\substack{n\neq m-1,m\\n=0}}^{N-1}\frac{\pi}{4}a_nP_{pr}\left(\frac{m-n-\varepsilon-0.5}{T_u}\right)\cos[\pi(m-n-\varepsilon)]+w_m^Q \tag{5.17a}$$

for $m=1,2,\cdots,N-1$, and

$$\hat{D}_0=\frac{\pi}{4}a_0P_{pr}\left(\frac{-\varepsilon-0.5}{T_u}\right)\cos(\pi\varepsilon)+\sum_{n=1}^{N-1}\frac{\pi}{4}a_nP_{pr}\left(\frac{-n-\varepsilon-0.5}{T_u}\right)\cos[\pi(n+\varepsilon)]+w_0^Q \tag{5.17b}$$

are used as estimates of the data symbol on the mth ($m\geq 1$) subcarrier and the 0th subcarrier, respectively. In eqs. (5.17a) and (5.17b), the sum term is the ICI due to frequency offset. The term $\hat{D}_0$ in (5.17b) is different from $\hat{D}_m$ in (5.17a) because there is no intentionally introduced ICI term.

In the case of a rectangular pulse-shaped OFDM system, the estimate of the data symbol on the mth subcarrier in the presence of normalized frequency offset ε will be

$$\hat{R}_m=a_mP_r\left(-\frac{\varepsilon}{T_u}\right)\cos(\pi\varepsilon)+\sum_{\substack{n\neq m\\n=0}}^{N-1}a_nP_r\left(\frac{m-n-\varepsilon}{T_u}\right)\cos[\pi(m-n-\varepsilon)]+w_m^I \tag{5.18}$$

where $P_r(f)=\mathrm{sinc}(fT_u)$. Note that in the absence of frequency offset, $\varepsilon=0$, eq. (5.18) becomes

$$\hat{R}_m=a_m+w_m^I. \tag{5.19}$$

This is different from eq. (5.9) since there is no intentionally introduced ICI in the absence of frequency offset.

It is known that the ICI power depends on the sidelobe amplitudes of the pulse-shaping functions [97]. In Fig. 5.1, it is observed that the partial-response signaling has smaller side-lobe amplitudes. Thus, it is expected that the employment of the partial-response signal pulse-shaping (or correlative coding) will achieve smaller ICI power than the employment of the rectangular pulse (without correlative coding). The ICI reduction achieved by correlative coding was shown in [96]. Our discussion of this phenomenon here views it from a different perspective, although it reaches the same conclusion. This effect should

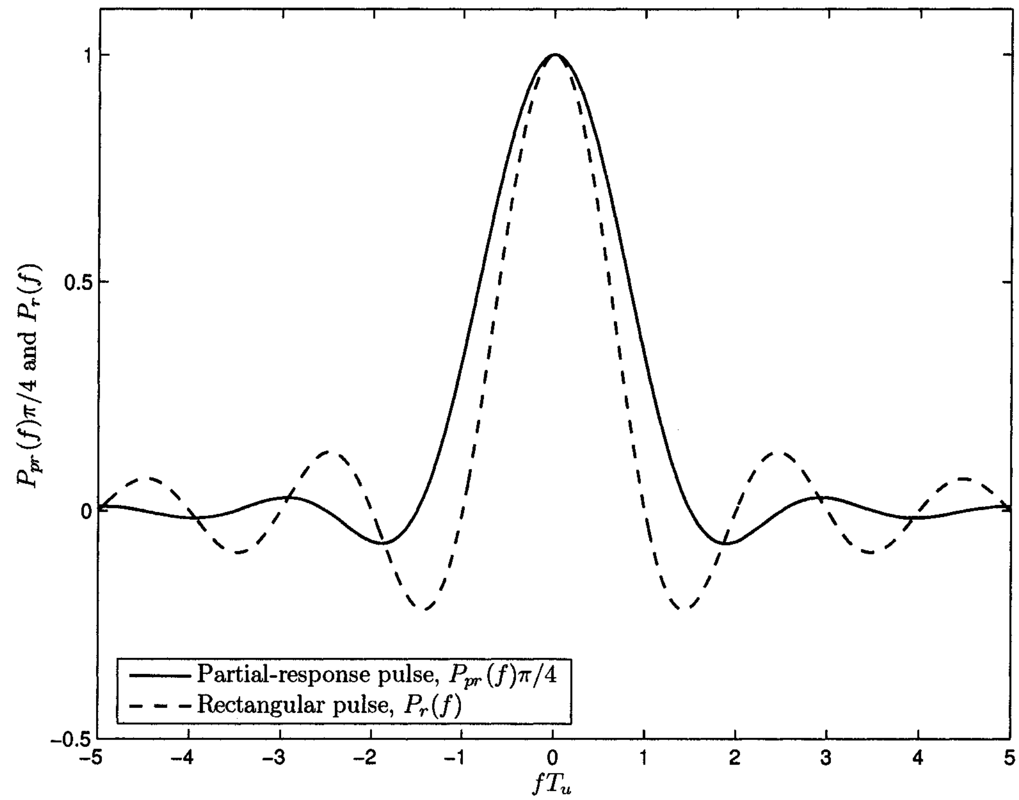

Fig. 5.1. The Fourier transforms of the partial-response pulse and the rectangular pulse.

contribute to reducing the BER for OFDM with partial-response pulse-shaping. On the other hand, however, it is seen in eq. (5.17a), that because of the introduction of multilevel signaling, without knowledge of normalized frequency offset, $\hat{D}_m$ will be compared with two thresholds at $\frac{\pi}{4}\sqrt{E_b}$ and $-\frac{\pi}{4}\sqrt{E_b}$ for data recovery. In contrast, in eq. (5.18), there is no intentionally introduced ICI term and the decision is based on threshold 0, that is, the decoder decides a "1" bit was transmitted if $\hat{R}_m > 0$, and otherwise a "0" is decided. The reduction of receiver decision distance will lead to BER performance degradation. The situation is clarified in Fig. 5.2 which shows the receiver decision regions for the two cases. Ignoring other effects, the reduction in receiver decision distance will cause a performance penalty of $(\frac{4}{\pi})^2 = 2.1$ dB for the correlative coding OFDM system.

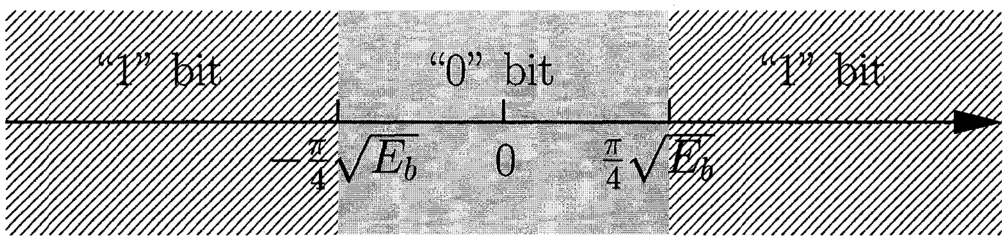

Decision region for partial-response pulse-shaped OFDM systems

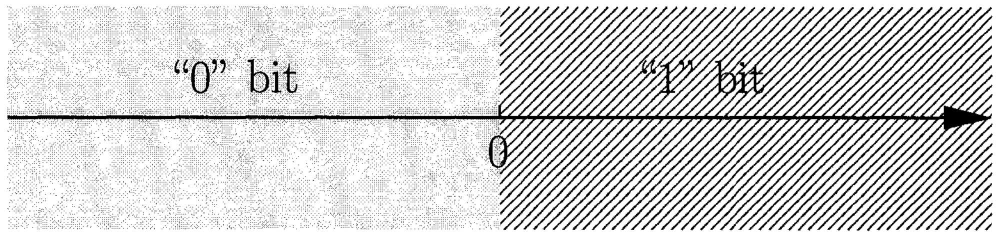

Decision region for rectangular pulse-shaped OFDM systems

Fig. 5.2. The receiver decision regions for the partial-response pulse-shaped OFDM system and the rectangular pulse-shaped OFDM system.

5.3 BER Analysis over AWGN Channels

We derive the BER of the two systems in AWGN channels using a characteristic function method in this section.

The characteristic function of $\hat{D}_m$ conditioned on a_m, a_{m-1} and ε can be written as

$$\Phi_m(\omega|a_{m-1}, a_m, \varepsilon) = \mathbf{E}(e^{j\omega\hat{D}_m}). \tag{5.20}$$

Conditioned on a_m, a_{m-1} and ε, the sum term

$$\frac{\pi}{4}a_m P_{pr}\left(\frac{-\varepsilon-0.5}{T_u}\right)\cos(\pi\varepsilon) + \frac{\pi}{4}a_{m-1}P_{pr}\left(\frac{0.5-\varepsilon}{T_u}\right)\cos[\pi(1-\varepsilon)] + w_m^Q \tag{5.21}$$

in eq. (5.17a) is a Gaussian random variable with mean

$$\frac{\pi}{4}a_m P_{pr}\left(\frac{-\varepsilon-0.5}{T_u}\right)\cos(\pi\varepsilon) + \frac{\pi}{4}a_{m-1}P_{pr}\left(\frac{0.5-\varepsilon}{T_u}\right)\cos[\pi(1-\varepsilon)] \tag{5.22}$$

and variance σ^2. The sequence a_n in (5.17a) is obtained after the precoding operation to reduce error propagation. In Appendix A, it is shown that the elements of the sequence a_n

are still independent. Therefore, the characteristic function of $\hat{D}_m$ can be written as

$$\Phi_m(w|a_{m-1},a_m,\varepsilon) = e^{j\omega\lambda(a_{m-1},a_m,\varepsilon)}\beta(\omega) \tag{5.23a}$$

where

$$\lambda(a_{m-1},a_m,\varepsilon) = \frac{\pi}{4}\cos(\pi\varepsilon)\left[a_m P_{pr}\left(\frac{-\varepsilon-0.5}{T_u}\right) - a_{m-1}P_{pr}\left(\frac{0.5-\varepsilon}{T_u}\right)\right] \tag{5.23b}$$

and

$$\beta(\omega) = e^{-\omega^2\sigma^2/2}\prod_{\substack{n\neq m-1,m\\ n=0}}^{N-1}\cos\left\{\frac{\pi}{4}\sqrt{E_b}\,\omega P_{pr}\left(\frac{m-n-\varepsilon-0.5}{T_u}\right)\cos[\pi(m-n-\varepsilon)]\right\} \tag{5.23c}$$

The mth $(m \geq 1)$ subcarrier BER can be written as

$$P_b(m) = \frac{1}{2}P_{b1}(m) + \frac{1}{2}P_{b2}(m) \tag{5.24}$$

where $P_{b1}(m)$ and $P_{b2}(m)$ are

$$\begin{aligned}
P_{b1}(m) &= \text{Prob}\left\{|\hat{D}_m| < \frac{\pi}{4}\sqrt{E_b} \mid a_m = \sqrt{E_b}, a_{m-1} = -\sqrt{E_b}, \varepsilon\right\}\\
&= \text{Prob}\left\{\hat{D}_m < \frac{\pi}{4}\sqrt{E_b} \mid a_m = \sqrt{E_b}, a_{m-1} = -\sqrt{E_b}, \varepsilon\right\}\\
&\quad - \text{Prob}\left\{\hat{D}_m < -\frac{\pi}{4}\sqrt{E_b} \mid a_m = \sqrt{E_b}, a_{m-1} = -\sqrt{E_b}, \varepsilon\right\}\\
&= \int_0^{+\infty}\frac{2\beta(\omega)\cos(\omega\gamma_1)\sin(\frac{\pi}{4}\sqrt{E_b}\,\omega)}{\pi\omega}\,d\omega
\end{aligned} \tag{5.25}$$

and

$$\begin{aligned}
P_{b2}(m) &= \text{Prob}\left\{\hat{D}_m \geq \frac{\pi}{4}\sqrt{E_b} \text{ or } \hat{D}_m \leq -\frac{\pi}{4}\sqrt{E_b} \mid a_m = a_{m-1} = \sqrt{E_b}, \varepsilon\right\}\\
&= \text{Prob}\{\hat{D}_m \leq -\frac{\pi}{4}\sqrt{E_b} \mid a_m = a_{m-1} = \sqrt{E_b}, \varepsilon\}\\
&\quad + \text{Prob}\{\hat{D}_m \geq \frac{\pi}{4}\sqrt{E_b} \mid a_m = a_{m-1} = \sqrt{E_b}, \varepsilon\}
\end{aligned}$$

$$= 1 - \int_0^{+\infty} \frac{2\beta(\omega)\cos(\omega\gamma_2)\sin(\frac{\pi}{4}\sqrt{E_b}\omega)}{\pi\omega} d\omega \tag{5.26}$$

respectively, and

$$\gamma_1 = \frac{\pi}{4}\sqrt{E_b}\cos(\pi\varepsilon)\left[P_{pr}\left(\frac{-\varepsilon - 0.5}{T_u}\right) + P_{pr}\left(\frac{0.5-\varepsilon}{T_u}\right)\right] \tag{5.27}$$

and

$$\gamma_2 = \frac{\pi}{4}\sqrt{E_b}\cos(\pi\omega)\left[P_{pr}\left(\frac{-\varepsilon - 0.5}{T_u}\right) - P_{pr}\left(\frac{0.5-\varepsilon}{T_u}\right)\right]. \tag{5.28}$$

Combining eqs. (5.24)-(5.28), one can obtain the BER for the mth ($m \geq 1$) subcarrier as

$$\begin{aligned} P_b(m) = \frac{1}{2} - \int_0^{+\infty} \frac{2\beta(\omega)\sin\left(\frac{\pi}{4}\sqrt{E_b}\omega\right)}{\pi\omega} \sin\left[\frac{\pi}{4}\sqrt{E_b}\omega\cos(\pi\varepsilon)P_{pr}\left(\frac{-\varepsilon-0.5}{T_u}\right)\right] \\ \times \sin\left[\frac{\pi}{4}\sqrt{E_b}\omega\cos(\pi\varepsilon)P_{pr}\left(\frac{0.5-\varepsilon}{T_u}\right)\right] d\omega. \end{aligned} \tag{5.29}$$

It is noted that, in eq. (5.17b), there is no intentionally introduced ICI term for subcarrier 0, and the decision is based on threshold 0. Applying the characteristic function method again, one can get the 0th subcarrier BER

$$\begin{aligned} P_b(0) &= \text{Prob}\left\{\hat{D}_0 < 0 \mid a_0 = \sqrt{E_b}, \varepsilon\right\} \\ &= \frac{1}{2} - \int_0^{+\infty} \frac{\sin[\frac{\pi}{4}\sqrt{E_b}\omega P_{pr}\left(\frac{-\varepsilon-0.5}{T_u}\right)\cos(\pi\varepsilon)]\beta(\omega)}{\pi\omega} d\omega. \end{aligned} \tag{5.30}$$

The average BER over different subcarriers in the presence of normalized frequency offset ε is

$$P_b(\varepsilon) = \frac{1}{N}\sum_{m=0}^{N-1} P_b(m). \tag{5.31}$$

Figs. 5.3 and 5.4 compare the BER performance of a 64 subcarrier BPSK-OFDM system with partial-response pulse-shaping and the system with rectangular pulse-shaping. The theoretical BER expression for rectangular pulse-shaped OFDM system has been developed in eq. (4.36) in Chapter 4 as

$$P_b^{rec}(m) = \frac{1}{2} - \int_0^{+\infty} \frac{\sin\left[\sqrt{E_b}\omega P_r(-\varepsilon/T_u)\cos(\pi\varepsilon)\right]}{\pi\omega} e^{-\frac{1}{2}\omega^2\sigma^2}$$

$$\times \prod_{\substack{n \neq m \\ n=0}}^{N-1} \cos\left\{ \sqrt{E_b} P_r \left(\frac{m-n-\varepsilon}{T_u} \right) \cos[\pi(m-n-\varepsilon)] \right\}. \tag{5.32}$$

The definition of partial-response pulse in eq. (5.14) has ensured that the transmitted OFDM symbol with partial-response pulse-shaping has the same energy as the transmitted OFDM symbol with rectangular pulse-shaping. The solid line and the dashed line represent theoretical BER results, and the symbols (square, diamond, *etc.*) represent Monte Carlo simulation results. The theoretical results and the simulation results are in excellent agreement. In Fig. 5.3, one can see that for small normalized frequency offset values 0.02, 0.05 and 0.1, the BER performance of the system with rectangular pulse-shaping is much better than the BER performance of the system with partial-response pulse-shaping. In particular, in the presence of normalized frequency offset 0.02 and at a BER of 10^{-3}, using partial-response pulse-shaping will lead to about 2.4 dB loss in signal-to-noise ratio (SNR). The reason for this is that for small frequency offset values, the ICI power is small. The benefit of ICI reduction by partial-response pulse-shaping can not compensate the loss due to multilevel signaling. As the normalized frequency offset increases, in Fig. 5.4, the benefit of using partial-response pulse-shaping can be observed. For example, in the case of normalized frequency offset 0.15, at a BER of 10^{-4}, about 1.6 dB performance gain in SNR can be achieved by using partial-response pulse-shaping rather than the rectangular pulse-shaping. Greater performance gain, about 3.9 dB in SNR, can be observed at a BER of 2×10^{-3} and normalized frequency offset $\varepsilon = 0.2$. However, when one further increases the normalized frequency offset value to 0.3, the BER performance favors the rectangular pulse-shaped system again. This is expected from examination of eqs. (5.17a) and (5.17b). In the presence of an unknown frequency offset, the desired signal amplitude is attenuated by a factor $P_{pr}\left(\frac{-\varepsilon-0.5}{T_u}\right)\cos(\pi\varepsilon)$ which decreases as the normalized frequency offset increases. The attenuation in signal amplitude has more adverse effect on the pulse-shaped OFDM system where the decision is more strongly influenced by the amplitude than on the rectangular-shaped OFDM system where the decision is more strongly influenced by the phase of the BPSK symbol.

5.4 Summary

Some ICI reduction in OFDM system can be achieved either by using partial-response pulse-shaping in the time-domain or by using correlative coding in the frequency-domain. The pulse-shaped OFDM system can be implemented by using digital filter techniques or a surface acoustic wave (SAW) chirp Fourier transform (CFT) [81]. Both pulse-shaping and correlative coding, which were shown to be equivalent in this work, will introduce multilevel signaling and BER performance degradation. For small frequency offset values, it is not beneficial to use these two techniques to reduce ICI because the BER loss caused by the reduced decision distance in the multilevel signaling is greater than the benefit obtained from ICI reduction. For some large frequency offset values, these two methods can both reduce ICI and improve BER performance.

Expressions for the BER of pulse-shaped OFDM systems with symbol-by-symbol detection operated in AWGN channels have been derived.

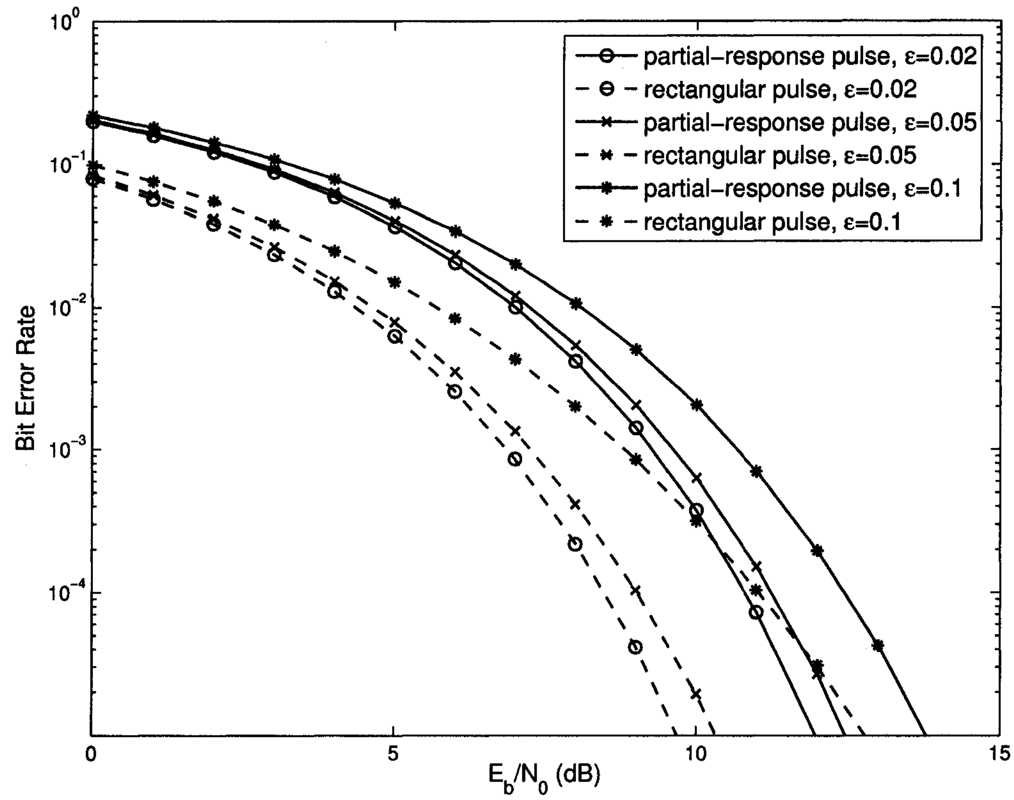

Fig. 5.3. Comparisons of the system BERs with partial-response pulse-shaping (or correlative coding) and the system with rectangular pulse-shaping (without correlative coding) transmitted over an AWGN channel in the presence of normalized frequency offsets 0.02, 0.05 and 0.1.

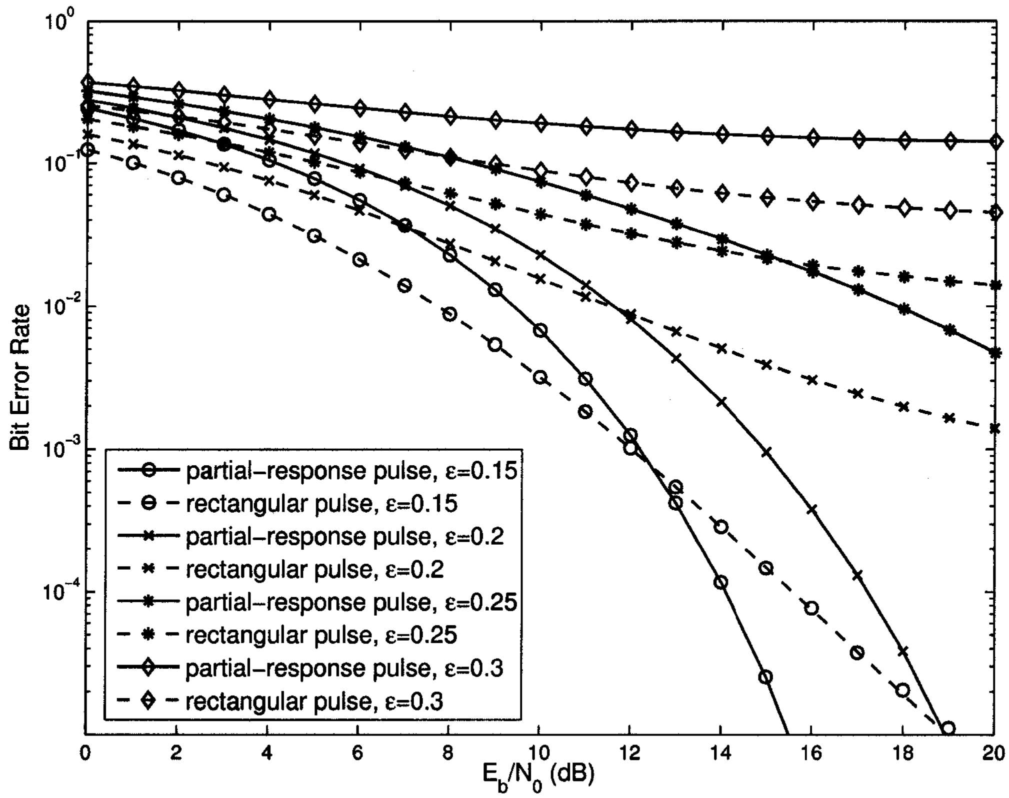

Fig. 5.4. Comparisons of the system BERs with partial-response pulse-shaping (or correlative coding) and the system with rectangular pulse-shaping (without correlative coding) transmitted over an AWGN channel in the presence of normalized frequency offsets 0.15, 0.2, 0.25 and 0.3.

Chapter 6

Receiver Windowing in OFDM Systems

6.1 Introduction

The application of Nyquist pulse-shaping and partial-response pulse at the transmitter of OFDM systems to reduce ICI has been investigated in Chapter 4 and Chapter 5, respectively. The Nyquist windows can also be applied to the ISI-free part of a received OFDM symbol to reduce the ICI power [73, 87, 98, 99]. One benefit of OFDM receiver windowing, compared with transmitter Nyquist pulse-shaping, lies in that the receiver windowing signal processing algorithm takes place at the receiver side only, and the OFDM transmitter can be left unchanged. The N-subcarrier OFDM receiver windowing algorithm can be implemented by an FFT structure which is slightly more complex than the conventional N-point FFT algorithm [98].

A raised-cosine window was used in [98]. Other Nyquist pulse shaping functions in Chapter 4 can also be used in the OFDM receiver windowing scenario. In this chapter, we first provide an ICI analysis for receiver windowing OFDM systems operating in a Rayleigh slowly fading channel when carrier frequency offset exists. All previous work [73, 86, 87, 98, 99] has considered the AWGN channel exclusively. The carrier frequency offset can not be known perfectly at the receiver. Therefore, we consider several robust frequency offset-independent windowing reception Nyquist shapes, including the raised-cosine window, BTRC window [88], SOCW [99], the polynomial window [91], the Franks window [86], and the double-jump shape [86, 87]. We then, using SIR as the performance measure, examine the effect of applying these receiver windowing functions on ICI reduction in OFDM systems. Although, a very recent work [100] presented an average signal-to-interference-plus-noise-ratio (SINR) analysis of OFDM systems in the presence of carrier frequency offset for fading channels, the application of receiver windowing functions was not included in that work. Moreover, [100] did not consider the BER performance of OFDM systems with receiver windowing in carrier frequency offset because of the difficulty of obtaining the exact distribution of the ICI. Therefore, in another contribution of this work, we derive an exact BER expression for a receiver windowing QPSK-OFDM system in fading environments. The exact BER expression is obtained by noting that the received signal conditioned on data symbols is Gaussian distributed. Proper complex Gaussian random process theory and a characteristic function method are then applied in the development of the BER expression. Based on the exact BER result, a performance comparison of different receiver windowing functions using the BER measure is then undertaken. It is interesting to note that the comparisons based on the BER measure do not necessarily coincide with the comparisons based on the SIR measure. This is because the desired signal and the ICI component are not independent in fading environments, and the BER is more related to the distribution of ICI than to the SIR value itself. Therefore, the application of pulses designed using ICI power minimization or SIR maximization as an objective may not give the smallest BER. In this sense, BER gives a more meaningful and effective performance measure. Our theoretical BER analysis is in excellent agreement with results obtained from computer simulation, and it provides an exact prediction tool for the BER performance of OFDM system when using different ICI-reducing windowings. We find that, for small to medium pulse roll-off factors, the BTRC windowing gives the smallest BER among the six windowing functions considered. However, when the roll-off factor approaches one, the Franks and SOCW windows exhibit better BER performance.

The remainder of this chapter is organized as follows. In Section 6.2, the system model is given. The ICI analysis and the effects of different window functions on the ICI power reduction are compared using the SIR performance measure in Section 6.3. Section 6.4 gives the BER analysis of a QPSK-OFDM system with windowing reception. In Section 6.5, we summarize our major findings of this chapter.

6.2 System Model

A continuous-time baseband OFDM signal, $s(t)$, including cyclic prefix (CP) can be expressed as

$$s(t) = \frac{1}{\sqrt{N}} \sum_{i=-\infty}^{+\infty} \sum_{n=0}^{N-1} D_{i,n} e^{\frac{j2\pi n(t-T_g-iT_s)}{T_u}} u(t-iT_s) \tag{6.1}$$

where $D_{i,n}$ is the complex symbol modulated onto the nth subcarrier in the ith OFDM symbol, T_u is the useful signal duration, T_g is the length of the cyclic prefix, $T_s = T_u + T_g$ is the duration of an OFDM symbol, and $u(t)$ is defined as

$$u(t) = \begin{cases} 1, & 0 \leq t < T_s \\ 0, & \text{otherwise.} \end{cases} \tag{6.2}$$

We also assume that

$$\mathbf{E}[D_{i,n}D_{j,m}^*] = \begin{cases} E_s, & i = j \text{ and } n = m \\ 0, & i \neq j \text{ or } n \neq m \end{cases} \tag{6.3}$$

where $D_{j,m}^*$ represents the complex conjugate of the complex symbol $D_{j,m}$.

By letting

$$b_{i,n} = \begin{cases} D_{i,n/2}, & n = 0,2,4,\cdots,2N-2 \\ 0, & n = 1,3,5,\cdots,2N-1 \end{cases} \tag{6.4}$$

one can write (6.1) as

$$s(t) = \frac{1}{\sqrt{N}} \sum_{i=-\infty}^{+\infty} \sum_{n=0}^{2N-1} b_{i,n} e^{\frac{j2\pi n(t-T_g-iT_s)}{2T_u}} u(t-iT_s). \tag{6.5}$$

Eqs. (6.5) and (6.1) are equivalent. We will use eq. (6.5), instead of eq. (6.1) in the following analysis because the receiver windowing OFDM reception can be implemented by a $2N$-point discrete Fourier transform (DFT) according to (6.5).

The channel impulse response (CIR) of the time-variant L-path fading channel considered is [17]

$$h(t,\tau) = \sum_{l=0}^{L-1} h_l(t)\delta(\tau-\tau_l) \tag{6.6}$$

where $h_l(t)$ and τ_l is the complex amplitude and propagation delay of the lth path, respectively. We further assume that

$$\tau_0 \leq \tau_1 \leq \cdots \leq \tau_{L-1} \tag{6.7}$$

and the complex stochastic processes $h_l(t)$ are independent and identically Gaussian distributed.

By design, the cyclic prefix T_g is usually much longer than the maximum channel delay spread $\tau_{max} = \tau_{L-1} - \tau_0$. In addition, the duration of one OFDM symbol is long enough that the ISI occurs only between two adjacent, say the $(k-1)$th and kth, OFDM symbols. As a result, the received signal in the presence of carrier frequency offset Δf is then described as

$$y(t) = \frac{1}{\sqrt{N}} \sum_{l=0}^{L-1} h_l(t) \sum_{i=k-1}^{k} \sum_{n=0}^{2N-1} b_{i,n} e^{\frac{j2\pi n(t-T_g-iT_s-\tau_l)}{2T_u}} e^{j2\pi\Delta f(t-iT_s-\tau_l)} u(t-iT_s-\tau_l) + w(t) \tag{6.8}$$

where $w(t)$ is a zero-mean, complex Gaussian noise process with variance $\frac{1}{2}\sigma^2$ per dimension.

We assume that a duration, T_v, of the cyclic prefix is not corrupted by the intersymbol interference. Thus the length of the ISI-free part of the OFDM symbol is $T_v + T_u$. Assuming that the receiver is synchronized to the 0th path with delay $\tau_0 = 0$, and sampling the continuous-time signal $y(t)$ at time instants $t_m = kT_s + T_g - T_v + mT_u/N$, one can obtain the discrete-time sample of the kth received OFDM symbol as

$$y_m = \frac{1}{\sqrt{N}} \sum_{n=0}^{2N-1} b_{k,n} e^{\frac{j2\pi m(2\varepsilon+n)}{2N}} e^{-jn\pi\alpha} H_{k,n} e^{j2\pi\varepsilon(\mu-\alpha)} + w_m \tag{6.9}$$

where $m = 0, 1, \cdots, N_u - 1$, $N_u = \lfloor (1+\alpha)N \rfloor + 1$, $\alpha = T_v/T_u$, and $\mu = T_g/T_u$. The operation $\lfloor a \rfloor$ represents a nearest integer less than or equal to a. The normalized frequency offset with respect to subcarrier frequency spacing $\frac{1}{T_u}$ is $\varepsilon = \Delta f T_u$. The channel response to the frequency $\frac{n}{2T_u} + \Delta f$ at the kth OFDM symbol is

$$H_{k,n} = \sum_{l=0}^{L-1} h_{l,k} e^{-j2\pi(n/2T_u + \Delta f)\tau_l} \tag{6.10}$$

where $h_{l,k} = h_l(kT_s + T_g - T_v + mT_u/N)$ is the channel impulse response of the lth multipath during the kth OFDM symbol. In a slowly fading channel, $h_{l,k}$ will not change during one OFDM symbol. Under the assumption of exponential distribution of the multipath time delay, the correlation between channel response $H_{k,n}$ and $H_{k,m}$ can be written as [66], [43]

$$\mathbf{E}[H_{k,n} H_{k,m}^*] = \frac{\sigma_f^2}{1 - j\pi(n-m)\eta} \tag{6.11}$$

where

$$\sigma_f^2 = \mathbf{E}[|H_{k,n}|^2] = \sum_{l_1=0}^{L-1} \sum_{l_2=0}^{L-1} \mathbf{E}[h_{l_1,k} h_{l_2,k}^*] e^{j2\pi(n/2T_u + \Delta f)(\tau_{l_2} - \tau_{l_1})} = \sum_{l=0}^{L-1} \mathbf{E}[|h_{l,k}|^2] \tag{6.12}$$

since the complex amplitudes of different path are independent and identically Gaussian distributed. In (6.11), $\eta = \overline{\tau}/T_u$ is the normalized mean time delay, and $\overline{\tau}$ is the mean time delay measure given in [66], [43].

We will compare six Nyquist window functions which are obtained by sampling the raised-cosine pulse, the BTRC pulse, the SOCW pulse, the polynomial pulse, the Franks pulse, and the double-jump pulse defined in Chapter 4. For the purpose of FFT implementation of the OFDM reception, samples y_m in (6.9) are first extended to $2N$ points by inserting zeros at both sides so that

$$\tilde{y}_m = \begin{cases} 0, & m = 0, 1, \cdots, \lfloor \frac{N}{2}(1-\alpha) \rfloor \\ y_{m-(\lfloor N(1-\alpha)/2 \rfloor + 1)}, & m = \lfloor \frac{N}{2}(1-\alpha) \rfloor + 1, \cdots, \lfloor \frac{N}{2}(1-\alpha) \rfloor + N_u \\ 0, & m = \lfloor \frac{N}{2}(1-\alpha) \rfloor + N_u + 1, \cdots, 2N-1. \end{cases} \tag{6.13}$$

The discrete-time samples obtained from the continuous-time pulses mentioned above, p_m, $m = 0, 1, \cdots, N_u - 1$, are also extended to $2N$ points by

$$g_m = \begin{cases} 0, & m = 0, 1, \cdots, \lfloor \frac{N}{2}(1-\alpha) \rfloor \\ p_{m-(\lfloor N(1-\alpha)/2 \rfloor + 1)}, & m = \lfloor \frac{N}{2}(1-\alpha) \rfloor + 1, \cdots, \lfloor \frac{N}{2}(1-\alpha) \rfloor + N_u \\ 0, & m = \lfloor \frac{N}{2}(1-\alpha) \rfloor + N_u + 1, \cdots, 2N-1. \end{cases} \tag{6.14}$$

One can then perform a $2N$-point DFT on $r_m = \tilde{y}_m g_m$, and obtain

$$\begin{aligned} \hat{D}_{k,p} &= \frac{1}{\sqrt{N}} \sum_{m=0}^{2N-1} r_m e^{-\frac{j2\pi mp}{2N}} \\ &= \frac{1}{N} \sum_{n=0}^{2N-1} b_{k,n} H_{k,n} e^{j\pi[2\varepsilon(\mu-\alpha) - n\alpha - n_1 p/N]} \sum_{m=0}^{N_u-1} p_m e^{\frac{j2\pi m(n-p+2\varepsilon)}{2N}} + \tilde{w}_p \end{aligned} \tag{6.15}$$

where $n_1 = \lfloor \frac{N}{2}(1-\alpha) \rfloor + 1$, $p = 0, 1, \cdots, 2N-1$, and

$$\tilde{w}_p = \frac{1}{\sqrt{N}} \sum_{m=0}^{N_u-1} w_m p_m e^{-\frac{j\pi(m+n_1)p}{N}} \tag{6.16}$$

The noise sample $\tilde{w}_p$ has mean zero and variance $\sigma_N^2 = \sum_{m=0}^{N_u-1} p_m^2 \sigma^2 / N$.

In the absence of carrier frequency offset, $\varepsilon = 0$, the sum $\sum_{m=0}^{N_u-1} p_m e^{\frac{j2\pi m(n-p+2\varepsilon)}{2N}}$ in (6.15) becomes

$$\sum_{m=0}^{2N-1} p_m e^{\frac{j2\pi m(n-p)}{2N}} = \begin{cases} 0, & n-p \neq 0 \text{ and } n-p \text{ is even} \\ N, & n-p = 0. \end{cases} \tag{6.17}$$

since $p_m, m = 0, 1, \cdots, N_u - 1$ are samples of a Nyquist pulse. Recalling that $b_{k,n}$ is zero when n is an odd number, one can choose only even bins $p = 2q$ in $\hat{D}_{k,p}$ to recover the transmitted data sequence $D_{k,q}$ where $q = 0, 1, 2, \cdots, N-1$. That is,

$$\hat{D}_{k,2q} = D_{k,q}\tilde{H}_{2q,2q} + \tilde{w}_{2q} \tag{6.18}$$

where

$$\tilde{H}_{n,p} = H_{k,n}S_{n,p} \tag{6.19}$$

and

$$S_{n,p} = \frac{1}{N}e^{j\pi[2\varepsilon(\mu-\alpha)-n\alpha-n_1 p/N]}\sum_{m=0}^{N_u-1} p_m e^{\frac{j2\pi m(n-p+2\varepsilon)}{2N}}. \tag{6.20}$$

Since only even bins are required to recover the transmitted data sequence, the $2N$-point DFT can be implemented by an improved N-point FFT structure slightly more complex than the conventional N-point FFT structure [98]. It is noted that there are no ICI components in (6.18) in the absence of carrier frequency offset. The optimal, minimum probability of error detection of the transmitted data can then be accomplished with a correlation demodulator.

6.3 Intercarrier Interference

In the presence of carrier frequency offset, ICI will be introduced. From (6.15) one has

$$\hat{D}_{k,p} = \sum_{n=0}^{2N-1} b_{k,n}\tilde{H}_{n,p} + \tilde{w}_p \tag{6.21}$$

Choosing only even bins $p = 2q$ at the receiver, one obtains

$$\hat{D}_{k,2q} = D_{k,q}\tilde{H}_{2q,2q} + \sum_{\substack{d\neq q\\ d=0}}^{N-1} D_{k,d}\tilde{H}_{2d,2q} + \tilde{w}_{2q}. \tag{6.22}$$

The first term in (6.22) is the desired signal, the second term is the ICI component, and the last term is the AWGN. The ICI power can be written as

$$\sigma_{ICI}^2 = \sum_{\substack{d_1\neq q\\ d_1=0}}^{N-1}\sum_{\substack{d_2\neq q\\ d_2=0}}^{N-1} \mathbf{E}\left[D_{k,d_1}D_{k,d_2}^*\right]\mathbf{E}\left[\tilde{H}_{2d_1,2q}\tilde{H}_{2d_2,2q}^*\right]$$

$$= \frac{E_s \sigma_f^2}{N^2} \sum_{\substack{d \neq q \\ d=0}}^{N-1} \sum_{m_1=0}^{N_u-1} \sum_{m_2=0}^{N_u-1} p_{m_1} p_{m_2} e^{\frac{j2\pi(m_1-m_2)(d-q+\varepsilon)}{N}} \tag{6.23}$$

The power of the desired signal, σ_s^2, is

$$\sigma_s^2 = \mathbf{E}[|D_{k,q}|^2]\mathbf{E}[|\tilde{H}_{k,2q}|^2] = \frac{E_s \sigma_f^2}{N^2} \sum_{m_1=0}^{N_u-1} \sum_{m_2=0}^{N_u-1} p_{m_1} p_{m_2} e^{\frac{j2\pi(m_1-m_2)\varepsilon}{N}}. \tag{6.24}$$

Previously, optimal pulses were designed in [86, 87] with the objective of minimizing the average interference power. Therefore, in order to examine the effect of different pulse designs on ICI reduction, we define the SIR as the ratio of the average desired signal power σ_s^2 to the average ICI power σ_{ICI}^2, and write it as

$$\text{SIR} = \frac{\sigma_s^2}{\sigma_{ICI}^2} = \frac{\sum_{m_1=0}^{N_u-1} \sum_{m_2=0}^{N_u-1} p_{m_1} p_{m_2} e^{\frac{j2\pi(m_1-m_2)\varepsilon}{N}}}{\sum_{\substack{d \neq q \\ d=0}}^{N-1} \sum_{m_1=0}^{N_u-1} \sum_{m_2=0}^{N_u-1} p_{m_1} p_{m_2} e^{\frac{j2\pi(m_1-m_2)(\varepsilon+d-q)}{N}}}. \tag{6.25}$$

Signal-to-interference ratio is commonly defined in another way where the average SIR is obtained by averaging the instantaneous fading SIR conditioned on given channel gains and data symbols. However, it is difficult to get an analytical expression for the average SIR defined this way because both the numerator and the denominator include the channel gain components, and they are correlated. In the next section, we will use a characteristic function approach to derive the BER, which is a more meaningful performance measure than the SIR.

Fig. 6.1 compares the SIRs for different receiver windowings applied in a 64-subcarrier OFDM system in the presence of carrier frequency offset. As suggested by [99], for the SOCW window, we choose a_1 as 0.4 and -0.5 for $\alpha = 0.3$ and $\alpha = 1.0$, respectively. The SIR is related to the frequency spectra sidelobe amplitude [97]. Some insight is gained from examining the frequency spectra of the different pulses in Fig. 6.2 in this chapter and Fig. 4.8 in Chapter 4 for $\alpha = 0.3$ and $\alpha = 1.0$, respectively. From Fig. 6.1 one can see that, in the case of $\alpha = 0.3$, the employment of the Franks window function gives the greatest SIR compared with the other four window functions because of the relatively small spectrum sidelobe amplitude of the Franks pulse, as shown in Fig. 6.2. In particular, for a normalized carrier frequency offset $\varepsilon = 0.1$, one achieves 0.18 dB, 0.30 dB, 0.54 dB, 1.11 dB, and 2.26 dB more SIR with the employment of the Franks window function rather than the polynomial window, the double-jump window, SOCW window, BTRC window, and the raised-cosine window, respectively. The situation is different when α is increased to 1.0. For $\alpha = 1.0$, in the case of large normalized carrier frequency offsets ε, larger than 0.17, the employment of both the BTRC window and the polynomial window gives slightly better SIR than the Franks window, or the SOCW window. However, when $\varepsilon < 0.17$, the SIR favors the Franks window (SOCW window). One can also observe that, different from the scenario of $\alpha = 0.3$, the double-jump window gives the worst SIR among the six pulses compared in the case of $\alpha = 1.0$. The reason for this is that, unlike the other windowing functions, the frequency domain sidelobe amplitude of the double-jump window (shown in Figs. 6.2 and 4.8) becomes very large when $\alpha = 1.0$.

6.4 Bit Error Rate Analysis

A SIR measure is not as meaningful as an appropriate BER measure, and the application of the former is often motivated by analytical tractability. In this section, we will develop a BER assessment of the OFDM system operating in frequency-selective Rayleigh fading. Then, the benefits of using the different receiver windows will be assessed in terms of BER. We will find that the BER and SIR measures can sometimes lead to contrary selections of the "best" window to use in particular conditions. We use a characteristic function method to evaluate the BER.

The subcarrier modulation format is assumed to be QPSK. Therefore, the real part $D^I_{k,q}$ and the imaginary part $D^Q_{k,q}$ of data symbol $D_{k,q}$ take values from the set $\{\sqrt{E_b}, -\sqrt{E_b}\}$ with equal probability. We further assume that the two bits b_1 and b_2, corresponding to one

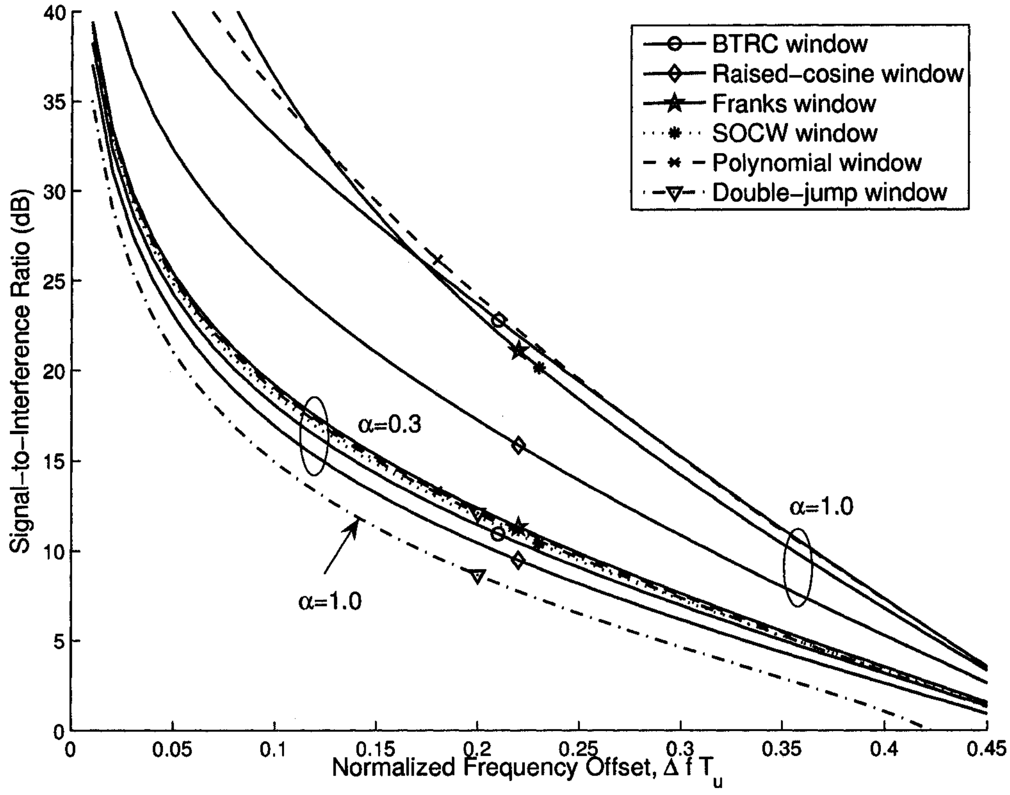

Fig. 6.1. The SIR in a 64-subcarrier OFDM receiver windowing with the employment of different window functions ($\alpha = 0.3$, and 1.0).

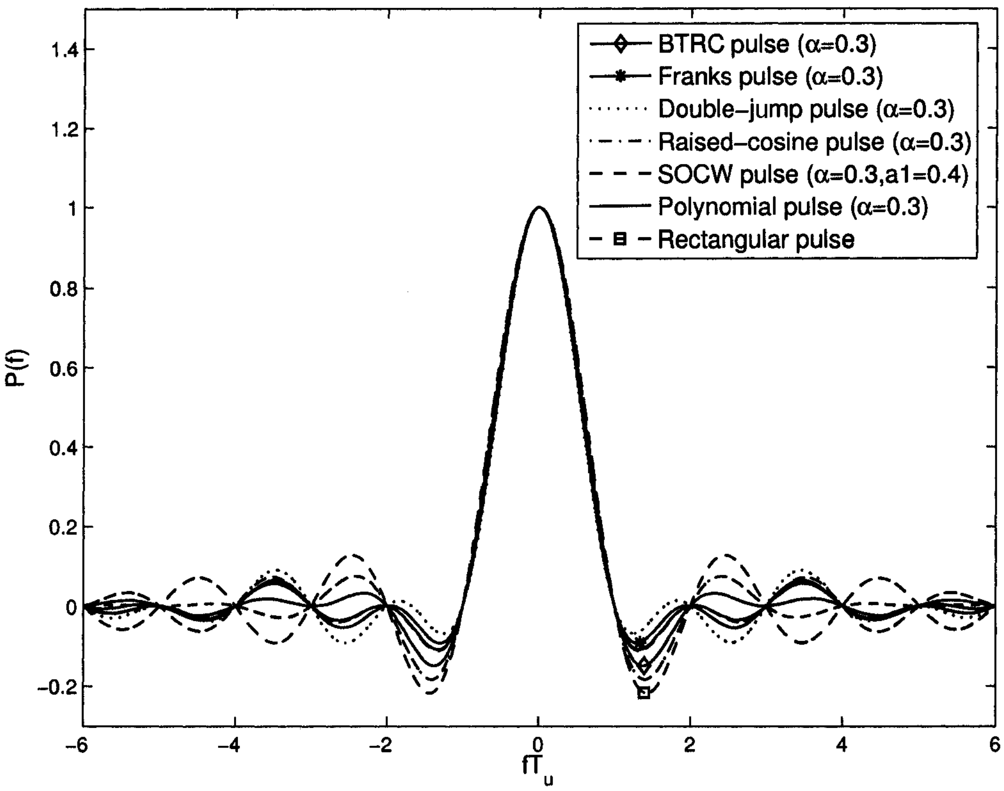

Fig. 6.2. The frequency spectra of different window functions ($\alpha = 0.3$).

QPSK symbol, are Gray-coded as in IEEE standards 802.11 and 802.16a. To manifest the effect of pulse-shaping on BER performance in the presence of frequency offset when using different receiver windowing functions, we assume that $\tilde{H}_{2q,2q}$ is perfectly known as in [27]. Therefore, the receiver can give the b_1 bit decision and b_2 bit decision of the QPSK symbol on the qth subcarrier from the in-phase component $\hat{b}_{1,q} = \Re\{\hat{D}_{k,2q}\tilde{H}^*_{2q,2q}\}$, and quadrature component $\hat{b}_{2,q} = \Im\{\hat{D}_{k,2q}\tilde{H}^*_{2q,2q}\}$, respectively.

The terms $\tilde{H}_{2d,2q}$ in (6.22) are joint complex Gaussian random variables since the channel frequency responses $H_{k,n}$ are joint complex Gaussian random variables [66], [43]. Furthermore, $\hat{D}_{k,2q}$ is a complex Gaussian random variable conditioned on data symbol set $\mathbb{A} = \{D_{k,0}, D_{k,1}, \cdots, D_{k,N-1}\}$ since a sum of joint complex Gaussian random variables is Gaussian [47]. Averaging over all data sequences of length $N-1$, the characteristic function of $\hat{b}_{1,q}$ conditioned on $D_{k,q}$ is given as

$$\Phi_{1,q}(\omega \mid D_{k,q}) = \frac{1}{4^{N-1}} \sum_{i=1}^{4^{N-1}} \Phi^i_{1,q}(\omega \mid D_{k,q}, \mathbb{A}_i) \tag{6.26}$$

where $\Phi^i_{1,q}(\omega \mid D_{k,q}, \mathbb{A}_i)$ is the characteristic function of $\hat{b}_{1,q}$ conditioned on $D_{k,q}$ and a specific data symbol set $\mathbb{A}_i = \{D^i_{k,0}, D^i_{k,1}, \cdots, D^i_{k,q-1}, D^i_{k,q+1}, \cdots, D^i_{k,N-1}\}$. From [39], one has

$$\Phi^i_{1,q}(\omega \mid D_{k,q}, \mathbb{A}_i) = \frac{1}{1 - j\omega\Re\{\sigma^i_{AB}\} + \frac{1}{4}(\sigma^i_A\sigma^i_B - |\sigma^i_{AB}|^2)\omega^2} \tag{6.27}$$

where the covariances σ^i_A, σ^i_{AB}, and σ^i_B are

$$\begin{aligned} \sigma^i_A &= \mathbf{E}\left[\hat{D}_{k,2q}\hat{D}^*_{k,2q} \mid D_{k,q}, \mathbb{A}_i\right] \\ &= 2E_b\sigma_f^2|S_{2q,2q}|^2 + 2\Re\left\{ D^*_{k,q}S^*_{2q,2q} \sum_{\substack{d\neq q\\ d=0}}^{N-1} \frac{D^i_{k,d}S_{2d,2q}\sigma_f^2}{1 - j2\pi(d-q)\eta} \right\} \\ &\quad + \sum_{\substack{d_1\neq q\\ d_1=0}}^{N-1} \sum_{\substack{d_2\neq q\\ d_2=0}}^{N-1} \frac{D^i_{k,d_1}D^{i*}_{k,d_2}S_{2d_1,2q}S^*_{2d_2,2q}\sigma_f^2}{1 - j2\pi(d_1-d_2)\eta} + \sigma_N^2 \end{aligned} \tag{6.28a}$$

$$\sigma^i_{AB} = \mathbf{E}\left[\hat{D}_{k,2q}\tilde{H}_{2q,2q} \mid D_{k,q}, \mathbb{A}_i\right] = D_{k,q}\sigma_f^2|S_{2q,2q}|^2 + \sum_{\substack{d\neq q\\ d=0}}^{N-1} \frac{D^i_{k,d}S_{2d,2q}S^*_{2q,2q}\sigma_f^2}{1 - j2\pi(d-q)\eta} \tag{6.28b}$$

$$\sigma_B^i = \mathbf{E}\left[\tilde{H}_{2q,2q}\tilde{H}^*_{2q,2q} \mid D_{k,q}, \mathbb{A}_i\right] = \sigma_f^2 |S_{2q,2q}|^2 \tag{6.28c}$$

respectively.

The b_1 bit error rate of the qth subcarrier in the presence of normalized carrier frequency offset ε can then be obtained by using the inversion theorem [49–52], as

$$\begin{aligned}
P_{b1}^q(\varepsilon) &= \frac{1}{2}\text{Prob}\left\{\hat{b}_{1,q} < 0 \mid D_{k,q} = \sqrt{E_b} + j\sqrt{E_b}\right\} + \frac{1}{2}\text{Prob}\left\{\hat{b}_{1,q} < 0 \mid D_{k,q} = \sqrt{E_b} - j\sqrt{E_b}\right\} \\
&= \text{Prob}\left\{\hat{b}_{1,q} < 0 \mid D_{k,q} = \sqrt{E_b} + j\sqrt{E_b}\right\} \\
&= \frac{1}{2} - \int_0^{+\infty} \frac{\Im\{\Phi_{1,q}(\omega|D_{k,q})\}}{\pi\omega} d\omega \\
&= \frac{1}{2} - \frac{1}{4^{N-1}} \sum_{i=1}^{4^{N-1}} \frac{\Re\{\sigma_{AB}^i\}}{2\sqrt{\sigma_A^i \sigma_B^i - \Im\{\sigma_{AB}^i\}^2}}.
\end{aligned} \tag{6.29}$$

According to symmetry, the b_2 bit has the same error rate as the b_1 bit, hence the average BER over different subcarriers is

$$P_b(\varepsilon) = \frac{1}{N}\sum_{q=0}^{N-1} P_{b1}^q(\varepsilon). \tag{6.30}$$

For a small number of subcarriers, for example, $N = 8$, the computational complexity of (6.29) is acceptable. For larger N, a Monte Carlo method [101] can give an excellent estimate of (6.29) by choosing randomly M data sequences and averaging as

$$P_{b1}^q(\varepsilon) = \frac{1}{2} - \frac{1}{M}\sum_{i=1}^{M} \frac{\Re\{\sigma_{AB}^i\}}{2\sqrt{\sigma_A^i \sigma_B^i - \Im\{\sigma_{AB}^i\}^2}}. \tag{6.31}$$

Through extensive experiment, a value of $M = 100$ was found to be large enough to give a result that is in excellent agreement with exact calculation when $N \leq 8$. Therefore, we use the Monte Carlo method with $M = 100$ to determine the BER results for $N = 64$ in the sequel. A larger value of M can improve the accuracy of the BER calculation at the expense of increased computation time [101].

Figs. 6.3 - 6.7 show the BER performance of a 64-subcarrier QPSK-OFDM system with windowing reception in several scenarios. Without further specification, the normalized mean time delay spread η is chosen as 0.03 in all the BER simulations and calculations.

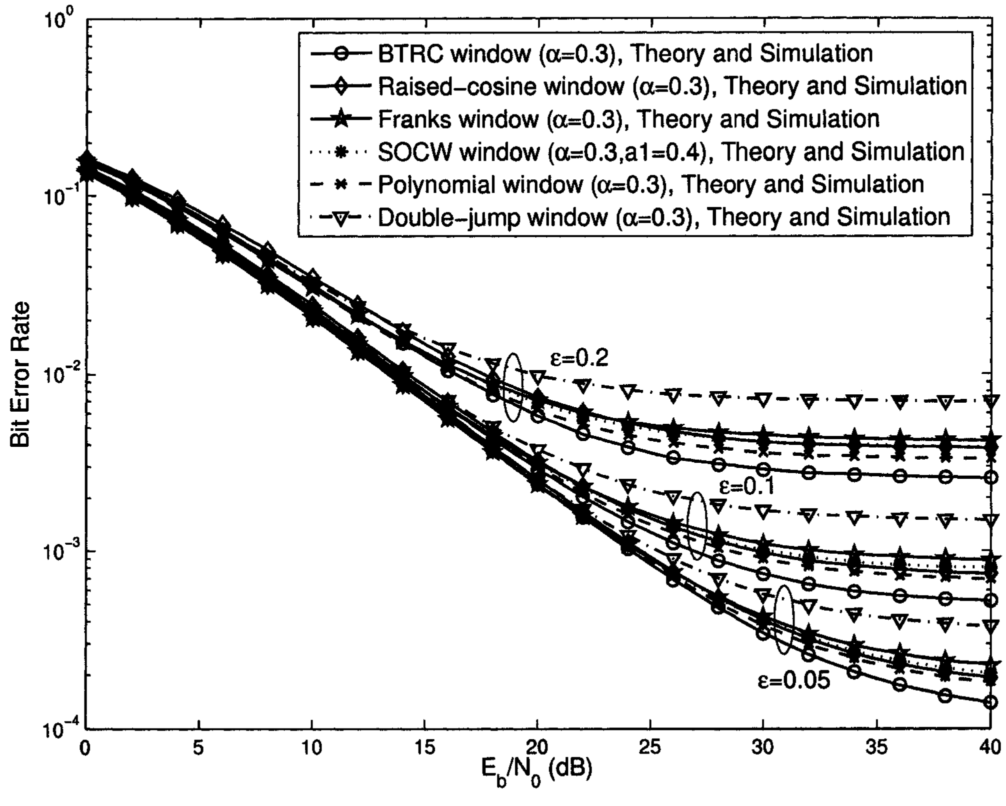

Fig. 6.3. The bit error rate in 64-subcarrier QPSK-OFDM receiver windowing with the employment of different window functions ($\alpha = 0.3$).

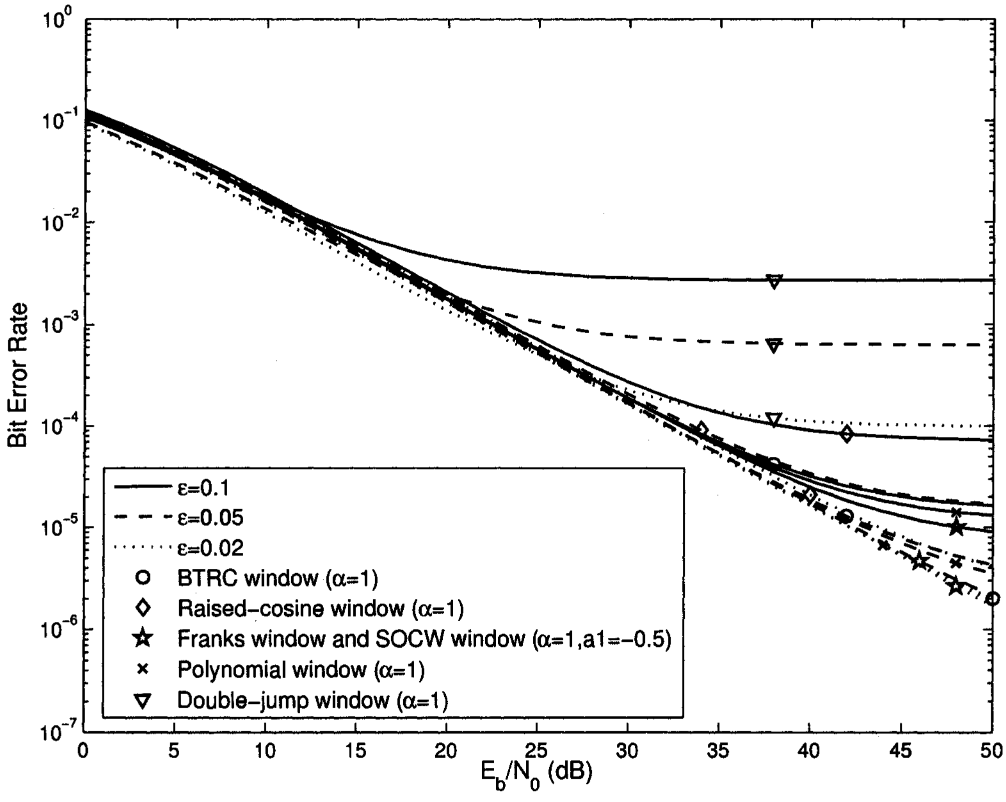

Fig. 6.4. The bit error rate in 64-subcarrier QPSK-OFDM receiver windowing with the employment of different window functions ($\alpha = 1.0$).

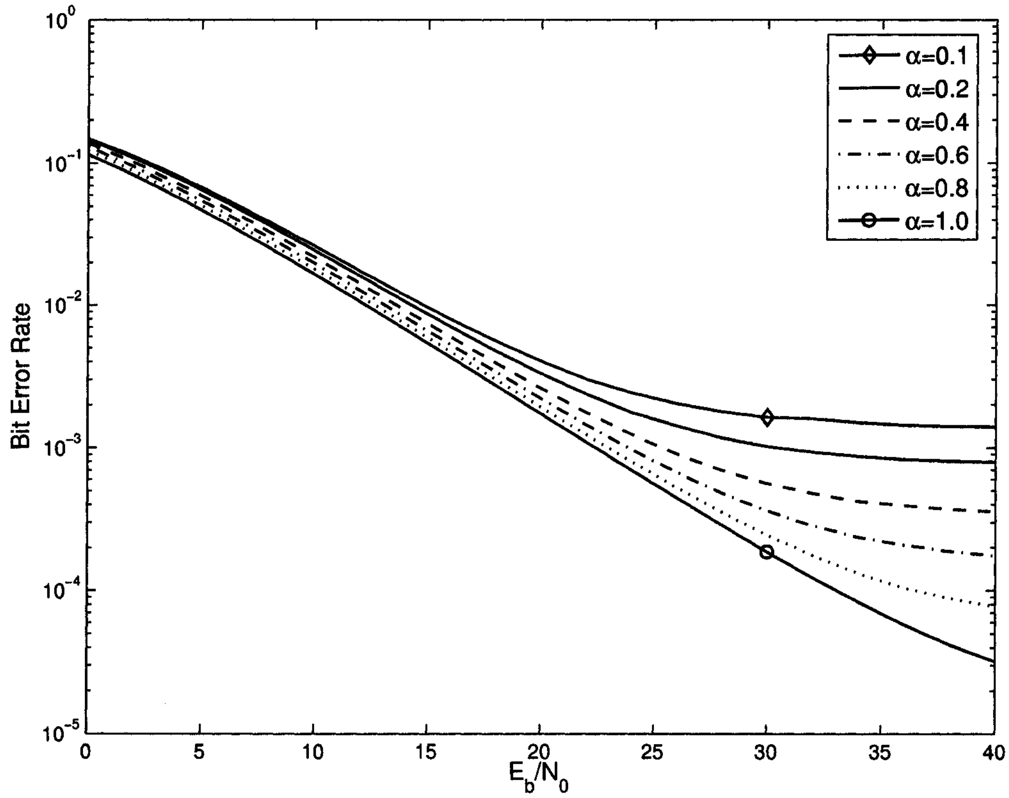

Fig. 6.5. The bit error rate in 64-subcarrier QPSK-OFDM receiver windowing with the employment of the BTRC window functions, $\varepsilon = 0.1$, and $\alpha = 0.1, 0.2, 0.4, 0.6, 0.8$ and 1.0.

In Fig. 6.3, the BERs of the QPSK-OFDM system with different windowings for $\alpha = 0.3$ in the cases of normalized carrier frequency offset values 0.05, 0.1 and 0.2 are compared. The lines (including the solid line, dashed line, dotted line, and so on) represent the theoretical results obtained from the BER analysis, and the symbols represent the simulation results. The theoretical results are in excellent agreement with the simulation results. Therefore, we give only theoretical results in the following figures. One can see that, different from the SIR comparisons in Section III, the Franks pulse does not display the best performance in BER comparisons. Instead, the BTRC pulse gives the smallest BER among the six pulses considered in this case. In particular, for $\varepsilon = 0.2$, the error floor occurs at a BER value of 2.6×10^{-3} in the case of the BTRC pulse, and at 4.5×10^{-3} in the case of the Franks pulse. In Fig. 6.4 where $\alpha = 1.0$, the BER comparison is consistent with the SIR comparison. In the case of $\varepsilon = 0.05$, the double-jump pulse has the worst BER performance, displaying an error rate floor at a BER of 6.1×10^{-4}.

It is found that the comparison based on the BER performance measure is not necessarily consistent with the comparison based on the SIR measure. The reason for that is in fading environments the BER is more related to the distribution of the ICI than to the long term average SIR. Note that the desired signal and the ICI component are not independent because they both experience channel fading gains which represent correlated channel responses at different subcarriers. Furthermore, the distribution of ICI will change with different window functions, roll-off factors, carrier frequency offsets, and channel conditions. These factors lead to the situation where the BER is not always consistent with the SIR. Observing the SIR comparisons in Fig. 6.1 and the BER comparisons in Figs. 6.3 - 6.4, one can find that, generally, if the SIR difference is small, it is difficult to predict whether one window function's BER performance is better or worse than another window function's BER performance based on the SIR comparison; however, if the SIR difference is significant, the BER comparison is consistent with the SIR comparison. On the other hand, one can readily verify that the BER comparison is always consistent with the SIR comparison for systems where the ICI component is Gaussian, and the ICI component is independent of the desired signal.

We also show the effect of different roll-off factors on the BER performance. Fig. 6.5 shows the BER performance of the system with the employment of BTRC windowing reception for $\alpha = 0.1, 0.2, 0.4, 0.6, 0.8$ and 1.0 in the case of $\varepsilon = 0.1$. As α increases, fewer samples are corrupted by ISI, and smaller BER can be achieved. However, this is not the case for the double-jump pulse. In Fig. 6.6 where the BER is plotted as a function of α in the case of $E_b/N_0 = 50$ dB and $\varepsilon = 0.1$, one can see that, for $\alpha > 0.1$, the BER will remain unchanged or become larger as α increases for the double-jump pulse. The reason for this is that although more samples are available to the receiver as α increases, the frequency domain side-lobe amplitude of the double-jump pulse will increase significantly at the same time, introducing more ICI. Also in this figure, one can observe that for $\alpha < 0.85$, the BTRC pulse gives the smallest BER, whereas for larger α, the Franks pulse or the SOCW pulse gives better BER performance. For the SOCW pulse, we choose a_1 as 0.4 and -0.5 for $\alpha \leq 0.5$ and $\alpha > 0.5$, respectively.

The theoretical BER expression can also be used to show the influence of the normalized mean time delay η on BER performance. In Fig. 6.7, we give the BER performance of a system with Franks windowing reception for $\alpha = 0.5$, $\varepsilon = 0.02$, and different mean delay spread values, $\eta = 0.01, 0.05, 0.1$, and 0.4. One can see the BER becomes worse when η increases, as expected. In particular, an increase of η from 0.01 to 0.1 will introduce about 2.4 dB performance loss in SNR at a BER of 10^{-4}.

6.5 Summary

An exact BER expression was derived for windowing reception OFDM systems operating over slowly Rayleigh fading channels in the presence of carrier frequency offset. The effects of several different Nyquist windows, including the BTRC window, the raised-cosine window, the SOCW window, the Franks window, the polynomial pulse, and the double-jump window, on the performance of the system was examined by the long term average SIR measure and the BER measure. It was found that the comparison based on the BER performance measure is not necessarily consistent with the comparison based on SIR measure. Hence window design based on minimizing ICI or maximizing SIR, may not give pulse designs with the best BER performance in fading environments. Pulse optimization according to BER is hard to conduct because of the complex BER expression. However, the proposed BER expression provides an exact BER performance prediction for the OFDM system with different ICI-reducing windowing. The BTRC windowing gives the smallest BER among the six windowing functions considered when the pulse roll-off factor is not large. However, the Franks windowing or SOCW windowing shows better BER performance when the roll-off factor approaches one.

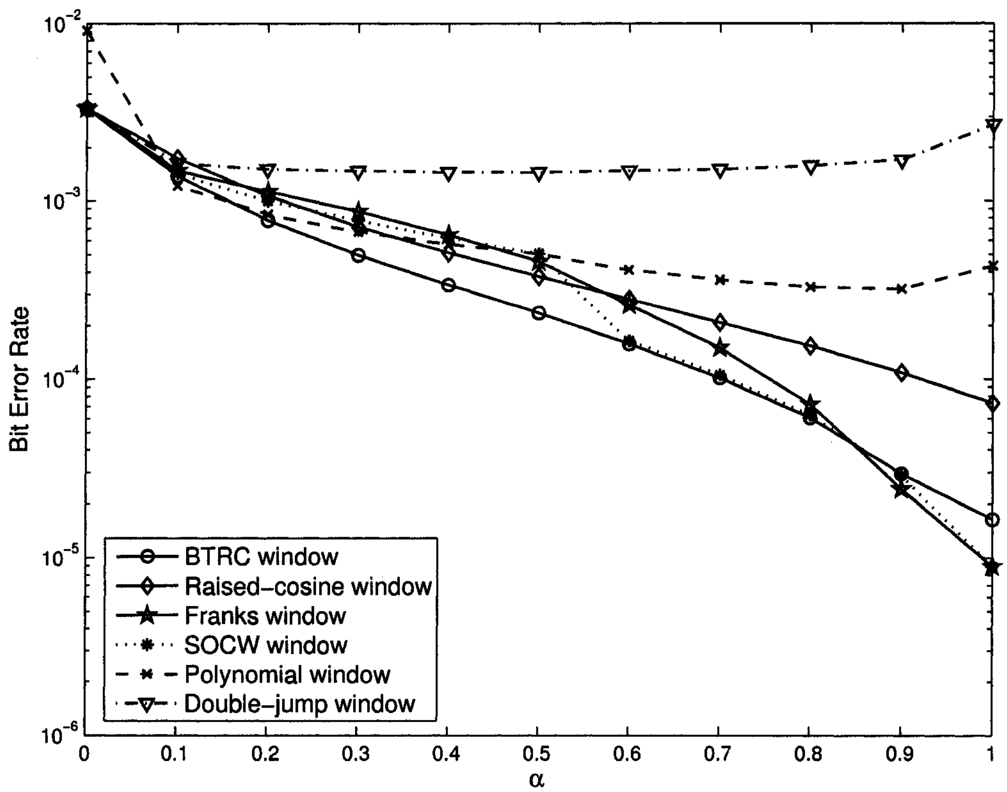

Fig. 6.6. The bit error rate as a function of roll-off factor α for 64-subcarrier QPSK-OFDM windowing reception with the employment of different window functions, $E_b/N_0 = 50$ dB, $\varepsilon = 0.1$.

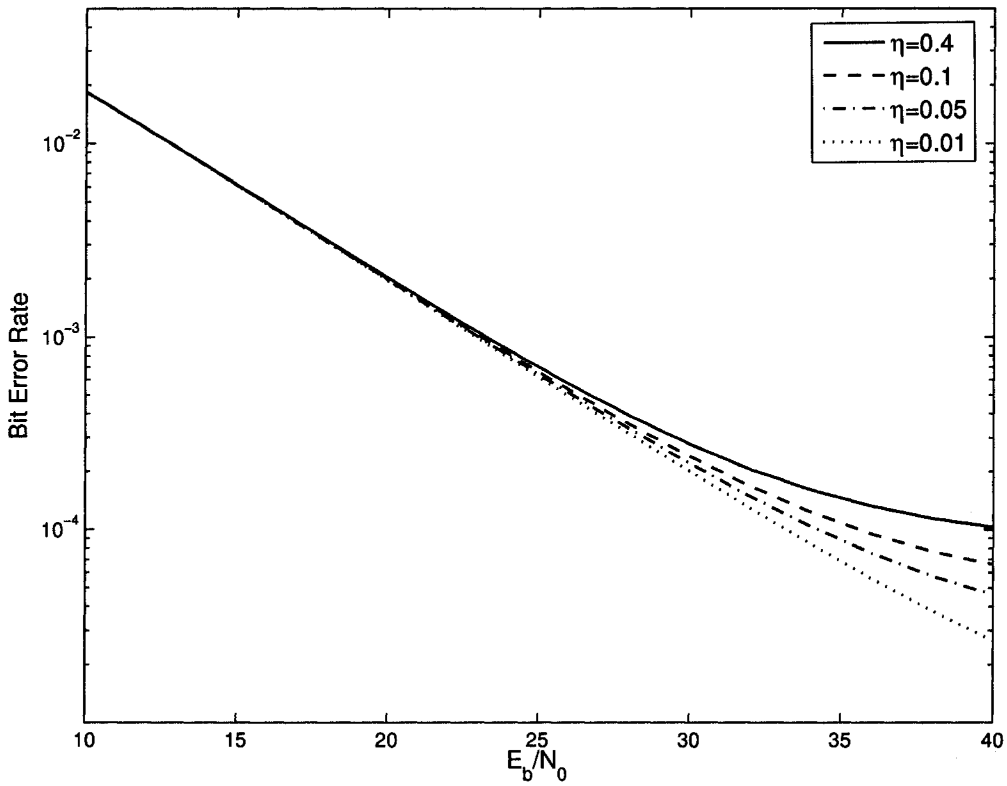

Fig. 6.7. The bit error rate in 64-subcarrier QPSK-OFDM receiver windowing with the employment of the Franks window functions, $\alpha = 0.5$, $\varepsilon = 0.02$, and $\eta = 0.01, 0.05, 0.1$ and 0.4.

Chapter 7

A DCT-Based OFDM Data Transmission Scheme

7.1 Introduction

Multicarrier modulation (MCM) is used not only in the physical layers of many wireless network standards, such as IEEE 802.11a, IEEE 802.16a, and HIPERLAN/2, but in wire-line digital communications systems, such as ADSL [8, 9, 102, 103]. All of these systems belong to the class of DFT-based MCM's. They employ the complex exponential functions set as orthogonal basis. In particular, in OFDM systems, digital modulations and demodulations can be realized with the IDFT and DFT, respectively [5]. Data obtained from general signaling (BPSK, M-ary PSK, and M-ary QAM, etc.) are first processed by an IDFT, or its fast algorithm, the IFFT; then the resulting complex samples are transmitted by in-phase and quadrature modulators [19]. The receiver performs a DFT, or its fast algorithm implementation, a FFT, to restore the original data.

However, the complex exponential functions set is not the only orthogonal basis that can be used to construct baseband multicarrier signals. A single set of cosinusoidal functions can be used as an orthogonal basis to implement the multicarrier modulation scheme and this scheme can be synthesized using a discrete cosine transform. Hence, we will denote the scheme as DCT-OFDM, and the conventional OFDM system as DFT-OFDM in this chapter. In particular, for one-dimensional (1-D) modulations (real-valued modulation formats), such as BPSK and pulse amplitude modulation (PAM), in the absence of a quadrature modulator, DCT-OFDM can completely avoid the IQ imbalance problem addressed in [104] inherent in conventional DFT-based OFDM systems. As far as fast implementation algorithms are concerned, the fast DCT algorithms proposed in [105] and [106] can provide fewer computational steps than FFT algorithms.

In the literature, reference [107] proposed using a DCT, rather than a DFT, to implement multicarrier modulation because of the bandwidth advantage a DCT-based system can achieve. Reference [108] proposed using a DCT to implement a coherent $\sqrt{M}$-ary amplitude shift keying OFDM system. A DCT implementation can also be employed in OFDM systems with two-dimensional (2-D) modulations (complex-valued modulation formats). In addition, carrier frequency offset, which was not considered in [108], will introduce ICI in both the DFT-OFDM system [27] and the DCT-OFDM system. Although the BER performance of the DFT-OFDM system with frequency offset in an AWGN channel has been discussed in reference [29], the effect of carrier frequency offset on the BER performance of DCT-OFDM systems has not been investigated.

Of concern is the fact that, as is the linear transformation modulation in [109], the subcarriers are not orthogonal without introduction of proper schemes after frequency-selective fading. In the case of frequency-selective slowly fading channels, different processing schemes for DCT-OFDM schemes have been investigated in several recent works. By using the circular convolution property of the DCT [110], reference [111] reported that by feeding a symmetrically extended data sequence into a DCT-OFDM system, in the case of static and exponentially decaying channel profiles, the throughput lower bound of the

DCT-based OFDM system is greater than that of the DFT-based OFDM system. On the other hand, [112] derived conditions required for the impulse response and input signal of a frequency-selective slowly fading channel to be diagonalizable by the DCT into parallel, decoupled, and memoryless subchannels. The conditions were then used to design a receiver to remove both intersymbol interference (ISI) [1] and ICI completely. In this work, we further consider the performance of DCT-OFDM in frequency-selective fast fading environments.

In this chapter we will first give an ICI analysis for a DCT-OFDM system operating in the presence of carrier frequency offset over AWGN channel. We show that DCT-OFDM gives smaller ICI power and greater SIR than DFT-OFDM in this case. We then derive exact expressions for the BER of DCT-OFDM systems with frequency offset in an AWGN channel, and compare the BER performance of the DCT-OFDM system with the conventional DFT-OFDM system by using the obtained BER performance expressions. Our results indicate that in the presence of carrier frequency offset, the BER performance of DCT-OFDM is superior to that of DFT-OFDM due to the energy compaction property [18] of the DCT; that is, the signal energy is concentrated in a few low-index DCT coefficients while the remaining coefficients are zero or are negligibly small. In this regard, reference [115] has shown that the DCT is close to optimal in terms of energy compaction capabilities.

Having shown the better BER performance of DCT-OFDM over the AWGN channel in the presence of carrier frequency offset, we further consider the BER performance of DCT-OFDM by simulation in frequency-selective fast Rayleigh fading environments where another kind of frequency offset, Doppler shift, exists. We propose using a zero-padding guard interval scheme in a DCT-OFDM system. The zero-padding scheme can not only eliminate ISI but also provide less penalty in terms of transmission efficiency than the scheme in [111]

[1] It is noted that two terms have been employed in the literature to represent inter-OFDM-symbol interference between successive OFDM symbols. Inter-block interference (IBI) was used in [112, 113], and ISI was used in [7, 20, 107, 109, 114]. We follow the latter usage, and call the inter-OFDM-symbol interference ISI in this chapter.

because it is not necessary to symmetrically extend the entire data sequence. Its application in DFT-OFDM has been reported in [113] where it was shown that the zero-padded (ZP) DFT-OFDM can achieve a better BER performance than cyclic prefix [6] DFT-OFDM. The performance of ZP-DCT-OFDM is then compared with ZP-DFT-OFDM by using simulation with the employment of two detection schemes including minimum mean-square error (MMSE) detection and MMSE decision feedback detection (DFD) with ordering. Some practical operation conditions including channel estimation, channel coding, and interleaving are considered in our simulations. The results show that the proposed ZP-DCT-OFDM system can achieve better BER performance than ZP-DFT-OFDM.

The remainder of this chapter is organized as follows. In Section 7.2, the system model is given. Then we introduce the ICI weighting coefficients for the DCT-OFDM system through ICI analysis in Section 7.3. The BER analysis for DCT-OFDM systems with different modulation formats in the presence of carrier frequency offset, performance comparisons with DFT-OFDM and some discussion are presented in Section 7.4. In Section 7.5, a ZP-DCT-OFDM is proposed. Its performance over frequency-selective fast Rayleigh fading channels is examined. Lastly, we summarize the chapter results in Section 7.6.

7.2 System Model

The DFT-based OFDM systems employ the complex exponential functions set

$$\sqrt{\frac{1}{T_u}}e^{j2\pi nF_\Delta t}, \quad 0 \le t < T_u, \quad n = 0, 1, \cdots, N-1 \tag{7.1}$$

as orthogonal basis. The minimum subcarrier frequency spacing F_Δ required to maintain the orthogonality of these functions in the sense

$$\int_0^{T_u} \sqrt{\frac{1}{T_u}}e^{j2\pi nF_\Delta t}\sqrt{\frac{1}{T_u}}e^{-j2\pi mF_\Delta t}\,dt = \begin{cases} 1, & n = m \\ 0, & n \neq m \end{cases} \tag{7.2}$$

is $1/T_u$ Hz, and T_u is the length of OFDM symbol without guard interval. Unlike conventional DFT-OFDM, a single cosinusoidal functions set $\cos(2\pi n F_\Delta t)$, $n = 0, \cdots, N-1$ will be used as orthogonal basis to implement multicarrier modulation in DCT-OFDM. The minimum F_Δ required to satisfy

$$\int_0^{T_u} \sqrt{\frac{2}{T_u}} \cos(2\pi k F_\Delta t) \sqrt{\frac{2}{T_u}} \cos(2\pi m F_\Delta t)\, dt = \begin{cases} 1, & k = m \\ 0, & k \neq m \end{cases} \tag{7.3}$$

is $1/2T_u$ Hz. The continuous-time representation of a baseband DCT-OFDM block $x(t)$ is

$$x(t) = \sqrt{\frac{2}{N}} \sum_{n=0}^{N-1} d_n \beta_n \cos\left(\frac{n\pi t}{T_u}\right) \tag{7.4}$$

where $d_0, d_1, \cdots, d_{N-1}$ are N independent data symbols obtained from a modulation constellation, and

$$\beta_n = \begin{cases} \frac{1}{\sqrt{2}}, & n = 0 \\ 1, & n = 1, 2, \cdots, N-1. \end{cases} \tag{7.5}$$

We will not consider ISI since it can be avoided by inserting a properly designed guard interval (see Section 7.5).

Fig. 7.1 gives a Welch spectrum estimation [18] for a 64-subcarrier DFT-OFDM baseband signal and a 64-subcarrier DCT-OFDM baseband signal, both with QPSK signaling. Although the subcarrier frequency spacing is $1/2T_u$ for DCT-OFDM, the bandwidth requirement of the DCT-OFDM system is the same as for the DFT-OFDM system with the same number of subcarriers because twice the channel bandwidth of the equivalent lowpass signal is required to transmit a passband DCT-OFDM signal. The frequency axis in this figure has been normalized with respect to $1/T_u$ Hz. The channel bandwidth of the bandpass signals of both systems is the same, that is, $64/T_u$ Hz. However, it is well worth noting that in DCT-OFDM systems, if the data symbols d_n are obtained by real-valued modulation formats, such as PAM and BPSK, the baseband DCT-OFDM signal $x(t)$ is still a real signal.

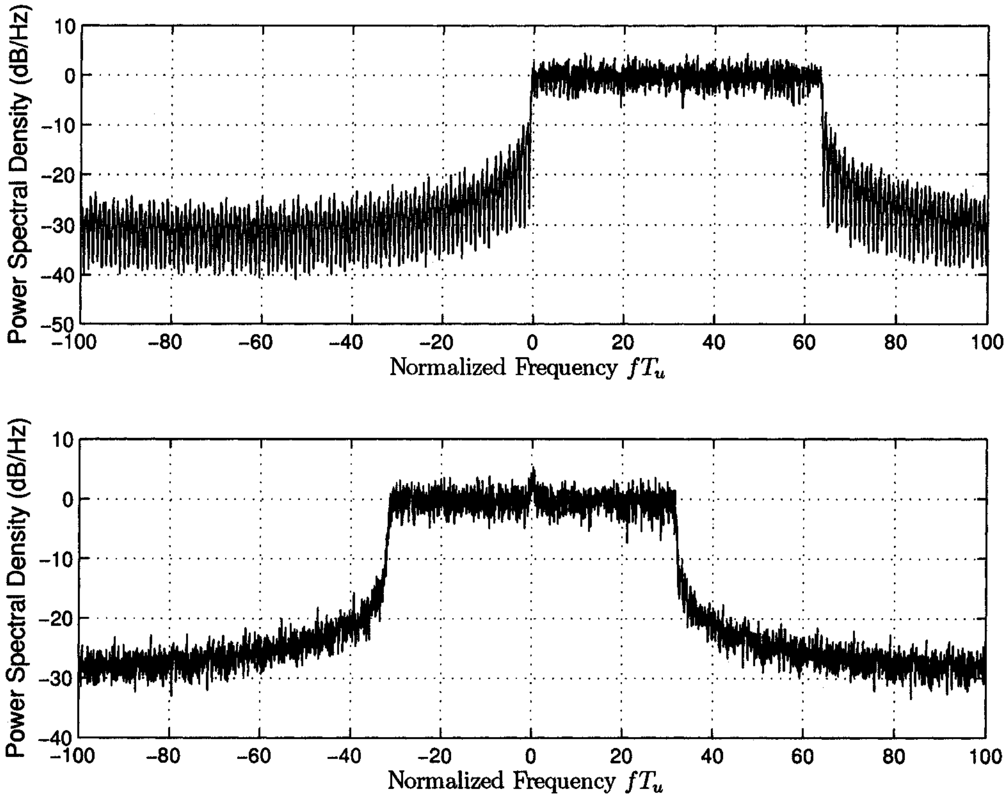

Fig. 7.1. The power spectral density of (a) a 64-subcarrier DFT-OFDM baseband signal and (b) a 64-subcarrier DCT-OFDM baseband signal.

Hence, single-sideband (SSB) transmission technology can be used to improve bandwidth efficiency as in [17]. Therefore, in this real-valued modulation case, the bandwidth of a DCT-OFDM system can be only half of the bandwidth required by a DFT-OFDM system with the same number of subcarriers. The SSB transmission technology can not be used if $x(t)$ is a complex-valued signal.

Sampling the continuous-time signal $x(t)$ at time instants $t_m = T_u(2m+1)/2N$ gives a discrete time sequence

$$x_m = \sqrt{\frac{2}{N}} \sum_{n=0}^{N-1} d_n \beta_n \cos\left(\frac{\pi n(2m+1)}{2N}\right), \quad m = 0, 1, \cdots, N-1 \tag{7.6}$$

which is the inverse discrete cosine transform (IDCT), referred to as IDCT-2 in [18]. Thus the continuous-time signal $x(t)$ can be obtained by first performing an IDCT operation on data sequence

$$\mathbf{d} = [d_0, d_1, \cdots, d_{N-1}]^{\mathrm{T}} \tag{7.7}$$

where $[\ ]^{\mathrm{T}}$ represents transpose operation, and then feeding serially the resulting samples $\mathbf{x} = [x_0, x_1, \cdots, x_{N-1}]^{\mathrm{T}}$ through a digital-to-analog (D/A) converter. At the receiver end, ignoring noise temporarily and under ideal channel conditions, the original signal d_n can be restored, by sampling the received signal and executing a discrete cosine transform (DCT), as

$$d_n = \sqrt{\frac{2}{N}} \beta_n \sum_{m=0}^{N-1} x_m \cos\left(\frac{\pi n(2m+1)}{2N}\right). \tag{7.8}$$

This process will be described in detail in Section 7.3.

The IDCT and DCT operations can also be represented in a matrix form which will be used in Section 7.5 to examine receivers in fading environments. The IDCT of the $N \times 1$ vector $\mathbf{d}$, and DCT of the $N \times 1$ vector $\mathbf{x}$ can be written as

$$\mathbf{x} = \mathbf{D}^{\mathrm{T}} \mathbf{d} \tag{7.9}$$

and

$$\mathbf{d} = \mathbf{D}\mathbf{x} \tag{7.10}$$

respectively, where the unitary $N \times N$ matrix $\mathbf{D}$ is the DCT matrix, and $\mathbf{D}^{\mathbb{T}}$ is the IDCT matrix. The rth ($0 \le r \le N-1$) row and cth ($0 \le c \le N-1$) column element $D(r,c)$ of the DCT matrix $\mathbf{D}$ is defined as

$$D(r,c) = \sqrt{\frac{2}{N}}\beta_r \cos\left(\frac{\pi r(2c+1)}{2N}\right). \tag{7.11}$$

7.3 Intercarrier Interference Analysis

We consider a DCT-OFDM system operating over AWGN channels in the presence of carrier frequency offset and phase error as described in Fig. 7.2 in this section and in Section 7.4 where the exact BER is evaluated.

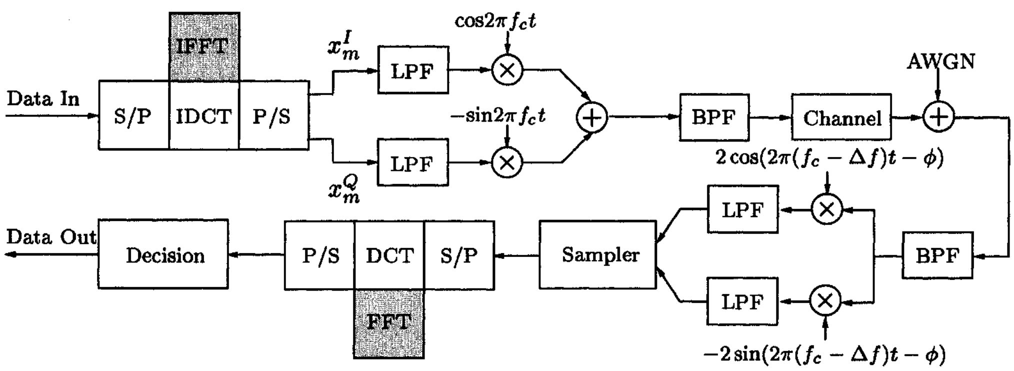

Fig. 7.2. The DCT-based orthogonal frequency-division multiplexing system.

Fig. 7.2 is a detailed block diagram for a DCT-OFDM system including in-phase and quadrature modulators in the presence of carrier frequency offset Δf and phase error ϕ. It becomes a DFT-OFDM system when the IDCT module and the DCT module are replaced with the IFFT module and the FFT module, respectively. Observe that, in a DCT-OFDM system, it is not necessary to use the quadrature modulator when one-dimensional signaling formats are used since the DCT is a real transform. However, when using DFT-OFDM, even for one-dimensional signaling formats, one must also include both the in-phase modulator and the quadrature modulator since, in general, the discrete Fourier transform gives complex sequences even if the signal is real.

In Fig. 7.2, a length N sequence including in-phase components x_m^I and quadrature components x_m^Q is obtained after the IDCT as

$$x_m^I + jx_m^Q = \sqrt{\frac{2}{N}} \sum_{n=0}^{N-1} (d_n^I + jd_n^Q)\beta_n \cos\left(\frac{\pi n(2m+1)}{2N}\right) \tag{7.12}$$

where d_n^I and d_n^Q are obtained from general modulation schemes, such as BPSK, QPSK, and QAM. Then the in-phase and quadrature components are serially fed into the in-phase and quadrature modulators, respectively. Hence the real part $x_b^I(t)$ and the imaginary part $x_b^Q(t)$ of one baseband DCT-OFDM signal frame can be written as

$$x_b^I(t) = \sum_{m=0}^{N-1} x_m^I f\left(t - \frac{(2m+1)T_u}{2N}\right) \tag{7.13a}$$

and

$$x_b^Q(t) = \sum_{m=0}^{N-1} x_m^Q f\left(t - \frac{(2m+1)T_u}{2N}\right) \tag{7.13b}$$

respectively, where $f(t)$ is the lowpass reconstruction filter which performs digital-to-analog (D/A) conversion. Consequently one block of the transmitted bandpass signal is

$$x(t) = \Re\left\{\left[x_b^I(t) + jx_b^Q(t)\right] e^{j2\pi f_c t}\right\} \tag{7.14}$$

where $\Re\{\gamma\}$ denotes the real part of γ. In an AWGN channel, the received in-phase signal $r^I(t)$ and quadrature signal $r^Q(t)$ in the presence of carrier frequency offset Δf and phase error ϕ after demodulation can be expressed as

$$\begin{aligned} r^I(t) = \sum_{m=0}^{N-1} \Bigg[& x_m^I q\left(t - \frac{(2m+1)T_u}{2N}\right) \cos(2\pi\Delta f t + \phi) \\ & - x_m^Q q - x_m^Q q\left(t - \frac{(2m+1)T_u}{2N}\right) \sin(2\pi\Delta f t + \phi)\Bigg] + w_i(t) \end{aligned} \tag{7.15a}$$

and

$$r^Q(t) = \sum_{m=0}^{N-1} \left[x_m^I q\left(t - \frac{(2m+1)T_u}{2N}\right) \sin(2\pi\Delta f t + \phi) + x_m^Q q\left(t - \frac{(2m+1)T_u}{2N}\right) \cos(2\pi\Delta f t + \phi) \right] + w_q(t) \tag{7.15b}$$

respectively. Here, $w_i(t)$ and $w_q(t)$ are each Gaussian noise with mean zero and variance $\sigma^2 = N_0/2$, and $q(t)$ is the cascade of the transmit filter and the receiver filter, satisfying the Nyquist theorem [17]; that is,

$$q\left(\frac{nT_u}{N}\right) = \begin{cases} 1, & n = 0 \\ 0, & \text{otherwise.} \end{cases} \tag{7.16}$$

The discrete samples r_k^I and r_k^Q can be obtained by sampling at instants $(2k+1)T_u/2N, k = 0, 1, \cdots, N-1$. To express them in a complex format, one has

$$\begin{aligned} \tilde{r}_k &= r_k^I + jr_k^Q + w_k^I + jw_k^Q \\ &= (x_k^I + jx_k^Q)e^{j\left[\frac{2\pi\Delta f T_u(2k+1)}{2N} + \phi\right]} + \tilde{w}_k \end{aligned} \tag{7.17}$$

where $\tilde{w}_k = w_k^I + jw_k^Q$ are complex Gaussian random variables. At the receiver, the DCT processing gives the decision variable d_k for the sampled signal in the kth subcarrier as

$$\begin{aligned} \hat{d}_k &= \hat{d}_k^I + j\hat{d}_k^Q \\ &= \left(d_k^I + jd_k^Q\right)\left(S_{k,k}^I + jS_{k,k}^Q\right) + \sum_{\substack{n=0 \\ n\neq k}}^{N-1} \left(d_n^I + jd_n^Q\right)\left(S_{n,k}^I + jS_{n,k}^Q\right) + \tilde{w}_k \end{aligned} \tag{7.18a}$$

where

$$S_{n,k}^I = \frac{1}{2N}\beta_k\beta_n[\Psi(n+k-\varepsilon) + \Psi(n-k-\varepsilon) + \Phi(n+k+\varepsilon) + \Phi(n-k+\varepsilon)] \tag{7.18b}$$

$$S_{n,k}^Q = \frac{1}{2N}\beta_k\beta_n[\Gamma(n+k-\varepsilon) + \Gamma(n-k-\varepsilon) + \Lambda(n+k+\varepsilon) + \Lambda(n-k+\varepsilon)] \tag{7.18c}$$

$$\Psi(x) = \frac{\sin\left(\frac{\pi x}{2}\right)\cos\left(\phi - \frac{\pi x}{2}\right)}{\sin\left(\frac{\pi x}{2N}\right)} \tag{7.18d}$$

$$\Phi(x) = \frac{\sin\left(\frac{\pi x}{2}\right)\cos\left(\phi + \frac{\pi x}{2}\right)}{\sin\left(\frac{\pi x}{2N}\right)} \tag{7.18e}$$

$$\Gamma(x) = \frac{\sin\left(\frac{\pi x}{2}\right)\sin\left(\phi - \frac{\pi x}{2}\right)}{\sin\left(\frac{\pi x}{2N}\right)} \tag{7.18f}$$

$$\Lambda(x) = \frac{\sin\left(\frac{\pi x}{2}\right)\sin\left(\phi + \frac{\pi x}{2}\right)}{\sin\left(\frac{\pi x}{2N}\right)} \tag{7.18g}$$

$$\Psi(0) = \Phi(0) = N\cos\phi \tag{7.18h}$$

$$\Gamma(0) = \Lambda(0) = N\sin\phi \tag{7.18i}$$

and $\varepsilon = 2T_u\Delta f$. Recalling that in DCT-OFDM the subcarrier frequency spacing is $1/2T_u$ Hz, ε is the normalized frequency offset with respect to the subcarrier frequency spacing.

When the normalized carrier frequency offset $\varepsilon = 0$ in (7.18) one has

$$S^I_{n,k} = S^Q_{n,k} = 0, \quad n \neq k \tag{7.19}$$

$$S^I_{k,k} = \cos\phi \ , \ S^Q_{k,k} = \sin\phi \tag{7.20}$$

Therefore, the decision variable $\hat{d}_k$ can be written as

$$\hat{d}_k = (d^I_k + jd^Q_k)e^{j\phi} + \tilde{w}_k. \tag{7.21}$$

In the presence of a fixed phase error ϕ only, the decision variable is a phase rotated version of the transmitted signal, and there is no ICI. Thus a DCT-OFDM system and a DFT-OFDM system have the same BER performance when there is only phase error and no carrier frequency offset. We will consider carrier frequency offset only in the following developments.

Similar to the sequence of ICI coefficients $S_{n,k} = S^I_{n,k} + jS^Q_{n,k}$ in DCT-OFDM, there is a sequence of ICI coefficients for N-subcarrier DFT-OFDM in the presence of normalized frequency offset $\xi = \Delta f T_u$. It was derived as

$$F_n = \frac{\sin\pi(n+\xi)}{N\sin\frac{\pi(n+\xi)}{N}} e^{\frac{j\pi(N-1)(n+\xi)}{N}} \tag{7.22}$$

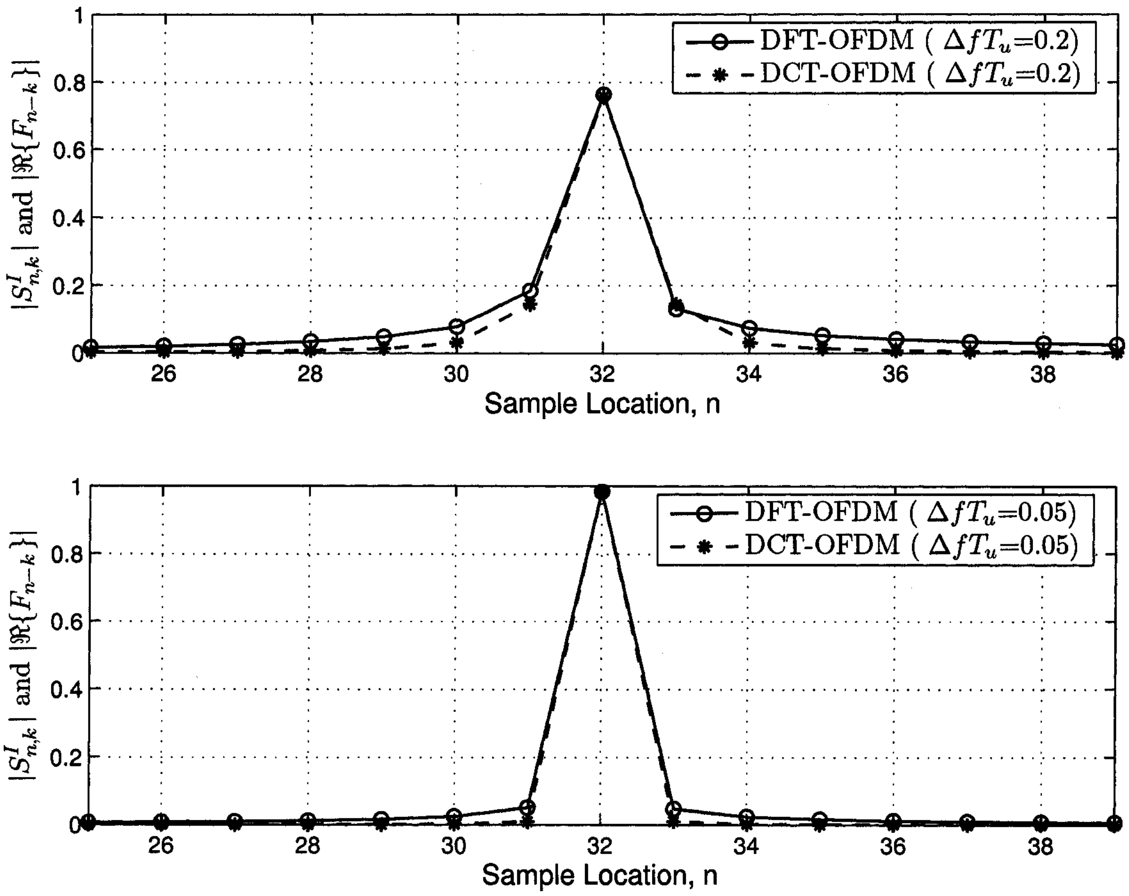

Fig. 7.3. The ICI weighting coefficients $|S^I_{n,k}|$ in a 64-subcarrier BPSK DCT-OFDM system and $|\Re\{F_{n-k}\}|$ in a 64-subcarrier BPSK DFT-OFDM system (a) $\Delta f T_u = 0.2$, (b) $\Delta f T_u = 0.05$, and $k = 32$.

in references [29] and [72, 73, 114]. The corresponding decision variable $\hat{u}_k$ is given as

$$\hat{u}_k = u_k F_0 + \sum_{\substack{n=0 \\ n \neq k}}^{N-1} u_n F_{n-k} + \tilde{w}_k, k = 0, 1, \cdots, N-1 \tag{7.23}$$

where u_k is the data symbol for the kth subcarrier.

We take BPSK as an example to investigate the previously mentioned energy compaction property of DCT-OFDM. In the case of BPSK, because there is not a quadrature branch for DCT-OFDM, the decision statistic in eq. (7.18a) reduces to

$$\hat{d}_k = d_k^I S_{k,k}^I + \sum_{\substack{n=0 \\ n \neq k}}^{N-1} d_n^I S_{n,k}^I + w_k^I. \tag{7.24}$$

Similarly, in DFT-OFDM, if $\{u_n\}_{n=0}^{N-1}$ are binary BPSK symbols, the corresponding decision statistic $\hat{u}_k$ is given as

$$\hat{u}_k = u_k \Re\{F_0\} + \sum_{\substack{n=0 \\ n \neq k}}^{N-1} u_n \Re\{F_{n-k}\} + w_k^I. \tag{7.25}$$

Assuming that the desired sample location is $k = 32$ in a 64-subcarrier OFDM system, the DCT-OFDM ICI weighting coefficients $|S_{n,k}^I|$ and the DFT ICI weighting coefficients $|\Re\{F_{n-k}\}|$ in the presence of normalized frequency offset $\Delta f T_u = 0.2$ and 0.05 are presented in Fig. 7.3 (a) and (b), respectively. To highlight the difference between these two sequences of ICI weighting coefficients, we show the coefficients of subcarrier index from 25 to 39. The remaining coefficients are sufficiently small to be ignored, and are not plotted in this figure. One observes in these two figures that the sequences of ICI coefficients tend to the shifted unit sample sequence $\delta[n-32]$ when the frequency offset Δf is close to 0. Here, the unit sample sequence $\delta[n]$ is defined as [18]

$$\delta[n] = \begin{cases} 0, & n \neq 0 \\ 1, & n = 0. \end{cases} \tag{7.26}$$

One can also see that the ICI weighting coefficients of DCT-OFDM are more highly concentrated near sample location 32 than the ICI coefficients of DFT-OFDM for the same value of $\Delta f T$. This is expected. In DFT-OFDM, ICI is introduced after the DFT operation at the receiver [29, 72, 73, 114]. Similarly, one can see from eq. (7.18a) that ICI is introduced after performing the DCT operation in a DCT-OFDM receiver. However, because of the energy compaction property of the DCT (this is explained in [18, 115]), the DCT operation distributes more energy to the desired signal and less energy to the ICI than the DFT operation. Therefore, the desired sample suffers less ICI coming from neighboring samples in DCT-OFDM than in DFT-OFDM.

One can also consider the signal-to-interference ratio (SIR) defined as

$$SIR_{DCT}^{k} = \frac{(S_{k,k}^{I})^2}{\sum_{\substack{n=0 \\ n \neq k}}^{N-1} (S_{n,k}^{I})^2} \tag{7.27}$$

and

$$SIR_{DFT}^{k} = \frac{(\Re\{F_0\})^2}{\sum_{\substack{n=0 \\ n \neq k}}^{N-1} (\Re\{F_{n-k}\})^2} \tag{7.28}$$

for DCT-OFDM and DFT-OFDM, respectively. Fig. 7.4 compares the SIR of a 64-subcarrier DCT-OFDM system and a 64-subcarrier DFT-OFDM system. One can see that the superiority of DCT-OFDM exists when $\Delta f T_u < 0.25$. The reason for that is the energy compaction property of the DCT holds for small frequency offset values.

The ICI and SIR analysis suggest that the desired sample suffers less intercarrier interference coming from neighboring samples in DCT-OFDM than in DFT-OFDM. The reduced interference will lead to better BER performance which can be observed from the exact BER expressions and simulation results in the following sections.

7.4 Exact BER Analysis on AWGN Channels

In this section, the exact BER performance of a DCT-OFDM system in the presence of frequency offset is evaluated by using the characteristic function method. The analysis is restricted to BPSK, QPSK, and 16-QAM, but our method can be used for other modulation formats.

7.4.1 QPSK modulation

In QPSK signaling, $d_k = d_k^I + j d_k^Q$ is a complex symbol in which d_k^I and d_k^Q are chosen from the set $\{-\sqrt{E_b}, \sqrt{E_b}\}$ independently. For the Gray-coded QPSK constellation, which

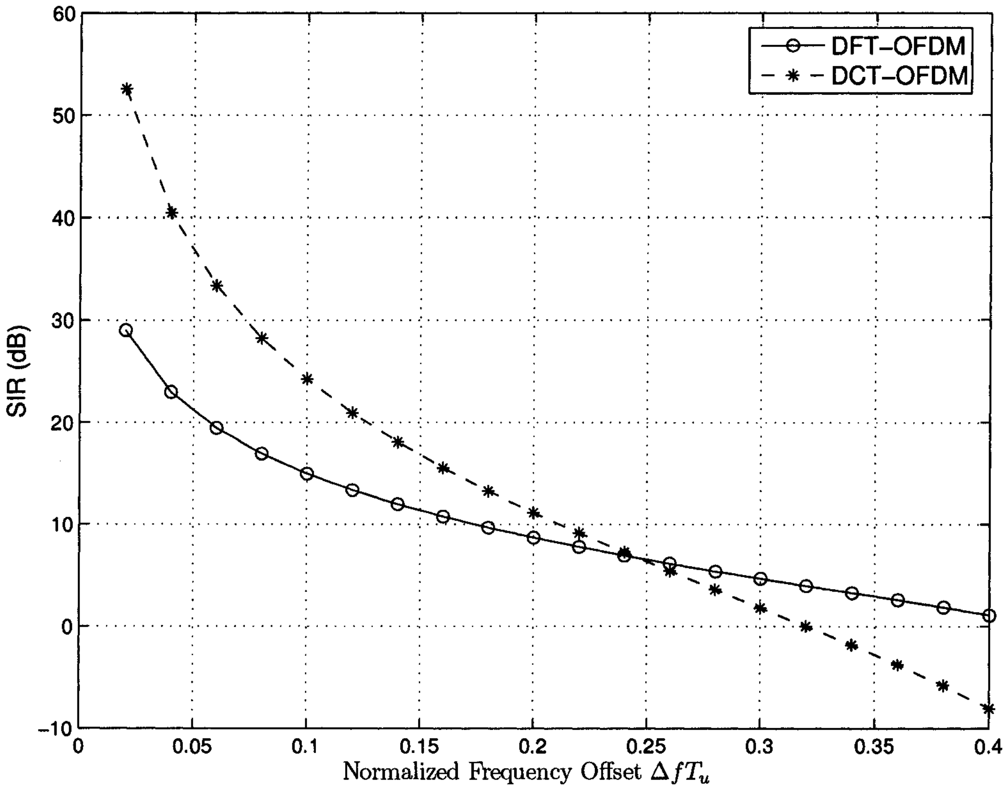

Fig. 7.4. The SIR of the DCT-OFDM system and the DFT-OFDM system as a function of the normalized carrier frequency offset.

is employed, for example, in the IEEE 802.11a standard and the IEEE 802.16a standard, the receiver can give the bit decision from the in-phase component $\hat{d}_k^I$ and quadrature component $\hat{d}_k^Q$ in (7.18a) independently; that is,

$$\begin{aligned}
&\text{if} \quad \hat{d}_k^I \geq 0, \quad \text{then} \quad i1 = 0 \\
&\text{if} \quad \hat{d}_k^I < 0, \quad \text{then} \quad i1 = 1 \\
&\text{if} \quad \hat{d}_k^Q \geq 0, \quad \text{then} \quad q1 = 0 \\
&\text{if} \quad \hat{d}_k^Q < 0, \quad \text{then} \quad q1 = 1
\end{aligned}$$

where $i1$ and $q1$ are two bits in one QPSK symbol.

To evaluate the $i1$ bit error probability, we first derive the characteristic function of $\hat{d}_k^I$ conditioned on d_k and Δf. From eq. (7.18a),

$$\hat{d}_k^I = d_k^I S_{k,k}^I - d_k^Q S_{k,k}^Q + \sum_{\substack{n \neq k \\ n=0}}^{N-1} \left(d_n^I S_{n,k}^I - d_n^Q S_{n,k}^Q \right) + w_k^I. \tag{7.29}$$

Since the data symbols are independent, the characteristic function of this sum can be written as the product of the characteristic function of each term, that is

$$\begin{aligned}
\Phi_k(\omega | d_k, \Delta f) &= \mathbf{E}\left[e^{j\omega \hat{d}_k^I}\right] = e^{j\omega\left(d_k^I S_{k,k}^I - d_k^Q S_{k,k}^Q\right) - \frac{1}{2}\omega^2\sigma^2} \prod_{\substack{n \neq k \\ n=0}}^{N-1} \mathbf{E}\left[e^{j\omega d_n^I S_{n,k}^I}\right] \mathbf{E}\left[e^{-j\omega d_n^Q S_{n,k}^Q}\right] \\
&= e^{j\omega\left(d_k^I S_{k,k}^I - d_k^Q S_{k,k}^Q\right) - \frac{1}{2}\omega^2\sigma^2} \prod_{\substack{n \neq k \\ n=0}}^{N-1} \cos(\omega\sqrt{E_b} S_{n,k}^I) \cos(\omega\sqrt{E_b} S_{n,k}^Q). \qquad (7.30)
\end{aligned}$$

The $i1$ bit error probability for the kth subcarrier can then be written as

$$\begin{aligned}
P_{i1}(k) = &\frac{1}{4}\text{Prob}\left\{\hat{d}_k^I < 0 \mid d_k = \sqrt{E_b} + j\sqrt{E_b}, \Delta f\right\} \\
&+ \frac{1}{4}\text{Prob}\left\{\hat{d}_k^I < 0 \mid d_k = \sqrt{E_b} - j\sqrt{E_b}, \Delta f\right\} \\
&+ \frac{1}{4}\text{Prob}\left\{\hat{d}_k^I \geq 0 \mid d_k = -\sqrt{E_b} + j\sqrt{E_b}, \Delta f\right\} \\
&+ \frac{1}{4}\text{Prob}\left\{\hat{d}_k^I \geq 0 \mid d_k = -\sqrt{E_b} - j\sqrt{E_b}, \Delta f\right\} \\
= &\frac{1}{2}\text{Prob}\left\{\hat{d}_k^I < 0 \mid d_k = \sqrt{E_b} + j\sqrt{E_b}, \Delta f\right\}
\end{aligned}$$

$$+\frac{1}{2}\text{Prob}\left\{\hat{d}_k^I < 0 \mid d_k = \sqrt{E_b} - j\sqrt{E_b}, \Delta f\right\} \tag{7.31a}$$

$$= \frac{1}{2}F_{\hat{d}_k^I}\left(0 \mid d_k = \sqrt{E_b} + j\sqrt{E_b}, \Delta f\right) + \frac{1}{2}F_{\hat{d}_k^I}\left(0 \mid d_k = \sqrt{E_b} - j\sqrt{E_b}, \Delta f\right) \tag{7.31b}$$

$$= \frac{1}{2} - \int_0^{+\infty} \sin(\omega\sqrt{E_b}S_{k,k}^I)\cos(\omega\sqrt{E_b}S_{k,k}^Q)\gamma(\omega)\, d\omega \tag{7.31c}$$

where

$$\gamma(\omega) = \frac{e^{-\frac{1}{2}\omega^2\sigma^2}}{\pi\omega}\prod_{\substack{n\neq k\\ n=0}}^{N-1}\cos(\omega\sqrt{E_b}S_{n,k}^I)\cos(\omega\sqrt{E_b}S_{n,k}^Q). \tag{7.31d}$$

The derivations from eq. (7.31a) to (7.31c) are obtained based on eq. (2.36). According to symmetry, the $i1$ bit and the $q1$ bit have the same BER, hence the BER for the kth subcarrier is

$$P_{b,QPSK}(k) = \frac{1}{2}P_{i1}(k) + \frac{1}{2}P_{q1}(k) = P_{i1}(k). \tag{7.31e}$$

Note that the BER is a function of the subcarrier index, k. This is because the ICI is a function of the subcarrier index. The average bit error rate is

$$P_{b,QPSK} = \frac{1}{N}\sum_{k=0}^{N-1} P_{b,QPSK}(k). \tag{7.32}$$

By removing the terms including $S_{n,k}^Q$ in eq. (7.31), one can obtain the BER in the case of BPSK modulation, as

$$P_{b,BPSK}(k) = \frac{1}{2} - \int_0^{+\infty} \frac{\sin(\sqrt{E_b}\omega S_{k,k}^I)}{\pi\omega} e^{-\frac{1}{2}\omega^2\sigma^2}\prod_{\substack{n\neq k\\ n=0}}^{N-1}\cos(\sqrt{E_b}\omega S_{n,k}^I)\, d\omega. \tag{7.33}$$

7.4.2 16-ary QAM

In 16-QAM signaling, $d_k = d_k^I + jd_k^Q, k = 0, \cdots, N-1$ is a complex symbol in which d_k^I and d_k^Q are chosen from the set $\{-3d, -d, d, 3d\}$ independently. To derive the BER, we divide the four bits $i1$ $i2$ $q1$ $q2$ in one 16-QAM symbol into two groups [69], in-phase bits $(i1, i2)$ and quadrature bits $(q1, q2)$. The decision on the in-phase bits is determined only by the real part of the received signal $\hat{d}_k$ in (7.18a). The imaginary part of $\hat{d}_k$ determines the decision of the quadrature bits $q1$ and $q2$. The decision rules for the in-phase bits can be summarized as follows:

$$\text{if} \quad \hat{d}_k^I \geq 0, \quad \text{then} \quad i1 = 0$$

$$\text{if} \quad \hat{d}_k^I < 0, \quad \text{then} \quad i1 = 1$$

$$\text{if} \quad \hat{d}_k^I \geq 2d \quad \text{or} \quad \hat{d}_k^I < -2d, \quad \text{then} \quad i2 = 1$$

$$\text{if} \quad -2d \leq \hat{d}_k^I < 2d, \quad \text{then} \quad i2 = 0.$$

There are similar decision rules for the quadrature bits $q1$ and $q2$. The conditional characteristic function of $\hat{d}_k^I$ is

$$\Phi_k^I(\omega|d_k,\Delta f) = e^{j\omega(d_k^I S_{k,k}^I - d_k^Q S_{k,k}^Q) - \frac{1}{2}\omega^2\sigma^2} \times \prod_{\substack{n \neq k \\ n=0}}^{N-1} \cos(2\omega d S_{n,k}^I)\cos(\omega d S_{n,k}^I)\cos(2\omega d S_{n,k}^Q)\cos(\omega d S_{n,k}^Q). \tag{7.34}$$

The $i1$ bit error probability can thus be written as

$$\begin{aligned}
P_{i1}(k) &= \frac{1}{16}\sum_{r=1}^{4}\Big(\text{Prob}\left\{\hat{d}_k^I < 0 \mid d_k = d + j(2r-5)d, \Delta f\right\} \\
&\quad + \text{Prob}\left\{\hat{d}_k^I < 0 \mid d_k = 3d + j(2r-5)d, \Delta f\right\} \\
&\quad + \text{Prob}\left\{\hat{d}_k^I \geq 0 \mid d_k = -d + j(2r-5)d, \Delta f\right\} \\
&\quad + \text{Prob}\left\{\hat{d}_k^I \geq 0 \mid d_k = -3d + j(2r-5)d, \Delta f\right\}\Big) \\
&= \frac{1}{8}\sum_{r=1}^{4}\Big(\text{Prob}\left\{\hat{d}_k^I < 0 \mid d_k = d + j(2r-5)d, \Delta f\right\} \\
&\quad + \text{Prob}\left\{\hat{d}_k^I < 0 \mid d_k = 3d + j(2r-5)d, \Delta f\right\}\Big) \\
&= \frac{1}{8}\sum_{r=1}^{4}\left[F_{\hat{d}_k^I}(0 \mid d_k = d + j(2r-5)d, \Delta f) + F_{\hat{d}_k^I}(0 \mid d_k = 3d + j(2r-5)d, \Delta f)\right] \\
&= \frac{1}{2} - \int_0^{+\infty} \cos(2\omega d S_{k,k}^Q)\cos(\omega d S_{k,k}^Q)\sin(2\omega d S_{k,k}^I)\cos(\omega d S_{k,k}^I)\beta(\omega)\,d\omega
\end{aligned} \tag{7.35a}$$

where

$$\beta(\omega) = \frac{e^{-\frac{1}{2}\omega^2\sigma^2}}{\pi\omega} \prod_{\substack{n\neq k\\ n=0}}^{N-1} \cos(2\omega d S^I_{n,k}) \cos(\omega d S^I_{n,k}) \cos(2\omega d S^Q_{n,k}) \cos(\omega d S^Q_{n,k}). \tag{7.35b}$$

For $i2$ bit, the error probability is

$$\begin{aligned}
P_{i2}(k) = \frac{1}{16}\sum_{r=1}^{4} \Big(&\mathrm{Prob}\left\{\hat{d}^I_k \geq 2d \text{ or } \hat{d}^I_k < -2d \mid d_k = d + j(2r-5)d, \Delta f\right\} \\
&+ \mathrm{Prob}\left\{\hat{d}^I_k \geq 2d \text{ or } \hat{d}^I_k < -2d \mid d_k = -d + j(2r-5)d, \Delta f\right\} \\
&+ \mathrm{Prob}\left\{-2d \leq \hat{d}^I_k < 2d \mid d_k = 3d + j(2r-5)d, \Delta f\right\} \\
&+ \mathrm{Prob}\left\{-2d \leq \hat{d}^I_k < 2d \mid d_k = -3d + j(2r-5)d, \Delta f\right\} \Big) \\
= \frac{1}{8}\sum_{r=1}^{4} \Big(&\mathrm{Prob}\left\{\hat{d}^I_k \geq 2d \text{ or } \hat{d}^I_k < -2d \mid d_k = d + j(2r-5)d, \Delta f\right\} \\
&+ \mathrm{Prob}\left\{-2d \leq \hat{d}^I_k < 2d \mid d_k = 3d + j(2r-5)d, \Delta f\right\} \Big) \\
= \frac{1}{8}\sum_{r=1}^{4} \Big(&1 - \mathrm{Prob}\left\{-2d \leq \hat{d}^I_k < 2d \mid d_k = d + j(2r-5)d, \Delta f\right\} \\
&+ \mathrm{Prob}\left\{-2d \leq \hat{d}^I_k < 2d \mid d_k = 3d + j(2r-5)d, \Delta f\right\} \Big) \\
= \frac{1}{8}\sum_{r=1}^{4} \Big[&1 - F_{\hat{d}^I_k}(2d \mid d_k = d + j(2r-5)d, \Delta f) + F_{\hat{d}^I_k}(-2d \mid d_k = d + j(2r-5)d, \Delta f) \\
&+ F_{\hat{d}^I_k}(2d \mid d_k = 3d + j(2r-5)d, \Delta f) - F_{\hat{d}^I_k}(-2d \mid d_k = 3d + j(2r-5)d, \Delta f) \Big] \\
= \frac{1}{2} - \int_0^{+\infty} &2\sin(2\omega d)\sin(2\omega d S^I_{k,k})\sin(\omega d S^I_{k,k})\cos(2\omega d S^Q_{k,k})\cos(\omega d S^Q_{k,k})\beta(\omega)\,d\omega
\end{aligned} \tag{7.35c}$$

It is noted that the $i1$ bit has the same BER as the $q1$ bit, and the $i2$ bit has the same BER as the $q2$ bit. Therefore, the average BER can be given as

$$P_{b,16QAM} = \frac{1}{2N}\sum_{k=0}^{N-1}\left[P_{i1}(k) + P_{i2}(k)\right]. \tag{7.35d}$$

Replacing ICI coefficients $S^I_{n,k}$ with $\Re\{F_{n-k}\}$ and $S^Q_{n,k}$ with $\Im\{F_{n-k}\}$ in eqs. (7.33), (7.31) and (7.35) gives the BER's of the kth subcarrier for DFT-OFDM with subcarrier modulation

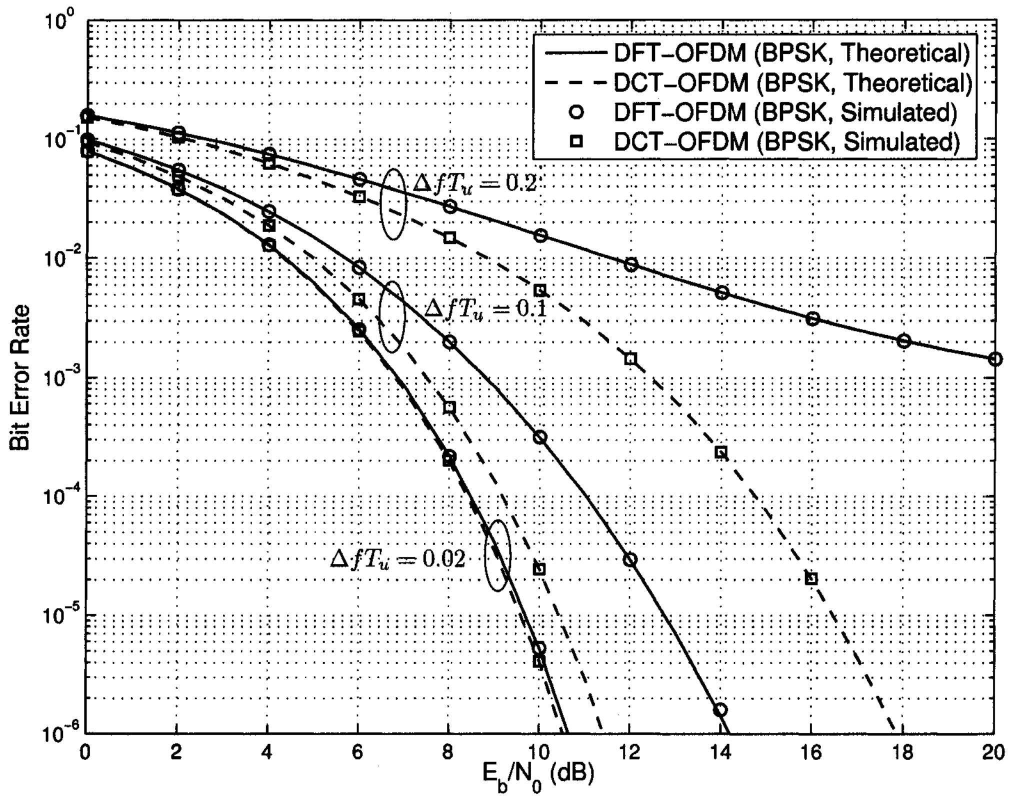

Fig. 7.5. The BER performances of 64-subcarrier DCT-OFDM with BPSK modulation and 64-subcarrier DFT-OFDM with BPSK modulation in the presence of normalized frequency offset $\Delta f T_u = 0.02, 0.1$ and 0.2.

formats BPSK, QPSK and 16-QAM, respectively.

7.4.3 Numerical Results

In this section, we will compare the performances of a 64-subcarrier DFT-OFDM system and a 64-subcarrier DCT-OFDM system using the exact BER analysis results obtained in the preceding section. Monte Carlo simulation results are also shown to substantiate the results. To ensure the reliability of the computer simulation, 10^6 OFDM frames are generated to obtain each BER value in Figs. 7.5 - 7.7. Importance sampling [116] is used to reduce the variance of the simulation estimates.

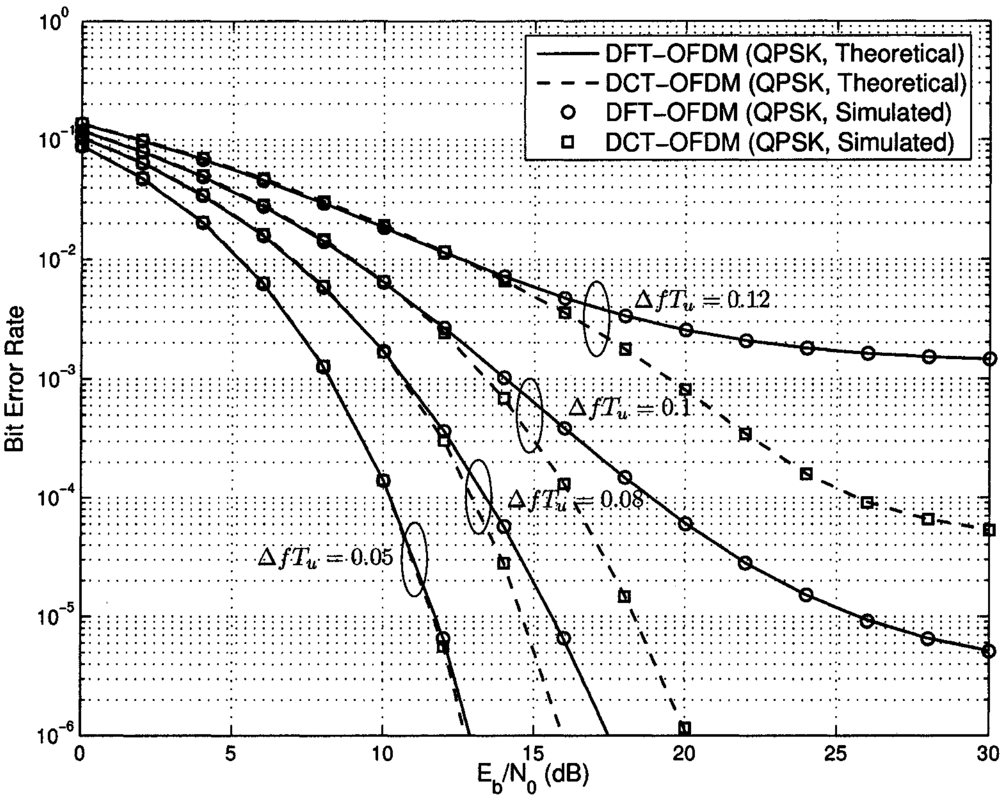

Fig. 7.6. The BER performances of 64-subcarrier DCT-OFDM with QPSK modulation and 64-subcarrier DFT-OFDM with QPSK modulation in the presence of normalized frequency offset $\Delta f T_u = 0.05, 0.08, 0.1$ and 0.12.

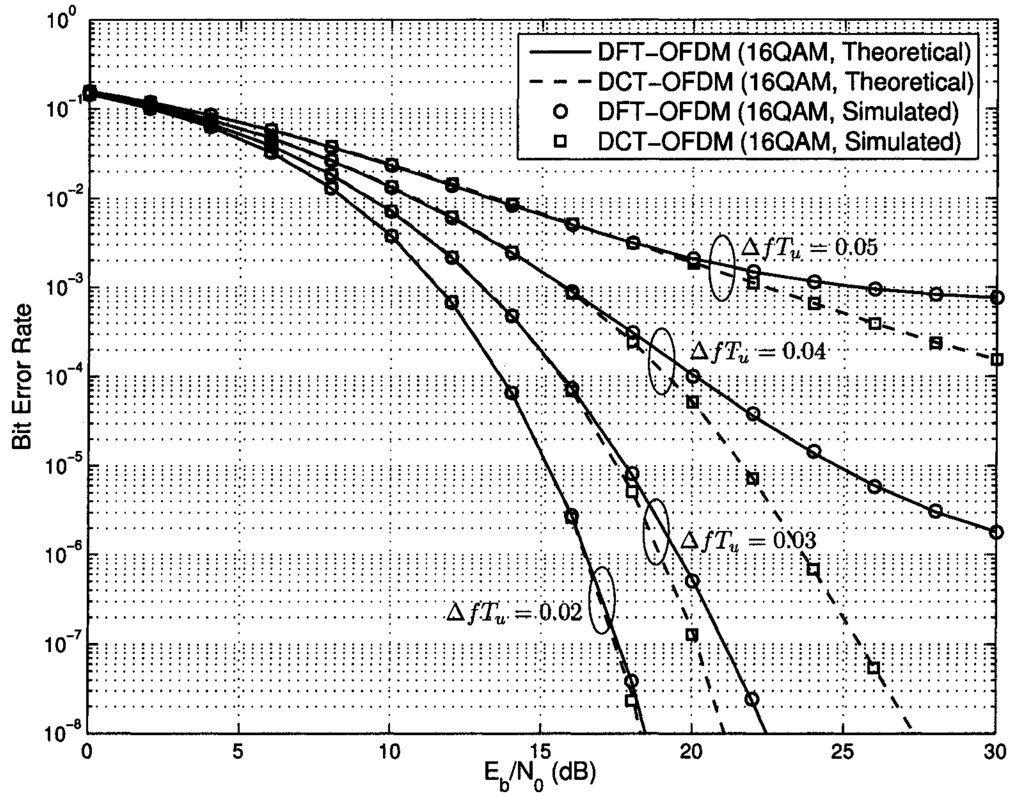

Fig. 7.7. The BER performances of 64-subcarrier DCT-OFDM with 16-QAM signaling and 64-subcarrier DFT-OFDM with 16-QAM signaling in the presence of normalized frequency offset $\Delta f T_u = 0.02, 0.03, 0.04$ and 0.05.

The carrier frequency offset values are chosen to be consistent with useful error rates. The comparisons are based on the same signal-to-noise ratio (SNR) per bit, E_b/N_0, where the average energy per bit E_b is $2.5d^2$ in the case of 16-QAM. Several performance curves are plotted where lines (including solid lines and dashed lines) represent results obtained from the exact analysis, and symbols (circles and squares) denote the average BER's obtained from Monte Carlo simulations. The theoretical results and the simulation results are in excellent agreement.

Fig. 7.5 shows the BER performance of a 64-subcarrier DCT-OFDM system and a 64-subcarrier DFT-OFDM system, both with BPSK modulations, in the presence of the same absolute frequency offset Δf. The considered normalized frequency offset values are $\xi = \Delta f T_u = 0.02$, 0.1 and 0.2 for DFT-OFDM, and $\varepsilon = 2\Delta f T_u = 0.04$, 0.2 and 0.4 for DCT-OFDM. We further assume that both systems are transmitted by the DSB technique, hence they have identical transmission bandwidth. These results clearly show that the DCT-OFDM outperforms DFT-OFDM. For example, when the normalized frequency offset ξ is 0.2, an error floor occurs in the case of DFT-OFDM, whereas, no error floor occurs in the case of DCT-OFDM. The reason for this is that the magnitude of the ICI term (the second term) in eq. (7.25) can exceed the magnitude of the desired signal component (the first term) in eq. (7.25) for DFT-OFDM but not in the case of DCT-OFDM. At a BER of 10^{-3}, DCT-OFDM gives a performance improvement of about 1.29 dB in SNR when $\Delta f T_u = 0.1$. One can also observe that in the case of DCT-OFDM at a BER of 10^{-3}, there is a 0.70 dB difference in SNR between the two curves with normalized frequency offsets 0.02 and 0.1. In contrast, this difference in the case of DFT-OFDM is about 1.94 dB. This suggests that DCT-OFDM is less sensitive to frequency offset than DFT-OFDM. The DCT-OFDM system can achieve only a slight performance improvement over the DFT-OFDM system, about 0.06 dB at BER=10^{-3} in the case of $\Delta f T_u = 0.02$, since the BER is dominated by the influence of the additive noise when frequency offset is small.

It is important to note that the performance curves of DFT-OFDM with BPSK modulation in this section do not include the effect of the IQ imbalance which will make the BER performance even worse [104]. However, in DCT-OFDM systems for 1-D signaling formats, the IQ imbalance problem does not exist.

The performance of QPSK modulated DFT-OFDM with normalized frequency offset $\xi = \Delta f T_u = 0.05, 0.08, 0.1$ and 0.12 is compared with the performance of QPSK modulated DCT-OFDM with corresponding normalized frequency offset $\varepsilon = 2\Delta f T_u = 0.1$, 0.16, 0.2 and 0.24 in Fig. 7.6. Normalized frequency offset $\xi = 0.1$ leads to an error rate floor in the case of DFT-OFDM, whereas no error floor exists in the case of $\varepsilon = 0.2$ for DCT-OFDM. In the case of $\Delta f T_u = 0.05$, the BER performance for the two systems are quite similar. The performance of two systems with 16-QAM signaling is shown in Fig. 7.7. The superiority of DCT-OFDM over DFT-OFDM can be clearly seen. The robustness of DCT-OFDM to frequency offset can also be observed from this figure.

7.5 Performance Over Frequency-Selective Fast Fading Channels

In the preceding sections, we have considered the performance of the DCT-OFDM in the presence of carrier frequency offset over AWGN channels. We will examine the performance of DCT-OFDM over frequency-selective fast fading channels in this section. Rapid change of channel states is modeled by the Doppler frequency shift, which can be thought of as a kind of frequency offset [117]. Therefore, it is expected that the performance of DCT-OFDM over time-varying fading channels should still be better than that of DFT-OFDM. In this section, we will first show that a zero-padding scheme can be used in the DCT-OFDM system to suppress ISI. We then examine the performance of ZP-DCT-OFDM in frequency-selective fast fading environments with the employment of MMSE detection and MMSE DFD with ordering by simulation. We focus on the effect of Doppler shift in this section, and the carrier frequency is assumed to be synchronized perfectly.

The length N source data sequence $\mathbf{d}$ in (7.7) after IDCT operation yields data sequence $\mathbf{x} = \mathbf{D}^{\mathbb{T}}\mathbf{d}$. A length G zero-padding sequence are then added after sequence $\mathbf{x}$. The zero-padded sequence $\mathbf{x}_{zp}$ of length $M(M = N+G)$ is given as

$$\mathbf{x}_{zp} = \mathbf{C}_{zp}\mathbf{x} \tag{7.36}$$

where $\mathbf{C}_{zp} = \begin{pmatrix} \mathbf{I}_N & \mathbf{0}_{N\times G} \end{pmatrix}^{\mathbb{T}}$ is an $M \times N$ zero-padding matrix, $\mathbf{I}_N$ is an $N \times N$ identity matrix, and $\mathbf{0}_{N\times G}$ is an $N \times G$ zero matrix. The data block $\mathbf{x}_{zp}$ is serially fed into the interpolating filter, and transmitted over a frequency-selective fast fading channel.

Under a wide-sense stationary uncorrelated scattering (WSSUS) assumption, a frequency-selective multipath fading channel $h(t,\tau)$ can be written as eq.(2.5) where the L time-varying coefficients $h_0(t)$, $h_1(t), \cdots$,and $h_{L-1}(t)$ are independent and identically distributed complex Gaussian stochastic processes. In discrete-time studies and simulations, the T-spaced tapped-delay-line (TDL) realization is desirable [117]. The $P+1$ TDL tap coefficients $\alpha_0(t)$, $\alpha_1(t), \cdots$, and $\alpha_P(t)$, which are, in general correlated, can be obtained from [118] $\alpha_l(t) = \sum_{i=0}^{L-1} h(t,\tau_i)\mathrm{sinc}(\tau_i/T - l)$ where $T = T_u/N$, T_u is the duration of a DCT-OFDM symbol without zero-padding, and $P = \lfloor \tau_P/T \rfloor + 1$ where $\lfloor \cdot \rfloor$ denotes the floor operation.

If we assume $G \geq P$, there will be no ISI components in the received signal. Thus, in a baseband signal model, after sampling the received signal, the $M \times 1$ fading signal-plus-noise vector will be

$$\mathbf{r} = \mathbf{H}\mathbf{x} + \mathbf{w} \tag{7.37}$$

where $\mathbf{H} = \mathbf{H}_0\mathbf{C}_{zp}$, and $\mathbf{H}_0$ is the $M \times M$ channel convolutional matrix whose element in the rth ($0 \leq r \leq M-1$) row and cth ($0 \leq c \leq M-1$) column is

$$H_0(r,c) = \begin{cases} \alpha_{r-c}(t_r), & 0 \leq r-c \leq P \\ 0, & \text{otherwise} \end{cases} \tag{7.38}$$

where $\alpha_{r-c}(t_r)$ denotes the channel impulse response (CIR) at the rth sampling instant in one OFDM symbol. The complex additive white Gaussian noise (AWGN) vector $\mathbf{w}$ has mean zero and variance $\sigma^2/2$ per dimension.

In slowly fading channel environments where the channel state will not change within one OFDM symbol, the channel matrix $\mathbf{H}$ becomes a circulant matrix in the case of CP-DFT-OFDM after removing the CP at the receiver. It can then be diagonalized by a DFT operation. Therefore, one can use a one-tap equalizer in the receiver to compensate the channel distortion. In the case of DCT-OFDM, by using a symmetric guard sequence and a prefilter at the receiver, the channel can be diagonalized by a DCT operation into parallel and decoupled subchannels as shown in [112]. It is noted, in both cases, that the ISI and ICI can be completely eliminated.

The case is different for fast fading channel environments where the channel state information will change from time to time in one OFDM symbol duration. The schemes designed for slowly fading channels do not work in this case. Zero-padding can effectively eliminate ISI caused by multipath. However, it can not remove the ICI caused by rapid time variation of the fading channel. Therefore, a signal detection scheme should be employed to mitigate ICI. In this case the optimum detection for (7.37) is maximal likelihood (ML) sequence detection but is complex. The use of linear MMSE detection to suppress ICI is suboptimum. As shown in [119], a MMSE successive cancellation can significantly outperform liner MMSE detection and can better exploit the available time diversity from Doppler. One may well ask: How would the relative performance of ZP-DCT-OFDM and ZP-DFT-OFDM change with a more advanced receiver? Therefore, in this work, we examine two suboptimum detection algorithms, that is MMSE and MMSE DFD with ordering (also known as MMSE successive detection in [119], and MMSE V-BLAST in [120–122]).

7.5.1 MMSE Detection

With perfect knowledge of channel matrix $\mathbf{H}$, a zero-forcing (ZF) detector can eliminate ICI components completely as

$$\hat{\mathbf{d}} = \mathbf{D}\mathbf{H}^{\dagger}\mathbf{r} \tag{7.39}$$

where $\mathbf{H}^{\dagger} = (\mathbf{H}^{\mathbb{H}}\mathbf{H})^{-1}\mathbf{H}^{\mathbb{H}}$ is the pseudo-inverse of matrix $\mathbf{H}$, and $(\cdot)^{\mathbb{H}}$ denotes the conjugate transpose operation. However, the involved matrix inversion will enhance the noise power significantly. The MMSE detection technique, on the other hand, can effectively avoid undesirable noise enhancement by minimizing the mean-square error between the transmitted data sequence $\mathbf{d}$ and the decision statistic vector $\hat{\mathbf{d}} = \mathbf{G}\mathbf{r}$ where $\mathbf{G}$ is the equalization matrix, and

$$\mathbf{G} = \mathbf{D}(\mathbf{H}^{\mathbb{H}}\mathbf{H} + \sigma^2\mathbf{I}_N)^{-1}\mathbf{H}^{\mathbb{H}}. \tag{7.40}$$

It is noted that unit symbol energy has been assumed to obtain eq. (7.40). For two-dimensional signaling formats, both the real and imaginary components of $\hat{\mathbf{d}}$ will be used as the decision statistic vector. For one-dimensional signaling formats, the real part of $\hat{\mathbf{d}}$ will be used as the decision statistic vector. The data is recovered on the basis of the decision statistic vector in systems without coding and in systems using hard decision decoding. In the latter, the data are input to a decoding operation. In systems using soft decision decoding, the decision statistic vector is input directly to a decoding operation. Note that the DCT has been included in the equalization matrix in (7.40) at the receiver side.

7.5.2 MMSE Decision-Feedback Detection with Ordering

The MMSE DFD with ordering can further improve the performance of linear MMSE detection. The MMSE scheme detects all of the symbols in the data block parallel at one time, whereas, the MMSE DFD with ordering performs successive detection and interference cancellation operations on the received data block. At each time, the scheme performs detection on the strongest signal which suffers from the smallest interference. The interference due to the strongest signal is then subtracted from the received data block to improve detection accuracy of the remaining signals in this data block.

The detailed algorithm can be found in [120–122]. Specifically, in the DCT-OFDM scenario, the covariance matrix for the estimation error between the source data vector $\mathbf{d}$ and the decision statistic vector $\hat{\mathbf{d}}$ can be written as

$$\mathbf{C} = \mathbf{E}\left[\left(\mathbf{d}-\hat{\mathbf{d}}\right)\left(\mathbf{d}-\hat{\mathbf{d}}\right)^{\mathbb{H}}\right] = \sigma^2\left(\bar{\mathbf{H}}^{\mathbb{H}}\bar{\mathbf{H}}+\sigma^2\mathbf{I}_N\right)^{-1} \tag{7.41}$$

where $\bar{\mathbf{H}} = \mathbf{H}\mathbf{D}^{\mathbb{T}}$. If the smallest main diagonal element of the $N \times N$ matrix $\mathbf{C}$ is $C[k,k]$, then the detection will start from the kth entry d_k of the data vector $\mathbf{d}$ because it suffers from the smallest interference. The decision statistic of d_k can be obtained as

$$\hat{d}_k = \mathbf{g}_k\mathbf{r} \tag{7.42}$$

where $\mathbf{g}_k$ is the kth row of the MMSE equalization matrix $\mathbf{G}$ in (7.40). Assuming a correct decision is obtained, the influence of d_k on the yet undetected symbols can be subtracted, and the received vector $\mathbf{r}$ will be updated as

$$\mathbf{r} = \mathbf{r} - \mathbf{v}_k d_k = \bar{\mathbf{H}}^{N-1}\mathbf{d}^{N-1} + \mathbf{w} \tag{7.43}$$

where $\mathbf{v}_k$ is the kth column of the matrix $\bar{\mathbf{H}}$, and $\bar{\mathbf{H}}^{N-1}$ and $\mathbf{d}^{N-1}$ are obtained by deleting the kth column of the matrix $\bar{\mathbf{H}}$ and kth entry of the vector $\mathbf{d}$, respectively. Clearly, eq. (7.43) is a reduced-order problem of (7.37). Therefore, after updating the covariance matrix $\mathbf{C}$ and equalization matrix $\mathbf{G}$, one can get the decision of the next candidate symbol. The interference cancellation is then implemented. The procedure will continue until all of the data symbols are detected.

7.5.3 Computational Complexity

The dominant complexity of MMSE comes from the calculation of $(\mathbf{H}^{\mathbb{H}}\mathbf{H}+\sigma^2\mathbf{I}_N)^{-1}\mathbf{H}^{\mathbb{H}}\mathbf{r}$ which can be further written as

$$\mathbf{Br} = \begin{bmatrix} \mathbf{H} \\ \sigma\mathbf{I}_N \end{bmatrix}^{\dagger} \begin{bmatrix} \mathbf{r} \\ \mathbf{0}_{N\times 1} \end{bmatrix} \tag{7.44}$$

where $\mathbf{B} = (\mathbf{H}^{\mathbb{H}}\mathbf{H}+\sigma^2\mathbf{I}_N)^{-1}\mathbf{H}^{\mathbb{H}}$. Several algorithms for the least squares problem in [123] can be used to calculate (7.44). For example, the method of normal equations gives a computational complexity of $7N^3/3+N^2G$. Recalling that N is the number of data symbols included in one OFDM block, and G is the length of guard interval, the per-symbol complexity is thus $7N^2/3+NG$. The decision statistic vector $\hat{\mathbf{d}}$ can be obtained from fast DCT operation and the FFT operation on the length-N sequence $\mathbf{Br}$ in the case of ZP-DCT-OFDM and in the case of ZP-DFT-OFDM/CP-DFT-OFDM (for CP-DFT-OFDM, the channel matrix $\mathbf{H}$ is defined in [113] and [119]), respectively. Both the fast DCT and FFT of a length-N sequence have a computational complexity $\mathcal{O}(N\log_2 N)$ where $\mathcal{O}(x)$ means on the order of x. The complexity for each data symbol in one OFDM block is thus $\mathcal{O}(\log_2 N)$. However, the fast DCT has some computational complexity reduction compared with the FFT because the fast DCT algorithm in [105] provides a factor of three improvement in computation when compared to the FFT algorithm. But the computational reduction is relatively small compared with the order of N^2. On the other hand, the MMSE DFD with ordering scheme when using the square-root algorithm in [121] has a per-symbol complexity of $29N^2/3+11NG+2G^2$. In summary, in the fast fading environments considered in this chapter, by using MMSE detection or MMSE DFD with ordering, all three schemes, ZP-DFT-OFDM, CP-DFT-OFDM and ZP-DCT-OFDM have a per-symbol computational complexity $\mathcal{O}(N^2)$.

In the slowly fading environment, the detection of CP-DFT-OFDM or the DCT-OFDM scheme in [112] can be implemented by a simple one-tap equalizer. A significant part of the computational complexity comes from the FFT or the fast DCT algorithm which has a per-symbol computational complexity $\mathcal{O}(\log_2 N)$. In this case, the complexity of the MMSE detection for ZP-DFT-OFDM and ZP-DCT-OFDM is much higher than CP-DFT-OFDM or the DCT-OFDM scheme in [112].

7.5.4 Computer Simulations

The BER performance of a ZP-DCT-OFDM system and a ZP-DFT-OFDM system operating over frequency-selective fast fading channels with both MMSE detection and MMSE DFD with ordering is evaluated by extensive simulation in several scenarios in this section. In the case of ZP-DFT-OFDM, the DCT matrix $\mathbf{D}$ should be replaced with the unitary DFT matrix to construct the detection algorithm.

We employ the HIPERLAN/2 channel model A [124], which describes the typical transmission environment for a large office with non-line-of-sight propagation, in the simulations. Different channel taps $\alpha_i(t)$ in (2.5) are independent and identically distributed zero-mean complex Gaussian random processes. However the same channel tap at different times are correlated according to the classical 2-D isotropic scattering omnidirectional receiver antenna Doppler spectrum model, and they are generated using the method in [125]. The number of subcarriers, N, in these simulations is 64, and the length of the zero-padding is $G = 16$. Since $L = 8$ in the T-spaced TDL model for HIPERLAN/2 channel model A, no ISI occurs in our simulations. All of the simulations assume a fast fading channel, that is, channel state information will change in one OFDM symbol. To ensure the reliability of the computer simulations, 2^{20} OFDM symbols are generated to obtain each BER value in the simulations.

In Fig. 7.8, under a perfect channel state information assumption, the BER performances of the MMSE receiver for 64-subcarrier ZP-DCT-OFDM, ZP-DFT-OFDM, and CP-DFT-OFDM are compared, all with BPSK modulation. For a fast fading channel, even a CP-DFT-OFDM receiver can not be implemented using a one-tap equalizer because the channel matrix $\mathbf{H}$ is no longer circulant. The MMSE receiver designed in [119] for CP-DFT-OFDM is employed here. One can see that the CP-DFT-OFDM is worse than the ZP-DFT-OFDM. This was also observed in [113]. Therefore, we will focus on comparing the performance of ZP-DCT-OFDM with the performance of ZP-DFT-OFDM in the sequel. Better BER performance can be achieved with the employment of the proposed ZP-DCT-OFDM scheme. In particular, in the case of $f_d T_u = 0.02$, a 4.93 dB gain in SNR over the ZP-DFT-OFDM system at a BER of 10^{-3} can be achieved by the ZP-DCT-OFDM system. At the same BER and Doppler shift value, the improvement of ZP-DCT-OFDM over the CP-DFT-OFDM is about 2.58 dB. The time diversity effect can be observed in the small to medium SNR region. The extremely large and impractical normalized Doppler shift values 0.1 and 0.2 are shown in this figure for the purpose of comparison.

The performance of a MMSE receiver with forward error correction and interleaving is examined in Fig. 7.9 where channel is assumed to be perfectly known. At the transmitter, a convolutional encoder of rate $1/2$ with generator polynomial $(133, 171)$ and the block interleaver used in the IEEE 802.11a standard (and the HIPERLAN/2 standard) are employed to improve system BER performance for a QPSK ZP-DCT-OFDM system and a QPSK ZP-DFT-OFDM system. At the receiver, after deinterleaving, the Viterbi algorithm [17] is used for decoding. One can observe that, the time diversity effect appearing in the small to medium SNR region in Fig. 7.8 now becomes more significant due to the coding gain. The ZP-DCT-OFDM is superior to ZP-DFT-OFDM in this case. Particularly, at a BER of 10^{-6}, in the presence of frequency offset $f_d T_u = 0.05$, about 1.0 dB performance gain in SNR can be achieved with the employment of ZP-DCT-OFDM, rather than the ZP-DFT-OFDM.

Residual interference may exist after MMSE equalization. The MMSE DFD with ordering scheme can further suppress the residue interference. Moreover, as the Doppler shift increases, the time diversity can be better exploited by this scheme. One can observe clearly

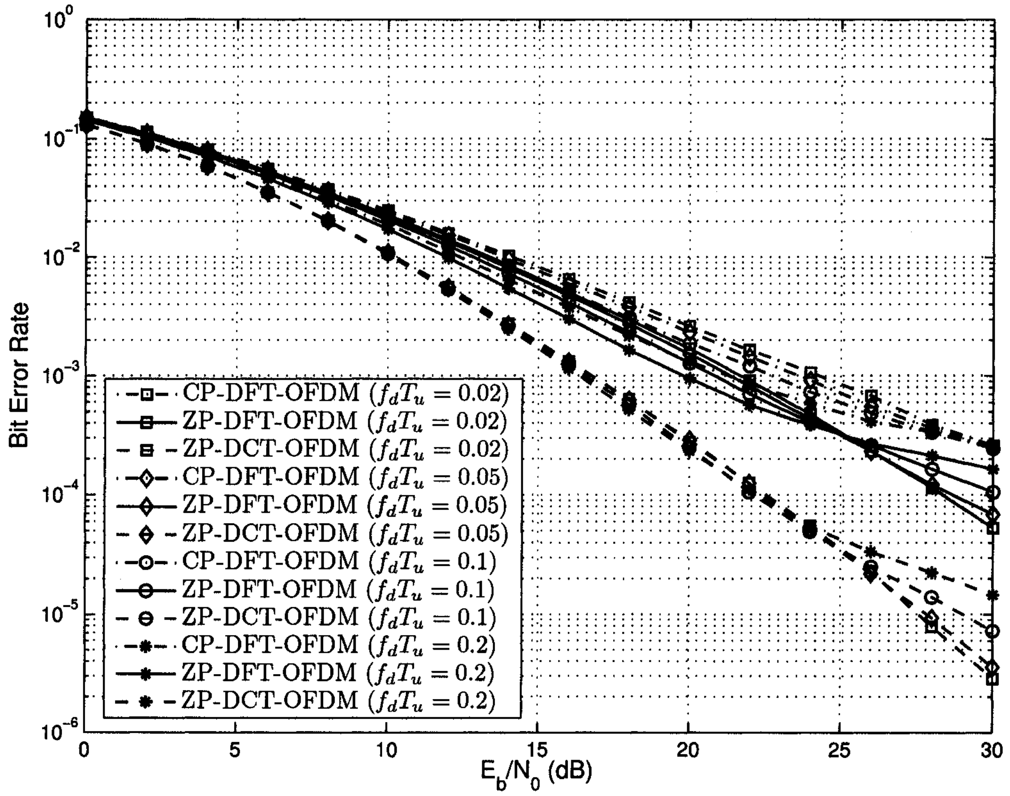

Fig. 7.8. The BER performance of the MMSE receiver for 64-subcarrier ZP-DCT-OFDM, ZP-DFT-OFDM, and CP-DFT-OFDM, with BPSK modulation and perfect channel state information.

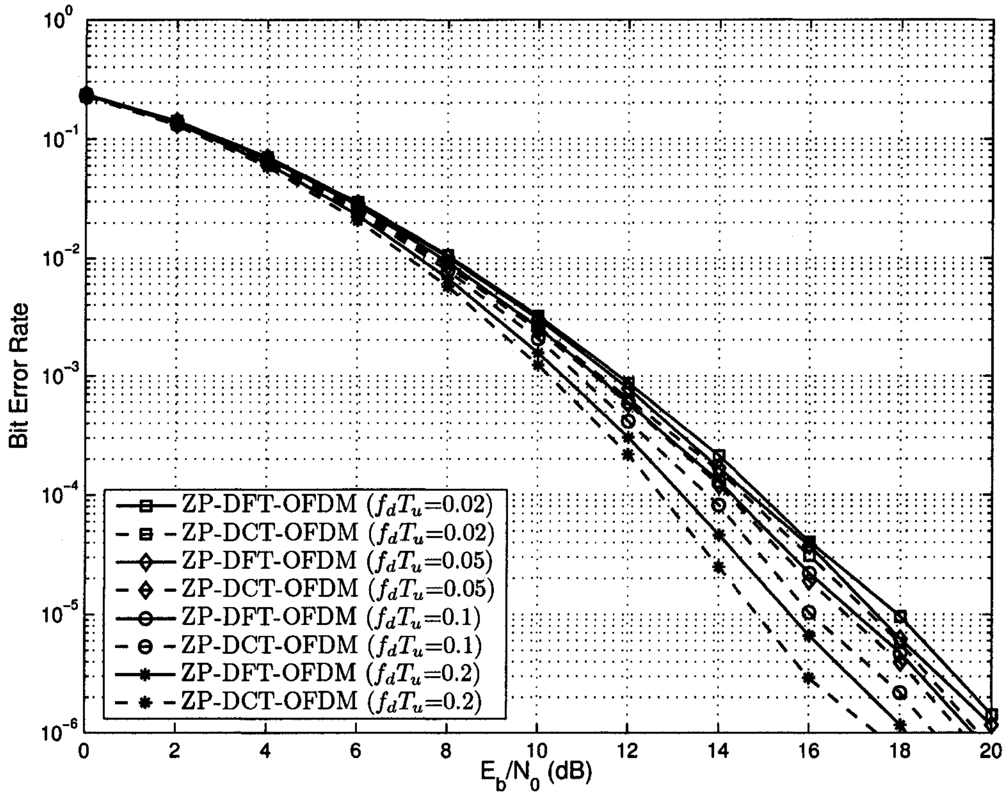

Fig. 7.9. The BER performance of the MMSE receiver for a 64-subcarrier QPSK ZP-DCT-OFDM and a 64-subcarrier QPSK ZP-DFT-OFDM with convolutional coding and interleaving.

in Fig. 7.10, that when the Doppler shift increases, the BER performances become better, not worse. The ZP-DCT-OFDM is still superior to the ZP-DFT-OFDM with this advanced receiver. In the case of QPSK modulation, for an uncoded system with perfect channel state information, the performance gain achieved by ZP-DCT-OFDM is about 3.87 dB at a BER of 10^{-3} in the case of $f_d T_u = 0.02$. In addition, one can observe that about 0.78 dB gain due to time diversity can be achieved when the normalized Doppler shift increases from 0.1 to 0.2 in the case of ZP-DCT-OFDM at a BER of 10^{-3}.

Perfect channel state information can not be known; therefore, channel estimation must be performed at the receiver. Reference [119] proposed a pilot-assisted fast fading channel estimation scheme where channel state information of the middle $S-1$ symbols is obtained from Q pilot symbols on both sides by using a Wiener filter method. This channel estimation scheme shows robustness to variations of channel characteristics. It was derived for a DFT-OFDM scenario; however, it can also be used in the ZP-DCT-OFDM system with some straightforward changes. For example, the DFT matrix should be modified to a DCT matrix. Fig. 7.11 shows the BER performance of a uncoded ZP-DCT-OFDM system and a uncoded ZP-DFT-OFDM system with the employment of this channel estimation algorithm and the MMSE detection in the case of QPSK modulation. In this simulation, we assume the pilot spacing $S = 2$ and number of pilot symbols $Q = 4$ as in [119]. In the case of $f_d T_u = 0.01$, a 2.18 dB SNR improvement over ZP-DFT-OFDM can be achieved at a bit error rate of 10^{-3} by using ZP-DCT-OFDM. The time diversity effect is not apparent due to the existence of the channel estimation error.

7.6 Summary

In this chapter, the zero-padded DCT-OFDM system was examined. The BER performance of the ZP-DCT-OFDM was compared with that of the ZP-DFT-OFDM in a frequency-

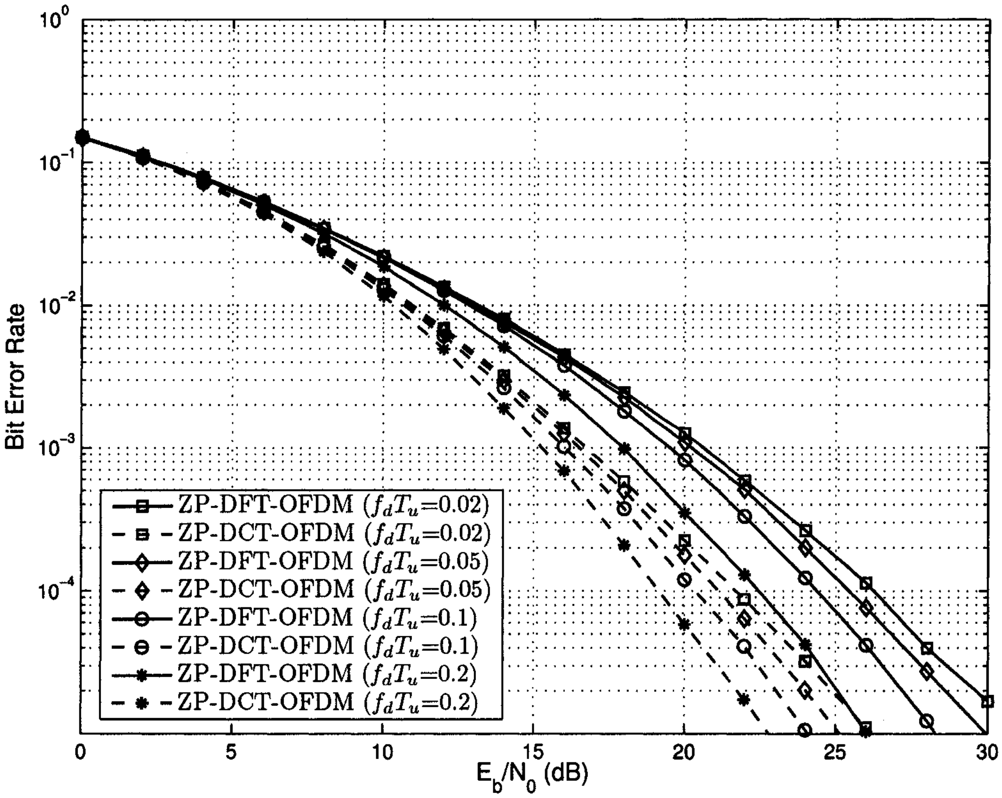

Fig. 7.10. The BER performance of the MMSE DFD with ordering scheme for a 64-subcarrier QPSK ZP-DCT-OFDM and a 64-subcarrier QPSK ZP-DFT-OFDM.

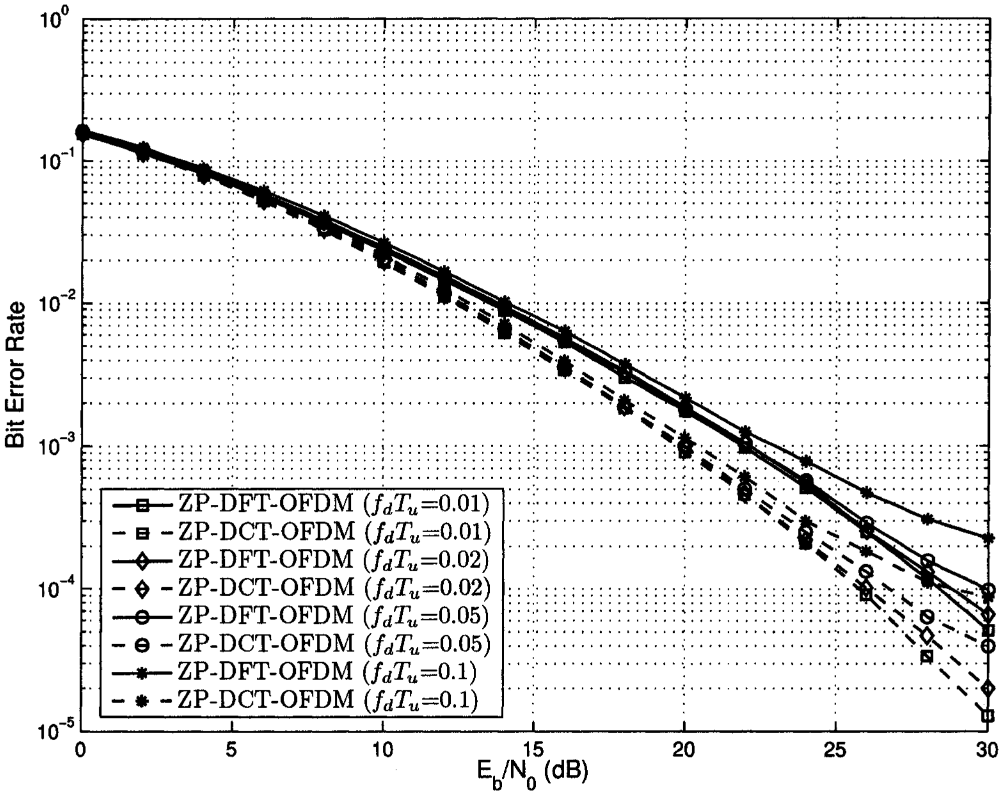

Fig. 7.11. The BER performances of the MMSE receiver for 64-subcarrier QPSK ZP-DCT-OFDM and 64-subcarrier QPSK ZP-DFT-OFDM with channel estimation.

selective fast fading environment with employment of both MMSE detection and MMSE DFD with ordering. The results indicate that the ZP-DCT-OFDM system has a smaller BER than the ZP-DFT-OFDM system. In convolutional coding systems, the performance benefit achieved by using the proposed ZP-DCT-OFDM is about 1 dB in SNR.

An exact method for calculating the BER of a DCT-OFDM system in the presence of carrier frequency offset in AWGN environments was also derived. The method was used to compare the performance of the DCT-OFDM system and the conventional DFT-OFDM system when carrier frequency offset is present in an AWGN transmission environment. Analysis and simulation results show that the DCT-OFDM systems reduce ICI compared to the DFT-OFDM systems, giving a smaller BER.

Chapter 8

Widely Linear MMSE Equalization for One-Dimensional Modulation OFDM Systems

8.1 Introduction

While most OFDM systems employ 2-D modulations on the subcarriers, some will employ 1-D modulations (real-valued modulation formats). In particular, the important IEEE 802.11a standard, IEEE 802.16 standard, and HIPERLAN/2 standard all provide the option of using BPSK modulation. Also 1-D modulations may be employed in some low data rate applications where robustness to severe channel conditions is essential.

It has been shown that, in a system where real-valued data symbols are transmitted over a complex-value channel, widely linear equalization can effectively improve system performance compared to conventional linear equalization design [126–128]. Several modulation formats, such as, BPSK, PAM, OQPSK and GMSK can satisfy this system model. In particular, it was shown in [129] that a widely linear MMSE equalization scheme for interference suppression can outperform the linear MMSE equalizer in CDMA systems with BPSK modulation. A widely linear zero-forcing equalizer was derived in [130] to mitigate ICI in multicarrier transmission systems with OQPSK modulation.

As shown in [113, 131], in conventional CP-DFT-OFDM, the equalizer function requires that the channel transfer function has non-zero values at the subcarrier frequencies, which may not be guaranteed in some wireless channel environments. The ZP-DFT-OFDM scheme has been proposed to overcome this disadvantage. The performance of a linear MMSE equalizer for ZP-DFT-OFDM was studied in [113]. It was shown that the BER of ZP-DFT-OFDM outperforms conventional CP-DFT-OFDM. In this chapter, we propose using a widely linear MMSE equalizer to mitigate ICI for ZP-DFT-OFDM systems, CP-DFT-OFDM systems, and ZP-DCT-OFDM systems with 1-D modulation formats in fast fading environments. The derivation of the widely linear MMSE equalizer is based on a gradient method, which is different from [126–130]. Our investigation indicates that the widely linear MMSE equalizer displays a smaller average error power and BER for 1-D modulation formats than the conventional linear MMSE equalizer in [113, 131]. When applying the widely linear MMSE criterion to design equalizer for OFDM systems with many 2-D modulation formats with symmetry in signal constellation, such as QPSK and 16-QAM, one obtains the conventional linear MMSE equalizer.

8.2 System Model

The length N source data sequence $\mathbf{d}$ after IDFT operation yields the data sequence

$$\mathbf{y} = \mathbf{F}\mathbf{d} \tag{8.1}$$

where $\mathbf{F}$ is the IDFT matrix whose rth $(0 \leq r \leq N-1)$ row and cth $(0 \leq c \leq N-1)$ column element $F(r,c)$ is defined as $e^{j2\pi rc/N}/\sqrt{N}$. We further assume that

$$\mathbf{E}\left(\mathbf{d}\mathbf{d}^{\mathbb{T}}\right) = E_s\mathbf{I}_N \tag{8.2}$$

where E_s is the average energy of data symbol. When a length G zero-padding sequence is added after sequence $\mathbf{y}$, the new sequence $\mathbf{y}_{zp}$ becomes a zero-padded sequence of length $M(M = N + G)$ given as

$$\mathbf{y}_{zp} = \mathbf{C}_{zp}\mathbf{y} \tag{8.3}$$

where

$$\mathbf{C}_{zp} = \begin{pmatrix} \mathbf{I}_N \\ \mathbf{0}_{G\times N} \end{pmatrix} \tag{8.4}$$

is an $M \times N$ zero-padding matrix, and $\mathbf{0}_{N\times G}$ denotes an $N \times G$ zero matrix. If we assume $G \geq L$, there will be no ISI components in the received $M \times 1$ fading signal-plus-noise vector

$$\mathbf{r} = \mathbf{H}\mathbf{y} + \mathbf{w} \tag{8.5}$$

where $\mathbf{H} = \mathbf{H}_0\mathbf{C}_{zp}$, and $\mathbf{H}_0$ is the $M \times M$ channel convolutional matrix defined in eq. (7.38). The complex AWGN vector $\mathbf{w}$ has mean zero and variance $\sigma^2/2$ per dimension. It is also assumed that the real parts and the imaginary parts of the complex Gaussian noise vector are uncorrelated. The linear MMSE equalizer for ZP-OFDM gives the decision vector

$$\hat{\mathbf{d}} = \begin{pmatrix} \hat{d}_0 \\ \vdots \\ \hat{d}_{N-1} \end{pmatrix} = \mathbf{G}_1\mathbf{r} \tag{8.6}$$

in the sense of minimizing the mean-square error

$$\mathbf{E}||\mathbf{G}_1\mathbf{r} - \mathbf{d}||^2 \tag{8.7}$$

where $||\mathbf{a}||$ denotes the Euclidean norm of the vector $\mathbf{a}$. In references [113, 131], the linear MMSE equalization matrix $\mathbf{G}_1$ is developed as

$$\mathbf{G}_1 = E_s\mathbf{F}^{\mathbb{H}}\mathbf{H}^{\mathbb{H}}(E_s\mathbf{H}\mathbf{H}^{\mathbb{H}} + \sigma^2\mathbf{I}_M)^{-1}. \tag{8.8}$$

On the other hand, if a length-G CP scheme is employed, the OFDM symbol with CP becomes

$$\mathbf{y}_{cp} = \mathbf{C}_{cp}\mathbf{y} \tag{8.9}$$

where

$$\mathbf{C}_{cp} = \begin{pmatrix} \mathbf{I}_{cp} \\ \mathbf{I}_N \end{pmatrix} \tag{8.10}$$

and $\mathbf{I}_{cp}$ is a $G \times N$ matrix whose elements are the last G rows of $\mathbf{I}_N$. To avoid the ISI, one must remove the prefix from the received signal. Thus the resulting $N \times 1$ signal vector can be written as

$$\mathbf{r}_{cp} = \mathbf{H}_{cp}\mathbf{y} + \mathbf{w} \tag{8.11}$$

where $\mathbf{H}_{cp} = \mathbf{R}_{cp}\mathbf{H}_0\mathbf{C}_{cp}$ and the $N \times M$ matrix $\mathbf{R}_{cp} = \begin{pmatrix} \mathbf{0}_{N\times G} & \mathbf{I}_N \end{pmatrix}$. The matrix $\mathbf{H}_{cp}$ will not be a circular matrix in the case of fast fading channels, and can not be diagonalized by IDFT and DFT operations. Thus, ICI will be introduced in this case. To overcome the ICI one can use a linear MMSE equalizer which can be obtained by replacing $\mathbf{H}$ and $\mathbf{I}_M$ with $\mathbf{H}_{cp}$ and $\mathbf{I}_N$ in eq. (8.8), respectively.

8.3 Widely Linear MMSE receiver for 1-D modulation formats

Note that the transmitted symbol sequence $\mathbf{d}$ in (8.7) is a complex vector and a real vector for 2-D modulation formats and 1-D modulation formats, respectively. Generally $\hat{\mathbf{d}}$ is a complex sequence even for 1-D signaling because the received vector $\mathbf{r}$ is complex. For 1-D signaling, the real part of $\hat{\mathbf{d}}$ will be used as the decision vector. However, minimization of (8.7) does not ensure that the Euclidean distance between the real part of $\hat{\mathbf{d}}$ and $\mathbf{d}$ is minimized. A better MMSE criterion for 1-D modulation formats is to minimize

$$\mathbf{E}\|\Re\{\mathbf{Gr}\}-\mathbf{d}\|^2 \tag{8.12}$$

where the equalizer matrix $\mathbf{G}$ is known as a widely linear equalizer in the literature [126–128].

Let $\mathbf{G}=\mathbf{G}_x+j\mathbf{G}_y$ where $\mathbf{G}_x$ and $\mathbf{G}_y$ are the matrices whose elements are the real parts and the imaginary parts respectively, of the corresponding elements of the matrix $\mathbf{G}$. Similarly, let $\mathbf{C}=\mathbf{HF}=\mathbf{C}_x+j\mathbf{C}_y$, and $\mathbf{r}=\mathbf{r}_x+j\mathbf{r}_y$. The problem at hand has become finding the widely linear MMSE equalization matrix $\mathbf{G}$ minimizing (8.12) which can be written as

$$\Lambda=\mathbf{E}\left\{tr\left[\left(\Re\{\mathbf{Gr}\}-\mathbf{d}\right)\left(\Re\{\mathbf{Gr}\}-\mathbf{d}\right)^{\mathrm{T}}\right]\right\} \tag{8.13}$$

$$\Lambda=\mathbf{E}\left\{tr\left[\left(\Re\{\mathbf{Gr}\}-\mathbf{d}\right)\left(\Re\{\mathbf{Gr}\}-\mathbf{d}\right)^{\mathrm{T}}\right]\right\}$$

$$\begin{aligned}
&= tr\Big(E_s\mathbf{G}_x\mathbf{C}_x\mathbf{C}_x^{\mathrm{T}}\mathbf{G}_x^{\mathrm{T}}-E_s\mathbf{G}_x\mathbf{C}_x\mathbf{C}_y^{\mathrm{T}}\mathbf{G}_y^{\mathrm{T}}-E_s\mathbf{G}_x\mathbf{C}_x-E_s\mathbf{G}_y\mathbf{C}_y\mathbf{C}_x^{\mathrm{T}}\mathbf{G}_x^{\mathrm{T}}\\
&\quad+E_s\mathbf{G}_y\mathbf{C}_y\mathbf{C}_y^{\mathrm{T}}\mathbf{G}_y^{\mathrm{T}}+E_s\mathbf{G}_y\mathbf{C}_y+\frac{\sigma^2}{2}\mathbf{G}_x\mathbf{G}_x^{\mathrm{T}}\\
&\quad+\frac{\sigma^2}{2}\mathbf{G}_y\mathbf{G}_y^{\mathrm{T}}-E_s\mathbf{C}_x^{\mathrm{T}}\mathbf{G}_x^{\mathrm{T}}+E_s\mathbf{C}_y^{\mathrm{T}}\mathbf{G}_y^{\mathrm{T}}+E_s\mathbf{I}_N\Big)
\end{aligned} \tag{8.14}$$

where $tr(\mathbf{A})$ denotes the trace of the matrix $\mathbf{A}$. We use a gradient approach to derive the solution to $\mathbf{G}$ in the sequel.

Assuming $\mathbf{H}$ is known to the receiver, the optimal $\mathbf{G}$ can be found by solving the following two gradient equations

$$\frac{\partial\Lambda}{\partial\mathbf{G}_x}=0 \tag{8.15}$$

$$\frac{\partial\Lambda}{\partial\mathbf{G}_y}=0. \tag{8.16}$$

Thus, eqs. (8.15) and (8.16) can be further written as

$$\mathbf{G}_x\left(E_s\mathbf{C}_x\mathbf{C}_x^{\mathrm{T}}+\frac{\sigma^2}{2}\mathbf{I}_M\right)=E_s\mathbf{G}_y\mathbf{C}_y\mathbf{C}_x^{\mathrm{T}}+E_s\mathbf{C}_x^{\mathrm{T}} \tag{8.17}$$

$$\mathbf{G}_y\left(E_s\mathbf{C}_y\mathbf{C}_y^{\mathrm{T}}+\frac{\sigma^2}{2}\mathbf{I}_M\right)=E_s\mathbf{G}_x\mathbf{C}_x\mathbf{C}_y^{\mathrm{T}}-E_s\mathbf{C}_y^{\mathrm{T}} \tag{8.18}$$

by noting that [67]

$$\frac{\partial \mathrm{tr}\left(\mathbf{X}^{\mathrm{T}}\mathbf{M}\mathbf{X}\right)}{\partial \mathbf{X}} = \mathbf{M}\mathbf{X} + \mathbf{M}^{\mathrm{T}}\mathbf{X} \tag{8.19}$$

$$\frac{\partial \mathrm{tr}\left(\mathbf{X}\mathbf{M}\mathbf{X}^{\mathrm{T}}\right)}{\partial \mathbf{X}} = \mathbf{X}\mathbf{M} + \mathbf{X}\mathbf{M}^{\mathrm{T}} \tag{8.20}$$

$$\frac{\partial \mathrm{tr}\left(\mathbf{A}\mathbf{X}\right)}{\partial \mathbf{X}} = \mathbf{A}^{\mathrm{T}} \tag{8.21}$$

$$\frac{\partial \mathrm{tr}\left(\mathbf{A}\mathbf{X}^{\mathrm{T}}\right)}{\partial \mathbf{X}} = \mathbf{A} \tag{8.22}$$

$$\frac{\partial \mathrm{tr}\left(\mathbf{X}\mathbf{X}^{\mathrm{T}}\right)}{\partial \mathbf{X}} = 2\mathbf{X} \tag{8.23}$$

where **X**, **A**, and **M** are matrices with proper sizes. Combining (8.17) and (8.18) together, one can immediately obtain

$$E_s\left(\mathbf{G}_x\mathbf{C}_x - \mathbf{G}_y\mathbf{C}_y\right)\left(\mathbf{C}_x^{\mathrm{T}} - \mathbf{C}_y^{\mathrm{T}}\right) + \frac{\sigma^2}{2}\left(\mathbf{G}_x + \mathbf{G}_y\right) = E_s\left(\mathbf{C}_x^{\mathrm{T}} - \mathbf{C}_y^{\mathrm{T}}\right) \tag{8.24}$$

that is,

$$\begin{aligned} &E_s\begin{pmatrix}\mathbf{G}_x & -\mathbf{G}_y\end{pmatrix}\begin{pmatrix}\mathbf{C}_x \\ \mathbf{C}_y\end{pmatrix}\begin{pmatrix}\mathbf{C}_x^{\mathrm{T}} & \mathbf{C}_y^{\mathrm{T}}\end{pmatrix}\begin{pmatrix}\mathbf{I}_M \\ -\mathbf{I}_M\end{pmatrix} + \frac{\sigma^2}{2}\begin{pmatrix}\mathbf{G}_x & -\mathbf{G}_y\end{pmatrix}\begin{pmatrix}\mathbf{I}_M \\ -\mathbf{I}_M\end{pmatrix} \\ &= E_s\begin{pmatrix}\mathbf{C}_x^{\mathrm{T}} & \mathbf{C}_y^{\mathrm{T}}\end{pmatrix}\begin{pmatrix}\mathbf{I}_M \\ -\mathbf{I}_M\end{pmatrix}. \end{aligned} \tag{8.25}$$

Constructing the $N \times 2M$ matrix $\bar{\mathbf{G}}$

$$\bar{\mathbf{G}} = \begin{pmatrix}\mathbf{G}_x & -\mathbf{G}_y\end{pmatrix} \tag{8.26}$$

and the $2M \times N$ matrix $\bar{\mathbf{C}}$

$$\bar{\mathbf{C}} = \begin{pmatrix}\mathbf{C}_x \\ \mathbf{C}_y\end{pmatrix} \tag{8.27}$$

one can finally obtain

$$\bar{\mathbf{G}} = E_s\bar{\mathbf{C}}^{\mathrm{T}}\left(E_s\bar{\mathbf{C}}\bar{\mathbf{C}}^{\mathrm{T}} + \frac{1}{2}\sigma^2\mathbf{I}_{2M}\right)^{-1}. \tag{8.28}$$

Eq. (8.28) can also be obtained by noticing that the cost function (8.12) can be written as $E\|\bar{\mathbf{G}}\bar{\mathbf{r}}-\mathbf{d}\|^2$ where

$$\bar{\mathbf{r}} = \begin{pmatrix} \mathbf{r}_x \\ \mathbf{r}_y \end{pmatrix}. \tag{8.29}$$

It is noted that $\Im\{\mathbf{G}^Q\mathbf{r}\}$, where $\Im\{A\}$ denotes the imaginary part of a complex matrix $\mathbf{A}$, also contains information about the transmitted vector $\mathbf{x}$. The complex $N \times M$ matrix $\mathbf{G}^Q$ is an MMSE equalization matrix. Minimizing

$$\mathbf{E}\|\Im\{\mathbf{G}^Q\mathbf{r}\}-\mathbf{d}\|^2 \tag{8.30}$$

gives $\mathbf{G}_x^Q = -\mathbf{G}_y$ and $\mathbf{G}_y^Q = \mathbf{G}_x$ where $\mathbf{G}_x^Q$ and $\mathbf{G}_y^Q$ are the matrices whose elements are the real parts and the imaginary parts respectively, of the corresponding elements of the matrix $\mathbf{G}^Q$. Therefore, the decision vector $\Re\{\mathbf{Gr}\}$ for the real part case is actually the same as the decision vector $\Im\{\mathbf{G}^Q\mathbf{r}\}$ for the imaginary part case. This result is reasonable according to the symmetry between the cost function (8.12) and the cost function (8.30).

For many 2-D modulation formats, such as QPSK and 16-QAM, due to a special symmetry in the signal constellation, one can assume that $\mathbf{E}[\mathbf{x}_r\mathbf{x}_r^{\mathbb{T}}] = \mathbf{E}[\mathbf{x}_i\mathbf{x}_i^{\mathbb{T}}] = E_s/2$ and $\mathbf{E}[\mathbf{x}_r\mathbf{x}_i^{\mathbb{T}}] = 0$ where $\mathbf{x} = \mathbf{x}_r + j\mathbf{x}_i$. Instead of using (8.7) as the optimal criterion, one can minimize $\mathbf{E}\|\Re\{\mathbf{G}_R\mathbf{r}\}-\mathbf{x}_r\|^2$ and $\mathbf{E}\|\Im\{\mathbf{G}_I\mathbf{r}\}-\mathbf{x}_i\|^2$ to get the equalization matrix $\mathbf{G}_R$ and $\mathbf{G}_I$ for $\mathbf{x}_r$ and $\mathbf{x}_i$, respectively. It is found that in this case $\mathbf{G}_R = \mathbf{G}_I = \mathbf{G}_1$ (a proof is given in the Appendix B). Therefore, one obtains the same equalization matrix as the conventional general equalization matrix. The reason for this is that the observation vector $\mathbf{r}$ and the pair $\{\mathbf{x},\mathbf{r}\}$ are circular and second circular [132], respectively in the case of 2-D modulation formats with symmetrical signal constellation but not in the case of 1-D modulation formats. That is, $\mathbf{E}[\mathbf{r}\mathbf{r}^{\mathbb{T}}] = 0$ and $\mathbf{E}[\mathbf{r}\mathbf{x}^{\mathbb{T}}] = 0$ for these 2-D modulation formats.

In the case of CP-DFT-OFDM, by using the criterion in eq. (8.12), the equalization matrices $\mathbf{G}_x$ and $\mathbf{G}_y$ can be obtained from

$$\bar{\mathbf{G}} = E_s \bar{\mathbf{C}}_{cp}^{\mathbb{T}} \left(E_s \bar{\mathbf{C}}_{cp} \bar{\mathbf{C}}_{cp}^{\mathbb{T}} + \frac{1}{2}\sigma^2 \mathbf{I}_{2N} \right)^{-1} \tag{8.31}$$

where

$$\bar{\mathbf{C}}_{cp} = \begin{pmatrix} \mathbf{C}_{cp}^{x} \\ \mathbf{C}_{cp}^{y} \end{pmatrix} \tag{8.32}$$

and

$$\mathbf{C}_{cp}^{x} + j\mathbf{C}_{cp}^{y} = \mathbf{C}_{cp} = \mathbf{H}_{cp}\mathbf{F}. \tag{8.33}$$

By using the criterion in eq. (8.30), one can also obtain $\mathbf{G}_x^Q = -\mathbf{G}_y$ and $\mathbf{G}_y^Q = \mathbf{G}_x$ in CP-DFT-OFDM case.

The widely linear MMSE equalizer can also be used in ZP-DCT-OFDM systems with real-valued modulation formats. Following the above gradient approach, one can obtain the equalization matrix for ZP-DCT-OFDM as

$$\bar{\mathbf{G}} = E_s \bar{\mathbf{C}}_{dct}^{\mathbb{T}} \left(E_s \bar{\mathbf{C}}_{dct} \bar{\mathbf{C}}_{dct}^{\mathbb{T}} + \frac{1}{2}\sigma^2 \mathbf{I}_{2M} \right)^{-1} \tag{8.34}$$

where $\bar{\mathbf{C}}_{dct} = \mathbf{H}\mathbf{D}^{\mathbb{T}}$.

8.4 Simulation Results

We employ the HIPERLAN/2 channel model A described in [124] and Chapter 7. The ZP-DFT-OFDM, CP-DFT-OFDM and ZP-DCT-OFDM systems, where the number of sub-carriers is 64 and zero padding or CP length is $G = 16$, are examined. Since $L = 8$ in the T-spaced TDL model for HIPERLAN/2 channel model A, no ISI occurs in our simulations. The error is composed of unequalized ICI plus noise.

Fig. 8.1, in the case of ZP-DFT-OFDM with BPSK modulation, compares the average error power of the widely linear MMSE equalizer, defined as $\sum_{p=1}^{P} \left(\Re\{\hat{x}_p\} - x_p\right)^2 / P$ where

P is the number of samples and $P = 10^5$, with the average error power of the conventional linear MMSE equalizer, defined as $\sum_{p=1}^{P} (\hat{x}_p - x_p)^2 / P$.

Fig. 8.2 gives BERs of the ZP-DFT-OFDM system and the CP-DFT-OFDM system with BPSK modulation using the linear MMSE equalizer in (8.8) and using the widely linear MMSE equalizer in (8.28) for $f_d T_u = 0.05$ where f_D is the maximum Doppler shift and T_u is the length of OFDM symbol without guard interval. The channel state information is assumed to be obtained perfectly. To ensure the reliability of the computer simulations, 2^{20} OFDM frames are generated to obtain each BER value. Although, the widely linear MMSE equalizer gives almost the same error power reduction as the general equalizer in the whole SNR range in Fig. 8.1, the BER superiority of the widely linear MMSE equalizer in Fig. 8.2 is significant only for large SNR values. The reason for this is that for small SNR values, the dominant interference is AWGN rather than the average error power. In particular, at a BER of 2×10^{-4}, the performance gains can be 1.2 dB in SNR for ZP-DFT-OFDM and more than 2 dB in SNR for CP-DFT-OFDM.

Under the same channel environments, the BER performance of the ZP-DFT-OFDM system and the CP-DFT-OFDM system with 4-ary PAM is compared in Fig. 8.3 using both MMSE equalizers. In the case of ZP-DFT-OFDM, the widely linear MMSE equalizer gives about 2 dB improvement in SNR at a BER of 3×10^{-4} over the linear MMSE equalizer.

The superiority of widely linear MMSE equalizer can also be observed from Fig. 8.4 where the BER performance of a 64-subcarrier ZP-DCT-OFDM system with BPSK modulation is given for the normalized Doppler shift values $f_d T_u = 0.001$, 0.02, 0.05, 0.1 and 0.2. Particularly, in the case of $f_d T_u = 0.001$, around 1.65 dB gain in SNR can be achieved by using the widely liner MMSE equalizer rather than the linear MMSE equalizer at a BER of 10^{-4}.

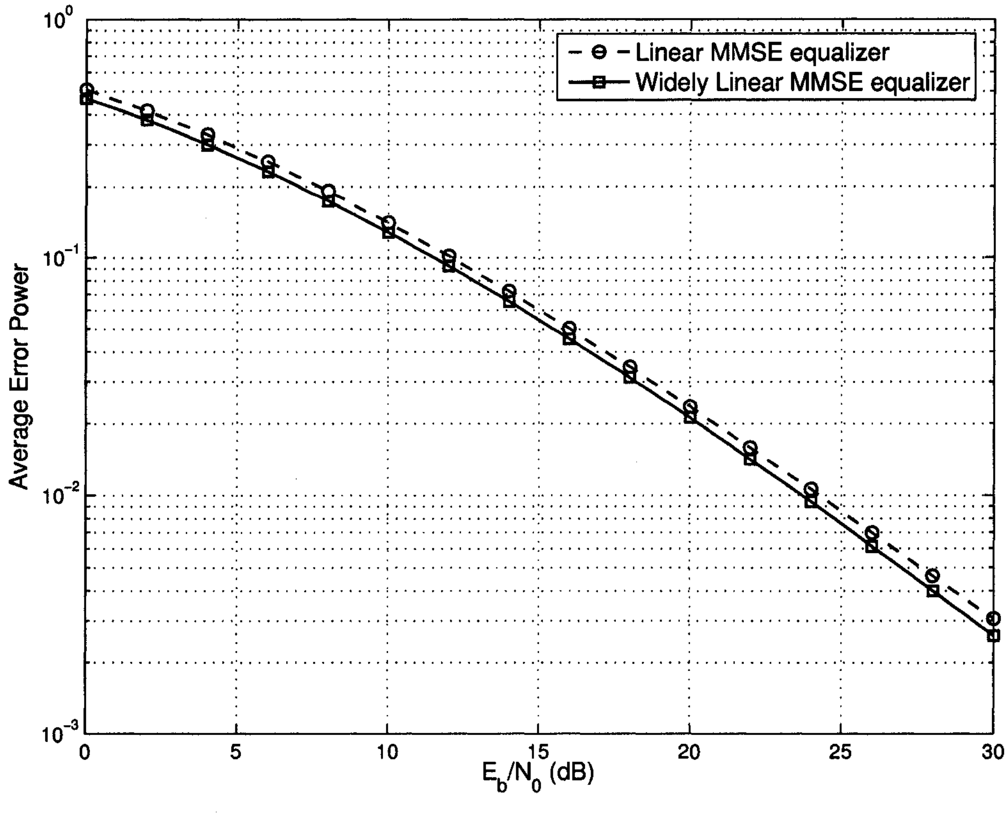

Fig. 8.1. The average error power of a 64-subcarrier ZP-DFT-OFDM (BPSK) system with the linear MMSE equalizer in (8.8) and with the widely linear MMSE equalizer for 1-D modulation formats in (8.28).

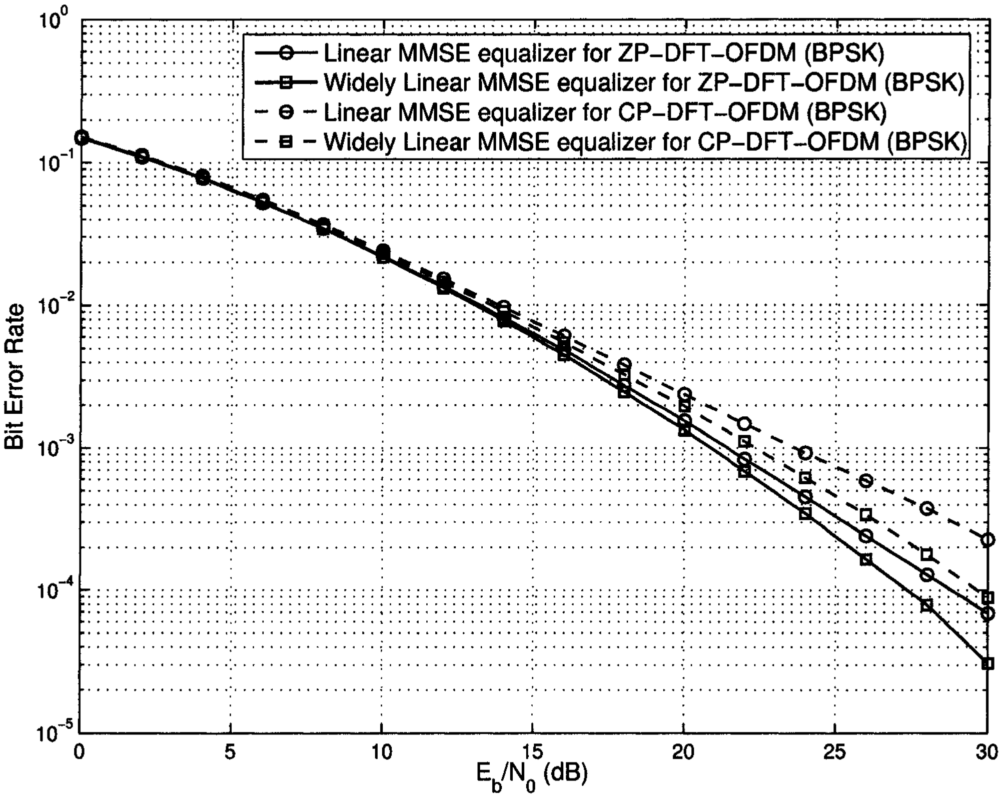

Fig. 8.2. The BERs of a 64-subcarrier ZP-DFT-OFDM (BPSK) system and a 64-subcarrier CP-DFT-OFDM (BPSK) system with the employment of a linear MMSE equalizer and a widely linear MMSE equalizer, $f_d T_u = 0.05$.

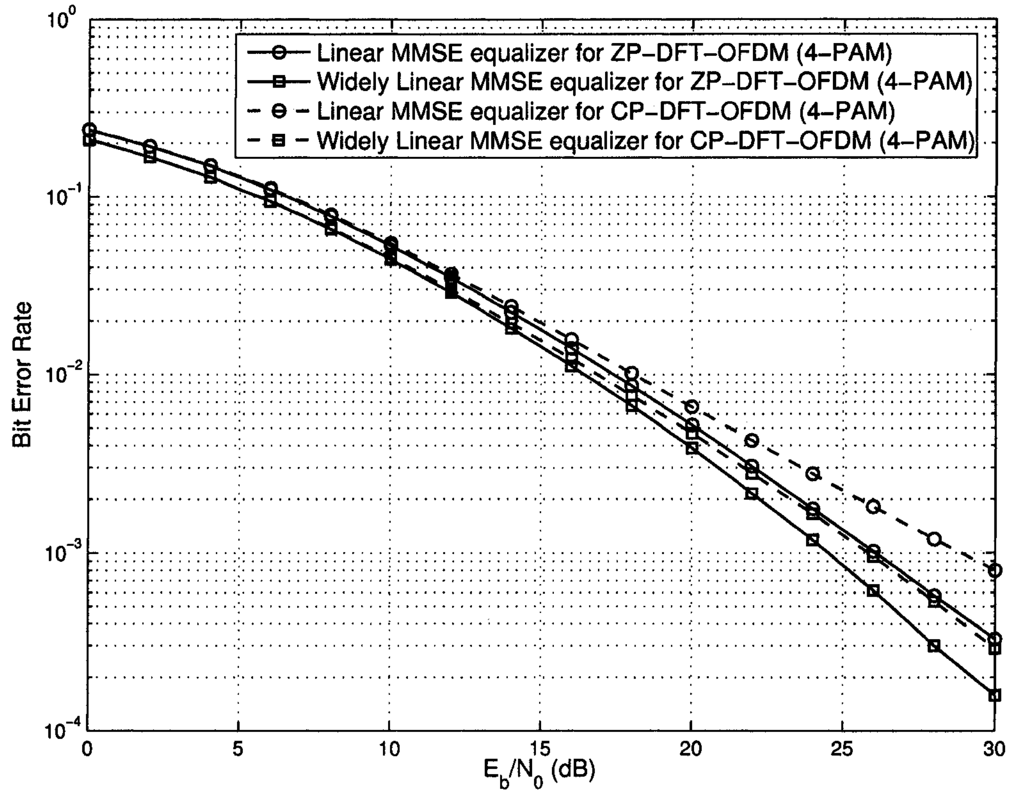

Fig. 8.3. The BERs of a 64-subcarrier ZP-DFT-OFDM (4PAM) system and a 64-subcarrier CP-DFT-OFDM (4PAM) system with the employment of a linear MMSE equalizer and a widely linear MMSE equalizer, $f_d T_u = 0.05$.

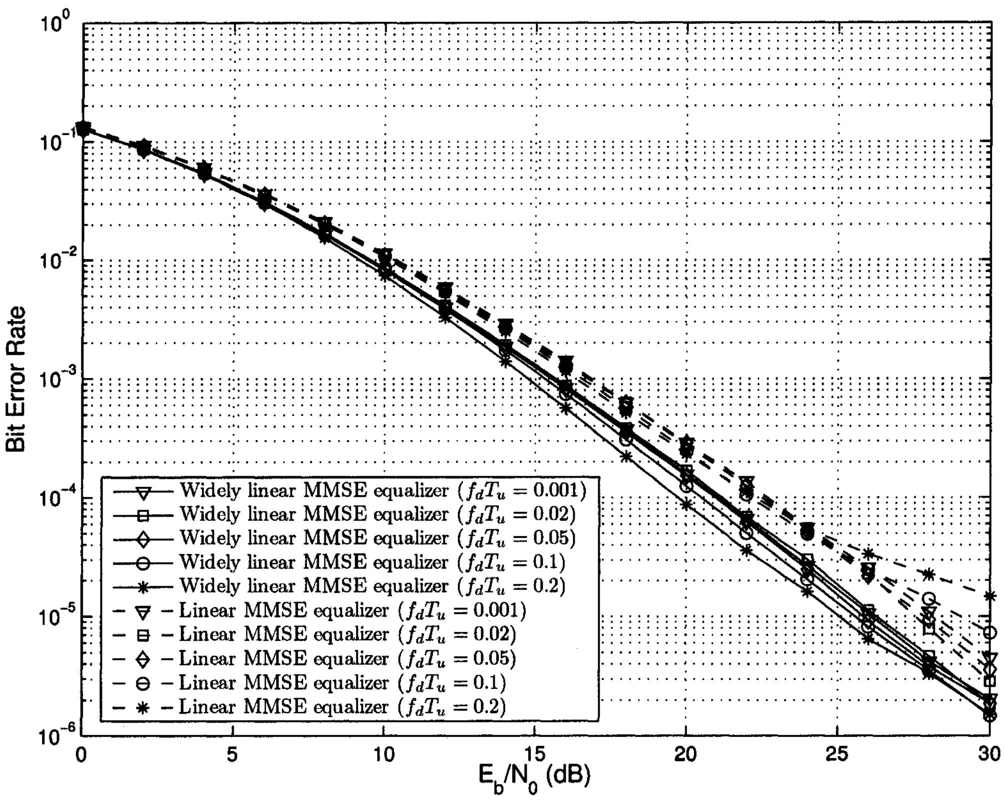

Fig. 8.4. The BERs of a 64-subcarrier ZP-DCT-OFDM (BPSK) with the employment of a linear MMSE equalizer and a widely linear MMSE equalizer, $f_dT_u = 0.001, 0.02, 0.05, 0.1$ and 0.2.

8.5 Summary

A widely linear MMSE equalizer was used in ZP-DFT-OFDM, CP-DFT-OFDM, and ZP-DCT-OFDM systems with real-valued modulation formats. It is concluded that smaller average error power and better BER performance can be achieved using the widely linear MMSE equalizer for 1-D modulation formats than the conventional linear MMSE equalizer. The practical performance gain can be as much as 2 dB.

Chapter 9

Conclusions and Future Work

9.1 Conclusions

In this thesis, we precisely evaluated the BER performance degradation of OFDM systems introduced by receiver imperfection and wireless fading environments. We further proposed several ICI reduction schemes to improve OFDM system performance. The major contributions of this thesis are listed as follows.

1. An exact method has been found to calculate the BER of a $\pi/4$-DQPSK OFDM system in the presence of frequency offset over frequency-selective fast Rayleigh fading channels for both single branch reception and multi-branch reception. An analytical BER expression has been obtained. The closed-form BER expression can be calculated directly for a small number of subcarriers. In the case of a large number of subcarriers, the BER expression can be evaluated by using a Monte Carlo method.

2. Doppler shift and delay spread of wireless channels will cause significant performance degradation. In particular, Doppler shift usually results in more performance degradation than the same amount of normalized carrier frequency offset for a $\pi/4$-DQPSK OFDM system in the presence of frequency offset over frequency-selective fast Rayleigh fading

channels.

3. In OFDM systems, there exists an optimum value of the number of subcarriers to achieve a minimum BER for a set of given system parameters. The optimum value can be found by using the analytical BER expression.

4. A closed-form and precise BER expression has been developed for the diversity reception of an OFDM system in the presence of channel estimation error over frequency-selective Rayleigh fading channels and frequency-selective Ricean fading channels .

5. It has been found in OFDM channel estimation, that sinc interpolation gives worse BER performance than the Wiener interpolation method.

6. The BTRC pulse and the Franks pulse have been proposed for use in the OFDM transmitter pulse-shaper to reduce ICI power.

7. The relations between two recently proposed Nyquist pulses, the SOCW pulse and the polynomial pulses, have been disclosed.

8. The effect of several Nyquist pulses on ICI reduction and SIR enhancement of OFDM systems in the presence of frequency offset has been examined.

9. Analytical BER expressions for an uncoded OFDM system with different transmitter pulse-shapings in the presence of carrier frequency offset in AWGN environments have been derived. It has been shown that the Franks pulse exhibits the best performance among the considered Nyquist pulses in most cases.

10. A partial-response pulse-shaped OFDM system has been proposed to reduce ICI.

11. The equivalence between the partial-response pulse-shaped OFDM system and the correlative coding OFDM system is revealed.

12. It has been proved that in the partial-response pulse-shaped OFDM system, or the correlative coding OFDM system, the data symbols with precoding are still independent.

13. Expressions for the BER of partial-response pulse-shaped OFDM systems with symbol-by-symbol detection operated in AWGN channels have been derived.

14. For small frequency offset values, it is not beneficial to use partial-response pulse-shaping or correlative coding to reduce ICI because the BER loss caused by the reduced decision distance in the multilevel signaling is greater than the benefit obtained from ICI reduction. For some large frequency offset values, these two methods can both reduce ICI and improve BER performance.

15. The BTRC windowing and the Franks windowing have been proposed using in the OFDM receiver windowing to reduce ICI.

16. An exact BER expression has been derived for windowing reception OFDM systems operating over slowly Rayleigh fading channels in the presence of carrier frequency offset.

17. The effects of several Nyquist windows, including the BTRC window, the raised-cosine window, the polynomial window, the SOCW window, the Franks window, and the double-jump window, on the performance of OFDM receiver windowing have been examined by the long term average SIR and BER measures.

18. It has been found that the comparison based on BER performance measure is not necessarily consistent with the comparison based on the SIR measure of receiver windowing OFDM systems in wireless fading environments.

19. Previous window design based on minimizing ICI or maximizing SIR, may not give pulse designs with the best BER performance in fading environments.

20. In slowly Rayleigh fading environments, the BTRC windowing OFDM reception gives the smallest BER among the six OFDM windowing reception systems considered in this thesis when the pulse roll-off factor is not large. However, the Franks windowing or the SOCW windowing shows better BER performance when the roll-off factor approaches one.

21. A zero-padded DCT-OFDM system has been proposed to improve OFDM system performance. With both MMSE detection and MMSE DFD with ordering, the ZP-DCT-OFDM achieves smaller BER than the ZP-DFT-OFDM system and CP-DFT-OFDM system. In convolutional coding systems, the performance benefit achieved by using the proposed ZP-DCT-OFDM is about 1 dB in SNR.

22. A set of ICI weighting coefficients has been developed for DCT-OFDM in the presence of frequency offset.

23. It has been shown that in the presence of frequency offset, the ICI coefficients in DCT-OFDM are more concentrated around the desired sample location, introducing less ICI leakage to adjacent subcarriers, than the DFT-OFDM.

24. The superiority of DCT-OFDM over the DFT-OFDM is related to the energy compaction property of DCT.

25. The exact BER performance of a DCT-OFDM system in the presence of carrier frequency offset in AWGN environments has been derived. It has been found that the DCT-OFDM exhibits a smaller BER than the conventional DFT-OFDM.

26. A widely linear MMSE equalizer has been proposed using in ZP-DFT-OFDM systems, CP-DFT-OFDM systems, and ZP-DCT-OFDM systems with real-valued modulation formats to further reduce ICI and improve BER performance.

27. It has been proved that the widely linear MMSE equalization matrices for some 2-D modulation formats with symmetry in the signal constellation, such as QPSK and 16-QAM, are the same as conventional linear MMSE equalization matrices.

9.2 Suggestions for Future Work

1. The performance of transmitter pulse-shaping OFDM systems and receiver windowing OFDM systems is related to the chosen polynomial coefficients with the employment of polynomial pulse and the SOCW pulse. Currently, these coefficients are determined empirically. It is of interest to derive an optimal method to find these coefficients.

2. We have derived the BER expressions of a $\pi/4$-DQPSK OFDM system in the presence of carrier frequency offset over frequency selective fast Rayleigh fading channels. It is also of interest to consider the exact BER analysis for the system in Ricean fading environments.

3. It is also beneficial to consider the exact BER performance of the $\pi/4$-DQPSK OFDM system when the differential encoding is performed in the time domain, OFDM symbol by OFDM symbol.

4. In Chapter 2 and Chapter 3, we calculated the exact BER degradation introduced by frequency offset and channel estimation error, respectively. It is of interest to evaluate the performance of a system exhibiting both frequency offset and channel estimation error. It should be noted that the channel estimation error is related to frequency offset in this case.

5. The MMSE and MMSE DFD with ordering is complex for a ZP-DCT-OFDM system with a large number of subcarriers due to the matrix inversion operation. It is interesting to design a simplified detection scheme. In a possible solution, we may consider

only several immediately neighboring subcarriers around the desired subcarrier, and ignore the ICI leakage introduced by other subcarriers. This simplification works because the dominant ICI power leakage actually comes from a small number of immediately neighboring subcarriers as shown in Fig. 7.3 in Chapter 7. This simplification will significantly decrease the size of equalization matrix.

References

[1] R. R. Mosier and R. G. Clabaugh, "Kineplex, a bandwidth-efficient binary transmission system," *AIEE Trans.*, vol. 76, pp. 723–728, Jan. 1958.

[2] R. W. Chang, "Synthesis of band-limited orthogonal signals for multichannel data transmission," *Bell System Technical Journal*, vol. 45, pp. 1775–1796, Dec. 1966.

[3] B. R. Saltzberg, "Performance of an efficient parallel data transmission system," *IEEE Trans. Commun. Technol.*, vol. 15, pp. 805–811, Dec. 1967.

[4] R. W. Chang and R. A. Gibbey, "A theoretical study of performance of an orthogonal multiplexing data transmission scheme," *IEEE Trans. Commun. Technol.*, vol. 16, pp. 529–540, Aug. 1968.

[5] S. B. Weinstein and P. M. Ebert, "Data transmission by frequency-division multiplexing using the discrete Fourier transform," *IEEE Trans. Commun. Technol.*, vol. 19, pp. 628–634, Oct. 1971.

[6] A. Peled and A. Ruiz, "Frequency domain data transmission using reduced computational complexity algorithms," in *Proc. IEEE Int. Conf. Acoust., Speech, Signal Processing*, Denver, USA, Apr. 1980, vol. 5, pp. 964–967.

[7] L. J. C. Jr., "Analysis and simulation of a digital mobile channel using orthogonal frequency division multiplexing," *IEEE Trans. Commun.*, vol. 33, pp. 665–675, July 1985.

[8] J. A. C. Bingham, "Multicarrier modulation for data transmission: an idea whose time has come," *IEEE Commun. Mag.*, vol. 28, pp. 5–8, May 1990.

[9] J. M. Cioffi, "A multicarrier primer," [Online]. Available: `http://www-isl.stanford.edu/people/cioffi/pdf/multicarrier.pdf`.

[10] W. Y. Zou and Y. Wu, "COFDM: an overview," *IEEE Trans. Broadcast.*, vol. 41, pp. 1–8, Mar. 1995.

[11] IEEE Std 802.11a-1999, "Wireless LAN medium access control (MAC) and physical layer (PHY) specifications: High-speed physical layer in the 5 GHz band," 1999.

[12] IEEE Std 802.16-2004, "Air interface for fixed broadband wireless access systems," June 2004.

[13] IEEE Std 802.16e-2005, "Air interface for fixed and mobile broadband wireless access systems - Amendment 2: Physical and medium access control layers for combined fixed and mobile operation in licensed bands and Corrigendum 1," Feb. 2006.

[14] ETSI EN 300 401 v1.3.3 (2001-05), "Radio broadcasting systems; Digital audio broadcasting (DAB) to mobile, portable and fixed receivers," May 2001.

[15] ETSI EN 300 429 v1.2.1 (1998-04), "Digital video broadcasting (DVB); Framing structure, channel coding and modulation for cable systems," 1998.

[16] ETSI TS 101 475 v1.3.1 (2001-12), "Broadband radio access networks (BRAN); HIPERLAN Type 2; Physical (PHY) layer," Dec. 2001.

[17] J. G. Proakis, *Digital Communications*, fourth ed. New York: McGraw-Hill, 2000.

[18] A. V. Oppenheim, R. W. Schafer, and J. R. Buck, *Discrete-Time Signal Processing*, second ed. New Jersey: Prentice Hall, 1998.

[19] A. Bahai and B. Saltzberg, *Multi-Carrier Digital Communications, Theory and Applications of OFDM*. New York: Kluwer Academic, 1999.

[20] H. Steendam and M. Moeneclaey, "Analysis and optimization of the performance of OFDM on frequency-selective time-selective fading channels," *IEEE Trans. Commun.*, vol. 47, pp. 1811–1819, Dec. 1999.

[21] Y. Kim, I. Song, H. G. Kim, T. Chang, and H. M. Kim, "Performance analysis of a coded OFDM system in time-varying multipath Rayleigh fading channels," *IEEE Trans. Veh. Technol.*, vol. 48, pp. 1610–1615, Sept. 1999.

[22] B. L. Floch, M. Alard, and C. Berrou, "Coded orthogonal frequency division multiplex," *Proc. IEEE*, vol. 83, pp. 982–996, June 1995.

[23] M. Ardakani, T. Esmailian, and F. R. Kschischang, "Near-capacity coding in multicarrier modulation systems," *IEEE Trans. Commun.*, vol. 52, pp. 1880–1889, Nov. 2004.

[24] T. Rappaport, *Wireless Communications Principles and Practice*, 2 ed. Upper Saddle River,NJ: Prentice Hall PTR, 2002.

[25] A. Jeffrey, *Handbook of Mathematical Formulas and Integrals*, 2 ed. San Diego: Academic Press, 2000.

[26] B. Sklar, "Rayleigh fading Channels in mobile digital communications systems - Part II: mitigation," *IEEE Commun. Mag.*, vol. 35, pp. 102–109, July 1997.

[27] T. Pollet, M. V. Bladel, and M. Moeneclaey, "BER sensitivity of OFDM systems to carrier frequency offset and wiener phase noise," *IEEE Trans. Commun.*, vol. 43, pp. 191–193, Feb./Mar./Apr. 1995.

[28] W. Hwang, H. Kang, and K. Kim, "Approximation of SNR degradation due to carrier frequency offset for OFDM in shadowed multipath channels," *IEEE Commun. Lett.*, vol. 7, pp. 581–583, Dec. 2003.

[29] K. Sathananthan and C. Tellambura, "Probability of error calculation of OFDM systems with frequency offset," *IEEE Trans. Commun.*, vol. 49, pp. 1884–1888, Nov. 2001.

[30] N. C. Beaulieu, "An infinite series for the computation of the complementary probability distribution function of a sum of independent random variables and its application to the sum of Rayleigh random variables," *IEEE Trans. Commun.*, vol. 38, pp. 1463–1474, Sept. 1990.

[31] N. C. Beaulieu, "The evaluation of error probabilities for intersymbol and cochannel interference," *IEEE Trans. Commun.*, vol. 39, pp. 1740–1749, Dec. 1991.

[32] L. Tomba, "On the effect of Wiener phase noise in OFDM systems," *IEEE Trans. Commun.*, vol. 46, pp. 580–583, May 1998.

[33] R. Narasimhan, "Performance of diversity schemes for OFDM systems with frequency offset, phase noise, and channel estimation errors," *IEEE Trans. Commun.*, vol. 50, pp. 1561–1565, Oct. 2002.

[34] L. Rugini and P. Banelli, "BER of OFDM systems impaired by carrier frequency offset in multipath fading channels," *IEEE Trans. Wireless Commun.*, vol. 4, pp. 2279–2288, Sept. 2005.

[35] G. Zimmermann, M. Rosenberger, and S. Dostert, "Theoretical bit error rate for uncoded and coded data transmission in digital audio broadcasting," in *Proc. IEEE International Conference on Communications*, Dallas, USA, June 1996, pp. 297–301.

[36] M. Lott, "Comparison of frequency and time domain differential modulation in an OFDM system for wireless ATM," in *Proc. IEEE 49th Vehicular Technology Conference*, Houston, USA, May 1999.

[37] J. Lu, T. T. Tjhung, F. Adachi, and C. L. Huang, "BER performance of OFDM-MDPSK system in frequency-selective Rician fading with diversity reception," *IEEE Trans. Veh. Technol.*, vol. 49, pp. 1216–1225, July 2000.

[38] K. Zhong, T. T. Tjhung, and F. Adachi, "A general SER formula for an OFDM system with MDPSK in frequency domain over Rayleigh fading channels," *IEEE Trans. Commun.*, vol. 52, pp. 584–594, Apr. 2004.

[39] G. L. Turin, "The characteristic function of Hermitian quadratic forms in complex normal variables," *Biometrika*, vol. 47, pp. 199–201, June 1960.

[40] N. R. Goodman, "Statistical analysis based on a certain multivariate complex Gaussian distribution (an introduction)," *The Annals of Mathematical Statistics*, vol. 34, pp. 152–177, Mar. 1963.

[41] F. D. Neeser and J. L. Massey, "Proper complex random processes with applications to information theory," *IEEE Trans. Inform. Theory*, vol. 39, pp. 1293–1302, July 1993.

[42] J. H. Halton, "A retrospective and prospective survey of the Monte Carlo method," *SIAM Review*, vol. 12, pp. 1–63, Jan. 1970.

[43] W. C. Jakes, *Microwave Mobile Communications*. Piscataway, NJ: IEEE Press, 1994.

[44] N. C. Beaulieu, "Generation of correlated Rayleigh fading envelopes," *IEEE Commun. Lett.*, vol. 3, pp. 172–174, June 1999.

[45] S. B. Bulumulla, S. A. Kassam, and S. S. Venkatesh, "A systematic approach to detecting OFDM signals in a fading channel," *IEEE Trans. Commun.*, vol. 48, pp. 725–728, May 2000.

[46] L. E. Miller and J. S. Lee, "BER expressions for differentially detected $\pi/4$ DQPSK modulation," *IEEE Trans. Commun.*, vol. 46, pp. 71–81, Jan. 1998.

[47] A. Papoulis and S. U. Pillai, *Probability, Random Variables, and Stochastic Processes*, 4 ed. New York: McGraw-Hill, 2002.

[48] J. Behboodian, "On a mixture of normal distributions," *Biometrika*, vol. 57, pp. 215–217, Apr. 1970.

[49] J. Gil-Pelaez, "Note on the inversion theorem," *Biometrika*, vol. 38, pp. 481–482, Dec. 1951.

[50] A. Papoulis, *The Fourier Integral and its Applications*. New York: McGraw-Hill, 1962.

[51] E. Lukacs, "Inversion formulae for characteristic functions of absolutely continuous distributions," *The American Mathematical Monthly*, vol. 71, pp. 44–47, Jan. 1964.

[52] G. Grimmett and D. Stirzaker, *Probability and Random Processes*, 3 ed. New York: Oxford University Press, 2001.

[53] J. W. Brown and R. V. Churchill, *Complex Variables and Applications*, 6 ed. New York: McGraw-Hill, 1996.

[54] E. Haas, "Aeronautical channel modeling," *IEEE Trans. Veh. Technol.*, vol. 51, pp. 254–264, Mar. 2002.

[55] Y. Li, L. J. Cimini, Jr., and N. R. Sollenberger, "Robust channel estimation for OFDM systems with rapid dispersive fading channels," *IEEE Trans. Commun.*, vol. 46, pp. 902–915, July 1998.

[56] Y. Li, "Pilot-symbol-aided channel estimation for OFDM in wireless systems," *IEEE Trans. Veh. Technol.*, vol. 49, pp. 1207–1215, July 2000.

[57] O. Edfors, M. Sandell, J. van de Beek, S. K. Wilson, and P. O. Börjesson, "OFDM channel estimation by singular value decomposition," *IEEE Trans. Commun.*, vol. 46, pp. 931–939, July 1998.

[58] P. Hoeher, S. Kaiser, and P. Robertson, "Two-dimensional pilot-symbol-aided channel estimation by Wiener filtering," in *Proc. 1997 IEEE International Conference on Acoustics, Speech, and Signal Processing*, Apr. 1997, vol. 3, pp. 21–24.

[59] F. Tufvesson and T. Maseng, "Pilot assisted channel estimation for OFDM in mobile cellular systems," in *Proc. 1997 IEEE 47th Vehicular Technology Conference*, May 1997, vol. 3, pp. 1639–1643.

[60] J. K. Cavers, "An analysis of pilot symbol assisted modulation for Rayleigh fading channels," *IEEE Trans. Veh. Technol.*, vol. 40, pp. 686–693, Nov. 1991.

[61] X. Tang, M. S. Alouini, and A. J. Goldsmith, "Effect of channel estimation error on M-QAM BER performance in Rayleigh fading," *IEEE Trans. Commun.*, vol. 47, pp. 1856–1864, Dec. 1999.

[62] L. Cao and N. C. Beaulieu, "Exact error-rate analysis of diversity 16-QAM with channel estimation error," *IEEE Trans. Commun.*, vol. 52, pp. 1019–1029, June 2004.

[63] B. Xia and J. Wang, "Effect of channel-estimation error on QAM systems with antenna diversity," *IEEE Trans. Commun.*, vol. 53, pp. 481–488, Mar. 2005.

[64] H. Cheon and D. Hong, "Effect of channel estimation error in OFDM-based WLAN," *IEEE Commun. Lett.*, vol. 6, pp. 190–192, May 2002.

[65] M. Chang and Y. T. Su, "Performance analysis of equalized OFDM systems in Rayleigh fading," *IEEE Trans. Wireless Commun.*, vol. 1, pp. 721–732, Oct. 2002.

[66] M. D. Yacoub, *Foundations of Mobile Radio Engineering*. Boca Raton, Florida: CRC Press, 1993.

[67] T. K. Moon and W. C. Stirling, *Mathematical Methods and Algorithms for Signal Processing*. New Jersey: Prentice Hall, 2000.

[68] J. W. Choi and Y. H. Lee, "Design of 2-D channel estimation filters for OFDM systems," in *Proc. 2005 IEEE International Conference on Communications*, Seoul, South Korea, May 2005, vol. 4, pp. 2568–2572.

[69] L. Hanzo, W. Webb, and T. Keller, *Single- and Multi-carrier Quadrature Amplitude Modulation*. IEEE Press, John Wiley, 2000.

[70] S. Haykin, *Adaptive Filter Theory*, 4 ed. Upper Saddle River, New Jersey: Prentice-Hall, 2002.

[71] J. G. Proakis, "On the probability of error for multichannel reception of binary signals," *IEEE Trans. Commun. Technol.*, vol. 16, pp. 68–71, Feb. 1968.

[72] Y. Zhao, J. Leclercq, and S. Häggman, "Intercarrier interference compression in OFDM communication systems by using correlative coding," *IEEE Commun. Lett.*, vol. 2, pp. 214–216, Aug. 1998.

[73] J. Armstrong, "Analysis of new and existing methods of reducing intercarrier interference due to carrier frequency offset in OFDM," *IEEE Trans. Commun.*, vol. 47, pp. 365–369, Mar. 1999.

[74] Y. Zhao and S. Häggman, "Intercarrier interference self-cancellation scheme for OFDM mobile communication systems," *IEEE Trans. Commun.*, vol. 49, pp. 1185–1191, July 2001.

[75] H. Zhang and Y. Li, "Optimum frequency-domain partial response encoding in OFDM system," *IEEE Trans. Commun.*, vol. 51, pp. 1064–1068, July 2003.

[76] A. Vahlin and N. Holte, "Optimal finite duration pulses for OFDM," *IEEE Trans. Commun.*, vol. 44, pp. 10–14, Jan. 1996.

[77] B. Hirosaki, "An orthogonally multiplexed QAM system using the discrete Fourier transform," *IEEE Trans. Commun.*, vol. 29, pp. 982–989, July 1981.

[78] R. Haas and J. C. Belefiore, "A time-frequency well-localized pulse for multiple carrier transmission," *Wireless Pers. Commun.*, vol. 5, pp. 1–18, July 1997.

[79] W. Kozek and A. F. Molisch, "Nonorthogonal pulseshapes for multicarrier communications in doubly dispersive channels," *IEEE J. Select. Areas Commun.*, vol. 16, pp. 1579–1589, Oct. 1998.

[80] T. Strohmer and S. Beaver, "Optimal OFDM design for time-frequency dispersive channels," *IEEE Trans. Commun.*, vol. 51, pp. 1111–1122, July 2003.

[81] R. Y. Li and G. Stette, "Time-limited orthogonal multicarrier modulation schemes," *IEEE Trans. Commun.*, vol. 43, pp. 1269–1272, Feb./Mar./Apr. 1995.

[82] L. Vangelista and N. Laurenti, "Efficient implementations and alternative architectures for OFDM-OQAM systems," *IEEE Trans. Commun.*, vol. 49, pp. 664–675, Apr. 2001.

[83] P. Siohan, C. Siclet, and N. Lacaille, "Analysis and design of OFDM/OQAM systems based on filterbank theory," *IEEE Trans. Commun.*, vol. 50, pp. 1170–1183, May 2002.

[84] M. Martone, "A multicarrier system based on the fractional Fourier transform for time-frequency-selective channels," *IEEE Trans. Commun.*, vol. 49, pp. 1011–1020, June 2001.

[85] V. Namias, "The fractional Fourier transform and its application in quantum mechanics," *J. Inst. Math. Applicant.*, vol. 25, pp. 241–265, 1980.

[86] L. E. Franks, "Further results on Nyquist's problem in pulse transmission," *IEEE Trans. Commun. Technol.*, vol. 16, pp. 337–340, Apr. 1968.

[87] S. H. Müller-Weinfurtner, "Optimum Nyquist windowing in OFDM receivers," *IEEE Trans. Commun.*, vol. 49, pp. 417–420, Mar. 2001.

[88] N. C. Beaulieu, C. C. Tan, and M. O. Damen, "A "better than" Nyquist pulse," *IEEE Commun. Lett.*, vol. 5, pp. 367–368, Sept. 2001.

[89] N. C. Beaulieu and M. O. Damen, "Parametric Construction of Nyquist-I Pulses," *IEEE Trans. Commun.*, vol. 52, pp. 2134–2142, Dec. 2004.

[90] R. Song and S. Leung, "A novel OFDM receiver with second order polynomial Nyquist window function," *IEEE Commun. Lett.*, vol. 9, pp. 391–393, May 2005.

[91] S. Chandan, P. Sandeep, and A. K. Chaturvedi, "A family of ISI free polynomial pulses," *IEEE Commun. Lett.*, vol. 9, pp. 496–498, June 2005.

[92] M. Russell and G. L. Stüber, "Interchannel interference analysis of OFDM in a mobile environment," in *Proc. IEEE 45th Vehicular Technology Conference*, July 1995, vol. 2, pp. 820–824.

[93] L. Wan and V. K. Dubey, "BER performance of OFDM system over frequency non-selective fast Ricean fading channels," *IEEE Commun. Lett.*, vol. 5, pp. 19–21, Jan. 2001.

[94] L. Rugini, P. Banelli, and S. Cacopardi, "Probability of error of OFDM systems with carrier frequency offset in frequency-selective fading channels," in *Proc. IEEE ICC 2004*, Paris, France, June 2004, vol. 6, pp. 3289–3293.

[95] N. C. Beaulieu and J. Cheng, "Precise error rate analysis of bandwidth efficient BPSK in Nakagami fading and co-channel interference," *IEEE Trans. Commun.*, vol. 52, pp. 149–158, Jan. 2004.

[96] Y. Zhao, J. D. Leclercq, and S. G. Häggman, "Intercarrier interference compression in OFDM communication systems by using correlative coding," *IEEE Commun. Lett.*, vol. 2, pp. 214–216, Aug. 1998.

[97] P. Tan and N. C. Beaulieu, "Reduced ICI in OFDM systems using the "better than" raised-cosine pulse," *IEEE Commun. Lett.*, vol. 8, pp. 135–137, Mar. 2004.

[98] C. Muschallik, "Improving an OFDM reception using an adaptive Nyquist windowing," *IEEE Trans. Consumer Electron.*, vol. 42, pp. 259–269, Aug. 1996.

[99] R. Song and S. Leung, "A novel OFDM receiver with second order polynomial Nyquist window function," *IEEE Commun. Lett.*, vol. 9, pp. 391–393, May 2005.

[100] J. Lee, H. Lou, D. Toumpakaris, and J. M. Cioffi, "SNR analysis of OFDM systems in the presence of carrier frequency offset for fading channels," *IEEE Trans. Wireless Commun.*, to be published.

[101] W. H. Press, S. A. Teukolsky, W. T. Vetterling, and B. P. Flannery, *Numerical Recipes in C : the art of scientific computing*, 2 ed. Cambridge, UK: Cambridge University Press, 1992.

[102] J. A. C. Bingham, *ADSL,VDSL, and multicarrier modulation.* West Sussex: John Wiley, 2000.

[103] J. S. Chow, J. C. Tu, and J. M. Cioffi, "A discrete multitone transceiver system for HDSL applications," *IEEE J. Select. Areas Commun.*, vol. 9, pp. 895–908, Aug. 1991.

[104] A. Schuchert, R. Hasholzner, and P. Antoine, "A novel IQ imbalance compensation scheme for the reception of OFDM signals," *IEEE Trans. Consumer Electron.*, vol. 47, pp. 313–318, Aug. 2001.

[105] W. H. Chen, C. H. Smith, and S. C. Fralick, "A fast computational algorithm for the discrete cosine transform," *IEEE Trans. Commun.*, vol. 25, pp. 1004–1009, Sept. 1977.

[106] Z. D. Wang, "Fast algorithms for the discrete w transform and for the discrete fourier transform," *IEEE Trans. Acoust., Speech, Signal Processing*, vol. 32, pp. 803–816, Aug. 1984.

[107] J. Tan and G. L. Stüber, "Constant envelope multi-carrier modulation," in *Proc. IEEE MILCOM 2002*, 2002, vol. 1, pp. 607–611.

[108] F. Xiong, "M-ary amplitude shift keying OFDM system," *IEEE Trans. Commun.*, vol. 51, pp. 1638–1642, Oct. 2003.

[109] X. G. Xia, "Precoded and vector OFDM robust to channel spectral nulls and with reduced prefix length in single transmit antenna systems," *IEEE Trans. Commun.*, vol. 49, pp. 1363–1374, Aug. 2001.

[110] S. A. Martucci, "Symmetric convolution and the discrete sine and cosine transform," *IEEE Trans. Signal Processing*, vol. 42, pp. 1038–1051, May 1994.

[111] G. D. Mandyam, "On the discrete cosine transform and OFDM systems," in *Proc. IEEE Int. Conf. Acoust., Speech, Signal Processing*, Apr. 2003, vol. 4, pp. 544–547.

[112] N. Al-Dhahir and H. Minn, "A new multicarrier transceiver based on the discrete cosine transform," in *Proc. IEEE Wireless Communications and Networking Conference*, New Orleans, Mar. 2005.

[113] B. Muquet, Z. Wang, G. B. Giannakis, M. Courville, and P. Duhamel, "Cyclic prefixing or zero padding for wireless multicarrier transmissions," *IEEE Trans. Commun.*, vol. 50, pp. 2136–2148, Dec. 2002.

[114] P. H. Moose, "A technique for orthogonal frequency division multiplexing frequency offset correction," *IEEE Trans. Commun.*, vol. 42, pp. 2908–2914, Oct. 1994.

[115] K. R. Rao and P. Yip, *Discrete Cosine Transform.* Academic Press, 1990.

[116] D. Lu and K. Yao, "Improved importance sampling technique for efficient simulation of digital communication systems," *IEEE J. Select. Areas Commun.*, vol. 6, pp. 67–75, Jan. 1988.

[117] G. L. Stüber, *Principles of Mobile Communication*, second ed. Boston: Kluwer Academic Publishers, 2001.

[118] J. Sykora, "Tapped delay line model of linear randomly time-variant WSSUS channel," *Electron. Lett.*, vol. 36, pp. 1656–1657, 14th September 2000.

[119] Y. S. Choi, P. J. Voltz, and F. A. Cassara, "On channel estimation and detection for multicarrier signals in fast and selective Rayleigh fading channels," *IEEE Trans. Commun.*, vol. 49, pp. 1375–1387, Aug. 2001.

[120] P. W. Wolniansky, G. J. Foschini, G. D. Golden, and R. A. Valenzuela, "V-BLAST: an architecture for realizing very high data rates over the rich-scattering wireless channel," in *Proc. URSI ISSSE'98*, Pisa, Italy, 1998, pp. 295–300.

[121] B. Hassibi, "An efficient square-root algorithm for BLAST," in *Proc. ICASSP*, 2000, vol. 2, pp. 737–740.

[122] G. Ginis and J. M. Cioffi, "On the relation between V-BLAST and the GDFE," *IEEE Commun. Lett.*, vol. 5, pp. 364–366, Sept. 2001.

[123] G. H. Golub and C. F. V. Loan, *Matrix Computation*, 3 ed. Baltimore: The Johns Hopkins University Press, 1996.

[124] ETSI Normalization Committee, "Channel models for HIPERLAN/2 in different indoor scenarios," European Telecommunications Standards Institute, Sophia-Antipolis, France, Document 3ERI085B, March 30, 1998.

[125] D. J. Young and N. C. Beaulieu, "The generation of correlated Rayleigh random variates by inverse discrete Fourier transform," *IEEE Trans. Commun.*, vol. 48, pp. 1114–1127, July 2000.

[126] B. Picinbono and P. Chevalier, "Widely linear estimation with complex data," *IEEE Trans. Signal Processing*, vol. 43, pp. 2030–2033, Aug. 1995.

[127] P. J. Schreier and L. L. Scharf, "Second-order analysis of improper complex random vectors and processes," *IEEE Trans. Signal Processing*, vol. 51, pp. 714–725, Mar. 2003.

[128] W. H. Gerstacker, "Receivers with widely linear processing for frequency-selective channels," *IEEE Trans. Commun.*, vol. 51, pp. 1512–1523, Sept. 2003.

[129] S. Buzzi, M. Lops, and A. M. Tulino, "A new family of MMSE multiuser receivers for interference suppression in DS/CDMA systems employing BPSK modulation," *IEEE Trans. Commun.*, vol. 49, pp. 154–167, Jan. 2001.

[130] D. Darsena, G. Gelli, L. Paura, and F. Verde, "Widely linear equalization and blind channel identification for interference-contaminated multicarrier systems," *IEEE Trans. Signal Processing*, vol. 53, pp. 1163–1177, Mar. 2005.

[131] Z. Wang and G. B. Giannakis, "Wireless multicarrier communications where Fourier meets Shannon," *IEEE Signal Processing Mag.*, vol. 17, pp. 29–48, May 2000.

[132] T. Kailath, A. H. Sayed, and B. Hassibi, *Linear Estimation*. Upper Saddle River, New Jersey: Prentice Hall, 2000.

Appendix A

In Chapter 5, we assume that the source binary data sequence and the precoded sequence are D_n and P_n, respectively. The transmitted BPSK data symbol with precoding is then $a_m = \sqrt{E_b}(2P_m - 1)$. In this Appendix, we will show that the data symbols a_m, $m = 0, \cdots, N-1$ are independent.

The source binary data D_n, $n = 0, 1, \cdots, N-1$, take value 0 or 1 independently with probability 0.5. The precoded sequence P_n is obtained as

$$P_n = D_n \oplus P_{n-1} \tag{A.1}$$

where $\oplus$ denotes modulo-2 plus. Without loss of generality, we assume $P_0 = D_0$, thus

$$\text{Prob}\{P_0 = 0\} = \text{Prob}\{P_0 = 1\} = 0.5. \tag{A.2}$$

Since $P_1 = D_1 \oplus P_0$, one has

$$\begin{aligned} &\text{Prob}\{P_1 = 0\} \\ &= \text{Prob}\{D_1 = 1 \text{ and } P_0 = 1\} + \text{Prob}\{D_1 = 0 \text{ and } P_0 = 0\} \\ &= 0.5. \end{aligned} \tag{A.3}$$

Following the same approach, we can also get $\text{Prob}\{P_1 = 1\} = 0.5$. As a result, it is proved that P_m takes values 0 or 1 with probability 0.5, that is

$$\text{Prob}\{P_n = 0\} = \text{Prob}\{P_n = 1\} = 0.5. \tag{A.4}$$

Now we consider an arbitrary length-N binary sequence b_n, $n = 0, 1, \cdots, N-1$, and b_n taking values 0 or 1. Let $\mathbf{X}_i$ denote event $\{P_i = b_i\}$. From (A.4), we have

$$\text{Prob}\{\ \mathbf{X}_i\ \} = \text{Prob}\{\ P_i = b_i\ \} = \frac{1}{2}. \tag{A.5}$$

The precoded sequence $P_0, P_1, \cdots$, and P_{N-1} are independent if the events $\mathbf{X}_0, \mathbf{X}_1, \cdots, \mathbf{X}_{N-1}$ are independent [47, pp. 244].

We will first show that any two of $\mathbf{X}_i$, $i = 0, \cdots, N-1$, are independent. Without loss of generality, we assume that $i > j$, so the probability of event $\mathbf{X}_i$ conditioned on $\mathbf{X}_j$ is

$$\begin{aligned}
&\text{Prob}\{\ \mathbf{X}_i \mid \mathbf{X}_j\ \} = \text{Prob}\{\ P_i = b_i \mid P_j = b_j\ \} \\
&= \text{Prob}\{\ D_i \oplus D_{i-1} \oplus \cdots \oplus D_{j+1} \oplus P_j = b_i \mid P_j = b_j\ \} \\
&= \begin{cases} \text{Prob}\{\ \text{the number of 1s in } D_i, D_{i-1}, \cdots, D_{j+1} \text{ is an even number}\ \}, & b_i = b_j \\ \text{Prob}\{\ \text{the number of 1s in } D_i, D_{i-1}, \cdots, D_{j+1} \text{ is an odd number}\ \}, & b_i \neq b_j \end{cases} \\
&= \begin{cases} \left(C_{i-j}^0 + C_{i-j}^2 + \cdots + C_{i-j}^{i-j-1}\right)\frac{1}{2^{i-j}} = \frac{1}{2}, & b_i = b_j \\ \left(C_{i-j}^1 + C_{i-j}^3 + \cdots + C_{i-j}^{i-j}\right)\frac{1}{2^{i-j}} = \frac{1}{2}, & b_i \neq b_j \end{cases} \quad \text{when } i-j \text{ is odd} \\
&= \begin{cases} \left(C_{i-j}^0 + C_{i-j}^2 + \cdots + C_{i-j}^{i-j}\right)\frac{1}{2^{i-j}} = \frac{1}{2}, & b_i = b_j \\ \left(C_{i-j}^1 + C_{i-j}^3 + \cdots + C_{i-j}^{i-j-1}\right)\frac{1}{2^{i-j}} = \frac{1}{2}, & b_i \neq b_j \end{cases} \quad \text{when } i-j \text{ is even.}
\end{aligned} \tag{A.6}$$

where C_n^k denotes the number of combinations of n things taken k at a time. On the other hand, $\text{Prob}\{\ \mathbf{X}_i\ \} = \frac{1}{2}$. Therefore $\text{Prob}\{\ \mathbf{X}_i \mid \mathbf{X}_j\ \} = \text{Prob}\{\ \mathbf{X}_i\ \}$, that is, the occurrence of event $\mathbf{X}_j$ does not change the probability that event $\mathbf{X}_i$ occurs. So any two events $\mathbf{X}_i$ and $\mathbf{X}_j$ are independent.

Now for any three events $\mathbf{X}_i$, $\mathbf{X}_j$ and $\mathbf{X}_k$, $i > j > k$, we have [47, pp.253]

$$\begin{aligned}
&\text{Prob}\{\ \mathbf{X}_i, \mathbf{X}_j, \mathbf{X}_k\ \} \\
&= \text{Prob}\{\ \mathbf{X}_i \mid \mathbf{X}_j, \mathbf{X}_k\ \}\text{Prob}\{\ \mathbf{X}_j \mid \mathbf{X}_k\ \}\text{Prob}\{\ \mathbf{X}_k\ \}
\end{aligned}$$

$$
\begin{aligned}
&= \text{Prob}\{\ D_i \oplus \cdots \oplus D_{j+1} \oplus P_j = b_i \mid P_j = b_j\ \} \\
&\quad \times \text{Prob}\{\ D_j \oplus \cdots \oplus D_{k+1} \oplus P_k = b_j \mid P_k = b_k\ \} \\
&\quad \times \text{Prob}\{\ P_k = b_k\ \} \\
&= \text{Prob}\{\ \mathbf{X}_i \mid \mathbf{X}_j\ \}\text{Prob}\{\ \mathbf{X}_j \mid \mathbf{X}_k\ \}\text{Prob}\{\ \mathbf{X}_k\ \} \\
&= \text{Prob}\{\ \mathbf{X}_i\ \}\text{Prob}\{\ \mathbf{X}_j\ \}\text{Prob}\{\ \mathbf{X}_k\ \} = \frac{1}{8}.
\end{aligned} \tag{A.8}
$$

Hence for any three events, we have

$$
\text{Prob}\{\ \mathbf{X}_i, \mathbf{X}_j, \mathbf{X}_k\ \} = \text{Prob}\{\mathbf{X}_i\}\text{Prob}\{\mathbf{X}_j\}\text{Prob}\{\mathbf{X}_k\}. \tag{A.9}
$$

As a result, any three events $\mathbf{X}_i$, $\mathbf{X}_j$, $\mathbf{X}_k$ are shown to be independent.

Now under the assumption that any $M-1$ ($M \leq N$) events are independent, following the same approach, we can show that

$$
\begin{aligned}
&\text{Prob}\{\ \mathbf{X}_{i_1}, \mathbf{X}_{i_2}, \cdots, \mathbf{X}_{i_M}\ \} \\
&= \text{Prob}\{\mathbf{X}_{i_1}\}\text{Prob}\{\mathbf{X}_{i_2}\}\cdots\text{Prob}\{\mathbf{X}_{i_M}\} = \frac{1}{2^M}.
\end{aligned} \tag{A.10}
$$

So any M events are independent.

Finally, when $M = N$, we have

$$
\begin{aligned}
&\text{Prob}\{\ \mathbf{X}_0, \mathbf{X}_1, \cdots, \mathbf{X}_{N-1}\ \} \\
&= \text{Prob}\{\mathbf{X}_0\}\text{Prob}\{\mathbf{X}_1\}\cdots\text{Prob}\{\mathbf{X}_{N-1}\} = \frac{1}{2^N}.
\end{aligned} \tag{A.11}
$$

This completes the proof of the independence of the precoded sequence $P_0, P_1, \cdots, P_{N-1}$.

The transmitted data a_n, $n = 0, 1, \cdots, N-1$, can be obtained from

$$
a_n = \sqrt{E_b}(2P_n - 1) \tag{A.12}
$$

and they are also mutually independent [47, pp.245].

Appendix B

In Chapter 8, we considered using the widely linear MMSE equalizer for 2-D modulation formats. For many 2-D modulation formats, such as QPSK and 16-QAM, due to a special symmetry in the signal constellation, one can assume that $\mathbf{E}[\mathbf{x}_r\mathbf{x}_r^{\mathbb{T}}] = \mathbf{E}[\mathbf{x}_i\mathbf{x}_i^{\mathbb{T}}] = E_s/2$ and $\mathbf{E}[\mathbf{x}_r\mathbf{x}_i^{\mathbb{T}}] = 0$ where $\mathbf{x} = \mathbf{x}_r + j\mathbf{x}_i$. Instead of eq. (8.7), one can minimize

$$\mathbf{E}\|\Re\{\mathbf{G}_R\mathbf{r}\} - \mathbf{x}_r\|^2 \tag{B.1}$$

and

$$\mathbf{E}\|\Im\{\mathbf{G}_I\mathbf{r}\} - \mathbf{x}_i\|^2 \tag{B.2}$$

to obtain the MMSE equalization matrix $\mathbf{G}_R$ and $\mathbf{G}_I$ for $\mathbf{x}_r$ and $\mathbf{x}_i$, respectively. It is found that in this case $\mathbf{G}_R = \mathbf{G}_I = \mathbf{G}_1$ by the following proof.

The equalization matrices $\mathbf{G}_R$, $\mathbf{G}_I$ and $\mathbf{G}_1$ are all complex matrices, and can be written as $\mathbf{G}_R = \mathbf{G}_{Rx} + j\mathbf{G}_{Ry}$, $\mathbf{G}_I = \mathbf{G}_{Ix} + j\mathbf{G}_{Iy}$ and $\mathbf{G}_1 = \mathbf{G}_{1x} + j\mathbf{G}_{1y}$, respectively.

One may construct $N \times 2M$ matrices

$$\bar{\mathbf{G}}_R = (\mathbf{G}_{Rx} \quad -\mathbf{G}_{Ry}) \tag{B.3}$$

and

$$\bar{\mathbf{G}}_I = (\mathbf{G}_{Ix} \quad -\mathbf{G}_{Iy}). \tag{B.4}$$

Following the same approach as in Section III, the matrices $\bar{\mathbf{G}}_R$ and $\bar{\mathbf{G}}_I$ can be obtained as

$$\bar{\mathbf{G}}_R = \bar{\mathbf{G}}_I = E_s\bar{\mathbf{C}}^{\mathbb{T}}(E_s\bar{\mathbf{C}}\bar{\mathbf{C}}^{\mathbb{T}} + E_s\bar{\mathbf{C}}_2\bar{\mathbf{C}}_2^{\mathbb{T}} + \sigma^2\mathbf{I}_{2M})^{-1} \tag{B.5}$$

where

$$\bar{\mathbf{C}}_2 = \begin{pmatrix} \mathbf{C}_y \\ -\mathbf{C}_x \end{pmatrix}. \tag{B.6}$$

Eq. (8.8) can be written in real-matrix form as

$$\begin{aligned}\bar{\mathbf{G}}_1 &= \begin{pmatrix} \mathbf{G}_{1x} & -\mathbf{G}_{1y} \\ \mathbf{G}_{1y} & \mathbf{G}_{1x} \end{pmatrix} \\ &= E_s \begin{pmatrix} \mathbf{C}_x^{\mathbb{T}} & \mathbf{C}_y^{\mathbb{T}} \\ -\mathbf{C}_y^{\mathbb{T}} & \mathbf{C}_x^{\mathbb{T}} \end{pmatrix} \left(E_s\bar{\mathbf{C}}\bar{\mathbf{C}}^{\mathbb{T}} + E_s\bar{\mathbf{C}}_2\bar{\mathbf{C}}_2^{\mathbb{T}} + \sigma^2\mathbf{I}_{2M}\right)^{-1}.\end{aligned} \tag{B.7}$$

It can be seen that

$$\bar{\mathbf{G}}_R = \bar{\mathbf{G}}_I = \begin{pmatrix} \mathbf{I}_N & \mathbf{0}_N \end{pmatrix} \bar{\mathbf{G}}_1 \tag{B.8}$$

where $\mathbf{0}_N$ is a $N \times N$ zero matrix. Thus, we have

$$\mathbf{G}_{Rx} = \mathbf{G}_{Ix} = \mathbf{G}_{1x} \tag{B.9a}$$

and

$$\mathbf{G}_{Ry} = \mathbf{G}_{Iy} = \mathbf{G}_{1y}. \tag{B.9b}$$

Therefore, $\mathbf{G}_R = \mathbf{G}_I = \mathbf{G}_1$, as required.